DESIGN AND OPTIMIZATION OF A NANOPARTICLE BASED MAGNETIC HYPERTHERMIA DEVICE

by

Serhat Ilgaz Yöner

B.S., in Biomedical Engineering, Yeditepe University, 2016

M.S., in Medical Engineering, Acıbadem University, 2018

Submitted to the Institute of Biomedical Engineering

in partial fulfillment of the requirements

for the degree of

Doctor

of

Philosophy

Boğaziçi University

2025

DESIGN AND OPTIMIZATION OF A NANOPARTICLE BASED MAGNETIC HYPERTHERMIA DEVICE

APPROVED BY:

Prof. Dr. Alpay Özcan (Thesis Advisor)	.....
Prof. Dr. Oğuz Akın	.....
Prof. Dr. Esin Öztürk	.....
Assoc. Prof. Dr. Kemalettin Erbatur	.....
Assist. Prof. Dr. Engin Baysoy	.....

DATE OF APPROVAL: 20 May 2025

ACKNOWLEDGMENTS

First and foremost, I would like to express my deepest gratitude to my advisor Prof. Dr. Alpay Özcan, for his invaluable guidance, unwavering support, and encouragement throughout this journey. His mentor–ship has been instrumental in shaping both this thesis and my growth as a researcher.

I am also grateful to my thesis committee members Prof. Dr. Oğuz Akın, Prof. Dr. Esin Öztürk Işık and Assoc. Prof. Dr. Kemalettin Erbatur, for their valuable feedback and guidance throughout this process. I would like to express my heartfelt gratitude to Assist. Prof. Dr. Engin Baysoy, whose support has been instrumental in paving the path for me in academia. His encouragement and belief in my potential played a crucial role in helping me gain acceptance into this PhD program, and for that, I am forever thankful.

Special thanks to my beloved wife and my baby girl, whose mere presence in my life has been a constant source of motivation and joy. Their smiles and the thought of their future have inspired me to strive for excellence and achieve great things.

Lastly, I sincerely thank Boğaziçi University for providing the financial support (Boğaziçi University Research Fund under grant number 19661) that made this work possible.

ACADEMIC ETHICS AND INTEGRITY STATEMENT

I, Serhat Ilgaz Yöner, hereby certify that I am aware of the Academic Ethics and Integrity Policy issued by the Council of Higher Education (YÖK) and I fully acknowledge all the consequences due to its violation by plagiarism or any other way.

Name :

Signature:

Date:

ABSTRACT

DESIGN AND OPTIMIZATION OF A NANOPARTICLE BASED MAGNETIC HYPERTHERMIA DEVICE

Compared to their healthy counterparts, cancer cells are affected more adversely by higher temperatures which can be achieved with magnetic nanoparticle magnetic hyperthermia (MNP–MH) by elevating the temperature to $41-45\,^{o}$C range. In MNP–MH the energy is transferred between an applied alternating magnetic field (AMF) and MNPs' magnetization. Accordingly, devices producing AMFs are designed around dedicated coils driven by RF amplifiers. Herein, new analytical coil performance criteria were conceived and used in assessing the performance of different coil geometries that were numerically simulated. Subsequently, three best performing geometries were physically implemented and experiments were realized using a novel placeholder grid for physical performance measurements and validating newly defined criteria. An economically viable RF amplifier was designed and built.

Keywords: Amplifier Design, Coil Design, Magnetic Hyperthermia, Nanoparticles.

ÖZET

NANOPARÇACIK TEMELLİ MANYETİK HİPERTERMİ CİHAZI TASARIMI VE OPTİMİZASYONU

Sağlıklı hücrelere kıyasla, kanser hücrelerinin yüksek sıcaklıklara olan dayanımı daha düşüktür. Söz konusu sıcaklıklar, manyetik nanoparçacık temelli olan manyetik hipertermi yöntemiyle sıcaklığın $41-45\,^{\circ}\mathrm{C}$ aralığına yükseltilmesiyle elde edilebilir. Manyetik nanoparçacık temelli olan manyetik hipertermi'de enerji, uygulanan alternatif manyetik alan ile manyetik nanoparçacıkların manyetizasyonu arasında transfer edilir. Buna bağlı olarak, alternatif manyetik alan üreten cihazlar, radyo frekans kuvvetlendiriciler tarafından sürülen özel bobinlere uygun bir biçimde tasarlanır. Bu çalışmada, yeni analitik bobin performans kriterleri geliştirilmiş ve farklı bobin geometrilerinin performansını değerlendirmek amacıyla sayısal analiz yöntemleri kullanılarak söz konusu kriterler uygulanmıştır. Daha sonra, en iyi performans gösteren üç bobin geometrisi üretilmiş ve fiziksel performans ölçümlerinde kullanılmak üzere yenilikçi bir taşıyıcı ızgara sistemi kullanılarak deneyler gerçekleştirilmiş ve yeni tanımlanan kriterler doğrulanmıştır. Ekonomik açıdan uygun bir radyo frekans amplifikatörü tasarlanmış ve üretilmiştir.

Anahtar Sözcükler: Kuvvetlendirici Tasarımı, Bobin Tasarımı, Manyetik Hipertermi, Nanoparçacıklar.

TABLE OF CONTENTS

ACKNOWLEDGMENTS iii
ACADEMIC ETHICS AND INTEGRITY STATEMENT iv
ABSTRACT v
ÖZET vi
LIST OF FIGURES ix
LIST OF TABLES xxxiii
LIST OF SYMBOLS xxxix
LIST OF ABBREVIATIONS xl
1. INTRODUCTION 1
1.1 Hyperthermia Therapy 2
1.2 Magnetic Hyperthermia Coil Optimization 8
2. METHODS AND MATERIALS 18
A Coil Optimization 18
2.1 Coil Simulations 19
2.2 Physical Implementation and Coil Measurements 23
2.3 Localizing and Fixing Measurement Points 26
2.4 Pickup Coil Selection 27
2.5 Magnetic Flux Density Measurements 29
2.6 Magnetic Hyperthermia Measurements 30
2.7 Design and Implementation of the AMF Signal Generator 33
2.8 Design and Implementation of the Impedance Matching Board 37
2.9 Power Calculations 41
B Novel Liquid Cooling System 42
2.10 Cooling System Simulations 42
2.11 Performance Index 46
2.12 Machine Learning Predictions 47
3. RESULTS 48
A Coil Optimization 48
3.1 Solenoid Coil with Round Wire Measurements 51

3.2 Solenoid Coil with Round Litz Wire Measurements 83
3.3 Helmholtz Coil with Round Wire Measurements 117
B Novel Liquid Cooling System 152
3.4 Electromagnetic Benchmarking 152
3.5 Thermal Benchmarking 159
3.6 Performance Index 166
4. DISCUSSION 171
A Coil Optimization 171
B Novel Liquid Cooling System 174
5. CONCLUSION 179
REFERENCES 183

LIST OF FIGURES

Figure 1.1 (a) Mechanism of Néel Relaxation; magnetic orientation change (b) Mechanism of Brownian Relaxation; physical rotation. 3

Figure 1.2 Schematic describing basic parts of a MH device. 4

Figure 1.3 Air core coil designed in COMSOL simulation program; showing (a) coil geometry, (b) magnetic field color map of horizontal middle slice and (c) area with 10% magnetic flux density deviation. 8

Figure 1.4 (a) Basic RLC model schematic and (b) magnitude plot consisting real and imaginary parts of the impedance for a basic solenoid coil. At the resonant frequency marked with a dashed line, the imaginary part changes sign ($R_s = 1\ \Omega$, $L_{coil} = 20$ H, $C_p = 1$ F). 10

Figure 1.5 Direction of magnetic field lines for (a) $f \ll f_0$ and (b) $f \gg f_0$. 12

Figure 2.1 Cross sectional view of coil wire types investigated during finite element analysis (FEA) simulations; (a) round wire, (b) square wire, 7 strand (c) round Litz wire and (d) hexagonal Litz wire (three turn wound each). 19

Figure 2.2 Physical coils: $N_w = 10$ turn solenoid coils (a) with round wire, (b) with round Litz wire and (c) Helmholtz coil with round wire. 23

Figure 2.3 In–house designed and 3D printed ABS guide frame; conduit with pickup coil, guide and guide holder tray with Helmholtz coil with round wire. 26

Figure 2.4 In–house designed and 3D printed ABS conduits holding pickup coils with (a) 3, (b) 6 and (c) 9 mm diameters. 27

Figure 2.5 Transversal view of 21 measurement points within MH coils, horizontally and vertically 6 mm apart. 29

Figure 2.6 In–house designed and 3D printed ABS cup designed to contain MNPs during MH measurements. 30

Figure 2.7 Top view of the designed RF generator. 33

Figure 2.8 Schematic drawing of the whole RF Generator circuit. 34

Figure 2.9 PCB design of the RF Generator circuit at Eagle PCB design environment. Red, blue, magenta, cyan and yellow colors indicate top layer copper traces, bottom layer copper traces, component names–positions and PCB edges respectively. 36

Figure 2.10 Impedance matching board. 37

Figure 2.11 Simple schematics showing all 3 designed impedance matching circuits with a 3 way slider switch for multiple MH coils. 37

Figure 2.12 Simplified Thevenin equivalent models of an amplifier's input and output. 39

Figure 2.13 Different coil cooling systems; (a) the conventional passive, (b) the conventional liquid with DLC and (c) novel liquid with various microchannel radii of 0.25, 0.30, and 0.35 mm. (Arrows indicate cooling liquid flow directions, (b) semi-transparent region around coil wires indicate outer shell of the DLC system). 45

Figure 3.1 Histograms of the spatial distributions of the time–domain RMS magnetic flux density (left) and corresponding amount of temperature rise with 166.5 (middle) and 120 mg/mL (right) MNPs for the solenoid coil with round Litz wire (blue), with round wire (maroon) and Helmholtz coil with round wire (green). 49

Figure 3.2 Amount of temperature rise, ΔT measured from two different SPION concentrations inside of solenoid coil with round wire design at three different axial positions; −12, 0, +12 mm and five different transverse positions; 0, −6 and +6 mm horizontally, −6 and +6 mm vertically for each axial position (15 positions in total) inside of the coil gap. 50

Figure 3.3 Time–domain root mean square magnetic flux density, $tRMS_B$ values measured from solenoid coil with round wire design for all power levels at three different axial positions; −6, 0, +6 mm and 21 different transverse positions; 6 mm apart at each axial position (63 positions in total, for each power level). 51

Figure 3.4 Time–domain root mean square magnetic flux density, $tRMS_B$ (left) and corresponding amount of temperature rise, ΔT with 166.5 (middle) and 120 mg/mL (right) SPION concentration values measured from solenoid coil with round wire design for 100% power level at three different axial positions; −6, 0, +6 mm. 52

Figure 3.5 Time–domain root mean square magnetic flux density, $tRMS_B$ (top) values measured from solenoid coil with round wire design for 75% power level at three different axial positions; −6, 0, +6 mm. 53

Figure 3.6 Time–domain root mean square magnetic flux density, $tRMS_B$ (top) values measured from solenoid coil with round wire design for 50% power level at three different axial positions; −6, 0, +6 mm. 54

Figure 3.7 Time–domain root mean square magnetic flux density, $tRMS_B$ (top) values measured from solenoid coil with round wire design for 25% power level at three different axial positions; −6, 0, +6 mm. 55

Figure 3.8 Time–domain root mean square magnetic flux density, $tRMS_B$ (top) values measured from solenoid coil with round wire design for 10% power level at three different axial positions; −6, 0, +6 mm. 56

Figure 3.9 40 minute temperature vs. time graph during MH experiments conducted with distilled water as the control experiment using solenoid coil with round wire at 0 mm axial position, 0 mm (center) position. Temperature–time data was fitted to a line using linear regression for analyzing positional related effects. 57

Figure 3.10 40 minute temperature rise vs. time graph during MH experiments conducted with 166.5 mg/mL concentration SPION using solenoid coil with round wire at −6 mm axial position, +6 mm off Y-axis. Temperature–time data was fitted to a line using linear regression for analyzing positional related effects. 57

Figure 3.11 40 minute temperature rise vs. time graph during MH experiments conducted with 166.5 mg/mL concentration SPION using solenoid coil with round wire at −6 mm axial position, −6 mm off X-axis. Temperature–time data was fitted to a line using linear regression for analyzing positional related effects. 58

Figure 3.12 40 minute temperature rise vs. time graph during MH experiments conducted with 166.5 mg/mL concentration SPION using solenoid coil with round wire at −6 mm axial position, 0 mm (center) position. Temperature–time data was fitted to a line using linear regression for analyzing positional related effects. 58

Figure 3.13 40 minute temperature rise vs. time graph during MH experiments conducted with 166.5 mg/mL concentration SPION using solenoid coil with round wire at −6 mm axial position, +6 mm off X-axis. Temperature–time data was fitted to a line using linear regression for analyzing positional related effects. 59

Figure 3.14 40 minute temperature rise vs. time graph during MH experiments conducted with 166.5 mg/mL concentration SPION using solenoid coil with round wire at −6 mm axial position, −6 mm off Y-axis. Temperature–time data was fitted to a line using linear regression for analyzing positional related effects. 59

Figure 3.15 40 minute temperature rise vs. time graph during MH experiments conducted with 166.5 mg/mL concentration SPION using solenoid coil with round wire at 0 mm axial position, +6 mm off Y-axis. Temperature–time data was fitted to a line using linear regression for analyzing positional related effects. 60

Figure 3.16 40 minute temperature rise vs. time graph during MH experiments conducted with 166.5 mg/mL concentration SPION using solenoid coil with round wire at 0 mm axial position, −6 mm off X-axis. Temperature–time data was fitted to a line using linear regression for analyzing positional related effects. 60

Figure 3.17 40 minute temperature rise vs. time graph during MH experiments conducted with 166.5 mg/mL concentration SPION using solenoid coil with round wire at 0 mm axial position, 0 mm (center) position. Temperature–time data was fitted to a line using linear regression for analyzing positional related effects. 61

Figure 3.18 40 minute temperature rise vs. time graph during MH experiments conducted with 166.5 mg/mL concentration SPION using solenoid coil with round wire at 0 mm axial position, +6 mm off X-axis. Temperature–time data was fitted to a line using linear regression for analyzing positional related effects. 61

Figure 3.19 40 minute temperature rise vs. time graph during MH experiments conducted with 166.5 mg/mL concentration SPION using solenoid coil with round wire at 0 mm axial position, −6 mm off Y-axis. Temperature–time data was fitted to a line using linear regression for analyzing positional related effects. 62

Figure 3.20 40 minute temperature rise vs. time graph during MH experiments conducted with 166.5 mg/mL concentration SPION using solenoid coil with round wire at +6 mm axial position, +6 mm off Y-axis. Temperature–time data was fitted to a line using linear regression for analyzing positional related effects. 62

Figure 3.21 40 minute temperature rise vs. time graph during MH experiments conducted with 166.5 mg/mL concentration SPION using solenoid coil with round wire at +6 mm axial position, −6 mm off X-axis. Temperature–time data was fitted to a line using linear regression for analyzing positional related effects. 63

Figure 3.22 40 minute temperature rise vs. time graph during MH experiments conducted with 166.5 mg/mL concentration SPION using solenoid coil with round wire at +6 mm axial position, 0 mm (center) position. Temperature–time data was fitted to a line using linear regression for analyzing positional related effects. 63

Figure 3.23 40 minute temperature rise vs. time graph during MH experiments conducted with 166.5 mg/mL concentration SPION using solenoid coil with round wire at +6 mm axial position, +6 mm off X-axis. Temperature–time data was fitted to a line using linear regression for analyzing positional related effects. 64

Figure 3.24 40 minute temperature rise vs. time graph during MH experiments conducted with 166.5 mg/mL concentration SPION using solenoid coil with round wire at +6 mm axial position, −6 mm off Y-axis. Temperature–time data was fitted to a line using linear regression for analyzing positional related effects. 64

Figure 3.25 40 minute temperature rise vs. time graph during MH experiments conducted with 120 mg/mL concentration SPION using solenoid coil with round wire at −6 mm axial position, +6 mm off Y-axis. Temperature–time data was fitted to a line using linear regression for analyzing positional related effects. 65

Figure 3.26 40 minute temperature rise vs. time graph during MH experiments conducted with 120 mg/mL concentration SPION using solenoid coil with round wire at −6 mm axial position, −6 mm off X-axis. Temperature–time data was fitted to a line using linear regression for analyzing positional related effects. 65

Figure 3.27 40 minute temperature rise vs. time graph during MH experiments conducted with 120 mg/mL concentration SPION using solenoid coil with round wire at −6 mm axial position, 0 mm (center) position. Temperature–time data was fitted to a line using linear regression for analyzing positional related effects. 66

Figure 3.28 40 minute temperature rise vs. time graph during MH experiments conducted with 120 mg/mL concentration SPION using solenoid coil with round wire at −6 mm axial position, +6 mm off X-axis. Temperature–time data was fitted to a line using linear regression for analyzing positional related effects. 66

Figure 3.29 40 minute temperature rise vs. time graph during MH experiments conducted with 120 mg/mL concentration SPION using solenoid coil with round wire at −6 mm axial position, −6 mm off Y-axis. Temperature–time data was fitted to a line using linear regression for analyzing positional related effects. 67

Figure 3.30 40 minute temperature rise vs. time graph during MH experiments conducted with 120 mg/mL concentration SPION using solenoid coil with round wire at 0 mm axial position, +6 mm off Y-axis. Temperature–time data was fitted to a line using linear regression for analyzing positional related effects. 67

Figure 3.31 40 minute temperature rise vs. time graph during MH experiments conducted with 120 mg/mL concentration SPION using solenoid coil with round wire at 0 mm axial position, −6 mm off X-axis. Temperature–time data was fitted to a line using linear regression for analyzing positional related effects. 68

Figure 3.32 40 minute temperature rise vs. time graph during MH experiments conducted with 120 mg/mL concentration SPION using solenoid coil with round wire at 0 mm axial position, 0 mm (center) position. Temperature–time data was fitted to a line using linear regression for analyzing positional related effects. 68

Figure 3.33 40 minute temperature rise vs. time graph during MH experiments conducted with 120 mg/mL concentration SPION using solenoid coil with round wire at 0 mm axial position, +6 mm off X-axis. Temperature–time data was fitted to a line using linear regression for analyzing positional related effects. 69

Figure 3.34 40 minute temperature rise vs. time graph during MH experiments conducted with 120 mg/mL concentration SPION using solenoid coil with round wire at 0 mm axial position, −6 mm off Y-axis. Temperature–time data was fitted to a line using linear regression for analyzing positional related effects. 69

Figure 3.35 40 minute temperature rise vs. time graph during MH experiments conducted with 120 mg/mL concentration SPION using solenoid coil with round wire at +6 mm axial position, +6 mm off Y-axis. Temperature–time data was fitted to a line using linear regression for analyzing positional related effects. 70

Figure 3.36 40 minute temperature rise vs. time graph during MH experiments conducted with 120 mg/mL concentration SPION using solenoid coil with round wire at +6 mm axial position, −6 mm off X-axis. Temperature–time data was fitted to a line using linear regression for analyzing positional related effects. 70

Figure 3.37 40 minute temperature rise vs. time graph during MH experiments conducted with 120 mg/mL concentration SPION using solenoid coil with round wire at +6 mm axial position, 0 mm (center) position. Temperature–time data was fitted to a line using linear regression for analyzing positional related effects. 71

Figure 3.38 40 minute temperature rise vs. time graph during MH experiments conducted with 120 mg/mL concentration SPION using solenoid coil with round wire at +6 mm axial position, +6 mm off X-axis. Temperature–time data was fitted to a line using linear regression for analyzing positional related effects. 71

Figure 3.39 40 minute temperature rise vs. time graph during MH experiments conducted with 120 mg/mL concentration SPION using solenoid coil with round wire at +6 mm axial position, −6 mm off Y-axis. Temperature–time data was fitted to a line using linear regression for analyzing positional related effects. 72

Figure 3.40 Slope of linear regression fit for 40 minute temperature rise vs. time graph during MH experiments conducted with 120 mg/mL concentration SPION using solenoid coil with round wire at three axial positions inside of the coil gap and five different transverse positions. 73

Figure 3.41 Slices showing slope of linear regression fit for 40 minute temperature rise vs. time graph during MH experiments conducted with 120 (top) and 166.5 mg/mL (bottom) SPION concentrations using solenoid coil with round wire at three axial positions. 74

Figure 3.42 Amount of temperature rise, ΔT measured from two different SPION concentrations inside of solenoid coil with round Litz wire design at three different axial positions; −12, 0, +12 mm and five different transverse positions; 0, −6 and +6 mm horizontally, −6 and +6 mm vertically for each axial position (15 positions in total) inside of the coil gap. 84

Figure 3.43 Time–domain root mean square magnetic flux density, $tRMS_B$ values measured in mT from solenoid coil with round Litz wire design for all power levels at three different axial positions; −6, 0, +6 mm and 21 different transverse positions; 6 mm apart at each axial position (63 positions in total, for each power level). 85

Figure 3.44 Time–domain root mean square magnetic flux density, $tRMS_B$ (left) and corresponding amount of temperature rise, ΔT with 166.5 (middle) and 120 mg/mL (right) SPION concentrations values measured from solenoid coil with round Litz wire design for 100% power level at three different axial positions; −6, 0, +6 mm. 86

Figure 3.45 Time–domain root mean square magnetic flux density, $tRMS_B$ (top) values measured from solenoid coil with round Litz wire design for 75% power level at three different axial positions; −6, 0, +6 mm. 87

Figure 3.46 Time–domain root mean square magnetic flux density, $tRMS_B$ (top) values measured from solenoid coil with round Litz wire design for 50% power level at three different axial positions; −6, 0, +6 mm. 88

Figure 3.47 Time–domain root mean square magnetic flux density, $tRMS_B$ (top) values measured from solenoid coil with round Litz wire design for 25% power level at three different axial positions; −6, 0, +6 mm. 89

Figure 3.48 Time–domain root mean square magnetic flux density, $tRMS_B$ (top) values measured from solenoid coil with round Litz wire design for 10% power level at three different axial positions; −6, 0, +6 mm. 90

Figure 3.49 40 minute temperature vs. time graph during MH experiments conducted with distilled water as the control experiment using solenoid coil with round Litz wire at 0 mm axial position, 0 mm (center) position. Temperature–time data was fitted to a line using linear regression for analyzing positional related effects. 91

Figure 3.50 40 minute temperature rise vs. time graph during MH experiments conducted with 166.5 mg/mL concentration SPION using solenoid coil with round Litz wire at −6 mm axial position, +6 mm off Y-axis. Temperature–time data was fitted to a line using linear regression for analyzing positional related effects. 91

Figure 3.51 40 minute temperature rise vs. time graph during MH experiments conducted with 166.5 mg/mL concentration SPION using solenoid coil with round Litz wire at −6 mm axial position, −6 mm off X-axis. Temperature–time data was fitted to a line using linear regression for analyzing positional related effects. 92

Figure 3.52 40 minute temperature rise vs. time graph during MH experiments conducted with 166.5 mg/mL concentration SPION using solenoid coil with round Litz wire at −6 mm axial position, 0 mm (center) position. Temperature–time data was fitted to a line using linear regression for analyzing positional related effects. 92

Figure 3.53 40 minute temperature rise vs. time graph during MH experiments conducted with 166.5 mg/mL concentration SPION using solenoid coil with round Litz wire at −6 mm axial position, +6 mm off X-axis. Temperature–time data was fitted to a line using linear regression for analyzing positional related effects. 93

Figure 3.54 40 minute temperature rise vs. time graph during MH experiments conducted with 166.5 mg/mL concentration SPION using solenoid coil with round Litz wire at −6 mm axial position, −6 mm off Y-axis. Temperature–time data was fitted to a line using linear regression for analyzing positional related effects. 93

Figure 3.55 40 minute temperature rise vs. time graph during MH experiments conducted with 166.5 mg/mL concentration SPION using solenoid coil with round Litz wire at 0 mm axial position, +6 mm off Y-axis. Temperature–time data was fitted to a line using linear regression for analyzing positional related effects. 94

Figure 3.56 40 minute temperature rise vs. time graph during MH experiments conducted with 166.5 mg/mL concentration SPION using solenoid coil with round Litz wire at 0 mm axial position, −6 mm off X-axis. Temperature–time data was fitted to a line using linear regression for analyzing positional related effects. 94

Figure 3.57 40 minute temperature rise vs. time graph during MH experiments conducted with 166.5 mg/mL concentration SPION using solenoid coil with round Litz wire at 0 mm axial position, 0 mm (center) position. Temperature–time data was fitted to a line using linear regression for analyzing positional related effects. 95

Figure 3.58 40 minute temperature rise vs. time graph during MH experiments conducted with 166.5 mg/mL concentration SPION using solenoid coil with round Litz wire at 0 mm axial position, +6 mm off X-axis. Temperature–time data was fitted to a line using linear regression for analyzing positional related effects. 95

Figure 3.59 40 minute temperature rise vs. time graph during MH experiments conducted with 166.5 mg/mL concentration SPION using solenoid coil with round Litz wire at 0 mm axial position, −6 mm off Y-axis. Temperature–time data was fitted to a line using linear regression for analyzing positional related effects. 96

Figure 3.60 40 minute temperature rise vs. time graph during MH experiments conducted with 166.5 mg/mL concentration SPION using solenoid coil with round Litz wire at +6 mm axial position, +6 mm off Y-axis. Temperature–time data was fitted to a line using linear regression for analyzing positional related effects. 96

Figure 3.61 40 minute temperature rise vs. time graph during MH experiments conducted with 166.5 mg/mL concentration SPION using solenoid coil with round Litz wire at +6 mm axial position, −6 mm off X-axis. Temperature–time data was fitted to a line using linear regression for analyzing positional related effects. 97

Figure 3.62 40 minute temperature rise vs. time graph during MH experiments conducted with 166.5 mg/mL concentration SPION using solenoid coil with round Litz wire at +6 mm axial position, 0 mm (center) position. Temperature–time data was fitted to a line using linear regression for analyzing positional related effects. 97

Figure 3.63 40 minute temperature rise vs. time graph during MH experiments conducted with 166.5 mg/mL concentration SPION using solenoid coil with round Litz wire at +6 mm axial position, +6 mm off X-axis. Temperature–time data was fitted to a line using linear regression for analyzing positional related effects. 98

Figure 3.64 40 minute temperature rise vs. time graph during MH experiments conducted with 166.5 mg/mL concentration SPION using solenoid coil with round Litz wire at +6 mm axial position, −6 mm off Y-axis. Temperature–time data was fitted to a line using linear regression for analyzing positional related effects. 98

Figure 3.65 40 minute temperature rise vs. time graph during MH experiments conducted with 120 mg/mL concentration SPION using solenoid coil with round Litz wire at −6 mm axial position, +6 mm off Y-axis. Temperature–time data was fitted to a line using linear regression for analyzing positional related effects. 99

Figure 3.66 40 minute temperature rise vs. time graph during MH experiments conducted with 120 mg/mL concentration SPION using solenoid coil with round Litz wire at −6 mm axial position, −6 mm off X-axis. Temperature–time data was fitted to a line using linear regression for analyzing positional related effects. 99

Figure 3.67 40 minute temperature rise vs. time graph during MH experiments conducted with 120 mg/mL concentration SPION using solenoid coil with round Litz wire at −6 mm axial position, 0 mm (center) position. Temperature–time data was fitted to a line using linear regression for analyzing positional related effects. 100

Figure 3.68 40 minute temperature rise vs. time graph during MH experiments conducted with 120 mg/mL concentration SPION using solenoid coil with round Litz wire at −6 mm axial position, +6 mm off X-axis. Temperature–time data was fitted to a line using linear regression for analyzing positional related effects. 100

Figure 3.69 40 minute temperature rise vs. time graph during MH experiments conducted with 120 mg/mL concentration SPION using solenoid coil with round Litz wire at −6 mm axial position, −6 mm off Y-axis. Temperature–time data was fitted to a line using linear regression for analyzing positional related effects. 101

Figure 3.70 40 minute temperature rise vs. time graph during MH experiments conducted with 120 mg/mL concentration SPION using solenoid coil with round Litz wire at 0 mm axial position, +6 mm off Y-axis. Temperature–time data was fitted to a line using linear regression for analyzing positional related effects. 101

Figure 3.71 40 minute temperature rise vs. time graph during MH experiments conducted with 120 mg/mL concentration SPION using solenoid coil with round Litz wire at 0 mm axial position, −6 mm off X-axis. Temperature–time data was fitted to a line using linear regression for analyzing positional related effects. 102

Figure 3.72 40 minute temperature rise vs. time graph during MH experiments conducted with 120 mg/mL concentration SPION using solenoid coil with round Litz wire at 0 mm axial position, 0 mm (center) position. Temperature–time data was fitted to a line using linear regression for analyzing positional related effects. 102

Figure 3.73 40 minute temperature rise vs. time graph during MH experiments conducted with 120 mg/mL concentration SPION using solenoid coil with round Litz wire at 0 mm axial position, +6 mm off X-axis. Temperature–time data was fitted to a line using linear regression for analyzing positional related effects. 103

Figure 3.74 40 minute temperature rise vs. time graph during MH experiments conducted with 120 mg/mL concentration SPION using solenoid coil with round Litz wire at 0 mm axial position, −6 mm off Y-axis. Temperature–time data was fitted to a line using linear regression for analyzing positional related effects. 103

Figure 3.75 40 minute temperature rise vs. time graph during MH experiments conducted with 120 mg/mL concentration SPION using solenoid coil with round Litz wire at +6 mm axial position, +6 mm off Y-axis. Temperature–time data was fitted to a line using linear regression for analyzing positional related effects. 104

Figure 3.76 40 minute temperature rise vs. time graph during MH experiments conducted with 120 mg/mL concentration SPION using solenoid coil with round Litz wire at +6 mm axial position, −6 mm off X-axis. Temperature–time data was fitted to a line using linear regression for analyzing positional related effects. 104

Figure 3.77 40 minute temperature rise vs. time graph during MH experiments conducted with 120 mg/mL concentration SPION using solenoid coil with round Litz wire at +6 mm axial position, 0 mm (center) position. Temperature–time data was fitted to a line using linear regression for analyzing positional related effects. 105

Figure 3.78 40 minute temperature rise vs. time graph during MH experiments conducted with 120 mg/mL concentration SPION using solenoid coil with round Litz wire at +6 mm axial position, +6 mm off X-axis. Temperature–time data was fitted to a line using linear regression for analyzing positional related effects. 105

Figure 3.79 40 minute temperature rise vs. time graph during MH experiments conducted with 120 mg/mL concentration SPION using solenoid coil with round Litz wire at +6 mm axial position, −6 mm off Y-axis. Temperature–time data was fitted to a line using linear regression for analyzing positional related effects. 106

Figure 3.80 Slope of linear regression fit for 40 minute temperature rise vs. time graph during MH experiments conducted with 120 mg/mL concentration SPION using solenoid coil with round Litz wire at three axial positions inside of the coil gap and five different transverse positions. 107

Figure 3.81 Slices showing slope of linear regression fit for 40 minute temperature rise vs. time graph during MH experiments conducted with 120 (top) and 166.5 mg/mL (bottom) SPION concentrations using solenoid coil with round Litz wire at three axial positions. 108

Figure 3.82 Amount of temperature rise, ΔT measured from two different SPION concentrations inside of Helmholtz coil with round wire design at three different axial positions; −12, 0, +12 mm and five different transverse positions; 0, −6 and +6 mm horizontally, −6 and +6 mm vertically for each axial position (15 positions in total) inside of the coil gap. 118

Figure 3.83 Time–domain root mean square magnetic flux density, $tRMS_B$ values measured from Helmholtz coil with round wire design for all power levels at three different axial positions; −6, 0, +6 mm and 21 different transverse positions; 6 mm apart at each axial position (63 positions in total, for each power level). 119

Figure 3.84 Time–domain root mean square magnetic flux density, $tRMS_B$ (left) and corresponding amount of temperature rise, ΔT with 166.5 (middle) and 120 mg/mL (right) SPION concentration values measured from Helmholtz coil with round wire design for 100% power level at three different axial positions; −6, 0, +6 mm. 120

Figure 3.85 Time–domain root mean square magnetic flux density, $tRMS_B$ (top) values measured from Helmholtz coil with round wire design for 75% power level at three different axial positions; −6, 0, +6 mm. 121

Figure 3.86 Time–domain root mean square magnetic flux density, $tRMS_B$ (top) values measured from Helmholtz coil with round wire design for 50% power level at three different axial positions; −6, 0, +6 mm. 122

Figure 3.87 Time–domain root mean square magnetic flux density, $tRMS_B$ (top) values measured from Helmholtz coil with round wire design for 25% power level at three different axial positions; −6, 0, +6 mm. 123

Figure 3.88 Time–domain root mean square magnetic flux density, $tRMS_B$ (top) values measured from Helmholtz coil with round wire design for 10% power level at three different axial positions; −6, 0, +6 mm. 124

Figure 3.89 40 minute temperature vs. time graph during MH experiments conducted with distilled water as the control experiment using Helmholtz coil with round wire at 0 mm axial position, 0 mm (center) position. Temperature–time data was fitted to a line using linear regression for analyzing positional related effects. 125

Figure 3.90 40 minute temperature rise vs. time graph during MH experiments conducted with 166.5 mg/mL concentration SPION using Helmholtz coil with round wire at −6 mm axial position, +6 mm off Y-axis. Temperature–time data was fitted to a line using linear regression for analyzing positional related effects. 125

Figure 3.91 40 minute temperature rise vs. time graph during MH experiments conducted with 166.5 mg/mL concentration SPION using Helmholtz coil with round wire at −6 mm axial position, −6 mm off X-axis. Temperature–time data was fitted to a line using linear regression for analyzing positional related effects. 126

Figure 3.92 40 minute temperature rise vs. time graph during MH experiments conducted with 166.5 mg/mL concentration SPION using Helmholtz coil with round wire at −6 mm axial position, 0 mm (center) position. Temperature–time data was fitted to a line using linear regression for analyzing positional related effects. 126

Figure 3.93 40 minute temperature rise vs. time graph during MH experiments conducted with 166.5 mg/mL concentration SPION using Helmholtz coil with round wire at −6 mm axial position, +6 mm off X-axis. Temperature–time data was fitted to a line using linear regression for analyzing positional related effects. 127

Figure 3.94 40 minute temperature rise vs. time graph during MH experiments conducted with 166.5 mg/mL concentration SPION using Helmholtz coil with round wire at −6 mm axial position, −6 mm off Y-axis. Temperature–time data was fitted to a line using linear regression for analyzing positional related effects. 127

Figure 3.95 40 minute temperature rise vs. time graph during MH experiments conducted with 166.5 mg/mL concentration SPION using Helmholtz coil with round wire at 0 mm axial position, +6 mm off Y-axis. Temperature–time data was fitted to a line using linear regression for analyzing positional related effects. 128

Figure 3.96 40 minute temperature rise vs. time graph during MH experiments conducted with 166.5 mg/mL concentration SPION using Helmholtz coil with round wire at 0 mm axial position, −6 mm off X-axis. Temperature–time data was fitted to a line using linear regression for analyzing positional related effects. 128

Figure 3.97 40 minute temperature rise vs. time graph during MH experiments conducted with 166.5 mg/mL concentration SPION using Helmholtz coil with round wire at 0 mm axial position, 0 mm (center) position. Temperature–time data was fitted to a line using linear regression for analyzing positional related effects. 129

Figure 3.98 40 minute temperature rise vs. time graph during MH experiments conducted with 166.5 mg/mL concentration SPION using Helmholtz coil with round wire at 0 mm axial position, +6 mm off X-axis. Temperature–time data was fitted to a line using linear regression for analyzing positional related effects. 129

Figure 3.99 40 minute temperature rise vs. time graph during MH experiments conducted with 166.5 mg/mL concentration SPION using Helmholtz coil with round wire at 0 mm axial position, −6 mm off Y-axis. Temperature–time data was fitted to a line using linear regression for analyzing positional related effects. 130

Figure 3.100 40 minute temperature rise vs. time graph during MH experiments conducted with 166.5 mg/mL concentration SPION using Helmholtz coil with round wire at +6 mm axial position, +6 mm off Y-axis. Temperature–time data was fitted to a line using linear regression for analyzing positional related effects. 130

Figure 3.101 40 minute temperature rise vs. time graph during MH experiments conducted with 166.5 mg/mL concentration SPION using Helmholtz coil with round wire at +6 mm axial position, −6 mm off X-axis. Temperature–time data was fitted to a line using linear regression for analyzing positional related effects. 131

Figure 3.102 40 minute temperature rise vs. time graph during MH experiments conducted with 166.5 mg/mL concentration SPION using Helmholtz coil with round wire at +6 mm axial position, 0 mm (center) position. Temperature–time data was fitted to a line using linear regression for analyzing positional related effects. 131

Figure 3.103 40 minute temperature rise vs. time graph during MH experiments conducted with 166.5 mg/mL concentration SPION using Helmholtz coil with round wire at +6 mm axial position, +6 mm off X-axis. Temperature–time data was fitted to a line using linear regression for analyzing positional related effects. 132

Figure 3.104 40 minute temperature rise vs. time graph during MH experiments conducted with 166.5 mg/mL concentration SPION using Helmholtz coil with round wire at +6 mm axial position, −6 mm off Y-axis. Temperature–time data was fitted to a line using linear regression for analyzing positional related effects. 132

Figure 3.105 40 minute temperature rise vs. time graph during MH experiments conducted with 120 mg/mL concentration SPION using Helmholtz coil with round wire at −6 mm axial position, +6 mm off Y-axis. Temperature–time data was fitted to a line using linear regression for analyzing positional related effects. 133

Figure 3.106 40 minute temperature rise vs. time graph during MH experiments conducted with 120 mg/mL concentration SPION using Helmholtz coil with round wire at −6 mm axial position, −6 mm off X-axis. Temperature–time data was fitted to a line using linear regression for analyzing positional related effects. 133

Figure 3.107 40 minute temperature rise vs. time graph during MH experiments conducted with 120 mg/mL concentration SPION using Helmholtz coil with round wire at −6 mm axial position, 0 mm (center) position. Temperature–time data was fitted to a line using linear regression for analyzing positional related effects. 134

Figure 3.108 40 minute temperature rise vs. time graph during MH experiments conducted with 120 mg/mL concentration SPION using Helmholtz coil with round wire at −6 mm axial position, +6 mm off X-axis. Temperature–time data was fitted to a line using linear regression for analyzing positional related effects. 134

Figure 3.109 40 minute temperature rise vs. time graph during MH experiments conducted with 120 mg/mL concentration SPION using Helmholtz coil with round wire at −6 mm axial position, −6 mm off Y-axis. Temperature–time data was fitted to a line using linear regression for analyzing positional related effects. 135

Figure 3.110 40 minute temperature rise vs. time graph during MH experiments conducted with 120 mg/mL concentration SPION using Helmholtz coil with round wire at 0 mm axial position, +6 mm off Y-axis. Temperature–time data was fitted to a line using linear regression for analyzing positional related effects. 135

Figure 3.111 40 minute temperature rise vs. time graph during MH experiments conducted with 120 mg/mL concentration SPION using Helmholtz coil with round wire at 0 mm axial position, −6 mm off X-axis. Temperature–time data was fitted to a line using linear regression for analyzing positional related effects. 136

Figure 3.112 40 minute temperature rise vs. time graph during MH experiments conducted with 120 mg/mL concentration SPION using Helmholtz coil with round wire at 0 mm axial position, 0 mm (center) position. Temperature–time data was fitted to a line using linear regression for analyzing positional related effects. 136

Figure 3.113 40 minute temperature rise vs. time graph during MH experiments conducted with 120 mg/mL concentration SPION using Helmholtz coil with round wire at 0 mm axial position, +6 mm off X-axis. Temperature–time data was fitted to a line using linear regression for analyzing positional related effects. 137

Figure 3.114 40 minute temperature rise vs. time graph during MH experiments conducted with 120 mg/mL concentration SPION using Helmholtz coil with round wire at 0 mm axial position, −6 mm off Y-axis. Temperature–time data was fitted to a line using linear regression for analyzing positional related effects. 137

Figure 3.115 40 minute temperature rise vs. time graph during MH experiments conducted with 120 mg/mL concentration SPION using Helmholtz coil with round wire at +6 mm axial position, +6 mm off Y-axis. Temperature–time data was fitted to a line using linear regression for analyzing positional related effects. 138

Figure 3.116 40 minute temperature rise vs. time graph during MH experiments conducted with 120 mg/mL concentration SPION using Helmholtz coil with round wire at +6 mm axial position, −6 mm off X-axis. Temperature–time data was fitted to a line using linear regression for analyzing positional related effects. 138

Figure 3.117 40 minute temperature rise vs. time graph during MH experiments conducted with 120 mg/mL concentration SPION using Helmholtz coil with round wire at +6 mm axial position, 0 mm (center) position. Temperature–time data was fitted to a line using linear regression for analyzing positional related effects. 139

Figure 3.118 40 minute temperature rise vs. time graph during MH experiments conducted with 120 mg/mL concentration SPION using Helmholtz coil with round wire at +6 mm axial position, +6 mm off X-axis. Temperature–time data was fitted to a line using linear regression for analyzing positional related effects. 139

Figure 3.119 40 minute temperature rise vs. time graph during MH experiments conducted with 120 mg/mL concentration SPION using Helmholtz coil with round wire at +6 mm axial position, −6 mm off Y-axis. Temperature–time data was fitted to a line using linear regression for analyzing positional related effects. 140

Figure 3.120 Slope of linear regression fit for 40 minute temperature rise vs. time graph during MH experiments conducted with 120 mg/mL concentration SPION using Helmholtz coil with round wire at three axial positions inside of the coil gap and five different transverse positions. 141

Figure 3.121 Slices showing slope of linear regression fit for 40 minute temperature rise vs. time graph during MH experiments conducted with 120 (top) and 166.5 mg/mL (bottom) SPION concentrations using Helmholtz coil with round wire at three axial positions. 142

Figure 3.122 Basic simulation results comparing 2D slice plots of the spatial maximum current density normal, smJ in solid coil wires and coil wires with microchannel radius of 0.25 mm at 0.1 and 2.9 MHz applied frequencies. Solid coil wire results are shown at (a) 0.1, and (b) 2.9 MHz, while results for coil wires with microchannel radius of 0.25 mm are shown at (c) 0.1, and (d) 2.9 MHz. (The color bar on the right indicates the magnitude of current density normal $\times 10^7$ A/m^2). 152

Figure 3.123 Simulation results showing 2D slice plots of the spatial maximum current density normal, smJ in coil wires at 0.1 MHz applied frequency for all cooling systems; (a) conventional passive, (b) conventional liquid, and (c–e) novel liquid with microchannel radii of 0.25, 0.30, and 0.35 mm, respectively. (The color bar on the right indicates the magnitude of current density normal $\times 10^8$ A/m^2). 153

Figure 3.124 Simulation results showing 2D slice plots of the spatial maximum current density normal, smJ in coil wires at 1.5 MHz applied frequency for all cooling systems; (a) conventional passive, (b) conventional liquid, and (c–e) novel liquid with microchannel radii of 0.25, 0.30, and 0.35 mm, respectively. (The color bar on the right indicates the magnitude of current density normal $\times 10^8$ A/m^2). 154

Figure 3.125 Simulation results showing 2D slice plots of the spatial maximum current density normal, smJ in coil wires at 2.9 MHz applied frequency for all cooling systems; (a) conventional passive, (b) conventional liquid, and (c–e) novel liquid with microchannel radii of 0.25, 0.30, and 0.35 mm, respectively. (The color bar on the right indicates the magnitude of current density normal $\times 10^8$ A/m^2). 155

Figure 3.126 Data and SVR model predictions of applied frequency, f_a vs. normalized spatial maximum current density normal, $nsmJ$ for various cooling systems: (a) conventional passive, (b) conventional liquid, and (c–e) novel liquid with microchannel radii of 0.25, 0.30, and 0.35 mm, respectively (Scatter: data, line: predicted). 156

Figure 3.127 Data and GPR model predictions of applied frequency, f_a vs. normalized spatial maximum current density normal, $nsmJ$ for various cooling systems: (a) conventional passive, (b) conventional liquid, and (c–e) novel liquid with microchannel radii of 0.25, 0.30, and 0.35 mm, respectively. (Error bars: uncertainty estimates of the predicted data at a 95% confidence level, line: predicted). 157

Figure 3.128 Computed coil power consumption across the range of applied frequencies for all design configurations. (Single line is used to represent all designs, as their wattage values were nearly identical across the frequency range). 158

Figure 3.129 Simulation results showing 2D slice plots of the spatial maximum temperature, smT in and around coil wires at 0.1 MHz applied frequency and 0.1 m/s water flow rate for liquid cooling systems; (a) conventional liquid, and (b–d) novel liquid with microchannel radii of 0.25, 0.30, and 0.35 mm, respectively. (The color bar on the right indicates the magnitude of temperature ^oC). 159

Figure 3.130 Simulation results showing 2D slice plots of the spatial maximum temperature, smT in and around coil wires at 2.9 MHz applied frequency and 0.1 m/s water flow rate for liquid cooling systems; (a) conventional liquid, and (b–d) novel liquid with microchannel radii of 0.25, 0.30, and 0.35 mm, respectively. (The color bar on the right indicates the magnitude of temperature ^oC). 160

Figure 3.131 Simulation results showing 2D slice plots of the spatial maximum temperature, smT in and around coil wires at 0.1 MHz applied frequency and 0.5 m/s water flow rate for liquid cooling systems; (a) conventional liquid, and (b–d) novel liquid with microchannel radii of 0.25, 0.30, and 0.35 mm, respectively. (The color bar on the right indicates the magnitude of temperature ^oC). 160

Figure 3.132 Simulation results showing 2D slice plots of the spatial maximum temperature, smT in and around coil wires at 2.9 MHz applied frequency and 0.5 m/s water flow rate for liquid cooling systems; (a) conventional liquid, and (b–d) novel liquid with microchannel radii of 0.25, 0.30, and 0.35 mm, respectively. (The color bar on the right indicates the magnitude of temperature ^oC). 160

Figure 3.133 Data and SVR model predictions of applied frequency, f_a – water flow rate, v_{wf} vs. normalized spatial maximum temperature, $nsmT$ for all liquid cooling systems: (a) conventional liquid, and (c–d) novel liquid with microchannel radii of 0.25, 0.30, and 0.35 mm, respectively. (Scatter: data, surface: predicted). 161

Figure 3.134 Data and GPR model predictions of applied frequency, f_a – water flow rate, v_{wf} vs. normalized spatial maximum temperature, $nsmT$ for all liquid cooling systems: (a) conventional liquid, and (c–d) novel liquid with microchannel radii of 0.25, 0.30, and 0.35 mm, respectively. (Scatter: data, surface: predicted, the lines encircling the color surface indicate uncertainty estimates at a 95% confidence level). 162

Figure 3.135 Data and SVR model predictions of applied frequency, f_a – water flow rate, v_{wf} vs. performance index, PI for all liquid cooling systems: (a) conventional liquid, and (c–d) novel liquid with microchannel radii of 0.25, 0.30, and 0.35 mm, respectively. (Scatter: data, surface: predicted). 166

Figure 3.136 Data and GPR model predictions of applied frequency, f_a – water flow rate, v_{wf} vs. performance index, PI for all liquid cooling systems: (a) conventional liquid, and (c–d) novel liquid with microchannel radii of 0.25, 0.30, and 0.35 mm, respectively. (Scatter: data, surface: predicted, the lines encircling the color surface indicate uncertainty estimates at a 95% confidence level). 167

LIST OF TABLES

Table 1.1 Specifications of MMONPs [1, 2, 3, 4, 5]. 5

Table 2.1 COMSOL Multiphysics® 5.5 simulation variables for different coil geometry–wire type combinations, 10 turn each. 22

Table 2.2 Measured L_{Coil}, f_{Coil} and calculated R_s, Z_{Coil} parameters for each physical coil design. 25

Table 2.3 Pickup coil performance metric values. 29

Table 2.4 Calculated C_{series} and $C_{parallel}$ values of each impedance matching L–network circuit for each physically implemented MH coil design. 40

Table 2.5 Simulation material properties for all cooling systems. 44

Table 3.1 Solenoid coil with round wire physical implementation measured magnetic variables. 75

Table 3.2 Time–domain root mean square magnetic flux density, $tRMS_B$ values measured in mT from solenoid coil with round wire design for 100% power level at three different axial positions; −6, 0, +6 mm and 21 different transverse positions; 6 mm apart at each axial position (63 positions in total, for each power level). 75

Table 3.3 Time–domain root mean square magnetic flux density, $tRMS_B$ values measured in mT from solenoid coil with round wire design for 75% power level at three different axial positions; −6, 0, +6 mm and 21 different transverse positions; 6 mm apart at each axial position (63 positions in total, for each power level). 76

Table 3.4 Time–domain root mean square magnetic flux density, $tRMS_B$ values measured in mT from solenoid coil with round wire design for 50% power level at three different axial positions; −6, 0, +6 mm and 21 different transverse positions; 6 mm apart at each axial position (63 positions in total, for each power level). 77

Table 3.5 Time–domain root mean square magnetic flux density, $tRMS_B$ values measured in mT from solenoid coil with round wire design for 25% power level at three different axial positions; −6, 0, +6 mm and 21 different transverse positions; 6 mm apart at each axial position (63 positions in total, for each power level). 78

Table 3.6 Time–domain root mean square magnetic flux density, $tRMS_B$ values measured in mT from solenoid coil with round wire design for 10% power level at three different axial positions; −6, 0, +6 mm and 21 different transverse positions; 6 mm apart at each axial position (63 positions in total, for each power level). 79

Table 3.7 Amount of temperature rise, Δ_T values measured in ^{o} C from 166.5 mg/mL concentration MNPs inside of solenoid coil with round wire design at three axial positions inside of the coil gap and five different transverse positions. 80

Table 3.8 Amount of temperature rise, Δ_T values measured in ^{o} C from 120 mg/mL concentration MNPs inside of solenoid coil with round wire design at three axial positions inside of the coil gap and five different transverse positions. 81

Table 3.9 Slope of linear regression fit for 40 minute temperature rise vs. time graph during MH experiments conducted with 166.5 mg/mL concentration SPION using solenoid coil with round wire at three axial positions inside of the coil gap and five different transverse positions. 82

Table 3.10 Slope of linear regression fit for 40 minute temperature rise vs. time graph during MH experiments conducted with 120 mg/mL concentration SPION using solenoid coil with round wire at three axial positions inside of the coil gap and five different transverse positions. 83

Table 3.11 Solenoid coil with round wire physical implementation measured thermal variables. 83

Table 3.12 Solenoid coil with round Litz wire physical implementation measured magnetic variables. 109

Table 3.13 Time–domain root mean square magnetic flux density, $tRMS_B$ values measured in mT from solenoid coil with round Litz wire design for 100% power level at three different axial positions; −6, 0, +6 mm and 21 different transverse positions; 6 mm apart at each axial position (63 positions in total, for each power level). 109

Table 3.14 Time–domain root mean square magnetic flux density, $tRMS_B$ values measured in mT from solenoid coil with round Litz wire design for 75% power level at three different axial positions; −6, 0, +6 mm and 21 different transverse positions; 6 mm apart at each axial position (63 positions in total, for each power level). 110

Table 3.15 Time–domain root mean square magnetic flux density, $tRMS_B$ values measured in mT from solenoid coil with round Litz wire design for 50% power level at three different axial positions; −6, 0, +6 mm and 21 different transverse positions; 6 mm apart at each axial position (63 positions in total, for each power level). 111

Table 3.16 Time–domain root mean square magnetic flux density, $tRMS_B$ values measured in mT from solenoid coil with round Litz wire design for 25% power level at three different axial positions; −6, 0, +6 mm and 21 different transverse positions; 6 mm apart at each axial position (63 positions in total, for each power level). 112

Table 3.17 Time–domain root mean square magnetic flux density, $tRMS_B$ values measured in mT from solenoid coil with round Litz wire design for 10% power level at three different axial positions; −6, 0, +6 mm and 21 different transverse positions; 6 mm apart at each axial position (63 positions in total, for each power level). 113

Table 3.18 Amount of temperature rise, Δ_T values measured in ^{o}C from 166.5 mg/mL concentration MNPs inside of solenoid coil with round Litz wire design at three axial positions inside of the coil gap and five different transverse positions. 114

Table 3.19 Amount of temperature rise, Δ_T values measured in ^{o}C from 120 mg/mL concentration MNPs inside of solenoid coil with round Litz wire design at three axial positions inside of the coil gap and five different transverse positions. 115

Table 3.20 Slope of linear regression fit for 40 minute temperature rise vs. time graph during MH experiments conducted with 166.5 mg/mL concentration SPION using solenoid coil with round Litz wire at three axial positions inside of the coil gap and five different transverse positions. 116

Table 3.21 Slope of linear regression fit for 40 minute temperature rise vs. time graph during MH experiments conducted with 120 mg/mL concentration SPION using solenoid coil with round Litz wire at three axial positions inside of the coil gap and five different transverse positions. 117

Table 3.22 Solenoid coil with round Litz wire physical implementation measured thermal variables. 117

Table 3.23 Helmholtz coil with round wire physical implementation measured magnetic variables. 143

Table 3.24 Time–domain root mean square magnetic flux density, $tRMS_B$ values measured in mT from Helmholtz coil with round wire design for 100% power level at three different axial positions; −6, 0, +6 mm and 21 different transverse positions; 6 mm apart at each axial position (63 positions in total, for each power level). 143

Table 3.25 Time–domain root mean square magnetic flux density, $tRMS_B$ values measured in mT from Helmholtz coil with round wire design for 75% power level at three different axial positions; −6, 0, +6 mm and 21 different transverse positions; 6 mm apart at each axial position (63 positions in total, for each power level). 144

Table 3.26 Time–domain root mean square magnetic flux density, $tRMS_B$ values measured in mT from Helmholtz coil with round wire design for 50% power level at three different axial positions; −6, 0, +6 mm and 21 different transverse positions; 6 mm apart at each axial position (63 positions in total, for each power level). 145

Table 3.27 Time–domain root mean square magnetic flux density, $tRMS_B$ values measured in mT from Helmholtz coil with round wire design for 25% power level at three different axial positions; −6, 0, +6 mm and 21 different transverse positions; 6 mm apart at each axial position (63 positions in total, for each power level). 146

Table 3.28 Time–domain root mean square magnetic flux density, $tRMS_B$ values measured in mT from Helmholtz coil with round wire design for 10% power level at three different axial positions; −6, 0, +6 mm and 21 different transverse positions; 6 mm apart at each axial position (63 positions in total, for each power level). 147

Table 3.29 Amount of temperature rise, Δ_T values measured in ^{o} C from 166.5 mg/mL concentration MNPs inside of Helmholtz coil with round wire design at three axial positions inside of the coil gap and five different transverse positions. 148

Table 3.30 Amount of temperature rise, Δ_T values measured in ^{o} C from 120 mg/mL concentration MNPs inside of Helmholtz coil with round wire design at three axial positions inside of the coil gap and five different transverse positions. 149

Table 3.31 Slope of linear regression fit for 40 minute temperature rise vs. time graph during MH experiments conducted with 166.5 mg/mL concentration SPION using Helmholtz coil with round wire at three axial positions inside of the coil gap and five different transverse positions. 150

Table 3.32 Slope of linear regression fit for 40 minute temperature rise vs. time graph during MH experiments conducted with 120 mg/mL concentration SPION using Helmholtz coil with round wire at three axial positions inside of the coil gap and five different transverse positions. 151

Table 3.33 Helmholtz coil with round wire physical implementation measured thermal variables. 151

Table 3.34 Simulation spatial maximum current density normal, smJ ($\times 10^8$ A/m^2) in coil wires for all cooling systems. 158

Table 3.35 Adjusted R^2 error metric calculations for model predictions of applied frequency, f_a vs. normalized spatial maximum current density normal, $nsmJ$ across all cooling systems. 159

Table 3.36 Key simulation results for the spatial maximum temperature, smT (^oC) in coil wires presented for all four liquid cooling system. 163

Table 3.37 Simulation spatial maximum temperature, smT (^oC) in coil wires for the conventional liquid cooling system. 163

Table 3.38 Simulation spatial maximum temperature data, smT (^oC) in coil wires for the novel liquid cooling system with 0.25 mm cooling microchannel radius. 164

Table 3.39 Simulation spatial maximum temperature data, smT (^oC) in coil wires for the novel liquid cooling system with 0.30 mm cooling microchannel radius. 164

Table 3.40 Simulation spatial maximum temperature data, smT (^oC) in coil wires for the novel liquid cooling system with 0.35 mm cooling microchannel radius. 165

Table 3.41 Adjusted R^2 error metric calculations for model predictions of applied frequency, f_a – water flow rate, v_{wf} vs. normalized spatial maximum temperature, $nsmT$ across all liquid cooling systems. 165

Table 3.42 Performance index, PI (unitless) for the conventional liquid cooling system. 168

Table 3.43 Performance index, PI (unitless) for the novel liquid cooling system with 0.25 mm microchannel radius. 168

Table 3.44 Performance index, PI (unitless) for the novel liquid cooling system with 0.30 mm microchannel radius. 169

Table 3.45 Performance index, PI (unitless) for the novel liquid cooling system with 0.35 mm microchannel radius. 169

Table 3.46 Adjusted R^2 error metric calculations for SVR and GPR–based model predictions of applied frequency, f_a – water flow rate, v_{wf} vs. performance index, PI across all liquid cooling systems. 170

Table 3.47 Sensitivity analysis of input parameter influence on SVR model predictions, and ReliefF feature weights indicating input parameter importance for predictions. 170

Table 3.48 Sensitivity analysis of input parameter influence on GPR model predictions, and ReliefF feature weights indicating input parameter importance for predictions. 170

LIST OF SYMBOLS

A_{pl}	Total Overlapping Area Between Facing Capacitor Plates
B	Magnetic Flux Density
C	Capacitance
C_p	Parallel Capacitance
f_0	Resonant Frequency
GHz	Gigahertz
H	Magnetic Field Strength
kHz	Kilohertz
kW	Kilowatt
$k\Omega$	Kilo ohms
L	Inductance
ℓ_{cl}	Coil Length
LFM	Linear Feet Per Minute
MHz	Megahertz
mg/mL	Milligram(s) per Milliliter
mm	Millimeter
N_w	Number of Wire Turns
nm	Nanometer
ppm	Parts Per Million
r	Coil Radius
R	Resistance
R_s	Series Resistance
V	Volts/Voltage
Ω	Ohms
μ	Magnetic Permeability
μm	Micrometer
^oC	Celsius Degree(s)

LIST OF ABBREVIATIONS

ABS	Acrylonitrile Butadiene Styrene
AC	Alternating Current
AMF	Alternating Magnetic Field
BJT	Bipolar Junction Transistor
BNC	Bayonet Neill–Concelman
DC	Direct Current
DLC	Direct Liquid Cooling
FEA	Finite Element Analysis
Fe_3O_4	Ferumoxytol
GBMs	Glioblastomas
GPR	Gaussian Process Regressionn
HCWRW	Helmholtz Coil With Round Wire
LTI	Linear Time–Invariant
MANP	Magnetic Alloy Nanoparticles
MH	Magnetic Hyperthermia
MMONP	Magnetic Metal Oxide Nanoparticle
MNP	Magnetic Nanoparticle
MRI	Magnetic Resonance Imaging
NIH	National Institutes of Health
NPN	Negative–Positive–Negative
OAT	One–at–a–Time
OP–AMP	Operational Amplifier
PCB	Printed Circuit Board
PNP	Positive–Negative–Positive
RF	Radio Frequency
RMS	Root Mean Square
RT	Radiation Therapy
SCWRW	Solenoid Coil With Round Wire

SCWLW	Solenoid Coil With Round Litz Wire
SNR	Signal–to–Noise Ratio
SMPS	Switched Mode Power Supply
SVR	Support Vector Regressionn
vs.	versus

1. INTRODUCTION

Cancer is the uncontrollable growth and spread of living cells throughout the body. It can start and grow in any part of the body to form lumps of tumor tissues. Early diagnosis of malignant tumors and execution of proper treatment techniques are highly important in terms of increasing patient's chance of survival [6]. The use of surgical resection, chemotherapy and radiotherapy are clinical standards for cancer treatment which are inadequate from several aspects. Although maximum success in the treatment of many types of cancer is pursued through combined use of these methods, the success rate is quite low in some, such as glioblastomas (GBMs) [7]. Therein, treatment is focused on slowing down the spread of cancer rather than healing/recovery of the patient, thus only lengthening patient's life on monthly basis. Even with modern techniques, surgical resection carries the risk of bleeding and infection [8]. Furthermore, it is not possible to fully eliminate cancer from patient's body through solely removal of the tumor itself. Following the surgery, adjuvant chemotherapy must be administered for full recovery [9]. On the other hand, effectiveness of chemotherapy greatly varies from patient to patient and regarding cancer type [10, 11]. When chemotherapeutic dose is increased towards enhancing effectiveness of treatment, damage to healthy cells is also increased. Different chemotherapy drugs can cause a variety of different side effects. In a high dose chemotherapy schedule, intense side effects can make chemotherapy unbearable for the patient [12]. Moreover, lack of a standard system for accurate chemotherapeutic dose calculations disrupts both efficiency and effectiveness of the treatment [13, 14, 15]. Also, occurrence of chemotherapeutic resistance is unpredictable [16]. Lastly, it is not practically possible to use radiotherapy (RT) in the treatment of metastatic cancers where the cancer is spread all around patient's body [17]. Even in a case of localized tumor treatment; most of the time, RT can damage healthy cells and sometimes trigger formation of new tumors [18]. For these reasons, many institutes and research centers from all around the world focus their efforts on discovering new clinical methods [19, 20, 21]. Therefore, new treatment methods are needed [19, 20, 21] and hyperthermia technology has an important place

among these innovative/novel methods as it can focus therapeutic effects directly on malignant areas [22].

1.1 Hyperthermia Therapy

Hyperthermia is an innovative approach in cancer treatment. First studies of hyperthermia date back to 1950's [23]. Cancerous cells are known to carry different metabolic characteristics compared to healthy cells. Cancerous cells, start dying roughly over 40^o C while healthy cells survive at the same temperatures [24]. This temperature characteristic difference renders the heat applied therapeutic approach known as "hyperthermia" possible.

Basically, there are three different hyperthermia approaches; local hyperthermia, regional hyperthermia and whole body hyperthermia. Local hyperthermia heats a very small area and is typically used for cancers located near or on the skin or near natural openings in the body [25]. In some cases, the goal is to heat and kill the tumor tissue without damaging other tissues. It can be generated by heat, microwave, radio frequency, ultrasound energy or by using magnetic hyperthermia [26, 27, 28]. Depending on the location of the tumor, heat can be applied to the body surface (superficial hyperthermia), normal body cavities (intraluminal hyperthermia) or deep into the tissue using needles or probes (interstitial hyperthermia). It should not be confused with ablation, in which higher temperatures ($> 55^o$ C) are applied to kill tumor cells. Regional hyperthermia which is another hyperthermia approach targets larger parts of the body; such as the entire organ or a limb. Generally, the aim is to weaken cancerous cells and facilitate their destruction with chemotherapeutic drugs and RT. To enhance treatment effectiveness, method can sometimes use the same approach as local hyperthermia and other times can use blood perfusion. In blood perfusion, the patient's blood is withdrawn from the body, heated and then delivered directly to the blood vessels leading to targeted part of the body. Normally, this technique is carried out in parallel with chemotherapeutic drug delivery. A particular variant of this approach is continuous hyperthermia peritoneal perfusion; which is used to treat difficult

cancers within the peritoneal cavity, including primary peritoneal mesothelioma and gastric cancer. In this method, hot chemotherapy drugs are pumped directly into the peritoneal cavity to kill cancer cells. Another type, whole–body hyperthermia warms up the entire body to temperatures of between 39^o-43^o C, which is typically used to treat metastatic cancer. The approach involves the use of infrared hyperthermia and placing the patient's entire body except the head in a warm room or wrapping the patient in a warm, wet blanket–like material or in a water tube. Some studies argue on the necessity of higher temperatures for effective treatment. [25].

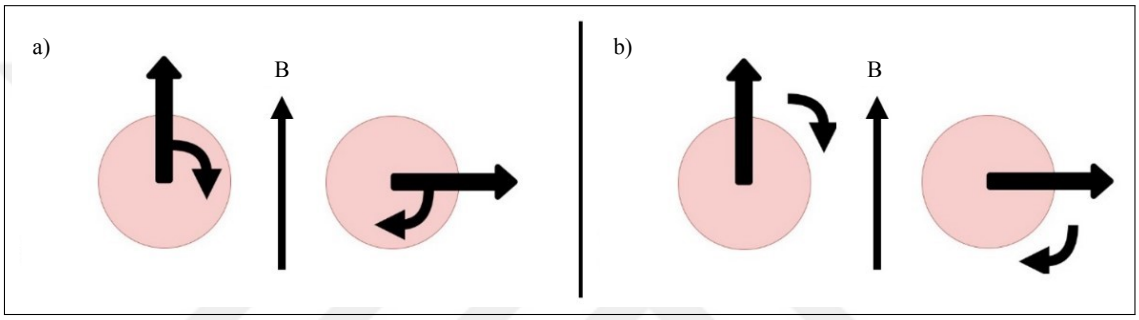


Figure 1.1 (a) Mechanism of Néel Relaxation; magnetic orientation change
(b) Mechanism of Brownian Relaxation; physical rotation.

The most promising type of hyperthermia is based on nanoparticles. First, magnetic nanoparticles (MNP) are injected to tumor site. Second, alternating magnetic fields (AMF) are applied to MNPs. Then, MNPs try to align themselves with magnetic field lines through magnetic orientation changes (Nèel Relaxations) and physical rotations (Brownian Relaxations) (See Figure 1.1). This results in heat production via frictional losses and hysteresis losses, thereby death of cancerous cells [29, 30]. The process is called magnetic hyperthermia (MH).

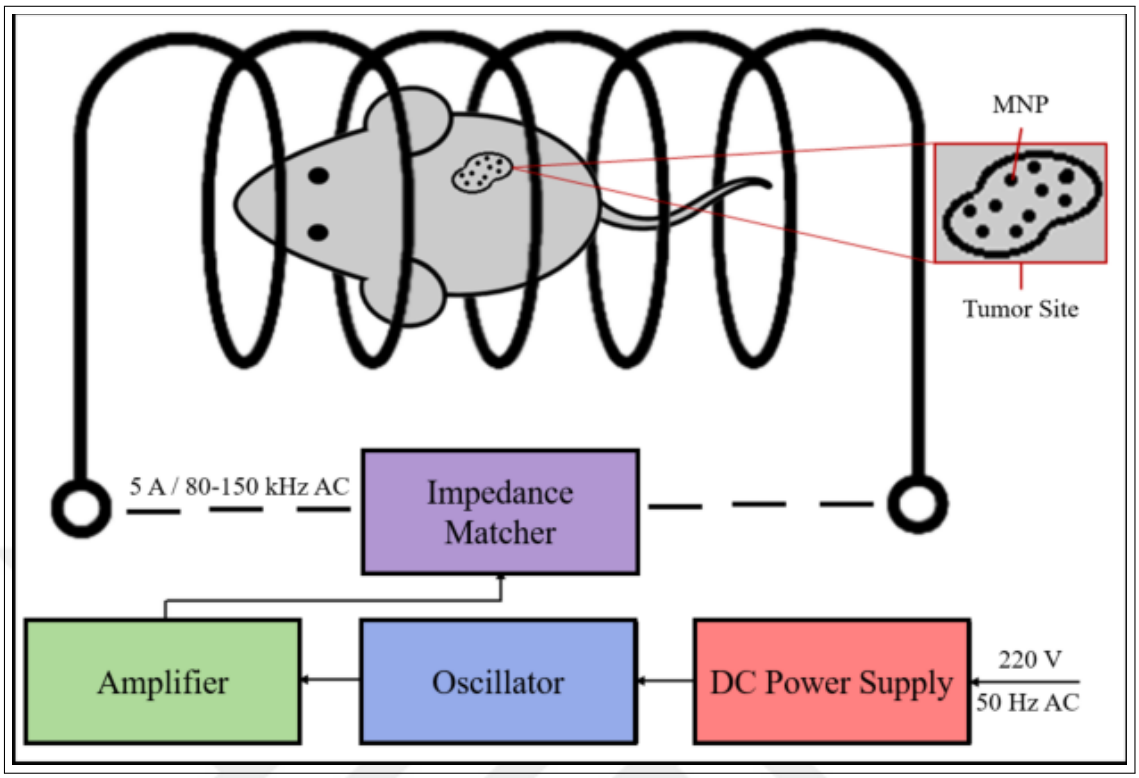


Figure 1.2 Schematic describing basic parts of a MH device.

MH devices are basically made up of a RF signal generator and a RF coil. RF generator consists following stages; DC power generator, oscillator, amplifier and impedance matcher. As an output of the RF generator, RF signals ($< 300\,\text{kHz}$) are produced at high amplitudes ($> 8\,\text{A}$ peak to peak). Then, an RF coil is fed with these signals to produce magnetic fields with the same frequency (See Figure 1.2) [31].

Primary motivation behind MH studies is to target cancer cells without harming healthy cells. Towards this end, some studies focused on design of MH devices that can control radio frequency (RF) exposure of healthy cells and target solely tumors. Others focused on discovery of efficient MNPs [32]. Although this non–invasive therapeutic approach has the potential to be a clinical alternative to current oncological treatment standards, there are number of limiting factors which hinder utilization of this technique in clinical settings.

Table 1.1 Specifications of MMONPs [1, 2, 3, 4, 5].

Most Notable MMONPs	**Advantages and Disadvantages**	**Application Areas**
	-High Saturation Magnetization	-Labeling Cells
	-High Magnetic Susceptibility	-Designing Ceramic
	-Low Toxicity	-MRI
-Fe_3O_4	-Physicochemical	-Drug Delivery
-γFe_2O_3	-Colloidal Stability	-Gene Therapy
-$NiFe_2O_4$	-High Magnetic Permeability	-Magnetic Hyperthermia
-$MnFe_2O_4$	-High Electrical Resistance	-In–Vitro Diagnostics
-$CoFe_2O_4$	-High Oxidative Stability	-Vaccine and Anti–Body Production
-NiO	-High Quality Monodisperse	-Gas Sensors
-Co_3O_4	-Superparamagnetism	-Catalysts
	-Light Absorbing	-Electromagnetic and Optical Devices
	-Tend to Aggregation	-Magnetic Data Storage
	-Large Surface Area to Volume Ratio	-Biosensing
		-Batteries

MNPs are ultra fine particles which are used as part of diagnostic and therapeutic systems [33, 34]. Due to their metal based structure, they are classified as inorganic materials and they can be used as heating nano–mediators. MNPs are zero–dimensional particles; meaning that their size in any direction is less than 100 nm [35]. Their size and shape not only affect their ability to travel in human body but also influence their magnetic properties. Hence, all of these parameters play a huge role in effectiveness of a MNP in MH therapy. Regarding their structure, MNPs are split into two categories; magnetic alloy nanoparticles (MANPs) and magnetic metal oxide nanoparticles (MMONPs). Among MMONPs (See Table 1.1), iron oxides and ferrites are best candidates for use in MH therapy. This is primarily caused by their superior bio–compatibility and magnetic properties. Out of iron oxides and ferrites, due to presence of Fe^{2+} and Fe^{3+} cations in valence states of the inverse spinal structure; Fe_3O_4 (Ferumoxytol) is considered to be the best choice by many researchers [36, 37].

Although MNPs can serve as heating nano–mediators and render MH therapy possible, they have some disadvantages; current MNPs are passive particles, meaning that they do not posses the ability to target and bind to specific molecules (in this case tumor). As a traditional workaround to this problem; instead of systemic delivery, MNPs are injected to tumor site. However, after some time, MNPs diffuse to other parts of the body. This behavior of MNPs limits the time frame that MH therapy can be applied [38]. To overcome this issue, instead of limiting MNP diffusion, some study groups worked on limiting the RF fields, thereby focusing the electromagnetic energy on tumor site only [39]. Still, to this day, this approach is not sufficiently tested and is not technologically mature.

A wide range of RF signals can be utilized to heat MNPs during MH therapy. However, some frequencies can cause direct heating of both healthy and cancerous tissues through Eddy currents [40]. In their study, Atkinson and Brezovich [41] applied AMF to human thorax then observed eddy current formation inside muscle tissues and its heating effects. With data they have collected through series of tests done on human thorax, they have come up with an equation (Atkinson–Brezovich limit) which defines the maximum amount of electromagnetic energy that can be tolerated by healthy cells

for long periods of time. Below in the Atkison–Brezovich limit;

$$H \times f \leq 4.85 \times 10^8\, A/m.s \tag{1.1}$$

H is the magnetic field strength and f is the applied frequency. Although higher values of H×f can be tolerated by human limbs, it is generally safer to observe Atkinson–Brezovich limit since a full body MH system is more desirable. Furthermore, their calculations suggest that an f value of ≤ 200 kHz is suitable for MH applications. On the other hand, in their study Khan and colleagues [42] state that f value must be ≥ 50 kHz to avoid interactions with skeletal muscles. Hence, a range of $50 - 200$ kHz can be considered as both practical and safe [41, 42].

1.2 Magnetic Hyperthermia Coil Optimization

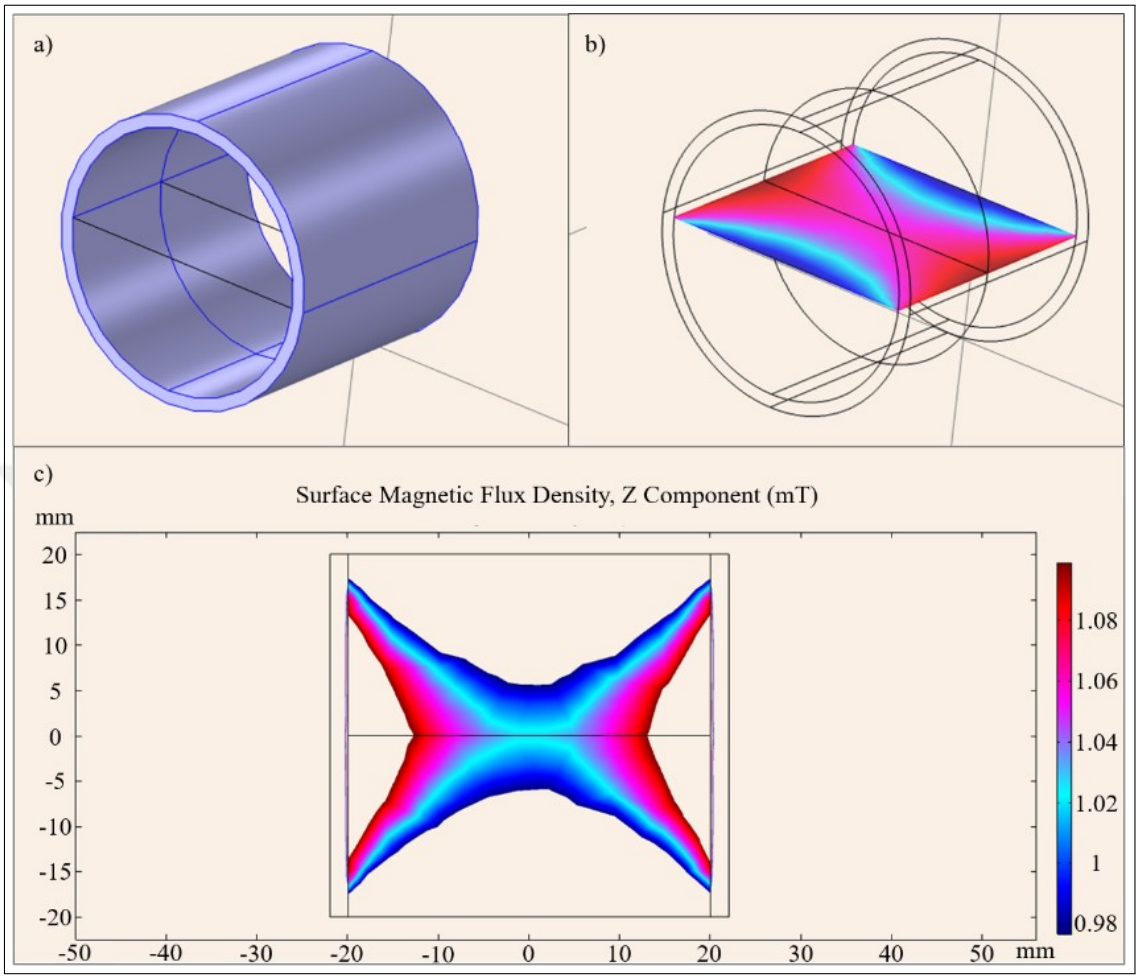


Figure 1.3 Air core coil designed in COMSOL simulation program; showing (a) coil geometry, (b) magnetic field color map of horizontal middle slice and (c) area with 10% magnetic flux density deviation.

In MH therapy, although it is a priority that the generated magnetic field has a high H; it is also important that it has a great magnetic field homogeneity. Magnetic field homogeneity is the uniformity of H for each point inside of the coil (See Figure 1.3(b)). A great magnetic field homogeneity should promote nearly equal electromagnetic heating of the tumor site, considering that the MNPs are equally distributed inside of the tumor. Although the magnetic field homogeneity of a coil can be enhanced through various techniques, such as use of active shim coils, passive shim coils, Helmholtz coils or Maxwell coils; it is practically impossible to attain an excellent field uniformity for each point inside of the coil. Therefore, some level of deviation

in H is considered acceptable regarding design requirements. The volume capable of keeping deviation of H under the targeted "%" limit is called "functional volume" (See Figure 1.3(c)) [43].

In an MH system, RF signal generator and the RF coil are parts of a whole, whereas one effects the performance of the other. Therefore, design process of both parts must be performed in a highly precise and detailed manner. Winding wires around a solenoid pipe to form a RF coil through Ampére's Circuital Law is an excessively simplified approach. This leads to misleading coil designs, thereby causes a mismatch of theory with practice. On the other hand, specific coil types such as a Maxwell Coil or a Helmholtz Coil have their tradeoffs between magnetic flux density, field homogeneity and current parameters. In their study, Attaluri and colleagues [44] utilized Maxwell Coils to achieve greater inductance with less current consumption, in which they have succeeded. However, they have also mentioned that Maxwell coils require more expensive materials compared to simple solenoid coils. Another study done by Skumiel and colleagues [45] compared three different coil designs; a two–layer solenoid, Helmholtz Coil and a coil with a ferromagnetic core. Their results suggested that all of these designs are capable of producing the adequate magnetic field intensity for MH therapy. Nevertheless, all three of them had significant cons. The two–layer solenoid was capable of producing approximately 2.7 times more magnetic flux density than Helmholtz coil, but with less field homogeneity. Coil with the ferromagnetic core was capable of producing signals with very high amplitudes but the magnetic field intensity was concentrated in a small air gap. Also this small air gap causes temperature stabilization problems. These issues are all related to maximum power transfer from signal generator to RF coil for a given frequency, which is also bound to resonant frequency (f_0) of systems.

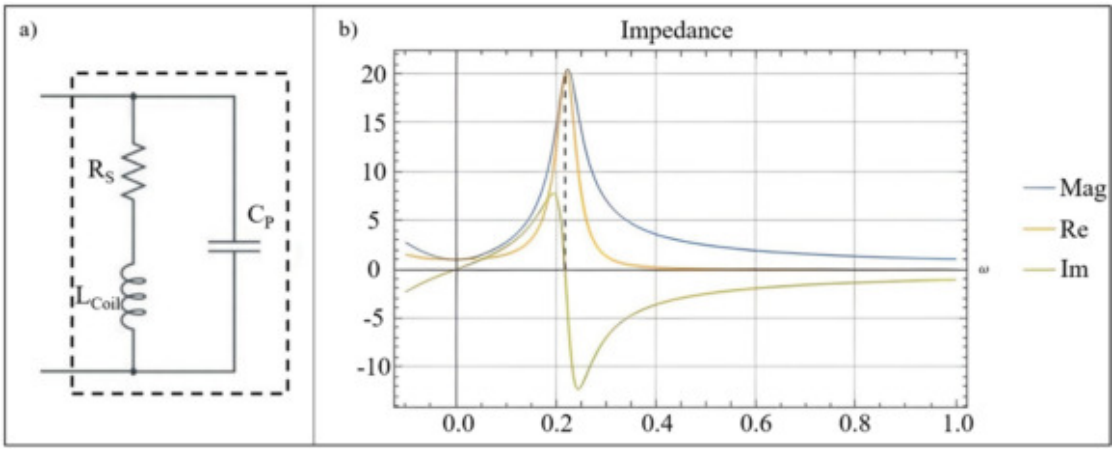


Figure 1.4 (a) Basic RLC model schematic and (b) magnitude plot consisting real and imaginary parts of the impedance for a basic solenoid coil. At the resonant frequency marked with a dashed line, the imaginary part changes sign
($R_s = 1\ \Omega$, $L_{coil} = 20$ H, $C_p = 1$ F).

In theory; when fed with their f_0, coils are prone to oscillate at maximum amplitude. However, due to parallel arrangement of coil's inductance (L_{coil}) and capacitance (C_p) with each other (See Figure 1.4(a)), impedance (Z_{coil}) reaches extreme highs (See Figure 1.4(b)). Hence, current across it reaches extreme lows which diminishes magnetic field strength (See Figure 1.4).

At f_0, coil starts to act as a choke and the current across it diminishes. In his book "High–Frequency Magnetic Components", M. K. Kazimierczuk states that the designed coil's f_0 must be much larger than its driving frequency (f) and mentions a maximum frequency limit for efficient driving of coils [46, 47];

$$f \leq 0.9 \times f_0 \tag{1.2}$$

Hence, f_0 of a RF coil must be configured. In a linear mechanical time–invariant (LTI) system, f_0 is directly bounded by the mass–spring–damper system. In an electrical system, resistor, capacitor and inductor components of that system behaves as

one of the components of the system mentioned above. For proper assignment of each mathematical component to each of these electronic components and formulate a mathematical equation, it is crucial to analyze these components' connections (parallel or series) with each other [48]. In a solenoid coil, gaps between each wire turn result in parasitic capacitance (C_p). Due to materialistic properties, wire itself has a series resistance (R_s). Most importantly, helical shape of coil adds an L_{coil} element to it.

To achieve resonance in a parallel LC system such as a solenoid coil, inductive and capacitive reactance should be equal, which in their currents cancel each other out and the total impedance is maximized;

$$\omega L_{coil} = \frac{1}{\omega C_p}. \tag{1.3}$$

Solving for angular frequency,

$$\omega^2 = \frac{1}{L_{coil} C_p}, \tag{1.4}$$

$$\omega = \frac{1}{\sqrt{L_{coil} C_p}}. \tag{1.5}$$

Express ω across $2\pi f_0$,

$$2\pi f_0 = \frac{1}{\sqrt{L_{coil}C_p}}. \tag{1.6}$$

Finally, solve for f_0,

$$f_0 = \frac{1}{2\pi\sqrt{L_{coil}C_p}}, \tag{1.7}$$

thereby retrieving the resonant frequency of a tank circuit [49].

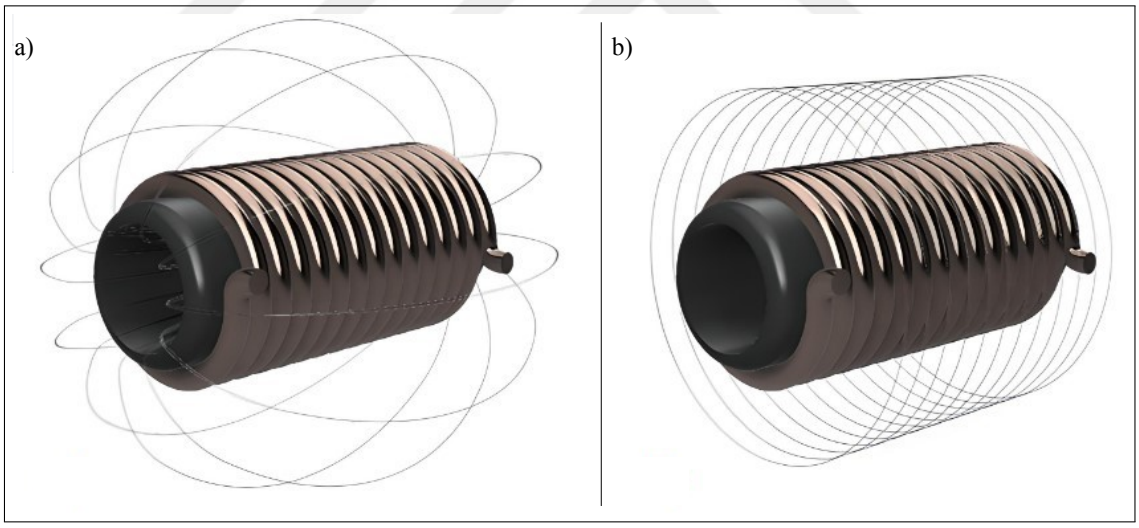


Figure 1.5 Direction of magnetic field lines for (a) $f \ll f_0$ and (b) $f \gg f_0$.

Due to the parallel arrangement of L_{coil} and C_p, coil acts as a band stop filter (choke coil) in which f_0 is the point of maximum signal attenuation. L_{coil} element has a low pass filter effect while C_p element has a high pass filter effect. Below f_0, coil's L_{coil} is the dominant factor. Therefore, nearly all the current follows the helical way. This ensures formation of a homogenous magnetic field (See Figure 1.5(a)). Above f_0, coil's C_p is the dominant factor. Therefore, nearly all the current follows a straight pathway

across the coil (See Figure 1.5(b)). This disrupts formation of a homogenous magnetic field.

With these information at hand, the logic behind the limit set by Eq. 1.2 can be easily understood. However, since Eq. 1.7 is directly related with $\mathrm{L_{coil}}$ and $\mathrm{C_p}$, one must also understand factors affecting these parameters for an optimized coil design. For a typical air–core coil, $\mathrm{L_{coil}}$ is calculated through;

$$\mathrm{L_{coil}} = \mu_0 \frac{\mathrm{N_w^2 \pi r^2}}{\ell_{\mathrm{cl}}} \tag{1.8}$$

In the formula above; μ_0 is the magnetic permeability of vacuum, N_w is the number of wire turns, r is the coil radius and ℓ_{cl} is the coil length. Any change in N_w, r and/or ℓ_{cl} affect the L_{coil}. On top of this relation, effect of wire length and diameter on C_p must be considered. In the basic C_p formula;

$$\mathrm{C_p} = \epsilon_0 \frac{\mathrm{A_{pl}}}{\mathrm{d_p}}. \tag{1.9}$$

ϵ_0 is the dielectric constant for vacuum ($\frac{10^{-9}}{36\pi}$), A_{pl} is the total overlapping area between facing coil wires acting as capacitive plates and d_p is the distance between these plates. It can be inferred from above equation that the total C_p is correlated with A_{pl} and d_{p}. Designing a short coil, coil with a small ℓ_{cl} value can reduce $\mathrm{C_p}$ by reducing A_{pl} [49]. While in high frequency systems, C_p becomes a major problem, MH systems utilize mostly from low frequencies ($30-300\,\mathrm{kHz}$) of RF spectrum which limits capacitive reactance that can be generated by $\mathrm{C_p}$, making its negative effects negligible. With these information at hand, the driving frequency of a coil influences its shape and size towards optimization, wherein the strategy is to design a coil with a resonant

frequency which is much higher than its operating frequency. However, to serve its purpose, sometimes coil design may face some geometrical limitations (maximums or minimums). So, values of some parameters such as N_w, r, A_{pl} or ℓ_{cl} may have to be fixed. In such cases, altering values of other parameters can make up for effects of fixed parameter. Below in the Ampére's law, the relationship between current (I) and N_w parameters is an example for this;

$$B = \mu H = \mu \frac{N_w I}{\ell_{cl}} \tag{1.10}$$

where μ is the magnetic permeability of coil's core material and H is the magnetic field strength which is independent from the medium. On the other hand, B is the magnetic flux density that is generated over a specific medium which is directly proportional with μ. Since both I and N_w are directly proportional with H; any change in I or N_w can be compensated by manipulating the other for retrieving the same H. Most of the time, primary goal is to attain the maximum level of H that can be generated by a specific coil design. Towards this end, parameter values must be adjusted with precision. Also Eq. 1.10 states; shorter the ℓ_{cl}, higher the H, thereby higher the B. Hence, to attain the maximum H, it is important to design the shortest coil possible that can serve its purpose. It can be easily noticed that for a coil; again, overall geometry affects f_0 and ℓ_{cl} affects H. Focusing on one of these parameters towards coil design optimization does not yield the best results. An optimized coil design that can provide the maximum electromagnetic energy output by balancing the effects of all these parameters must be found, which are discussed so far [49].

Also, as mentioned before, design related problems of the RF generator and RF coil affect each other's performances. Extended frequency response of the amplifier stage causes the C_p between the input and the output to act as a feedback path, which causes the circuit to oscillate at higher frequencies. Another major design parameter is thermal characteristics; it plays a huge role in efficiency and effectiveness of high

power coils such as in MH. Poor heat dissipation results in overheating of the coil which in return shifting of electrical characteristics, thus loss of stability and power conversion [49]. This is primarily related to positive correlation between temperature and Z. The current passing through the copper coil wire generates heat. If the heat is generated at a rate higher than it is dissipated, it results in overheating of the wire, hence rise in wire impedance. Instead of electrical to magnetic energy conversion, all of these result in electrical to heat energy conversion which is considered as a power loss. To prevent MH systems from such problems, some study groups [39, 44] designed water jackets for their coil designs. With constant cool water flowing inside of these water jackets, they have successfully managed to keep the coil temperatures down and stable at a decent level.

In summary, the lack of optimized coil designs incorporating all the parameters impede creating efficient devices for MH. Numerous parameters such as coil geometry, impedance, winding resistance, skin effects, inductance, wire size, wire material, heat losses, parasitic capacitance and resonant frequency must be taken into account for an optimized MH device.

Economic feasibility of currently available MH devices is another important issue, mostly due to utilization of general purpose, broadband, commercial RF amplifier devices, rather than custom designs tailored for specific needs. Case in point; Garaio and colleagues [50] designed a multi–frequency electromagnetic applicator for MH therapy. Since they have focused their efforts on building the RF coil, they have preferred to use 1140LA (Electronics and Innovation, Rochester, NY, USA) as the RF amplifier which has a retail price of $23.65K [51], as the writing of this thesis. Due to Atkinson–Brezovich limit, there is a upper limit for H $\times$ f that can be applied to biological tissues. 1140LA's frequency bandwidth is wider and maximum signal power is much higher than required for an MH system. Even though such approach yields same scientific results in MH therapy, it hinders technology's adoptability by the healthcare industry which causes it to remain as an academic study field. In another study done by Attaluri and colleagues [44], they have utilized from a 120 kW industrial induction heater (AMF LifeSystems) to feed their Maxwell type induction coil. Since the product

is an industrial device, the retail price was not available. Nevertheless, with a simple market research; it is found that systems with only 3.5 kW of power have retail prices around $4.5K [52], as of writing of this thesis. Based on data, it can be estimated that the price of a 120 kW system utilizing the same technology must be much higher. Similar RF amplifiers are used in settings where extremely high signal–to–noise ratio (SNR) is required just as in Magnetic Resonance Imaging (MRI) [53]. However, such levels of SNR is not required in an MH system. Plus, it increases the total system cost tremendously. Finally, Zhao and colleagues [54] designed RF coils for MH experimenting and conducted simulation studies. They have performed device validation tests through small animal trials, in which they have used a commercial power amplifier Model# P3000 (Hafler, Vancouver, BC, Canada) to feed their designed coil. Since the mentioned amplifier is a commercial audio amplifier, using this system is not the optimal approach to feed RF coils which use low RF signals during MH therapy for maximum efficiency and effectiveness. So far, these are primary drawbacks of existing MH studies. RF generators should be designed considering targeted operation frequency and total energy levels to be transmitted during the MH therapy. Accordingly, the complexity of the device can be minimized and the performance can be optimized, while providing a low cost design compared to existing systems. It is crucial that the RF generator can operate across a range of frequencies, enabling optimal electromagnetic coupling by allowing different combinations of magnetic field strength (H) and frequency (f) to be tailored for various magnetic nanoparticles (MNPs). Considering the current technological maturity of power electronics and RF systems, it is feasible to design the entire MH system at a low cost, in a university laboratory setting.

To address these limitations, this study focused on the development of optimized coil designs and a cost–effective RF amplifier to enhance MH device efficiency and accessibility (See Section A). In addition to the core studies presented throughout this thesis, a complementary research effort was conducted to address a critical technical challenge in MH systems–thermal management of RF coils. Recognizing that excessive heating of RF coils can compromise system performance and patient safety, a novel liquid cooling system leveraging the skin effect was designed and optimized (See Section B). While the thermal management study expands the technical background related

to MH systems, it is not within the primary scope of this thesis.

2. METHODS AND MATERIALS

A Coil Optimization

Herein, considering MH devices' aim of creating AMFs with the highest efficacy for inducing heat generation by MNPs, novel new analytical criteria were defined for optimizing coil performance. Several coil designs were initially simulated and three best performers were physically realized. The coils were driven by a newly designed and constructed economically viable RF amplifier. A novel volumetric guide grid was designed and implemented with the purpose of obtaining both magnetic flux density and thermal measurements from the same positions. The coil performances were compared after calculating the values of the aforementioned criteria from the measurements.

To address the inefficiencies associated with commercially available RF amplifiers which often exceed the fidelity requirements for MH applications and achieve an optimal balance between performance and cost–effectiveness, a dedicated RF amplifier prototype was designed and implemented. The amplifier design included a custom RF oscillator stage operating within the $50 - 400\,\mathrm{kHz}$ frequency range, cascaded with a high–efficiency class AB amplifier stage. Multiple impedance matching networks were specifically developed to maximize energy transfer to each coil with varying impedance characteristics. Additionally, the amplifier's design incorporated active cooling systems to manage thermal dissipation during prolonged high-power operation, ensuring operational stability.

2.1 Coil Simulations

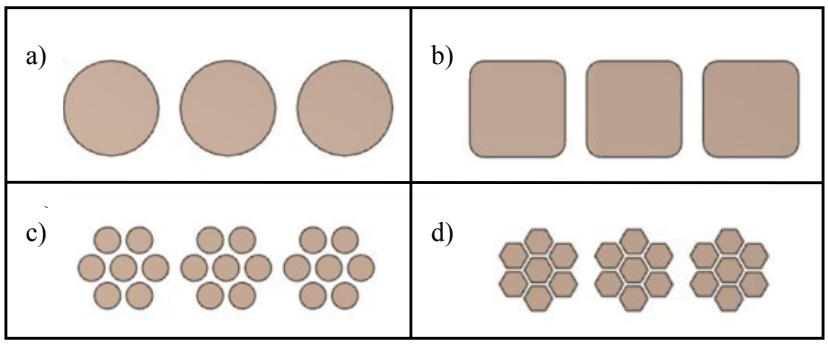


Figure 2.1 Cross sectional view of coil wire types investigated during finite element analysis (FEA) simulations; (a) round wire, (b) square wire, 7 strand (c) round Litz wire and (d) hexagonal Litz wire (three turn wound each).

Prior to physical implementation, several coil designs created by combining solenoid and Helmholtz geometries with different enameled wire types, namely, conventional round, square, round Litz, hexagonal Litz, (See Figure 2.1), were simulated for selecting best performers for coil construction. Square and round Litz wires were evaluated for their potential to minimize parallel capacitance and AC resistance, respectively, while hexagonal Litz wire was investigated for its potential to reduce both parallel capacitance and AC resistance.

FEA methods (maximum/minimum numerical spatial mesh sizes of 10 mm/20 μm) with COMSOL Multiphysics® 5.5 software package (COMSOL AB, Stockholm, Sweden), were used for simulating coil designs. Magnetic Fields, Heat Transfer in Solids and Electromagnetic Heating Physics toolboxes were used with Frequency–Transient One–Way Coupled Study toolbox in 2D–Axisymmetric space of COMSOL Multiphysics® 5.5 package for calculating magnetic flux density and temperature maps. For all of the designs, coil diameter was set to 44 mm which provided a coil gap size suitable for experimenting with rats. The dimensions of all of the wire types were determined so that their cross sectional area corresponded to 1.13 mm^2. The electrical conductivity of the wires were set to 5.87×10^7 S/m which ensured same total wire resistance across coil designs. All of the wires were coated with 90 μm electrical insulation. Litz wire variations were constructed using 7 strands. Solenoid geometries were designed with 10 number of windings (N_w), while Helmholtz geometries with 10

number of windings for each branch. In all of the simulations, the coils were driven with a 150 kHz AC root mean square (RMS) signal, solenoid and Helmholtz geometries were driven with 6.5 and 4.5 A currents, respectively. In total, five coil geometry–wire type combinations: solenoid coils with round wire, with square wire, with round Litz wire, with hexagonal Litz wire, Helmholtz coil with round wire were simulated on an HP Z640 workstation with 2.50 GHz Xeon®, E5 − 2680 v3 processor (Intel® CA, USA), 128 GB of memory and Quadro 4000 graphics card (NVIDIA, CA, USA).

For all of the coil simulations, the maximum of the magnetic flux density's magnitude at each position was defined as

$$max_B(r) = \max_{t\in[0,T]} \|B(r,t)\|_2 \tag{2.1}$$

where $r \in I\!R^3$ is the position, t is the time and $B(r,t) = [B_1(r,t),\ B_2(r,t),\ B_3(r,t)]^T \in I\!R^3$, is the magnetic flux density with $T = \frac{1}{150}$ms as the period of the applied signal.

Two more important assumptions were made for finite element analysis. First, linearity assumption implied that all signals were sinusoidal at 150 kHz implying that the value of Eq. 2.1 was the magnitude at 150 kHz in the frequency domain. Second, the geometry of the coils created a field such that the horizontal component of the magnetic flux density, $B_3(r,t)$, dominated the remaining components:

$$|B_3(r,t)| \gg \| \begin{bmatrix} B_1(r,t) \\ B_2(r,t) \end{bmatrix} \|_2 \tag{2.2}$$

implying

$$\|B(r,t)\|_2 \approx |B_3(r,t)| \Rightarrow max_B(r) \approx \max_{t\in[0,T]} |B_3(r,t)|. \tag{2.3}$$

Under these assumptions, as COMSOL® directly provides time domain RMS values of the signals, which is proportional to their maximum values, $max_B(r)$ was

directly obtained from the RMS values of $B_3(r,t)$:

$$max_B(r) = \sqrt{2}\, RMS(B_3(r,\cdot)). \tag{2.4}$$

The approximation in Eq. 2.3 was used in calculating spatial maximum magnetic flux density magnitude defined as

$$smax_B = \max_{r\in V} max_B(r), \tag{2.5}$$

$$smin_B = \min_{r\in V} max_B(r), \tag{2.6}$$

within a volume of interest (VOI), V, consisting of a 16 mm diameter sphere at the center of each coil.

Spatial mean magnetic flux density defined as

$$sm_B = \int_V max_B(r)\, dr, \tag{2.7}$$

and spatial standard deviation of magnetic flux density defined as

$$s\sigma_B = \left(\int_V (max_B(r) - sm_B)^2\, dr \right)^{\frac{1}{2}}. \tag{2.8}$$

For $smax_B$ and $smin_B$ were computed from the values at the FEA mesh points, the range $srange_B$ was calculated as the difference thereof and

$$scenter_B = max_B(\text{center of the coil}). \tag{2.9}$$

Likewise, first sm_B and subsequently $s\sigma_B$ were calculated by numerical integration at the mesh points.

A new **spatial magnetic field homogeneity index**,

$$sHom_B = \frac{sm_B}{s\sigma_B}, \tag{2.10}$$

was defined for creating a novel spatial **coil performance index**,

$$sP_{coil} = smax_B \times sHom_B. \tag{2.11}$$

Herein, $sHom_B$ gets higher with a increasing spatial mean value and decreasing spatial distribution of the maximum value with respect to time. sP_{coil}, therefore, rewards coils with large maximum values with a homogeneous distribution within the coil. Table 2.1 displays the results of the simulations.

Table 2.1 COMSOL Multiphysics® 5.5 simulation variables for different coil geometry–wire type combinations, 10 turn each.

	$\mathbf{sm_B}$ (mT)	$\mathbf{smin_B}$ (mT)	$\mathbf{smax_B}$ (mT)	$\mathbf{srange_B}$ (mT)	$\mathbf{scenter_B}$ (mT)	$\mathbf{s\sigma_B}$ (mT)	$\mathbf{sHom_B}$	$\mathbf{sP_{coil}}$
Solenoid Coil with Round Wire	1.726	1.618	1.857	0.239	1.772	0.089	19.393	36.013
Solenoid Coil with Square Wire	1.768	1.666	1.876	0.210	1.784	0.073	24.219	45.435
Solenoid Coil with Round Litz Wire	1.716	1.610	1.844	0.234	1.753	0.087	19.724	36.371
Solenoid Coil with Hexagonal Litz Wire	1.757	1.578	1.841	0.263	1.752	0.104	16.894	31.102
Helmholtz Coil with Round Wire	1.831	1.803	1.855	0.052	1.839	0.014	130.786	242.608

2.2 Physical Implementation and Coil Measurements

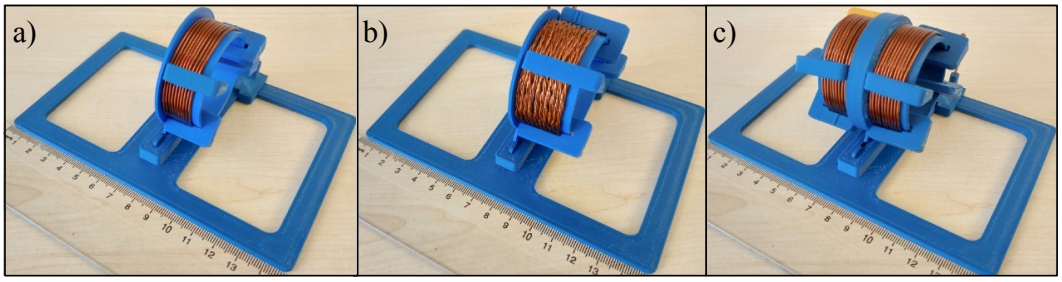


Figure 2.2 Physical coils: $N_w = 10$ turn solenoid coils (a) with round wire, (b) with round Litz wire and (c) Helmholtz coil with round wire.

While the main criteria for physical implementation selection was sP_{coil}, the remaining variables in Table 2.1 were also taken into account. Consequently, the square and hexagonal Litz wire designs, which cost more because of the special wires, were excluded due to their insufficient performance gain in Table 2.1.

Solenoid coils with round wire and **with round Litz wire** with the number of windings $N_w = 10$ and, Helmholtz coil with round wire with the number of windings $N_w = 10$ for each branch, were selected for physical implementation.

Enameled copper wires (EMTEL, İstanbul, Türkiye) with 1.2 mm (round wire) and 0.45 mm (round Litz wire) diameters were used for creating the same cross sectional area of 1.13 mm^2 as in Section 2.1. Furthermore, all of the remaining coil parameter values were the same as in FEA simulations described in Section 2.1. Economical considerations required producing the Litz wire in–house, with seven 0.45, mm strands that were first bundled together and then manually stranded.

The wires were wound using an MTT2000 coil winding machine (Eray Online, İstanbul, Türkiye) around the tubes that were designed on Fusion 360 software (Autodesk, San Francisco, CA, USA) and were in–house printed on an Ender 3 Pro model 3D printer (Creality, Shenzhen, China) using acrylonitrile butadiene styrene (ABS) (eSUN, Shenzhen Esun Industrial Co., Shenzhen, China) filament which is both non–magnetic and suitable for high temperature applications [55] (See Figure 2.2).

Coil impedances were measured and appropriate impedance matching circuits were built for the RF amplifier as described in Section 2.8. The standard electrical two port model of a typical coil consists of inductance, L_{Coil}, wire resistance, R_s and parasitic capacitance, C_p, shown in Figure 1.4, has an impedance, Z_{Coil} :

$$Z_{\text{Coil}}(\omega) = \frac{R_s + \jmath\omega\, L_{\text{Coil}}}{1 - \omega^2\, L_{\text{Coil}}\, C_p + \jmath\omega\, C_p\, R_s} \tag{2.12}$$

where ω is the frequency. For this circuit, there are three resonant frequencies, which were analytically obtained after cumbersome but straightforward calculations:

$$\omega_1 = 0, \quad \omega_2 = \frac{\sqrt{L_{\text{Coil}} - C_p\, R_s^2}}{L_{\text{Coil}}\sqrt{C_p}}, \quad \omega_3 = -\omega_2 \tag{2.13}$$

with

$$Z_{\text{Coil}}(0) = R_s, \quad Z_{\text{Coil}}(\omega_2) = Z_{\text{Coil}}(\omega_3) = \frac{L_{\text{Coil}}}{C_p\, R_s}. \tag{2.14}$$

Taylor expanding $Z_{\text{Coil}}(\omega)$ in Eq. 2.12 near $\omega_1 = 0$ and far away from the resonant frequencies, shows that the coil can be treated as a resistance in series with an inductor:

$$Z_{\text{Coil}}(\bar{\omega}) = R_s + \jmath\bar{\omega}L_{\text{Coil}} \tag{2.15}$$

where $\bar{\omega}$ denotes frequencies within the aforementioned range.

Table 2.2 Measured L_{Coil}, f_{Coil} and calculated R_s, Z_{Coil} parameters for each physical coil design.

	$\mathbf{L_{Coil}}$ (μH)	$\mathbf{R_s}$ (Ω)	$\mathbf{f_{Coil}}$ (MHz)	$\mathbf{Z_{Coil}}$ at 150kHz (Ω)
Solenoid Coil with Round Wire	6.562	0.021	79.632	6.185
Solenoid Coil with Round Litz Wire	5.745	0.020	82.845	5.415
Helmholtz Coil with Round Wire	10.508	0.042	96.914	9.904

For physical implementations, L_{Coil}, R_s and resonant frequency, $f_{\text{Coil}} = \dfrac{\omega_2}{2\pi}$ coils were measured with an Analog Discovery 2 device (Digilent Inc., Austin, TX, USA) and Impedance Analyzer board (Digilent Inc., Austin, TX, USA) using the Waveforms software (Digilent Inc., Austin, TX, USA) (See Table 2.2). As the resonant frequencies were much higher than the operating frequency (See Table 2.2), $f_{\text{Coil}} \gg f_o = \dfrac{\omega_o}{2\pi} = 150\,\text{kHz}$, the simplified model of Eq. 2.15 was assumed. Appropriate impedance matching circuits were built and used for guaranteeing maximum energy transfer.

2.3 Localizing and Fixing Measurement Points

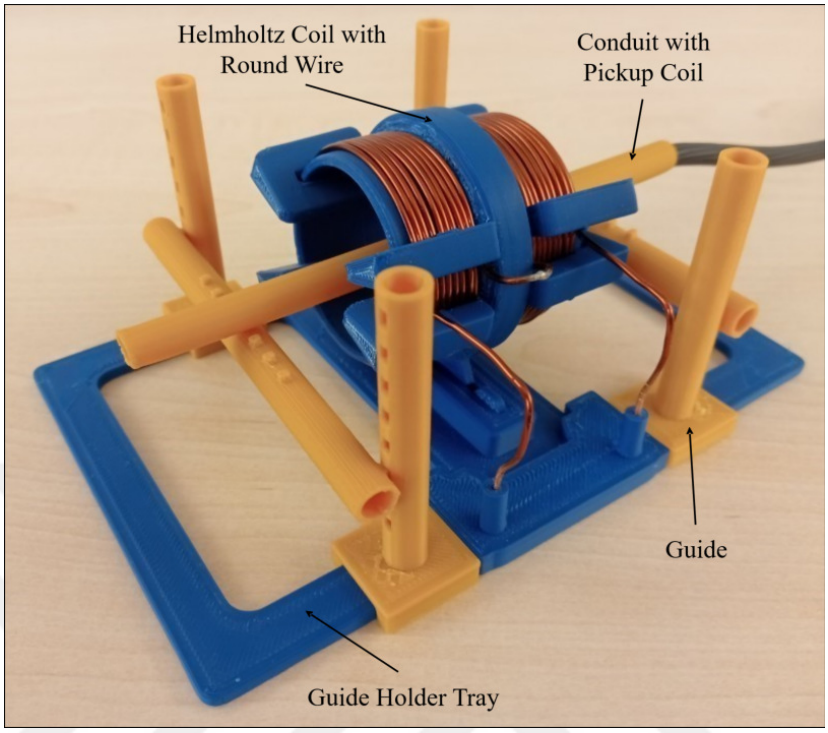


Figure 2.3 In–house designed and 3D printed ABS guide frame; conduit with pickup coil, guide and guide holder tray with Helmholtz coil with round wire.

For assuring proper repeatability, measurement positions within coil volume were localized and fixated using an in–house designed and 3D printed guide frame made of ABS. Overall, 20 placeholders on the conduit carrying pickup coils (See Section 2.4), 7 placeholders on the horizontal and 8 placeholders on the vertical guides (1120 different possible positions in total) were implemented with 6 mm separation for accurately positioning pickup coils (See Figure 2.3).

For measuring magnetic flux density within unloaded volumes, single turn pickup coils of diameters 3, 6 and 9 mm, using enameled copper wires (EMTEL, İstanbul, Türkiye) with 1.2 mm diameter were constructed and 6 mm diameter coil was selected based on performance measurements described in Section 2.4.

2.4 Pickup Coil Selection

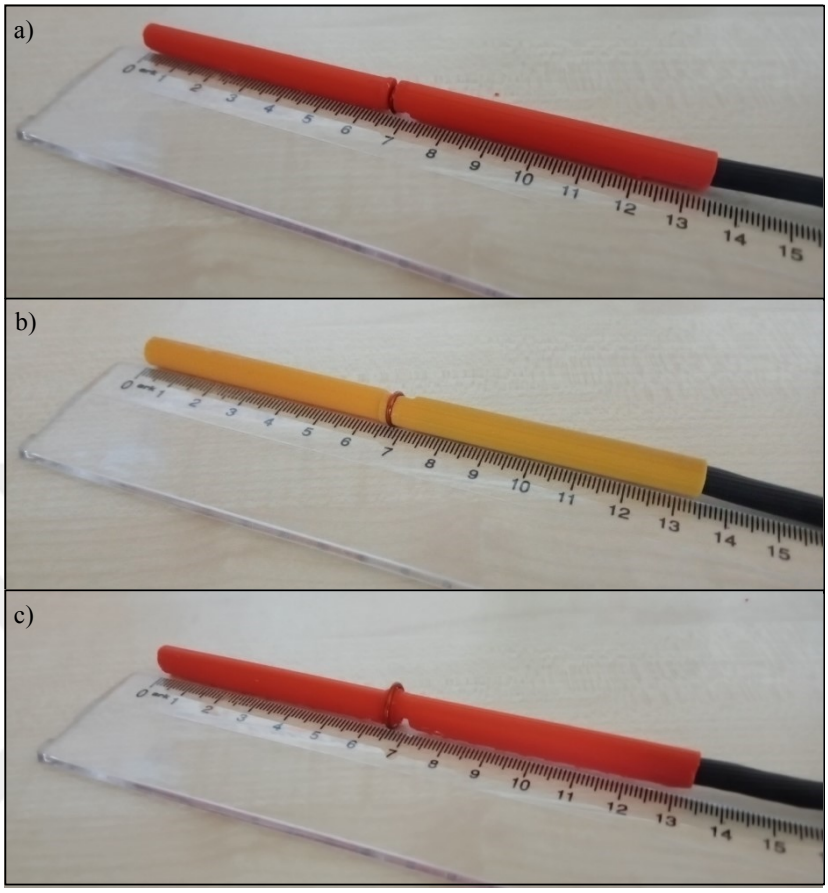


Figure 2.4 In–house designed and 3D printed ABS conduits holding pickup coils with (a) 3, (b) 6 and (c) 9 mm diameters.

For measuring magnetic flux density within unloaded volumes, lack of Gauss-meters in the MH frequency range of 50–400 kHz required constructing single turn pickup coils of diameters 3, 6 and 9 mm, using enameled copper wires (EMTEL, İstanbul, Türkiye) with 1.2 mm diameter providing a range of coil sensitivity and resolution options.

For selecting the pickup coil with the best signal–to–noise ratio (SNR), measurements were made within the center of Helmholtz coil with round wire which had the highest sP_{coil}. Each pickup coil was connected to the Analog Discovery 2 device with magnetically insulated coaxial cables (RG178RF, Huber+Suhner, Herisau, Switzerland) and positioned within MH coil as prescribed by the guide frame for localizing the center measurement point. The MH coil was driven with 150 kHz sine waves at

$p_w = 10, 25, 50, 75, 100\%$ of the RF generator's maximum output power. Induced voltages across the pickup coil terminals were recorded for 163.82 μs at the sampling period of 10 ns using the Waveforms software. For SNR assessment across various power levels, **time–domain root mean square** of the signals, $tRMS_V(p_w)$, were calculated over a half period with an in–house developed MATLAB® software.

For noise measurements, the AMF amplifier was turned on without supplying power to MH coils ($p_w = 0\%$) and the voltage was recorded at the pickup coil terminals under exactly the same conditions for $tRMS_V$ measurements. The standard deviation of the collected time–domain data, $t\sigma_n$, was calculated over a half period with an in–house MATLAB® code.

All measurements were carried after assuring that the MH coil was at 22^o C by tracking the temperature with a GTC 400 C infrared camera (Bosch, Gerlingen, Germany).

An in–house MATLAB® software was developed for calculating the **time–domain electromagnetic signal–to–noise ratio**, $tSNR_e(p_w)$:

$$tSNR_e(p_w) = \frac{tRMS_V(p_w)}{t\sigma_n}. \tag{2.16}$$

Finally, **the mean power electromagnetic SNR**, $mpSNR_e$ value was calculated:

$$mpSNR_e = \frac{1}{5} \sum_{p_w=10,25,50,75,100} tSNR_e(p_w). \tag{2.17}$$

The pickup coil with the smallest area satisfying an $mpSNR_e > 10$ (pickup coil with 6 mm diameter, see Figure 2.4) was chosen for magnetic flux density measurements.

Table 2.3 Pickup coil performance metric values.

Diameter	**tSNR$_e$**					**mpSNR$_e$**
	10%	**25%**	**50%**	**75%**	**100%**	
3 mm	2.026	3.835	7.752	10.272	14.623	7.702
6 mm	8.124	15.371	30.961	41.061	58.627	30.829
9 mm	18.272	34.572	69.685	92.352	132.045	69.385

2.5 Magnetic Flux Density Measurements

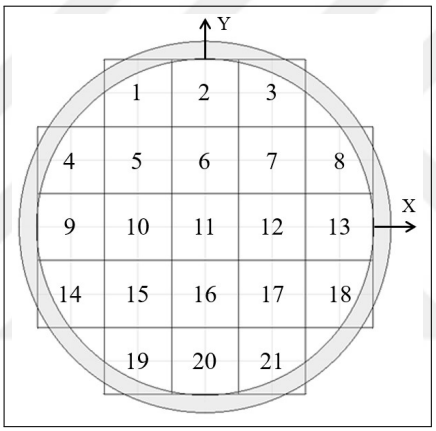


Figure 2.5 Transversal view of 21 measurement points within MH coils, horizontally and vertically 6 mm apart.

For physical implementations, the dominance of the third component of the magnetic flux density, $B_3(r,t)$, (See Eq. 2.3) was also assumed and the pickup coil surface was always placed parallel to the MH coil surface. In accordance with Section 2.3, the measurement locations were chosen in the center of the coil, i.e., positions 6, 10, 11, 12 and 16 in Figure 2.5 which was longitudinally slid within each MH coil at three different axial positions; -6, 0, $+6$ mm using the guide (See Figure 2.3). The frequency (150 kHz) and power levels ($p_w = 10, 25, 50, 75, 100\%$) in pickup coil selection were also used.

At each prescribed position $r \in I\!R^3$ the induced voltage, e_{ind}, was recorded for 163.82 μs at the sampling period of $\Delta t = 10$ ns. The flux was assumed to be homogenous

across the pickup coil's surface. Using Faraday's Law,

$$e_{ind}(r, p_w, t) = -\pi\,(6\,\mathrm{mm})^2\,\frac{d}{dt}B_3(r, p_w, t), \tag{2.18}$$

where 6 mm was the radius of the pickup coil, magnetic flux density, $B_3(r, p_w, t)$, was calculated from the collected data by numerically integrating Eq. 2.18:

$$B_3(r, p_w, t_k) = -\frac{\Delta t}{\pi\,(6\mathrm{mm})^2}\sum_{k=1}^{K} e_{ind}(r, p_w, t_k) \tag{2.19}$$

where $t_k = (k-1)\Delta t$ and K denotes the number of samples.

At the prescribed positions, $B_3(r, p_w, t)$ was itself numerically integrated over a half–period for calculating **time domain root mean square of magnetic flux density**, $tRMS_B(r, p_w)$, at the listed power levels for observing correlations between magnetic flux density and MNP heating during MH measurements (See Results Section).

2.6 Magnetic Hyperthermia Measurements

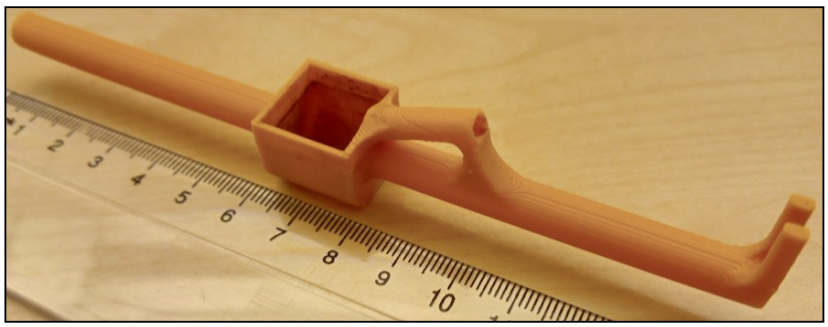


Figure 2.6 In–house designed and 3D printed ABS cup designed to contain MNPs during MH measurements.

Superparamagnetic iron oxide nanoparticle (SPION) based MNP samples with 166.5 mg/mL concentration were prepared by coating 13 nm diameter nm diameter iron oxide nanoparticles coated with beta-cyclodextrin structures and dispersing in distilled water. The average hydrodynamic diameter of MNPs was measured as 52 nm using

Zetasizer Nano S90 dynamic light scattering device (Malvern Panalytical, Malvern, UK) and average diameter of iron oxide nanoparticles was measured as 13 nm using Quattro S ESEM scanning transmission electron microscope (Thermo Fisher Scientific, Waltham, MA, USA). Furthermore, a portion of MNP samples were diluted by adding distilled water to obtain samples with 120 mg/mL concentration.

A 4.096 mL ABS cubic cup with a guide frame (See Figure 2.6) incorporating pathways for connecting fiber optic temperature probes was designed and printed for placing the MNPs within the MH coils. A strong magnetic field compatible fiber optic temperature probe TS2 (Weidmann–Optocon, Dresden, Germany) was used in combination with FOTEMP OEM (Weidmann–Optocon, Dresden, Germany) thermometer system and FOTEMP Assistant 2 (Weidmann–Optocon, Dresden, Germany) software for tracking and recording temperature variations at the maximum sampling period of 250 ms. Control experiments were carried using the same cup filled with distilled water. The data were analyzed with in–house MATLAB® software. The measurements were carried by placing the ABS cubic cup within the MH coils at the prescribed positions. Effectively, referring to the scheme of Figure 2.5, the measurements were conducted at transversal positions numbered; 6, 10, 11, 12, 16 at three different axial positions; -6, 0, $+6$ mm, within the MH coils at 22^o C ambient temperature, using a 2 mL solution of 166.5 mg/mL MNP solution. Each measurement was conducted for 40 minutes, at 150 kHz, 100% RF generator power and after assuring that the MH coil was cooled off to 22^o C temperature. Starting temperatures of experiments with MNP samples and distilled water were at 22^o C with a maximum deviation of $\pm 0.1^o$ C. With the exception of few noisy time points, distilled water did not heat up and its temperature remained constant at 22^o C, demonstrating lack of heat transfer from the setup. Time domain data were fitted to a line, and the slope of each fitted line was calculated to assess the heating rates (See Results Section).

The increase in temperature was calculated by taking the difference between $T(r, t_k)$ and $T(r, 0)$:

$$\Delta T(r, t_k) = T(r, t_k) - T(r, 0), \tag{2.20}$$

where, $r \in I\!R^3$ is the position, t_k, is the k^{th} sampling point with a total of K samples.

Similar to Section 2.1, definitions for the last temperature point are provided as, maximum temperature rise:

$$smax_T = \max_{r \in V} \Delta T(r, t_K), \tag{2.21}$$

$$smin_T = \min_{r \in V} \Delta T(r, t_K), \tag{2.22}$$

spatial mean temperature rise:

$$sm_T = \int_V \Delta T(r, t_K)\, dr, \tag{2.23}$$

and spatial standard deviation of temperature rise:

$$s\sigma_T = \left(\int_V (\Delta T(r, t_K) - sm_T)^2\, dr \right)^{\frac{1}{2}}, \tag{2.24}$$

where the volume of interest (VOI), V, was prescribed by the guide frame (See Section 2.5).

A new spatial MH homogeneity index,

$$sHom_T = \frac{sm_T}{s\sigma_T}, \tag{2.25}$$

was defined for creating a novel spatial **coil thermal index**

$$sT_{coil} = smax_T \times sHom_T. \tag{2.26}$$

2.7 Design and Implementation of the AMF Signal Generator

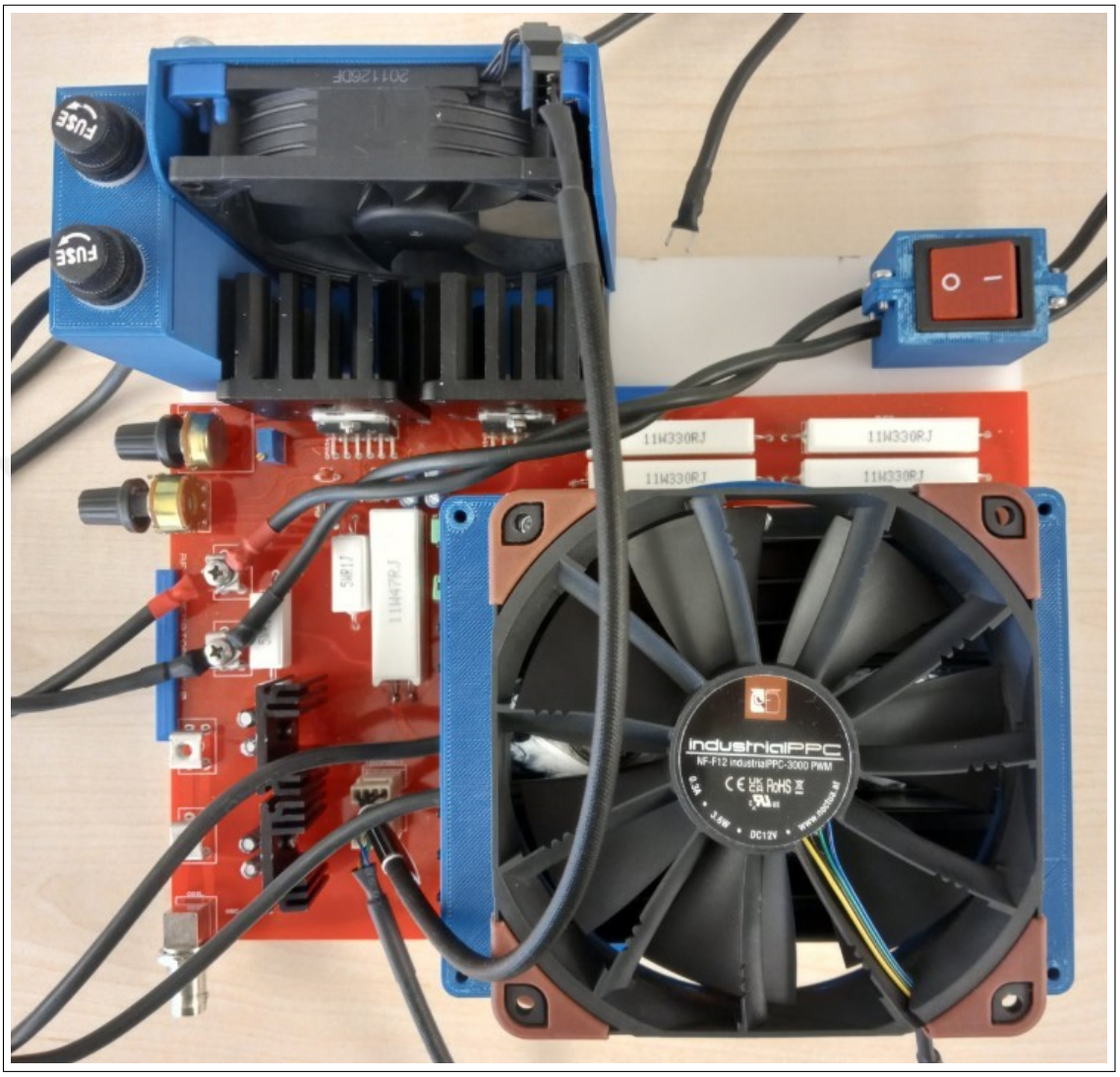


Figure 2.7 Top view of the designed RF generator.

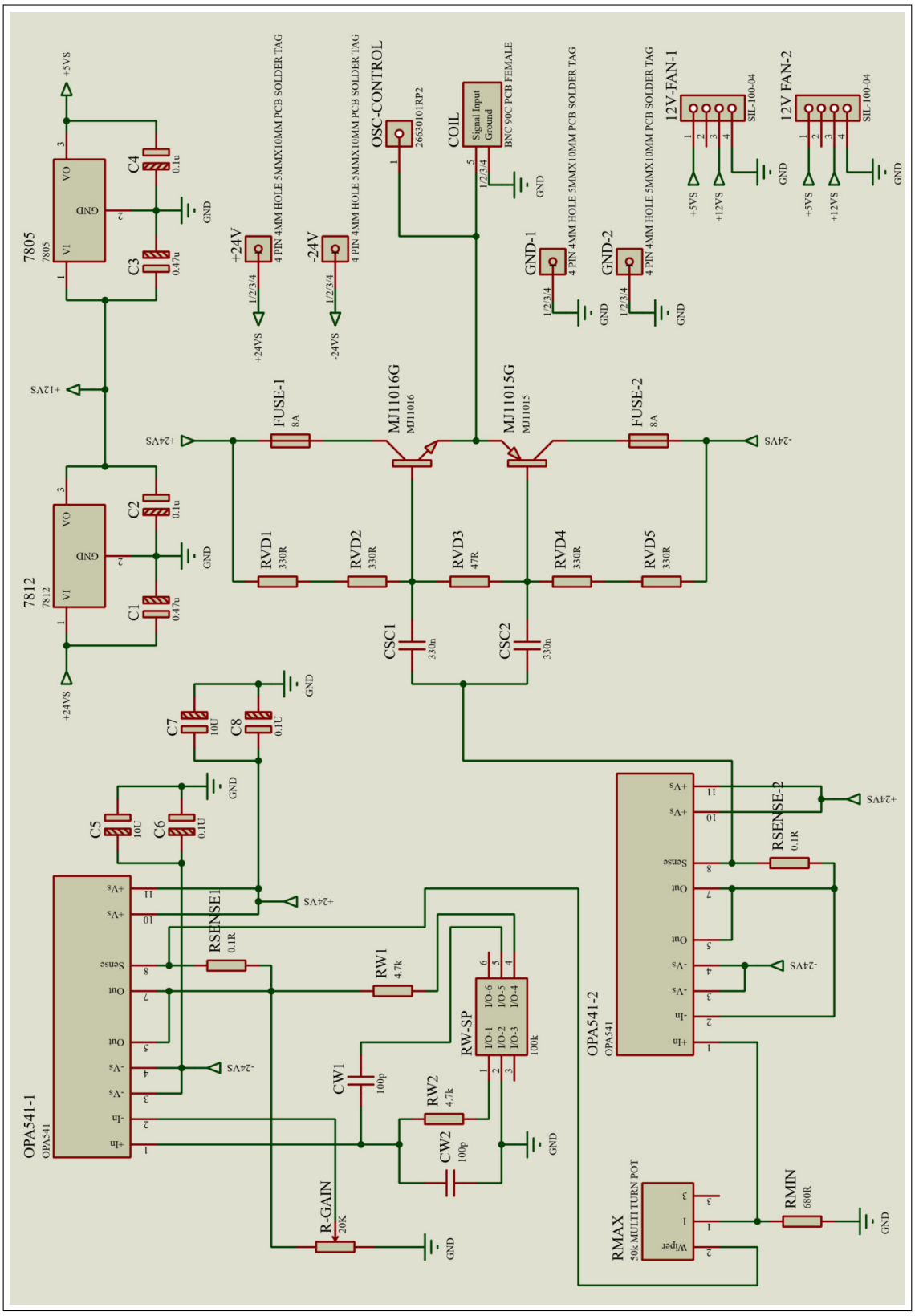


Figure 2.8 Schematic drawing of the whole RF Generator circuit.

A standard AMF signal generator design that can stably operate in the low RF range of $50 - 200\,\text{kHz}$ was implemented for driving MH coils (See Figures 2.7, 2.8). Power and voltage calculations are provided under Section 2.9). Whole system was fed with two identical 750 W, 48 V UHP-750-48 model (Mean Well, New Taipei City, Taiwan) switched mode power supplies (SMPS), one supplying $+48\,\text{V}$ and the other $-48\,\text{V}$, to the oscillator and amplifier stages by power supply splitting. As the oscillator stage, Wien–Bridge Oscillator circuit was used. An OPA541 (Texas Instruments, Dallas, TX, USA, $\pm$ 40 V supply voltage, 10 A output current, 1 MHz bandwidth, programmable current limiting function) high–power OP–AMP was used to create a high gain resonator. Wien–Bridge Oscillator is cascaded with a Class AB Amplifier structure to form a high power AMF generator device. Another OPA541 was used to isolate Wien–Bridge Oscillator stage from the Class AB Amplifier stage, thereby converting a high impedance–low current signal into a low impedance–high current signal. In the Class AB amplifier stage, positive and negative half cycles of the generated sine waves were amplified by MJ11016G (On Semiconductor, Phoenix, AZ, USA) and MJ11015G (On Semiconductor, Phoenix, AZ, USA) Darlington transistors suited for high–power and high–gain applications, respectively [49].

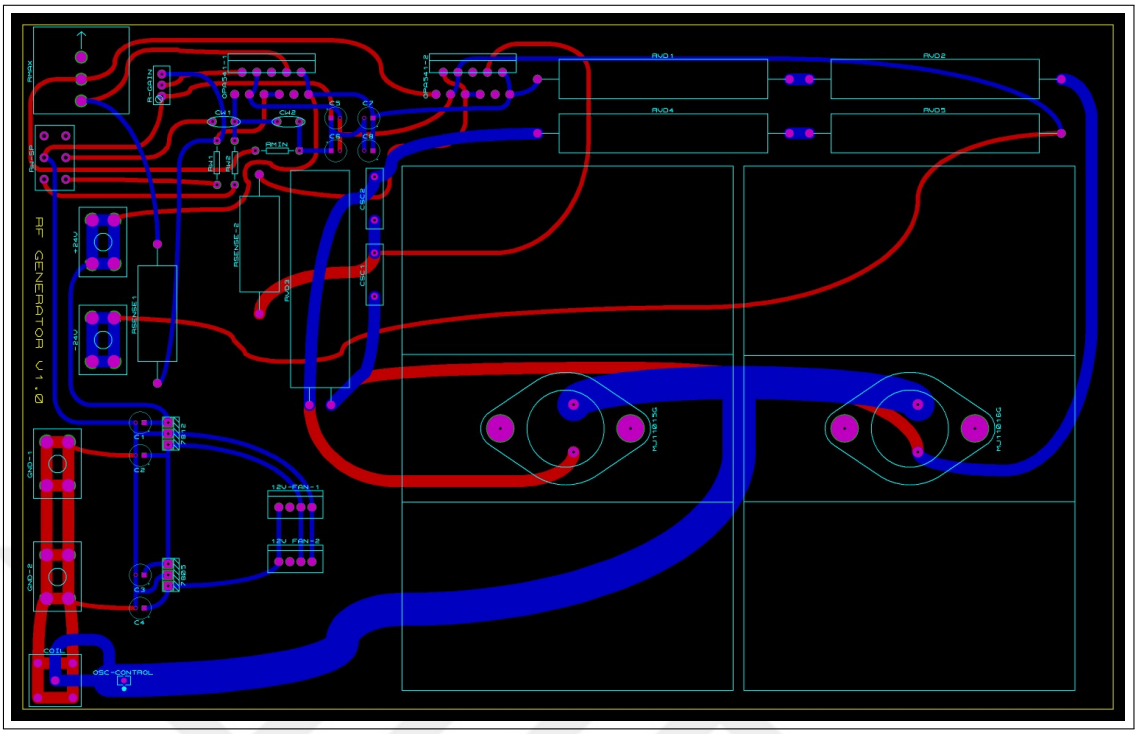


Figure 2.9 PCB design of the RF Generator circuit at Eagle PCB design environment. Red, blue, magenta, cyan and yellow colors indicate top layer copper traces, bottom layer copper traces, component names–positions and PCB edges respectively.

AMF generator's PCB was designed at Eagle (Autodesk, San Francisco, CA, USA) environment, consulting IPC-2221 (Generic Standard on Printed Board Design) document and using standard RF circuit design criteria regarding literature (See Figure 2.9) [47]. For thermal management; OP–AMPs were equipped with $680 - 125220$ model (Wakefield–Vette, Nashua, NH, USA) heat sinks and actively cooled with a NF-A9 PWM Chromax (Noctua, Vienna, Austria) fan. Darlington transistors were equipped with 413K model (Wakefield–Vette, Nashua, NH, USA) heat sinks and actively cooled with a NF-F12 Industrial PPC (Noctua, Vienna, Austria) fan. Silicone based thermal paste with metal oxide filling (DLG, İstanbul, Türkiye) was used as the thermal interface between components and heat sinks to ensure minimum thermal resistance. AMF generator's temperature was tracked using GTC 400 C infrared camera that was used for tracking thermal performance of MH coils. Combined effect of electromagnetic and thermal noises on the performance of AMF generator circuit was assessed using DS1102E oscilloscope (Rigol, Beijing, China) with standard measurement probes. Time–domain RMS, $tRMS_V$ of the signal and time–domain standard

deviation of the noise, $t\sigma_n$ were measured for each connection node of the AMF generator circuit. Then, following equation;

$$tSNR_e = \frac{tRMS_V}{t\sigma_n}. \tag{2.27}$$

was used to calculate time-domain electromagnetic SNR, $tSNR_e$ for each connection node. A joint limit of $tSNR_e > 10$ at each connection node under 150 kHz sine wave, 100% output power level, while Helmholtz coil with round wire connected was set to pass the noise performance test.

2.8 Design and Implementation of the Impedance Matching Board

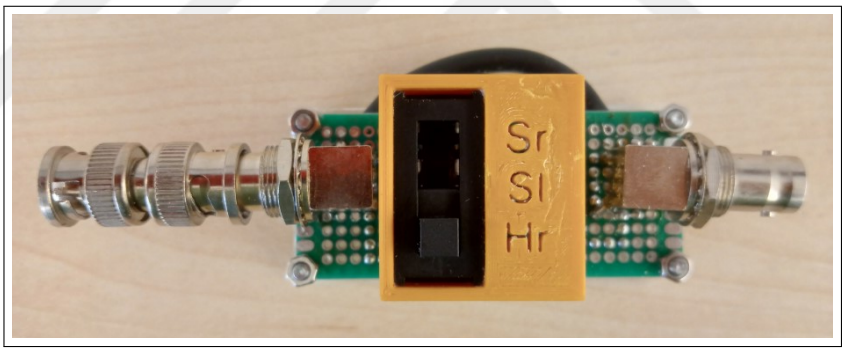


Figure 2.10 Impedance matching board.

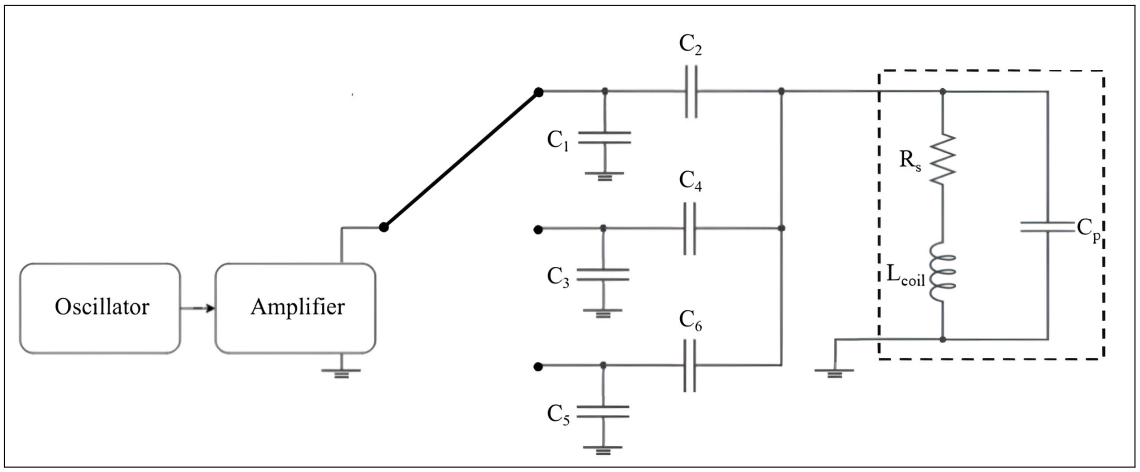


Figure 2.11 Simple schematics showing all 3 designed impedance matching circuits with a 3 way slider switch for multiple MH coils.

Three impedance matching intermediate circuits, one for each MH coil, designed in the form of high pass L–networks integrated to one board, were realized for maximum power transfer from the AMF generator to each MH coil (See Figure 2.10). A three way slider switch enabled switching between any of the three impedance matching circuits with ease as needed. **MH coils' impedance**, Z_{Coil} (See Section 2.2) and **AMF generator's output impedance**, Z_{Amp} at 150 kHz output frequency were determined in advance for calculating impedance matching circuit parameters. Female type Bayonet Neill–Concelman (BNC) connectors with 50 Ω impedance are utilized for both the RF generator board and the impedance matching board as signal input and output points. Female type BNC connectors were connected via male to male type BNC adapters. A custom made BNC to alligator clips structure was constructed with an RG-213 coaxial cable (50 Ω impedance, up to 2.4 GHz frequency range and 40 A current carrying capacity) to connect impedance matching board with corresponding MH coils. All 3 L–networks were designed with only capacitors, without the need of any inductors for proper impedance matching. Detailed schematics for 3 MH coil impedance matching circuits are provided in Figure 2.11 with the basic RLC model of a MH coil.

High–voltage (since capacitors are reactive components voltage limit is the important factor, rather than wattage) polyester type capacitors (Jackcon, New Taipei City, Taiwan) are used. Capacitor values in the impedance matching circuit were determined by the MH coils' impedance and the amplifier stage's output impedance. First, amplifier's output impedance for operating frequency (150 kHz) was calculated [56];

$$Z_{Source} = R_{Load} \times \left(\frac{V_{RMS-Open}}{V_{RMS-Loaded}} - 1 \right) \tag{2.28}$$

Output RMS AC voltage of the amplifier stage was measured without any load ($V_{RMS–Open}$) using the AC voltmeter mode of the Analog Discovery 2 device. Then, a 2 W, 1 kΩ carbon film resistor was connected between the output of the amplifier

stage and the ground. Output RMS AC voltage across R_{Load} was measured which gave $V_{RMS–Loaded}$. Measurement data were inserted to Eq. 2.28 to calculate Z_{Source} as 1.55 Ω at 150 kHz operating frequency.

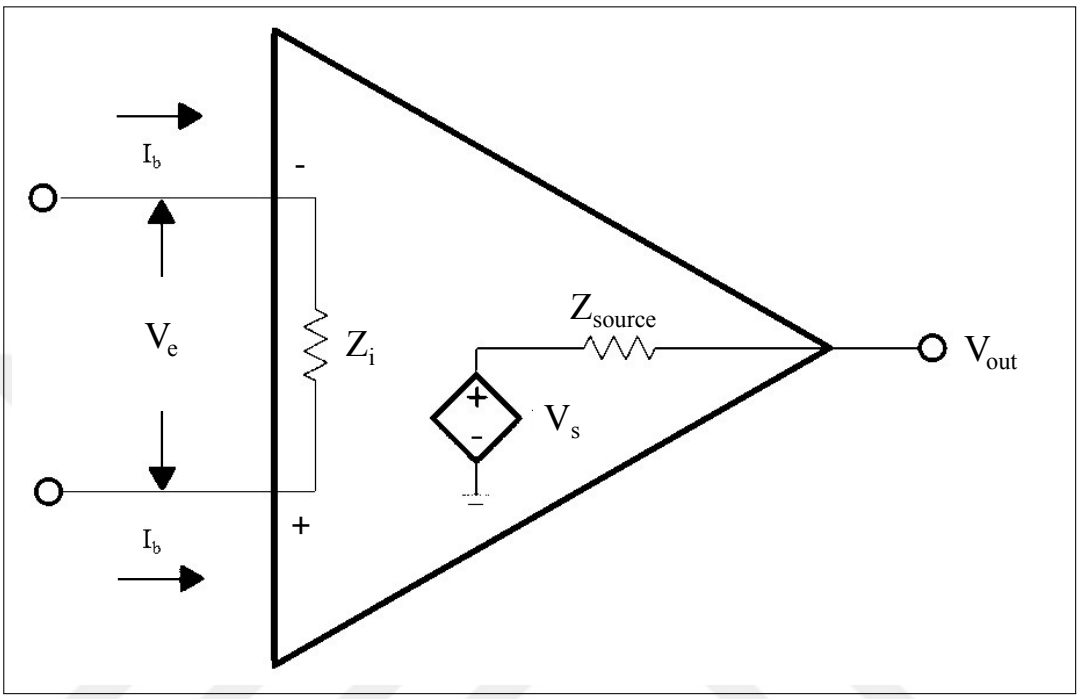


Figure 2.12 Simplified Thevenin equivalent models of an amplifier's input and output.

Eq. 2.28 can be obtained with theoretical calculations over Thevenin equivalent model of an amplifier's output (See Figure 2.12) which consists of a dependent voltage source connected to ground from one end, and to an impedance component from other. It must be noted that; since equation is bounded by RMS values, calculations are independent from signal phase.

After calculating Z_{Source} from mentioned measurements, the L–network's components were selected for impedance matching [57] at the 150 kHz operating AMF frequency [49] using the following steps, first coil impedance is normalized regarding the source impedance,

$$Z_L^{norm} = \frac{Z_{coil}}{Z_{source}} \tag{2.29}$$

then the admittance is calculated,

$$Y_L^{norm} = \frac{1}{Z_L^{norm}}. \tag{2.30}$$

To cancel the imaginary part of the admittance, a parallel capacitor should be added to the system. Susceptance added by the parallel capacitor is calculated as,

$$B_{parallel} = -Im\left(Y_L^{norm}\right) \tag{2.31}$$

and the capacitance corresponding to the calculated susceptance is,

$$C_{parallel} = \frac{B_{parallel}}{2\pi f}. \tag{2.32}$$

After adding the parallel capacitor to the system, admittance of the system should become purely real, Y_{series} and the transformed normalized impedance is calculated as,

$$Z_{series}^{norm} = \frac{1}{Y_{series}} \tag{2.33}$$

Lastly, series capacitor is added to the system to match the impedance,

$$C_{series} = \frac{1}{2\pi f \left|1 - Z_{series}^{norm}\right|} \tag{2.34}$$

Table 2.4 Calculated C_{series} and $C_{parallel}$ values of each impedance matching L–network circuit for each physically implemented MH coil design.

	C_{series} (nF)	C_{parallel} (nF)
Solenoid Coil with Round Wire	177	5249
Solenoid Coil with Round Litz Wire	203	5249
Helmholtz Coil with Round Wire	109	5249

All the steps for calculating impedance matching board series and parallel capacitor values (See Table 2.4) were repeated for each physical coil implementation.

2.9 Power Calculations

In a scenario where the coils' impedance are perfectly matched with the RF generator's output impedance for maximum power transfer; the total power consumption of the system, including both the RF generator and the coil is determined by the real power. Also, the voltage across the coil is half of the RF generator's open–circuit output voltage [58]. Accordingly, **post impedance matching impedance**, $pimZ_{coil}$ value which is equal to Z_{source} after the impedance matching was used for calculating **post impedance matching AMF generator output RMS voltage**, $pimV_{source}$ at 150 kHz, considering the targeted maximum **post impedance matching MH coils' RMS current** $pimI_{coil}$ of 6.5 A,

$$pimV_{source} = 2\left(pimI_{coil}\right)\left(pimZ_{coil}\right), \tag{2.35}$$

and the required real power, P RMS levels are calculated.

$$P_{source} = \left(pimV_{source}\right)\left(pimI_{coil}\right), \tag{2.36}$$

B Novel Liquid Cooling System

2.10 Cooling System Simulations

Three different coil cooling systems were simulated using the FEA in COMSOL Multiphysics® Software 5.5 [59, 60]: a conventional passive cooling system that transfers heat through stagnant air via natural convection, a conventional liquid cooling system wherein the coolant flows axially along the coil axis and contacts the outer surface of the wires, and a novel liquid cooling system wherein the coolant flows through a microchannel inside the wires, axially along the wire axis and contacts the inner wire surface. The conventional passive cooling system served as the electromagnetic benchmark, assessing the coil wires' current distribution influenced by the frequency of electromagnetic fields, while the conventional liquid cooling system served as the thermal benchmark, evaluating the system's temperature, which is affected by heat dissipation from the coil wires to the cooling liquid.

The 2D–Axisymmetric option was chosen as the simulation space due to its computational efficiency [61] and ability to accurately capture the Axisymmetric geometry of the coil cooling system. The Electrical Circuits module was used to supply 25 A peak alternating current (AC) to the coil wires, generating magnetic fields in space via the Magnetic Fields module, relying on Poisson's equation,

$$E = -\nabla\phi, \tag{2.37}$$

where E is the electric field, ∇ is the Del operator, and ϕ is the electric potential. The expression $\nabla\phi$ gives the rate and direction of change in the electric field at each point in space, and the negative sign $(-)$ indicates that the electric field points in the direction of the greatest decrease in electric potential. Accordingly, the Magnetic Fields module

uses Ohm's Law within the context of electromagnetics to compute the current density,

$$J = \sigma_{\mathrm{e}} E, \tag{2.38}$$

where σ_{e} is the electrical conductivity of the material. The Magnetic Fields module was one–way coupled with the Heat Transfer in Solids module to compute the electromagnetic heating,

$$Q = J \cdot E, \tag{2.39}$$

COMSOL computes the final temperature, T, for each point in the simulation space, considering the steady–state scenario, with the following expression:

$$0 = \nabla \cdot (k \nabla T) + Q, \tag{2.40}$$

where k is the thermal conductivity of the material, ∇T is the gradient of temperature, which gives the rate of change in temperature at a point in space, indicating the direction of the steepest temperature increase. The expression $\nabla \cdot (k \nabla T)$ is the divergence of the heat flux, describing how heat is diffusing through the material. The combined use of these modules ensured a detailed replication of the magnetic and thermal physics. The same coil geometry, with a 22 mm radius, 12.4 mm length, and 10 wire turns was used with 1.2 mm diameter wires to test the performance of both cooling systems inside a cylindrical space with a 500 mm radius and 1000 mm length. Copper's material properties and coil boundary conditions were assigned to the coil wires to fully replicate electrical, magnetic, and thermal characteristics. To prevent the accumulation of thermal energy within the confined cylindrical space and maintain simulation realism,

a convective heat flux boundary condition was applied to the domain's edges using the external natural convection option at 1 atm absolute pressure. Additionally, the cylindrical space was defined as an ideal gas with the material properties of air. The conventional liquid cooling system utilizes direct liquid cooling (DLC) [62, 63], where the coolant flows axially along the coil axis, surrounding the coil wires with a thickness of 1.5 mm. In contrast, the novel liquid cooling system directs the coolant through an internal microchannel running parallel inside the wires. Three versions of this system were designed, each featuring a different microchannel radius: 0.25, 0.30, and 0.35 mm. Distilled water was selected as the cooling fluid, and material properties were assigned to the relevant domains of both the conventional and novel liquid cooling systems. All material properties are provided in Table 2.5 with values sourced from reference [64], and Figure 2.13 illustrates all coil cooling systems.

Table 2.5 Simulation material properties for all cooling systems.

Material	Property	Cooling Systems
Copper	Relative Permeability	999.994×10^{-3}
	Relative Permittivity	1
	Electrical Conductivity (S/m)	5.87×10^{7}
	Heat Capacity at Constant Pressure $(J \times kg^{-1} \times K^{-1})$	385
	Density (kg/m)	8960
	Thermal Conductivity $(W \times m^{-1} \times K^{-1})$	401
Air	Relative Permeability	1
	Relative Permittivity	1
	Electrical Conductivity (S/m)	0
	Heat Capacity at Constant Pressure $(J \times kg^{-1} \times K^{-1})$	1005
	Specific Gas Constant $(J \times kg^{-1} \times K^{-1})$	287
	Thermal Conductivity $(W \times m^{-1} \times K^{-1})$	1
Distilled Water	Relative Permeability	0.99
	Relative Permittivity	80.1
	Electrical Conductivity (S/m)	0
	Heat Capacity at Constant Pressure $(J \times kg^{-1} \times K^{-1})$	4184
	Density (kg/m)	997
	Thermal Conductivity $(W \times m^{-1} \times K^{-1})$	0.598
	Ratio of Specific Heats	1

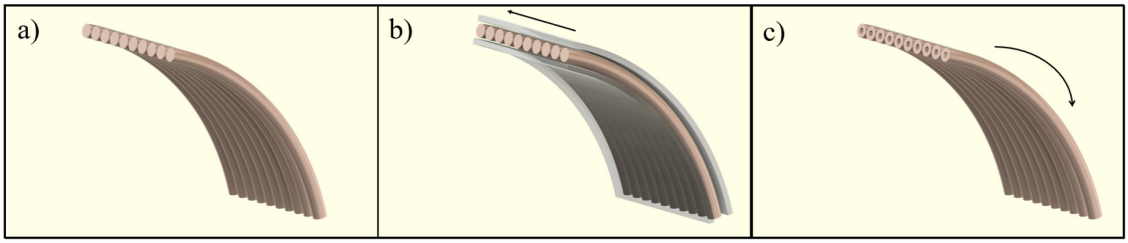


Figure 2.13 Different coil cooling systems; (a) the conventional passive, (b) the conventional liquid with DLC and (c) novel liquid with various microchannel radii of 0.25, 0.30, and 0.35 mm. (Arrows indicate cooling liquid flow directions, (b) semi-transparent region around coil wires indicate outer shell of the DLC system).

All simulation geometries were meshed using free triangular elements, with minimum and maximum mesh sizes of 0.02 and 10 mm, respectively. Additionally, a boundary layer was assigned to the edges of the coil wires, with the number of boundary layers set to 12 and the boundary layer stretching factor set to 1.2. This approach enhanced the mesh quality, enabling high–resolution current distribution maps to be obtained. The initial step of the simulations involved Frequency Domain Analysis to compute magnetic fields and current distributions, followed by Time–Dependent Analysis to compute temperatures. Simulations were conducted at an ambient starting temperature of 20 ^{o}C and solved at the 60–minute mark for different combinations of applied frequency, f_a and water flow rate, v_{wf} parameters. The applied frequency ranged from 0.1 to 2.9 MHz with a step size of 0.2 MHz, while the water flow rate varied from 0.1 to 0.5 m/s with a step size of 0.1 m/s, resulting in 75 separate simulations for each coil cooling system. A domain probe was defined in COMSOL Multiphysics® to evaluate current distributions for electromagnetic benchmarking by computing the spatial maximum current density normal,

$$smJ = \underset{V}{max}(J)\, A/m^2, \tag{2.41}$$

wherein J is the current density vector component perpendicular to the wire surface and V is the spatial volume over which the maximum current density is computed. 2D

slice plots of the spatial maximum current density normal were generated for all designs at 0.1, 1.5, and 2.9 MHz applied frequencies. Another domain probe was defined to compute the spatial maximum temperature for thermal benchmarking,

$$smT = \underset{V}{max}(T)\,^{o}C, \tag{2.42}$$

wherein T is the temperature of the coil wires at any given point. 2D slice plots of the spatial maximum temperature were generated for all designs with liquid cooling systems at 0.1 and 2.9 MHz applied frequencies, combined with 0.1 and 0.5 m/s water flow rates. Coil wattage as a function of applied frequency were computed in simulation and related line plot was generated for all coil designs, to showcase thermal power output trends across the operational frequency range. The resulting dataset consisting spatial maximum current density normal and spatial maximum temperature was then imported into MATLAB® software for further analysis.

2.11 Performance Index

All variables, applied frequency, water flow rate, spatial maximum current density normal, and spatial maximum temperature were normalized between 0 and 1 corresponding to nf_a, nv_{wf}, $nsmJ$, $nsmT$ respectively, ensuring comparability across different scales, with 0 representing the lowest observed value and 1 the highest.

$$nf_a = \frac{f_a - f_{a,min}}{f_{a,max} - f_{a,min}}, \tag{2.43}$$

$$nv_{wf} = \frac{v_{wf} - v_{wf,min}}{v_{wf,max} - v_{wf,min}}, \tag{2.44}$$

$$nsmJ = \frac{smJ - smJ_{min}}{smJ_{max} - smJ_{min}}, \tag{2.45}$$

$$nsmT = \frac{smT - smT_{min}}{smT_{max} - smT_{min}} \tag{2.46}$$

These normalizations allow for an unbiased performance index calculation,

$$PI = \frac{1 + nf_a}{1 + nsmT + nv_{wf}}, \tag{2.47}$$

wherein the numerator accounts for the applied frequency, which enhances therapeutic effectiveness by increasing the energy transfer [41, 65]. The denominator accounts for the spatial maximum temperature and the water flow rate, as higher coil wire temperatures reduce selectivity of MH thermal therapy [66, 67], and increased water flow rates impose higher power demands on the pumping system. Using summation in the denominator ensures that no single factor dominates, maintaining a balanced assessment. The addition of 1 to the denominator prevents division by zero, ensuring numerical stability, while the 1 in the numerator ensures that the performance index remains sensitive to changes in either normalized spatial maximum temperature or the normalized water flow rate even at the lowest normalized applied frequency (Zero) [68, 69]. This formulation provides a normalized, stable, and intuitive metric for comparing different cooling system designs.

2.12 Machine Learning Predictions

The dataset was modeled using both Support Vector Regression (SVR) and Gaussian Process Regression (GPR) in MATLAB® software to evaluate multiple relationships within the system. Specifically, the relationship between applied frequency and normalized spatial maximum current density normal was modeled separately. Ad-

ditionally, the relationship between applied frequency, water flow rate, and normalized spatial maximum temperature was analyzed. Lastly, both models were used to predict the performance index as a function of applied frequency and water flow rate. Hold–out validation [70] was conducted using an $80 - 20\%$ split for training and testing, respectively. Model performance was assessed using adjusted R^2 as the error metric to ensure a fair comparison of predictive accuracy [71].

Following model training, a sensitivity analysis [72] was performed to evaluate the relative influence of applied frequency and water flow rate in the GPR and SVR models of the predicted performance index outcomes, providing insights into parameter significance within the system. Sensitivity analysis was conducted using a One-at–a–Time (OAT) method, where applied frequency and water flow rate were systematically varied by $\pm 10\%$ to assess their influence on predicted outcomes. Additionally, the ReliefF algorithm [73, 74] was applied to rank the relative importance of applied frequency and water flow rate in the GPR and SVR models of the performance index.

3. RESULTS

A Coil Optimization

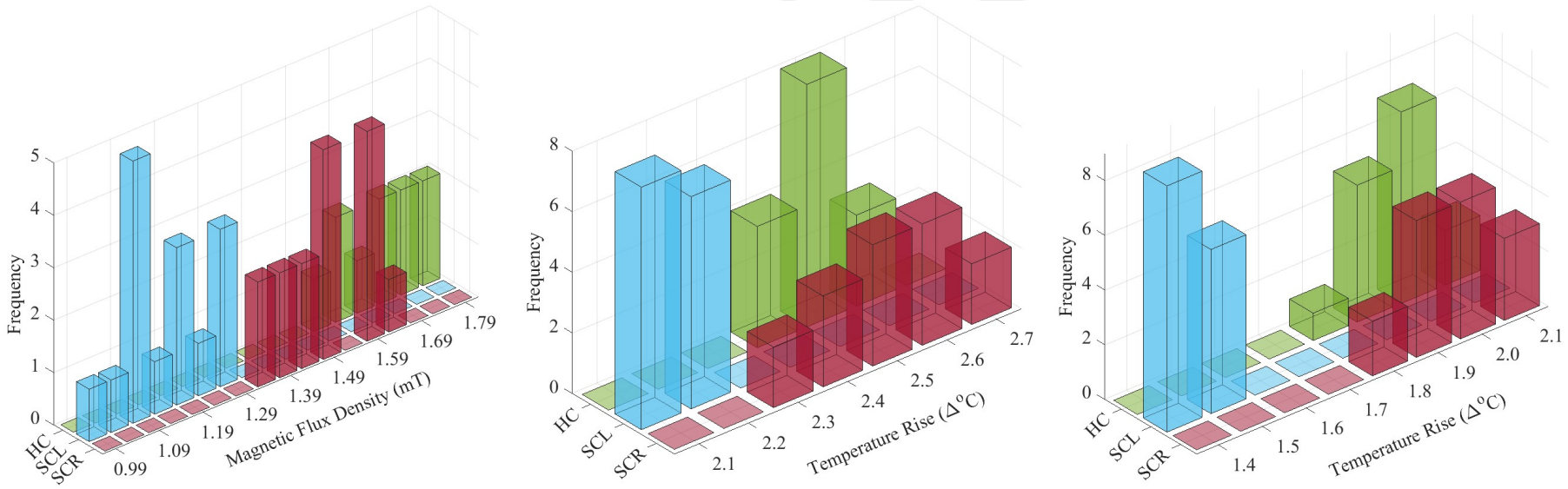


Figure 3.1 Histograms of the spatial distributions of the time–domain RMS magnetic flux density (left) and corresponding amount of temperature rise with 166.5 (middle) and 120 mg/mL (right) MNPs for the solenoid coil with round Litz wire (blue), with round wire (maroon) and Helmholtz coil with round wire (green).

3.1. Solenoid Coil with Round Wire Measurements

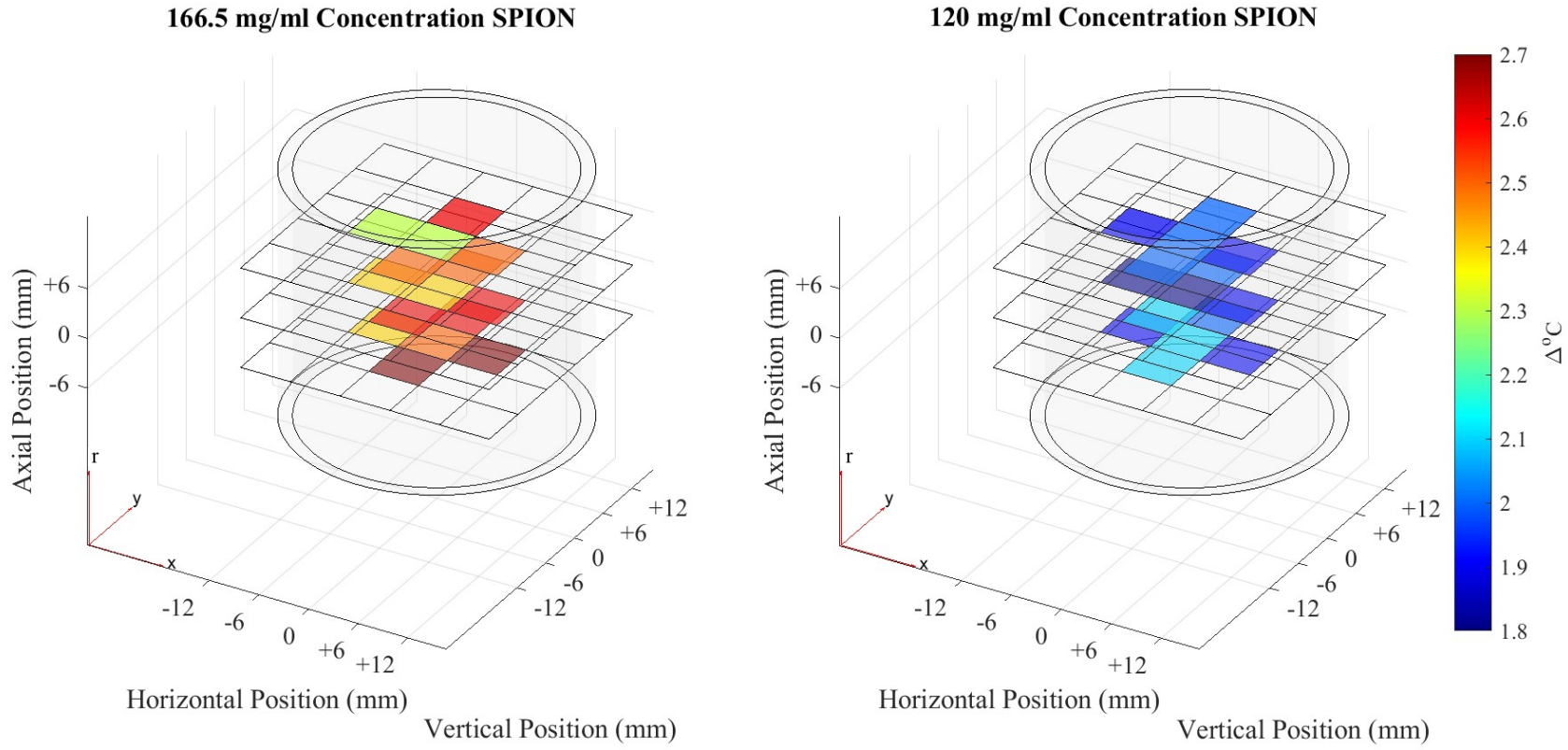


Figure 3.2 Amount of temperature rise, ΔT measured from two different SPION concentrations inside of solenoid coil with round wire design at three different axial positions; -12, 0, $+12$ mm and five different transverse positions; 0, -6 and $+6$ mm horizontally, -6 and $+6$ mm vertically for each axial position (15 positions in total) inside of the coil gap.

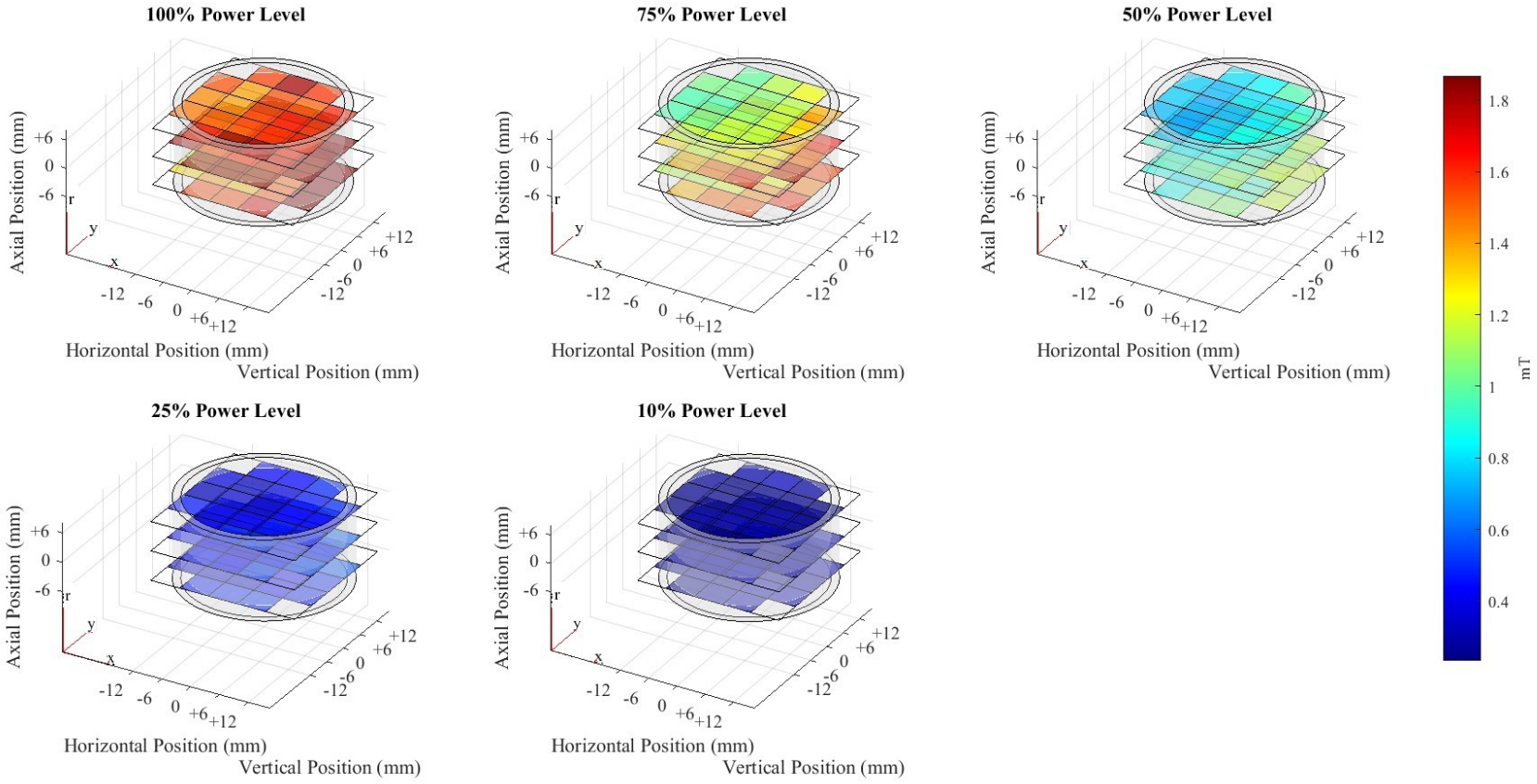


Figure 3.3 Time–domain root mean square magnetic flux density, $tRMS_B$ values measured from solenoid coil with round wire design for all power levels at three different axial positions; −6, 0, +6 mm and 21 different transverse positions; 6 mm apart at each axial position (63 positions in total, for each power level).

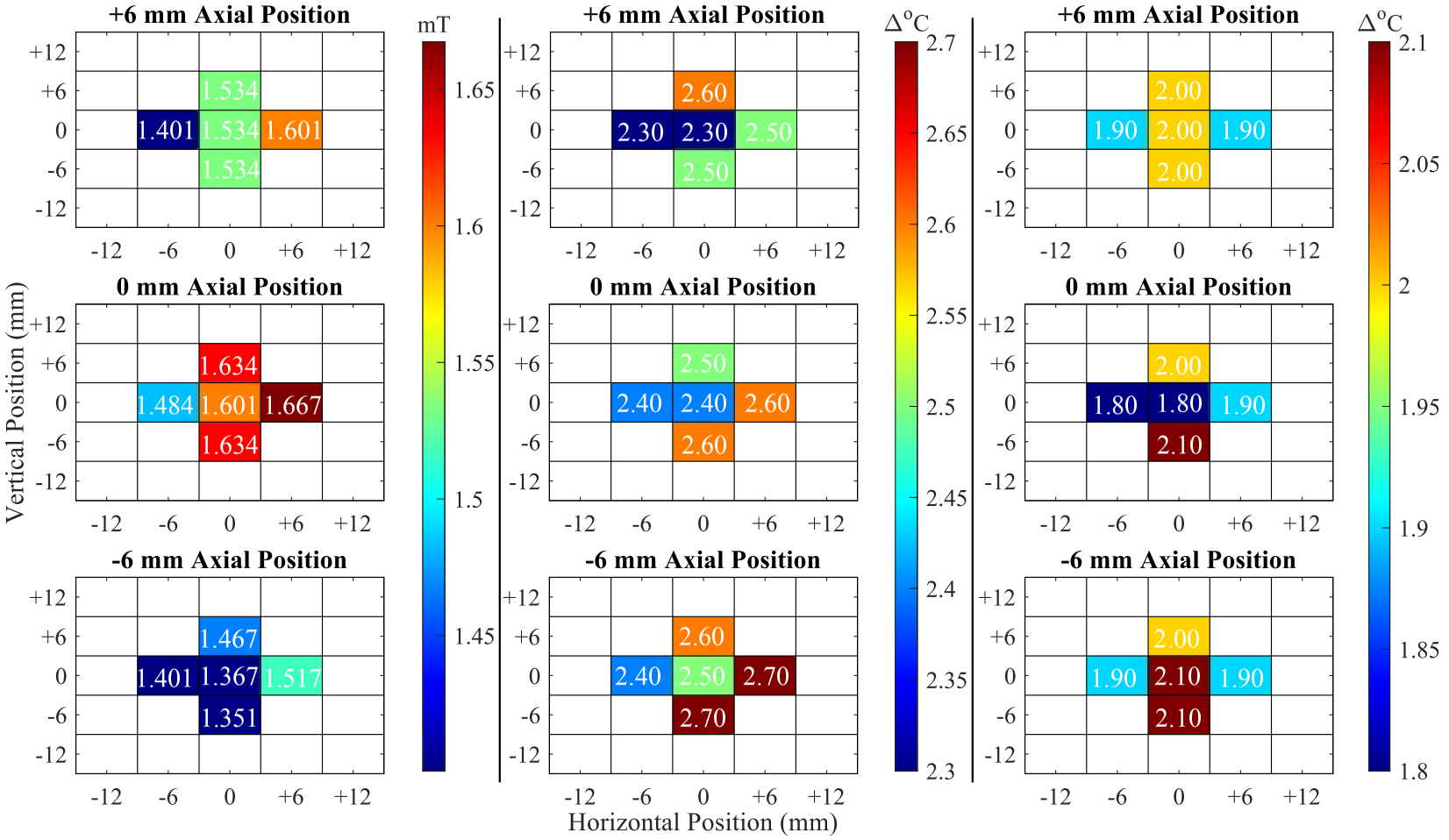


Figure 3.4 Time–domain root mean square magnetic flux density, $tRMS_B$ (left) and corresponding amount of temperature rise, ΔT with 166.5 (middle) and 120 mg/mL (right) SPION concentration values measured from solenoid coil with round wire design for 100% power level at three different axial positions; −6, 0, +6 mm.

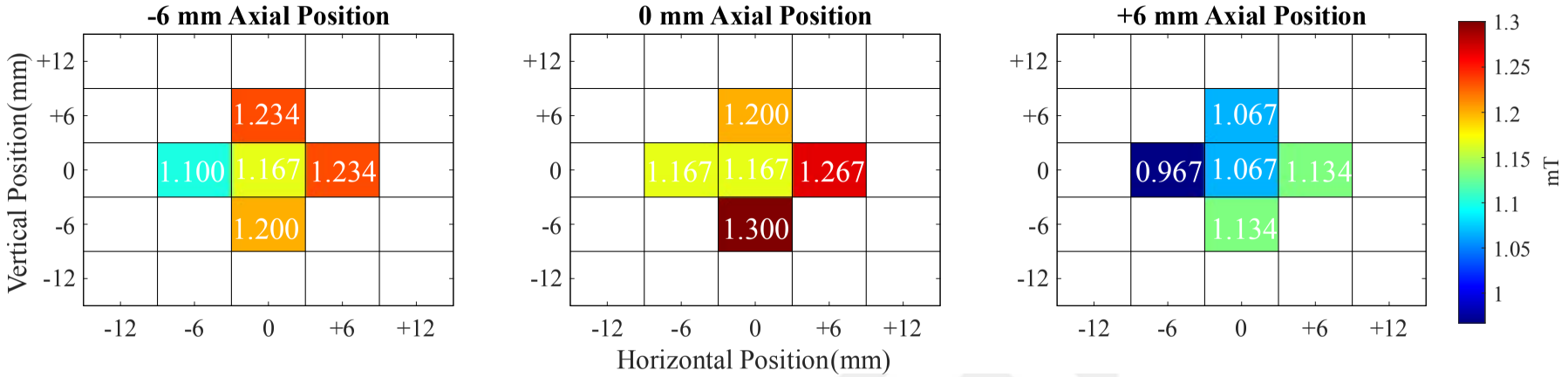


Figure 3.5 Time–domain root mean square magnetic flux density, $tRMS_B$ (top) values measured from solenoid coil with round wire design for 75% power level at three different axial positions; −6, 0, +6 mm.

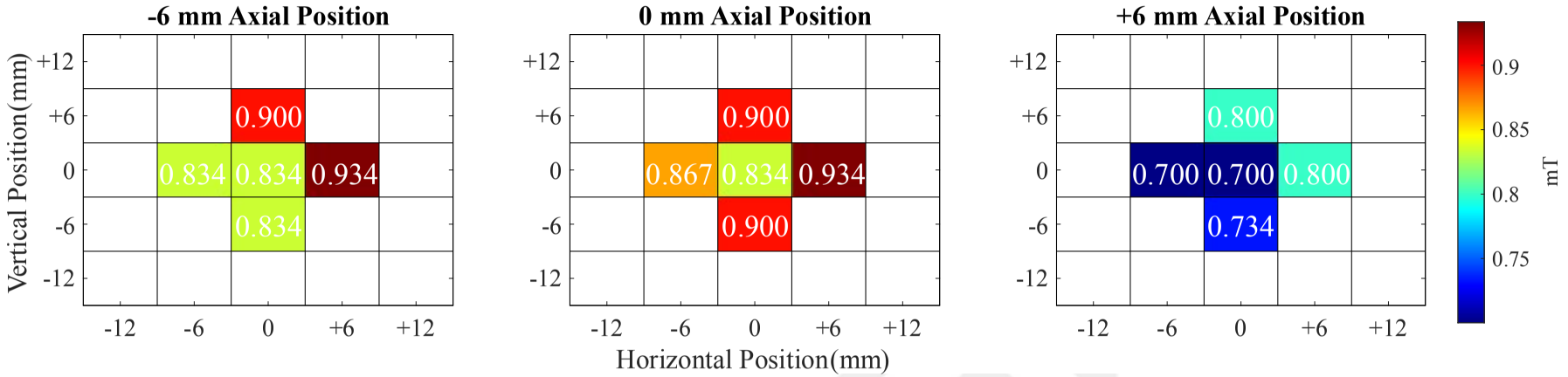


Figure 3.6 Time–domain root mean square magnetic flux density, $tRMS_B$ (top) values measured from solenoid coil with round wire design for 50% power level at three different axial positions; −6, 0, +6 mm.

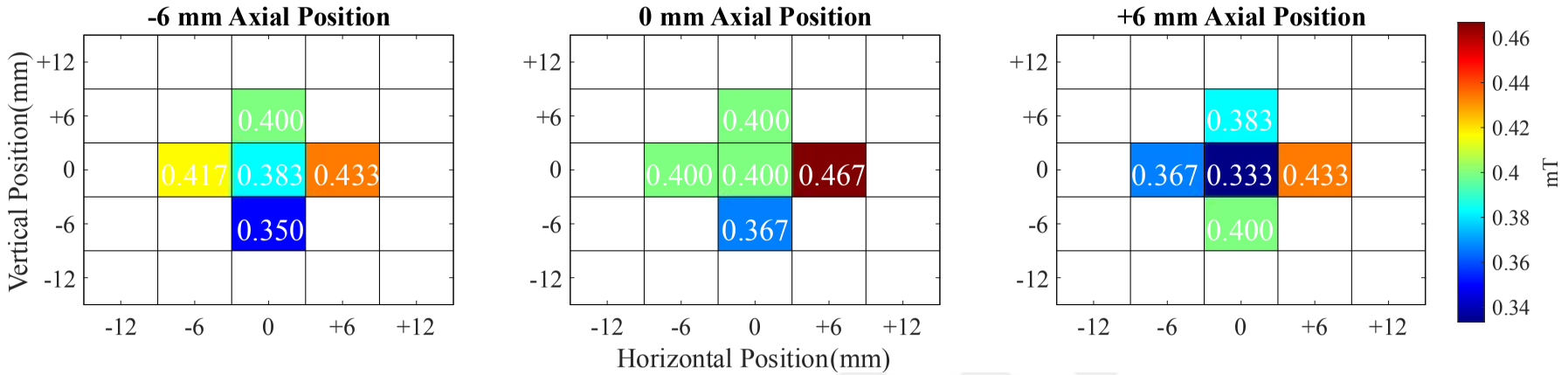


Figure 3.7 Time–domain root mean square magnetic flux density, $tRMS_B$ (top) values measured from solenoid coil with round wire design for 25% power level at three different axial positions; −6, 0, +6 mm.

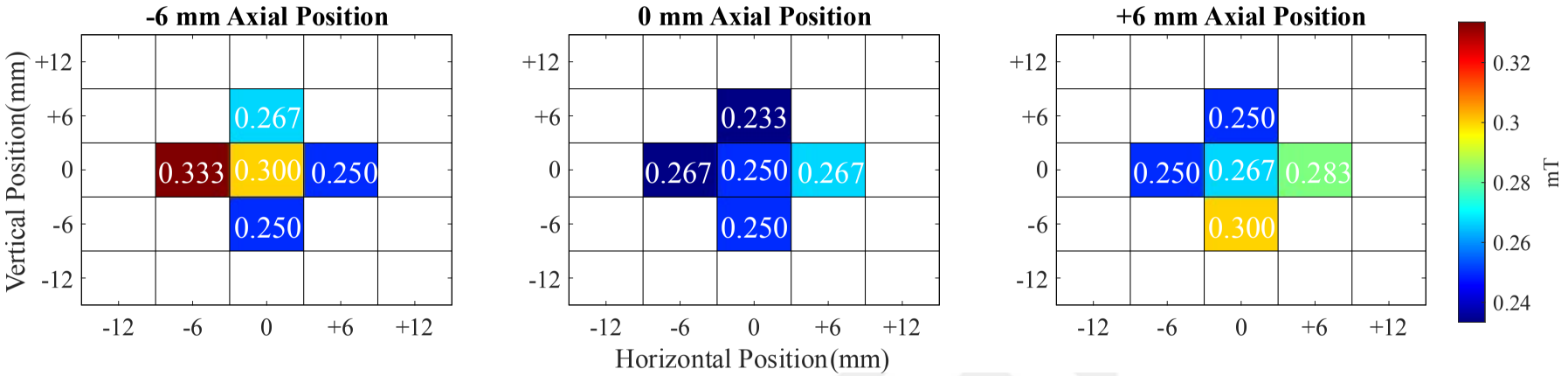


Figure 3.8 Time–domain root mean square magnetic flux density, $tRMS_B$ (top) values measured from solenoid coil with round wire design for 10% power level at three different axial positions; −6, 0, +6 mm.

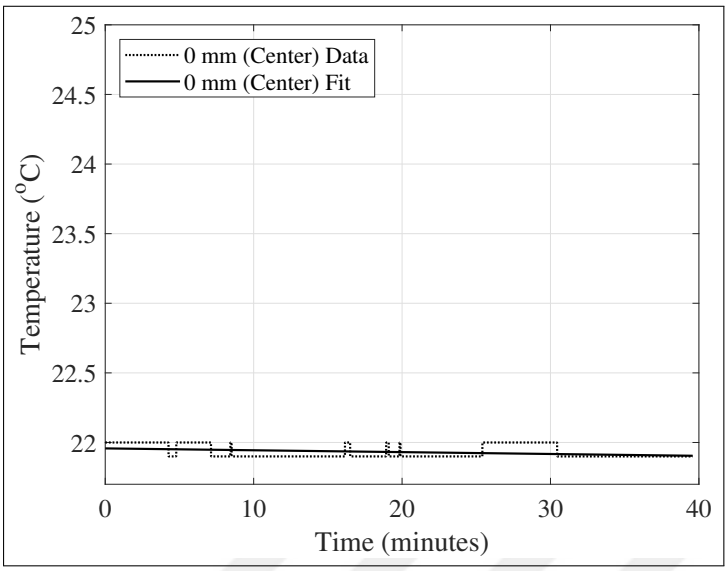


Figure 3.9 40 minute temperature vs. time graph during MH experiments conducted with distilled water as the control experiment using solenoid coil with round wire at 0 mm axial position, 0 mm (center) position. Temperature–time data was fitted to a line using linear regression for analyzing positional related effects.

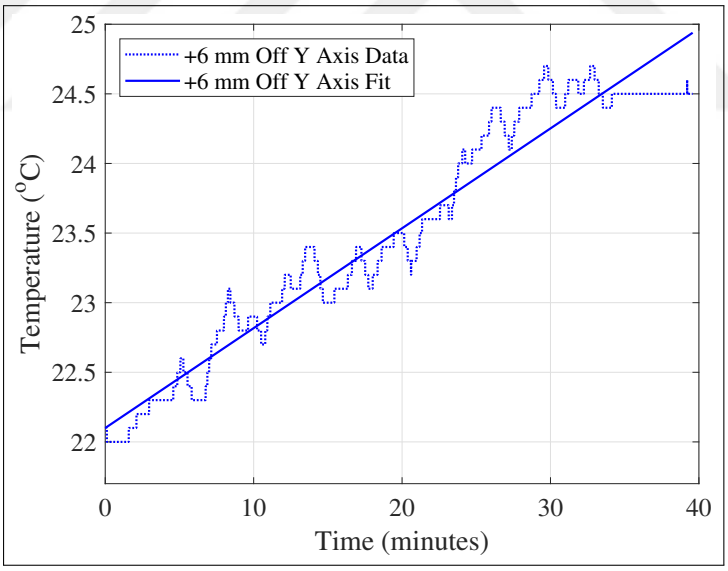


Figure 3.10 40 minute temperature rise vs. time graph during MH experiments conducted with 166.5 mg/mL concentration SPION using solenoid coil with round wire at −6 mm axial position, +6 mm off Y-axis. Temperature–time data was fitted to a line using linear regression for analyzing positional related effects.

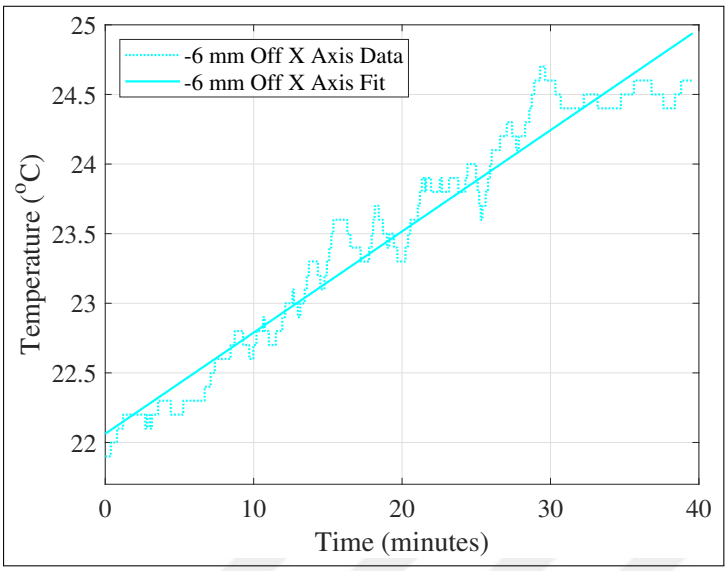


Figure 3.11 40 minute temperature rise vs. time graph during MH experiments conducted with 166.5 mg/mL concentration SPION using solenoid coil with round wire at −6 mm axial position, −6 mm off X-axis. Temperature–time data was fitted to a line using linear regression for analyzing positional related effects.

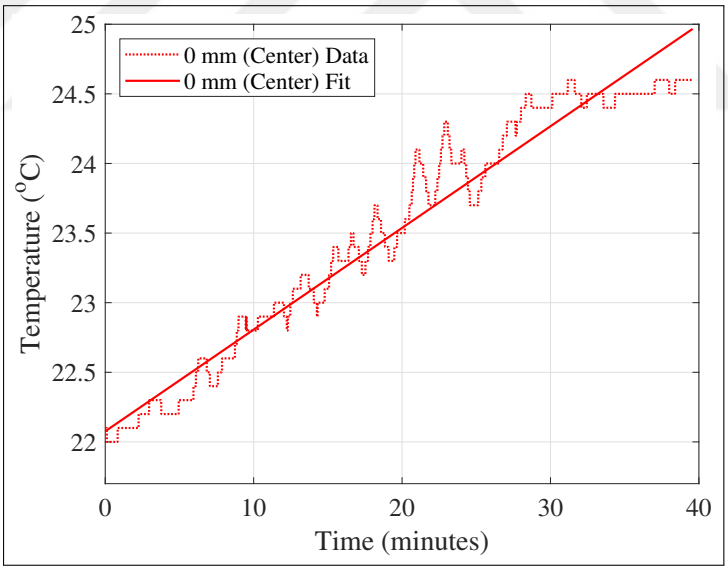


Figure 3.12 40 minute temperature rise vs. time graph during MH experiments conducted with 166.5 mg/mL concentration SPION using solenoid coil with round wire at −6 mm axial position, 0 mm (center) position. Temperature–time data was fitted to a line using linear regression for analyzing positional related effects.

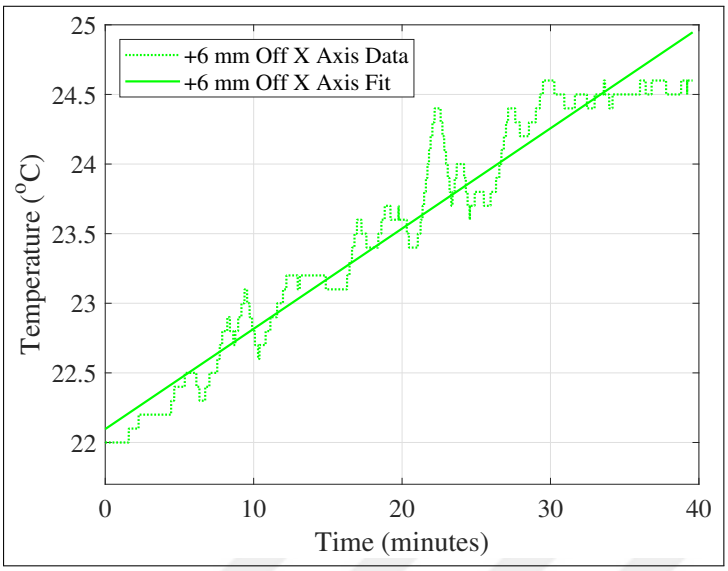


Figure 3.13 40 minute temperature rise vs. time graph during MH experiments conducted with 166.5 mg/mL concentration SPION using solenoid coil with round wire at −6 mm axial position, +6 mm off X-axis. Temperature–time data was fitted to a line using linear regression for analyzing positional related effects.

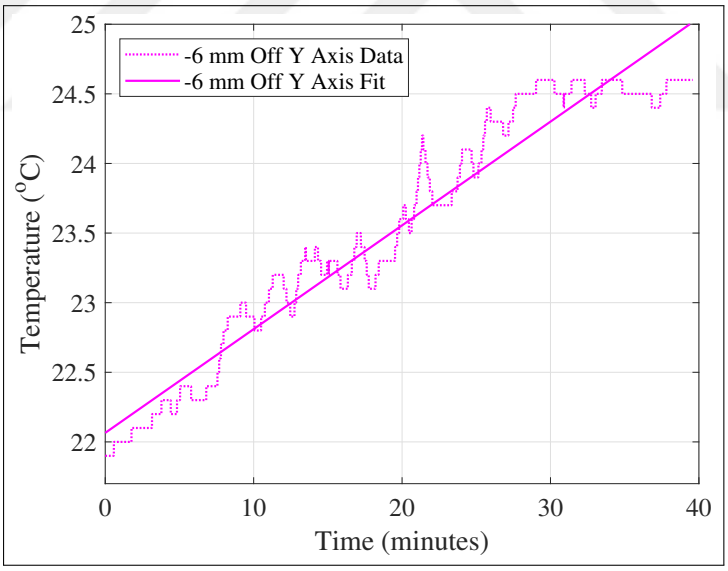


Figure 3.14 40 minute temperature rise vs. time graph during MH experiments conducted with 166.5 mg/mL concentration SPION using solenoid coil with round wire at −6 mm axial position, −6 mm off Y-axis. Temperature–time data was fitted to a line using linear regression for analyzing positional related effects.

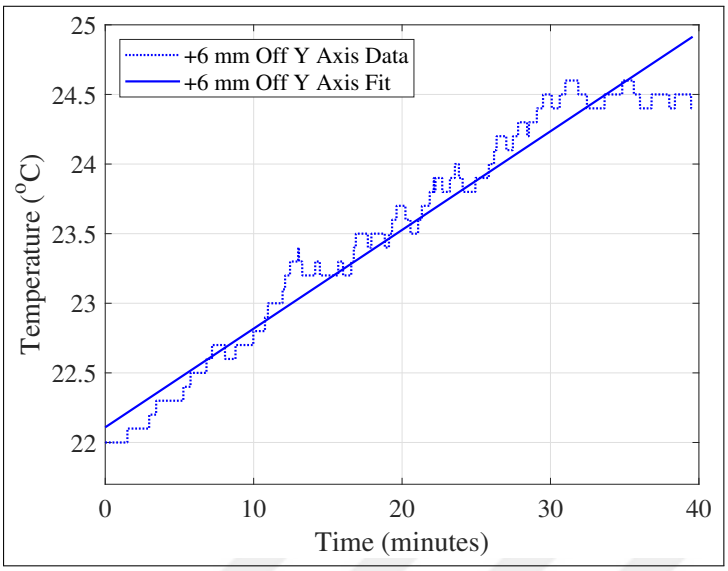


Figure 3.15 40 minute temperature rise vs. time graph during MH experiments conducted with 166.5 mg/mL concentration SPION using solenoid coil with round wire at 0 mm axial position, +6 mm off Y-axis. Temperature–time data was fitted to a line using linear regression for analyzing positional related effects.

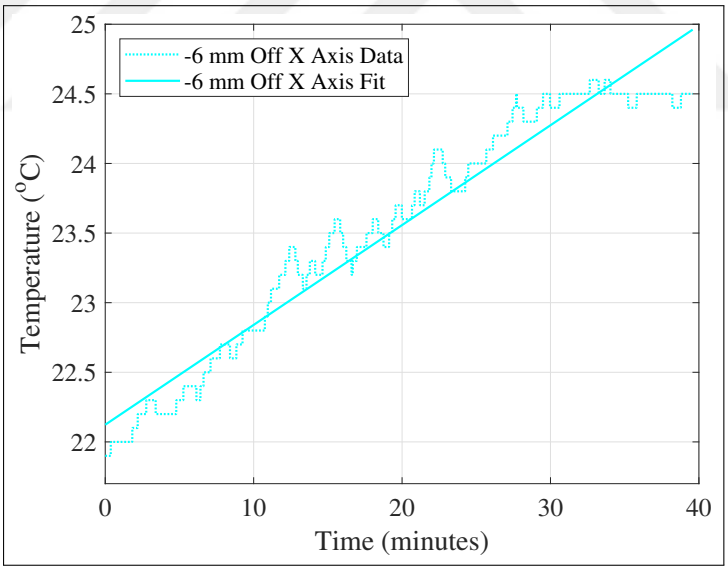


Figure 3.16 40 minute temperature rise vs. time graph during MH experiments conducted with 166.5 mg/mL concentration SPION using solenoid coil with round wire at 0 mm axial position, −6 mm off X-axis. Temperature–time data was fitted to a line using linear regression for analyzing positional related effects.

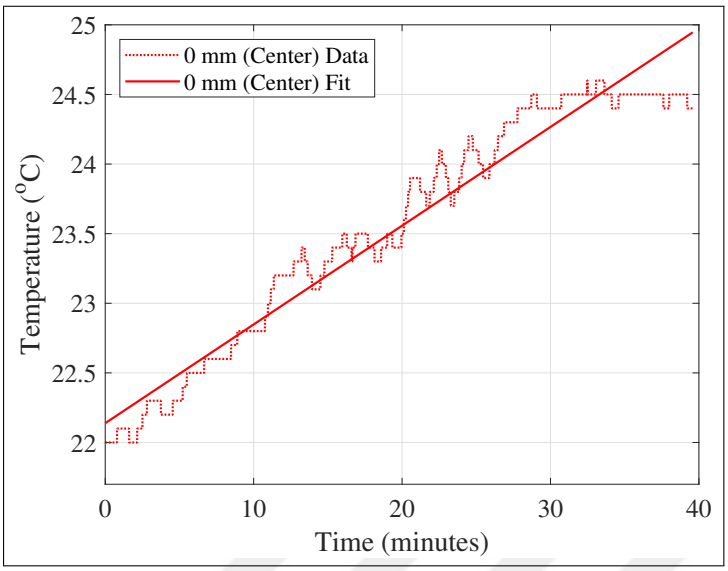


Figure 3.17 40 minute temperature rise vs. time graph during MH experiments conducted with 166.5 mg/mL concentration SPION using solenoid coil with round wire at 0 mm axial position, 0 mm (center) position. Temperature–time data was fitted to a line using linear regression for analyzing positional related effects.

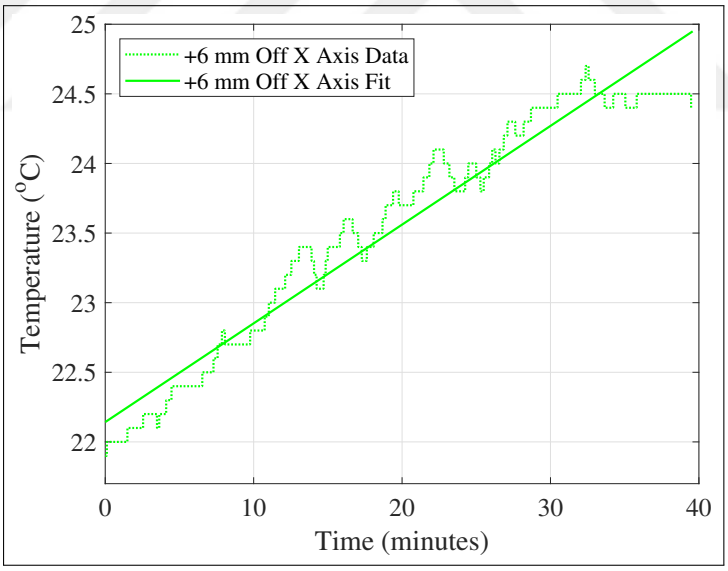


Figure 3.18 40 minute temperature rise vs. time graph during MH experiments conducted with 166.5 mg/mL concentration SPION using solenoid coil with round wire at 0 mm axial position, +6 mm off X-axis. Temperature–time data was fitted to a line using linear regression for analyzing positional related effects.

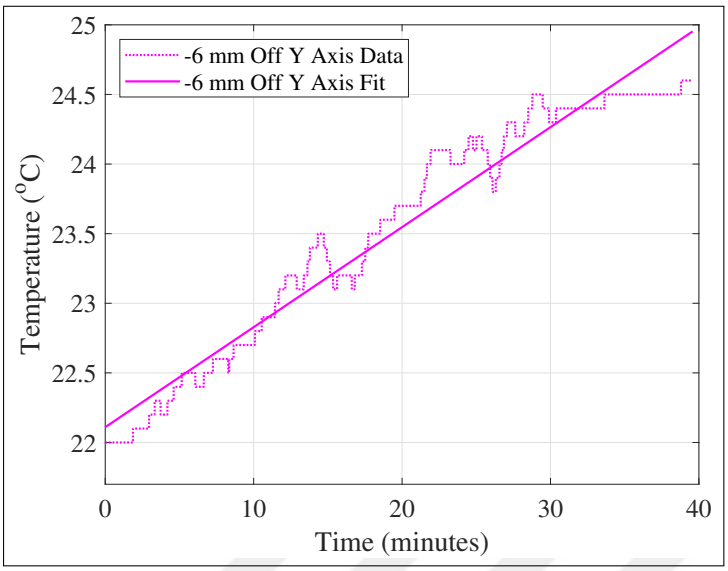


Figure 3.19 40 minute temperature rise vs. time graph during MH experiments conducted with 166.5 mg/mL concentration SPION using solenoid coil with round wire at 0 mm axial position, −6 mm off Y-axis. Temperature–time data was fitted to a line using linear regression for analyzing positional related effects.

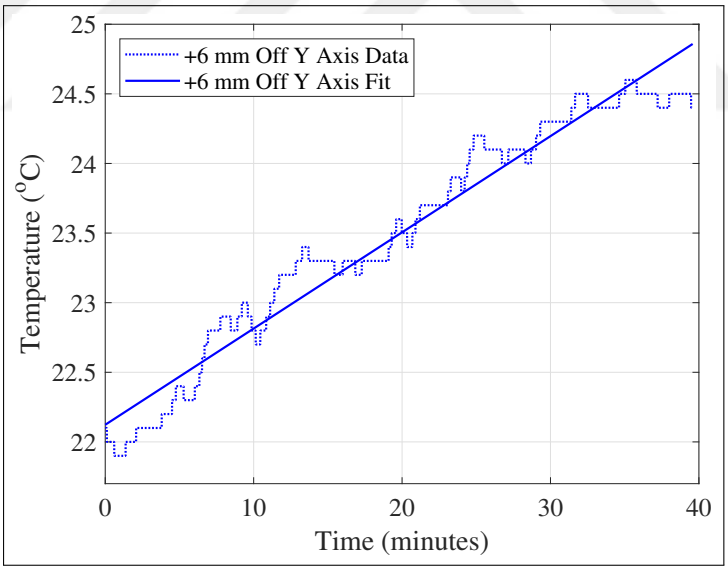


Figure 3.20 40 minute temperature rise vs. time graph during MH experiments conducted with 166.5 mg/mL concentration SPION using solenoid coil with round wire at +6 mm axial position, +6 mm off Y-axis. Temperature–time data was fitted to a line using linear regression for analyzing positional related effects.

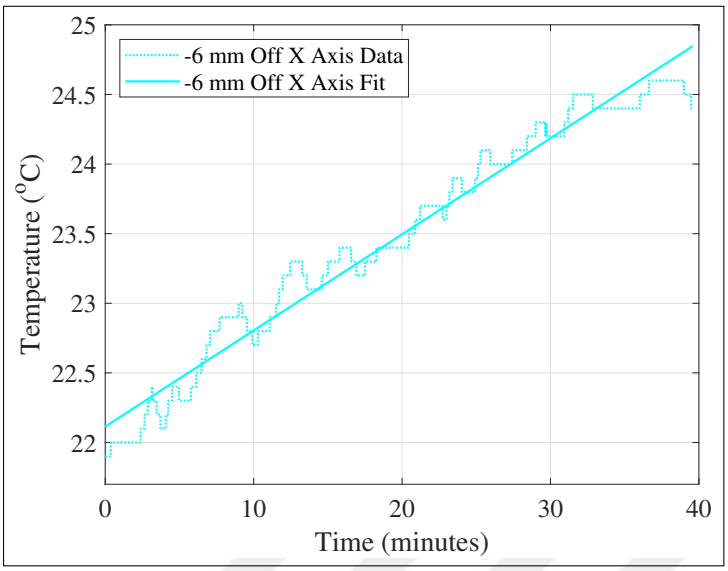


Figure 3.21 40 minute temperature rise vs. time graph during MH experiments conducted with 166.5 mg/mL concentration SPION using solenoid coil with round wire at +6 mm axial position, −6 mm off X-axis. Temperature–time data was fitted to a line using linear regression for analyzing positional related effects.

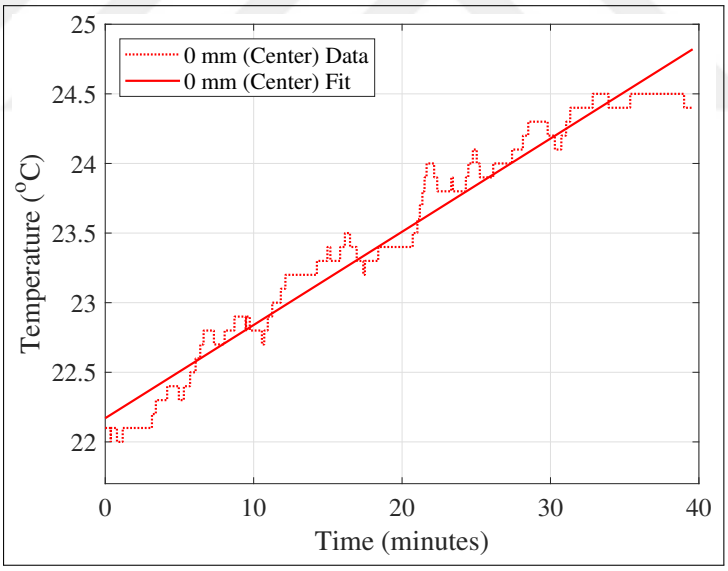


Figure 3.22 40 minute temperature rise vs. time graph during MH experiments conducted with 166.5 mg/mL concentration SPION using solenoid coil with round wire at +6 mm axial position, 0 mm (center) position. Temperature–time data was fitted to a line using linear regression for analyzing positional related effects.

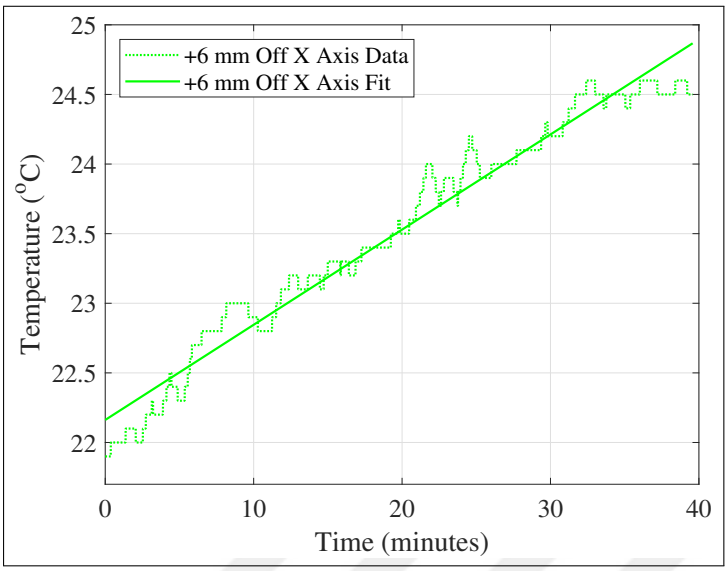


Figure 3.23 40 minute temperature rise vs. time graph during MH experiments conducted with 166.5 mg/mL concentration SPION using solenoid coil with round wire at +6 mm axial position, +6 mm off X-axis. Temperature–time data was fitted to a line using linear regression for analyzing positional related effects.

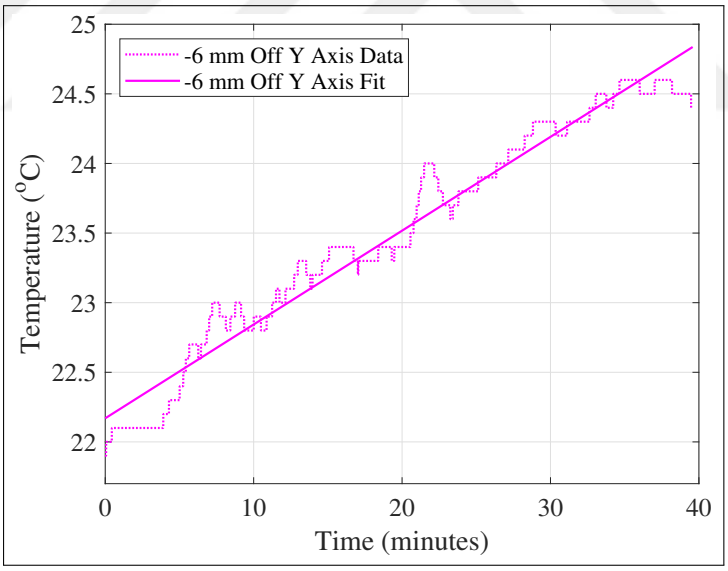


Figure 3.24 40 minute temperature rise vs. time graph during MH experiments conducted with 166.5 mg/mL concentration SPION using solenoid coil with round wire at +6 mm axial position, −6 mm off Y-axis. Temperature–time data was fitted to a line using linear regression for analyzing positional related effects.

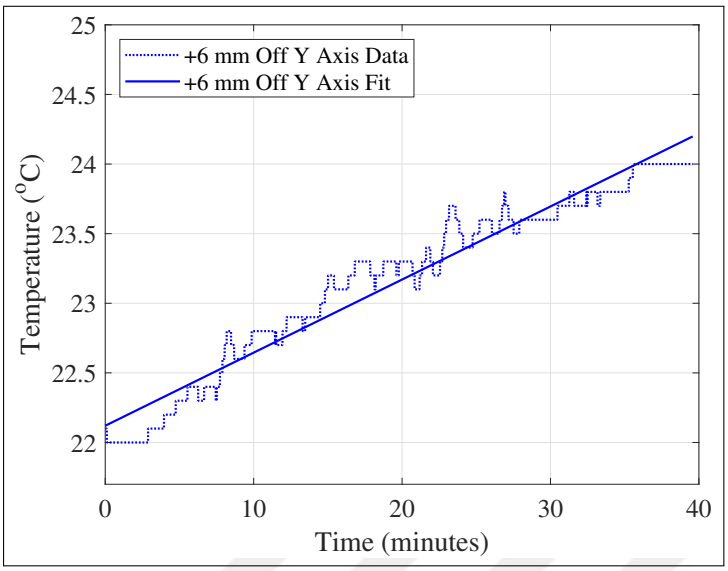


Figure 3.25 40 minute temperature rise vs. time graph during MH experiments conducted with 120 mg/mL concentration SPION using solenoid coil with round wire at −6 mm axial position, +6 mm off Y-axis. Temperature–time data was fitted to a line using linear regression for analyzing positional related effects.

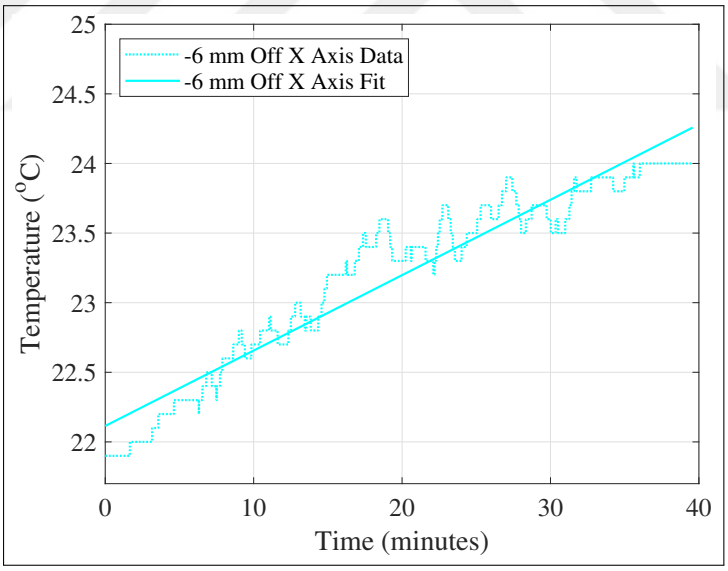


Figure 3.26 40 minute temperature rise vs. time graph during MH experiments conducted with 120 mg/mL concentration SPION using solenoid coil with round wire at −6 mm axial position, −6 mm off X-axis. Temperature–time data was fitted to a line using linear regression for analyzing positional related effects.

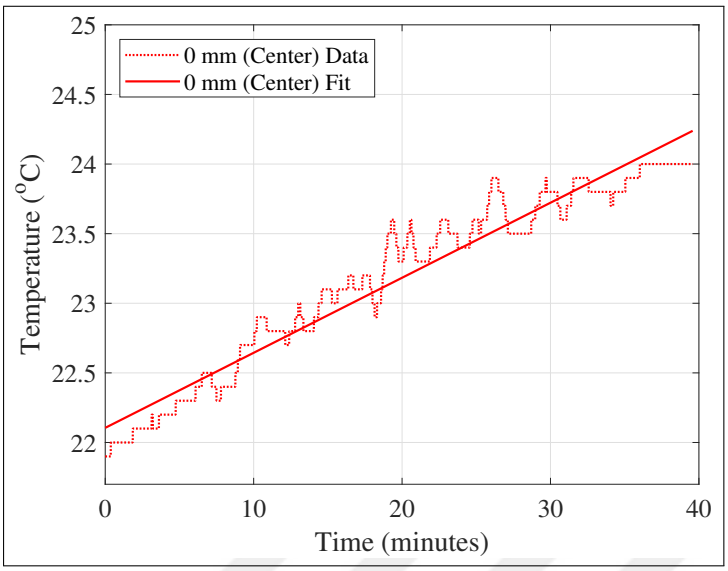


Figure 3.27 40 minute temperature rise vs. time graph during MH experiments conducted with 120 mg/mL concentration SPION using solenoid coil with round wire at −6 mm axial position, 0 mm (center) position. Temperature–time data was fitted to a line using linear regression for analyzing positional related effects.

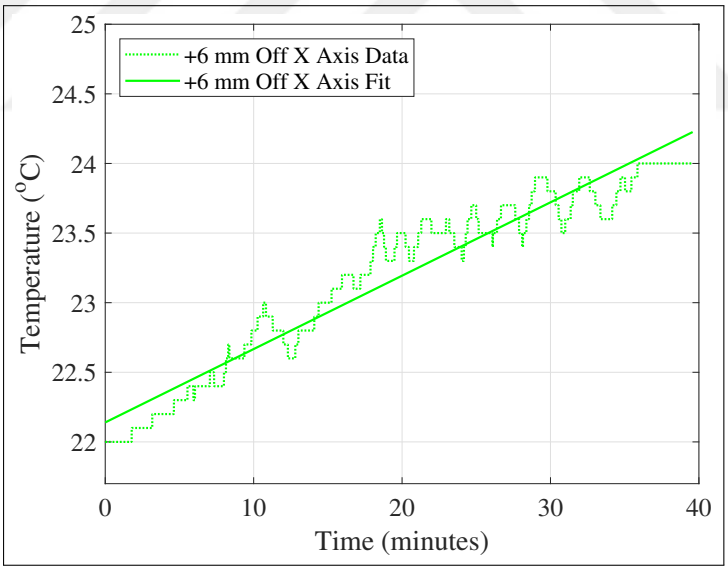


Figure 3.28 40 minute temperature rise vs. time graph during MH experiments conducted with 120 mg/mL concentration SPION using solenoid coil with round wire at −6 mm axial position, +6 mm off X-axis. Temperature–time data was fitted to a line using linear regression for analyzing positional related effects.

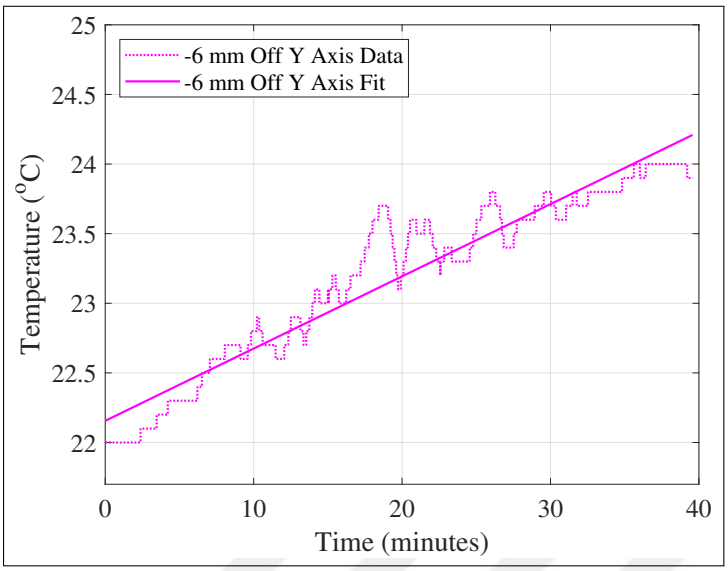


Figure 3.29 40 minute temperature rise vs. time graph during MH experiments conducted with 120 mg/mL concentration SPION using solenoid coil with round wire at −6 mm axial position, −6 mm off Y-axis. Temperature–time data was fitted to a line using linear regression for analyzing positional related effects.

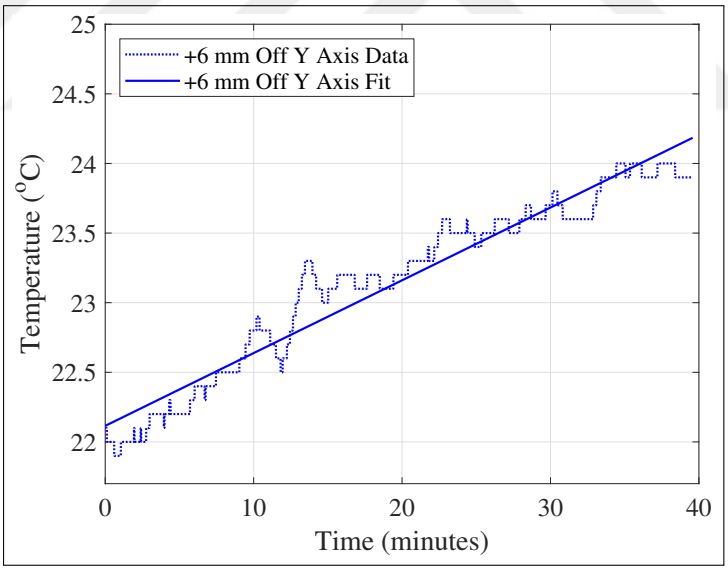


Figure 3.30 40 minute temperature rise vs. time graph during MH experiments conducted with 120 mg/mL concentration SPION using solenoid coil with round wire at 0 mm axial position, +6 mm off Y-axis. Temperature–time data was fitted to a line using linear regression for analyzing positional related effects.

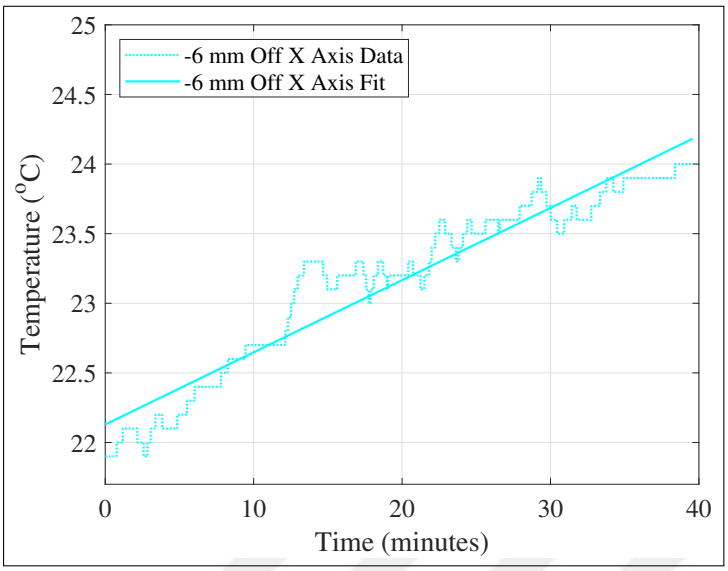


Figure 3.31 40 minute temperature rise vs. time graph during MH experiments conducted with 120 mg/mL concentration SPION using solenoid coil with round wire at 0 mm axial position, −6 mm off X-axis. Temperature–time data was fitted to a line using linear regression for analyzing positional related effects.

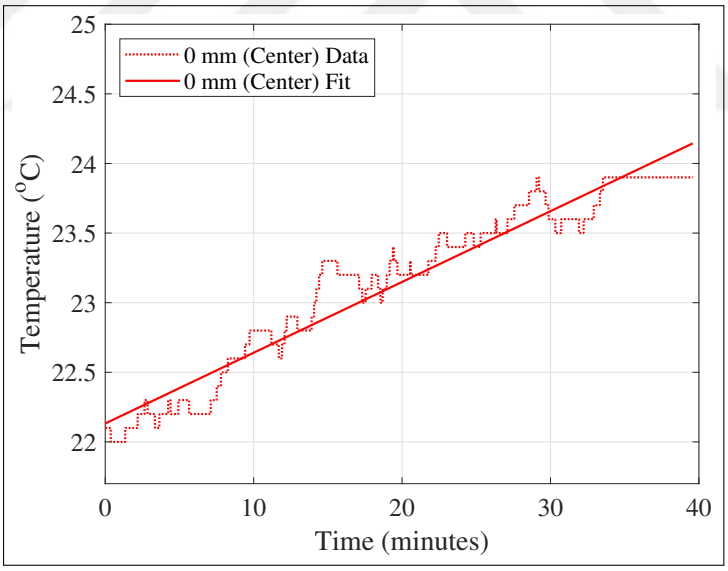


Figure 3.32 40 minute temperature rise vs. time graph during MH experiments conducted with 120 mg/mL concentration SPION using solenoid coil with round wire at 0 mm axial position, 0 mm (center) position. Temperature–time data was fitted to a line using linear regression for analyzing positional related effects.

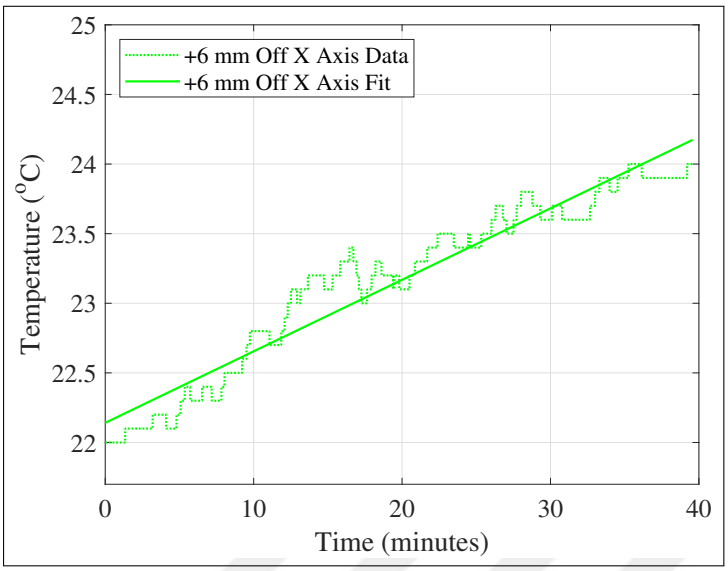


Figure 3.33 40 minute temperature rise vs. time graph during MH experiments conducted with 120 mg/mL concentration SPION using solenoid coil with round wire at 0 mm axial position, +6 mm off X-axis. Temperature–time data was fitted to a line using linear regression for analyzing positional related effects.

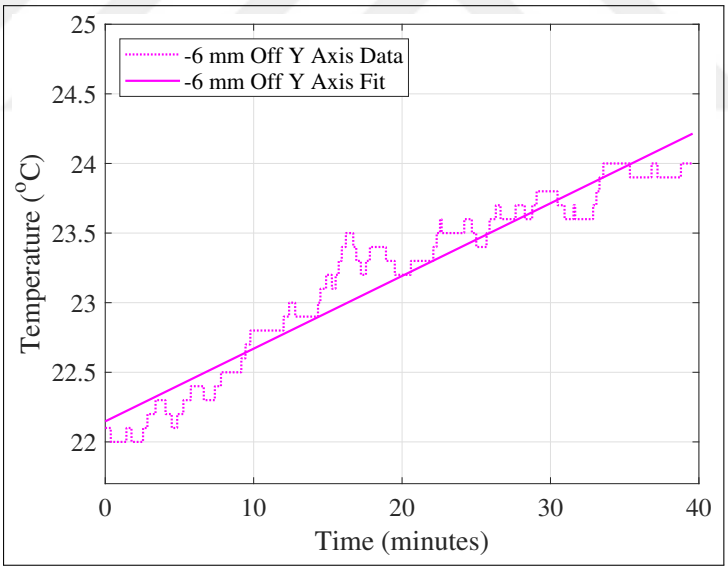


Figure 3.34 40 minute temperature rise vs. time graph during MH experiments conducted with 120 mg/mL concentration SPION using solenoid coil with round wire at 0 mm axial position, −6 mm off Y-axis. Temperature–time data was fitted to a line using linear regression for analyzing positional related effects.

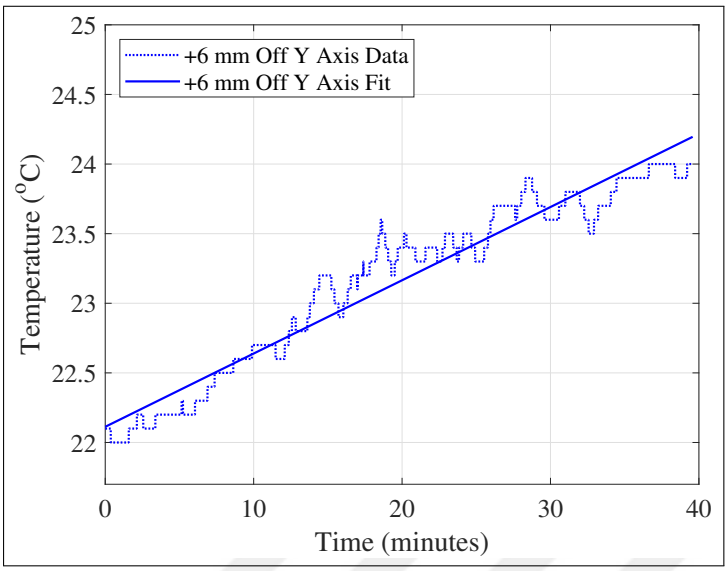


Figure 3.35 40 minute temperature rise vs. time graph during MH experiments conducted with 120 mg/mL concentration SPION using solenoid coil with round wire at +6 mm axial position, +6 mm off Y-axis. Temperature–time data was fitted to a line using linear regression for analyzing positional related effects.

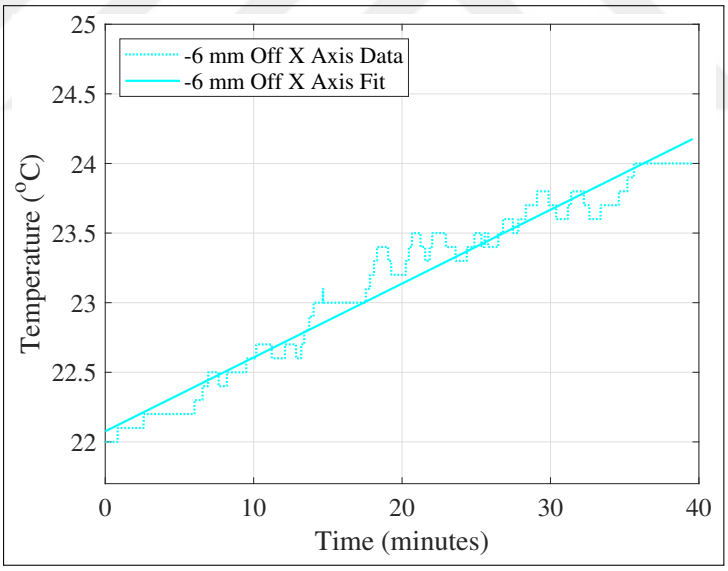


Figure 3.36 40 minute temperature rise vs. time graph during MH experiments conducted with 120 mg/mL concentration SPION using solenoid coil with round wire at +6 mm axial position, −6 mm off X-axis. Temperature–time data was fitted to a line using linear regression for analyzing positional related effects.

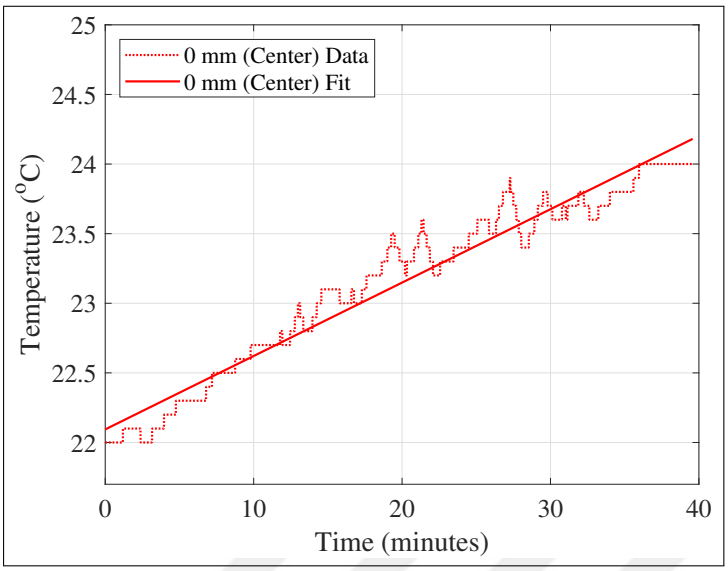


Figure 3.37 40 minute temperature rise vs. time graph during MH experiments conducted with 120 mg/mL concentration SPION using solenoid coil with round wire at +6 mm axial position, 0 mm (center) position. Temperature–time data was fitted to a line using linear regression for analyzing positional related effects.

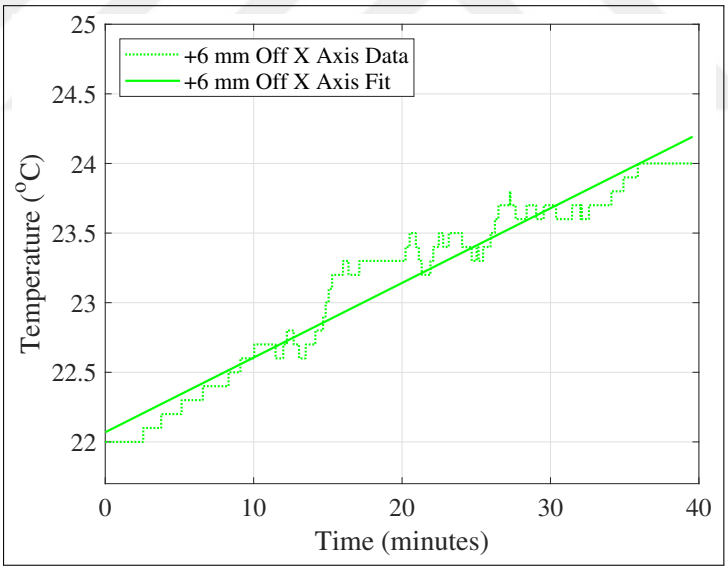


Figure 3.38 40 minute temperature rise vs. time graph during MH experiments conducted with 120 mg/mL concentration SPION using solenoid coil with round wire at +6 mm axial position, +6 mm off X-axis. Temperature–time data was fitted to a line using linear regression for analyzing positional related effects.

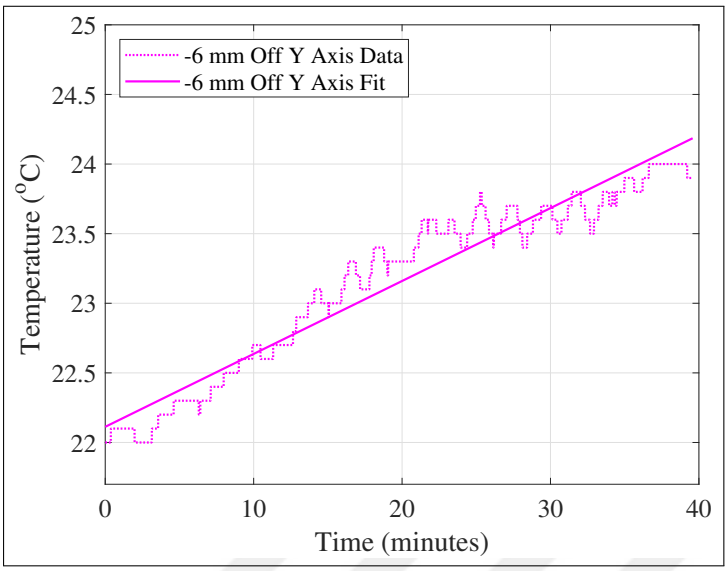


Figure 3.39 40 minute temperature rise vs. time graph during MH experiments conducted with 120 mg/mL concentration SPION using solenoid coil with round wire at +6 mm axial position, −6 mm off Y-axis. Temperature–time data was fitted to a line using linear regression for analyzing positional related effects.

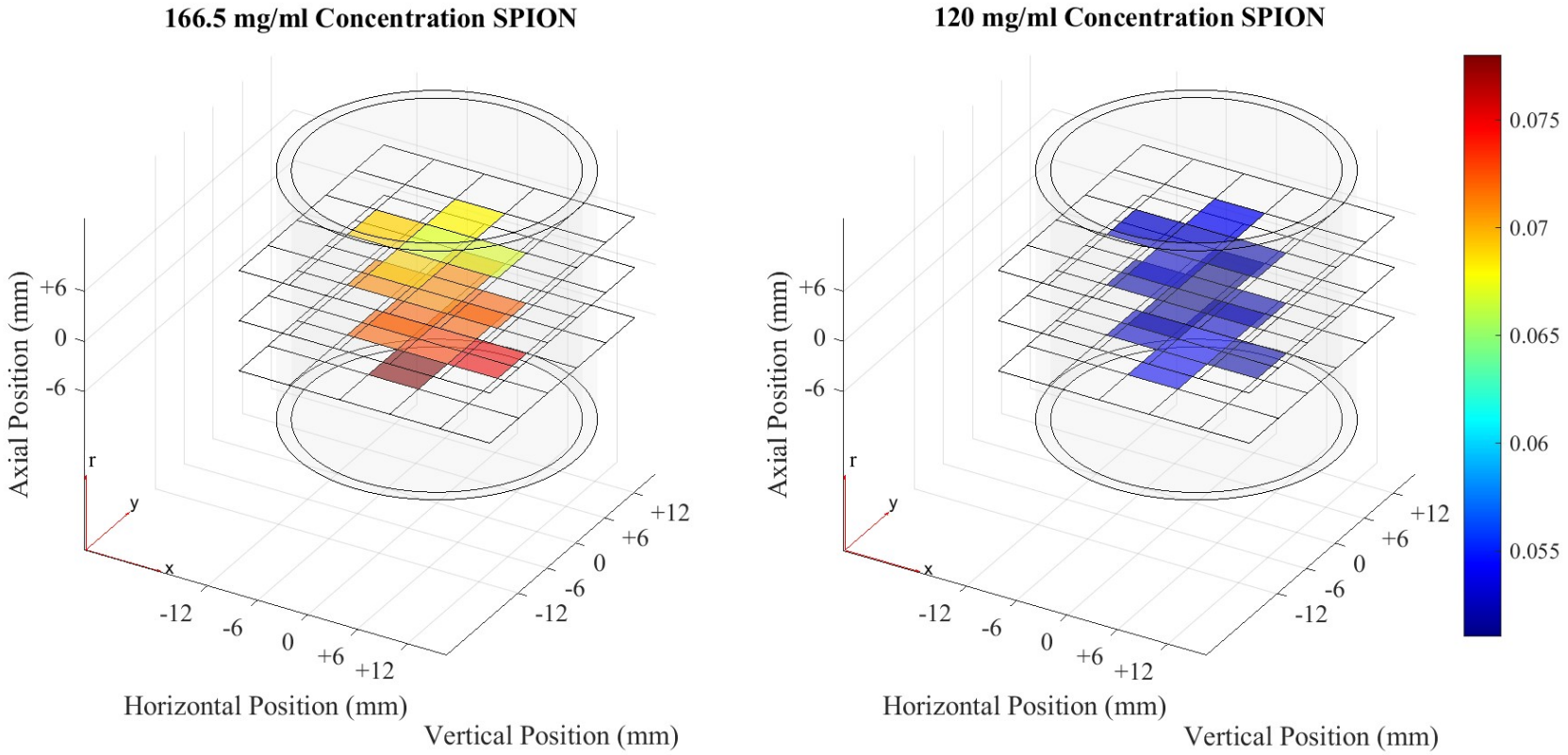


Figure 3.40 Slope of linear regression fit for 40 minute temperature rise vs. time graph during MH experiments conducted with 120 mg/mL concentration SPION using solenoid coil with round wire at three axial positions inside of the coil gap and five different transverse positions.

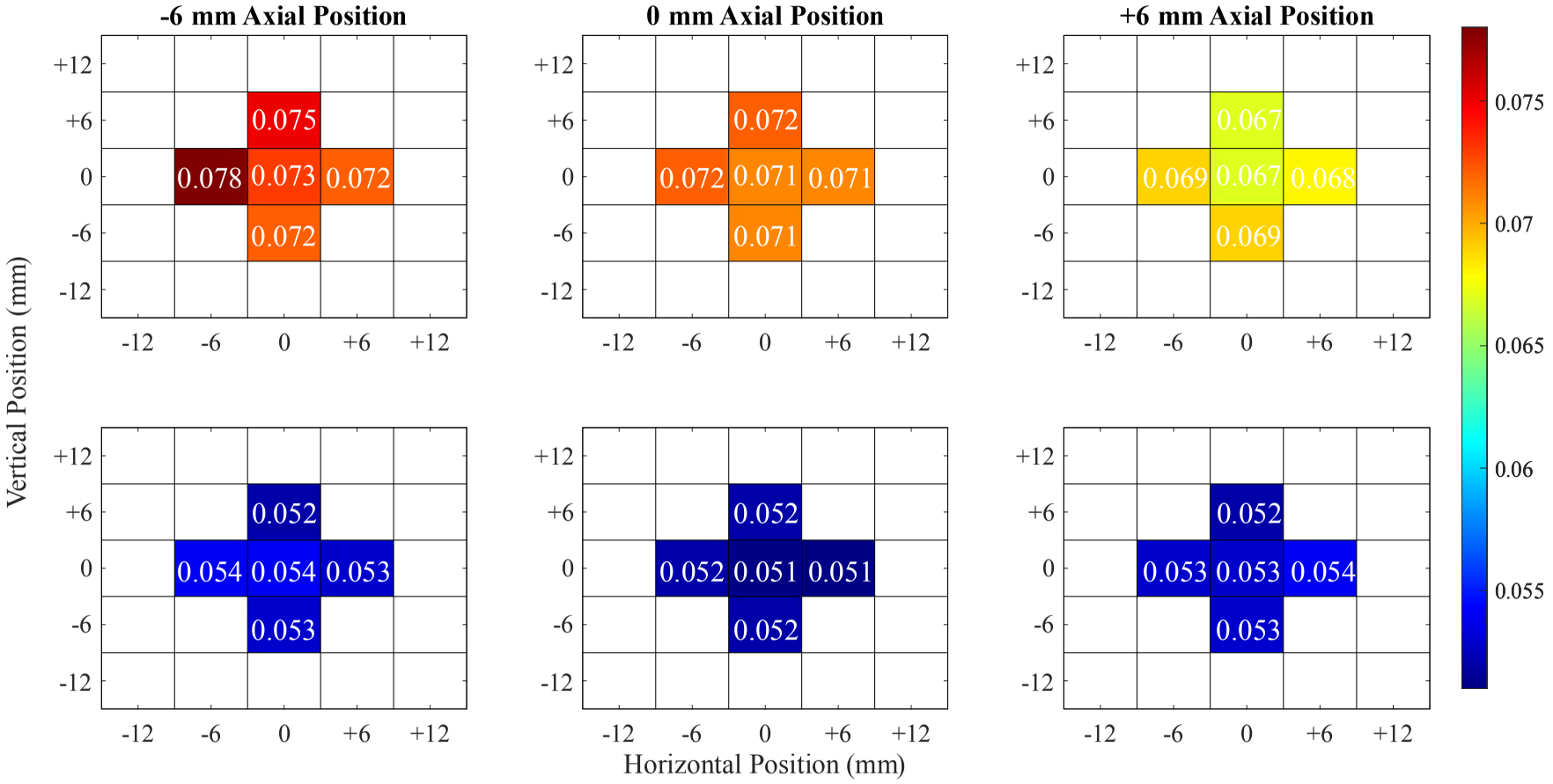


Figure 3.41 Slices showing slope of linear regression fit for 40 minute temperature rise vs. time graph during MH experiments conducted with 120 (top) and 166.5 mg/mL (bottom) SPION concentrations using solenoid coil with round wire at three axial positions.

Table 3.1 Solenoid coil with round wire physical implementation measured magnetic variables.

Power Levels	**sm_B (mT)**	**$smin_B$ (mT)**	**$smax_B$ (mT)**	**$srange_B$ (mT)**	**$scenter_B$ (mT)**	**$s\sigma_B$ (mT)**	**$sHom_B$**	**sP_{coil}**
100%	1.668	1.234	1.712	0.478	1.600	0.106	15.736	26.940
75%	1.161	0.967	1.304	0.337	1.167	0.086	13.500	17.604
50%	0.832	0.667	0.930	0.263	0.834	0.076	10.947	10.181
25%	0.395	0.334	0.474	0.140	0.400	0.035	11.286	5.350
10%	0.265	0.233	0.334	0.101	0.250	0.028	9.464	3.161

Table 3.2 Time–domain root mean square magnetic flux density, $tRMS_B$ values measured in mT from solenoid coil with round wire design for 100% power level at three different axial positions; −6, 0, +6 mm and 21 different transverse positions; 6 mm apart at each axial position (63 positions in total, for each power level).

-6 mm Axial Position						
				X Axis		
		−12 mm	−6 mm	Center	+6 mm	+12 mm
Y Axis	+12 mm	-	1.667	1.584	1.784	-
	+6 mm	1.417	1.467	1.467	1.517	**1.867**
	Center	1.234	1.401	1.367	1.517	**1.867**
	−6 mm	1.301	1.417	1.351	1.534	**1.867**
	−12 mm	-	1.551	1.551	1.717	-
Center Axial Position						
				X Axis		
		−12 mm	−6 mm	Center	+6 mm	+12 mm
Y Axis	+12 mm	-	**1.867**	1.784	**1.867**	-
	+6 mm	1.801	1.601	1.634	1.734	**1.867**
	Center	1.601	1.484	1.601	1.667	**1.867**
	−6 mm	1.801	1.601	1.634	1.734	**1.867**
	−12 mm	-	1.851	**1.867**	**1.867**	-
+6 mm Axial Position						
				X Axis		
		−12 mm	−6 mm	Center	+6 mm	+12 mm
Y Axis	+12 mm	-	1.567	1.801	1.584	-
	+6 mm	1.534	1.401	1.534	1.501	1.601
	Center	1.434	1.401	1.534	1.601	1.567
	−6 mm	1.467	1.467	1.534	1.567	1.584
	−12 mm	-	1.601	1.834	1.801	-

Table 3.3 Time–domain root mean square magnetic flux density, $tRMS_B$ values measured in mT from solenoid coil with round wire design for 75% power level at three different axial positions; −6, 0, +6 mm and 21 different transverse positions; 6 mm apart at each axial position (63 positions in total, for each power level).

-6 mm Axial Position						
				X Axis		
		−12 mm	−6 mm	Center	+6 mm	+12 mm
	+12 mm	-	1.267	1.267	1.434	-
	+6 mm	1.267	1.134	1.234	1.334	1.567
Y Axis	Center	1.167	1.100	1.167	1.234	1.467
	−6 mm	1.134	1.134	1.200	1.434	1.601
	−12 mm	-	1.367	1.501	1.534	-
Center Axial Position						
				X Axis		
		−12 mm	−6 mm	Center	+6 mm	+12 mm
	+12 mm	-	1.434	1.300	1.534	-
	+6 mm	1.367	1.200	1.200	1.367	1.634
Y Axis	Center	1.234	1.167	1.167	1.267	1.534
	−6 mm	1.300	1.167	1.300	1.367	**1.767**
	−12 mm	-	1.400	1.534	1.701	-
+6 mm Axial Position						
				X Axis		
		−12 mm	−6 mm	Center	+6 mm	+12 mm
	+12 mm	-	1.000	1.134	1.234	-
	+6 mm	1.034	1.034	1.067	1.134	1.367
Y Axis	Center	0.967	0.967	1.067	1.134	1.267
	−6 mm	0.967	1.000	1.134	1.134	1.367
	−12 mm	-	1.134	1.167	1.234	-

Table 3.4 Time–domain root mean square magnetic flux density, $tRMS_B$ values measured in mT from solenoid coil with round wire design for 50% power level at three different axial positions; −6, 0, +6 mm and 21 different transverse positions; 6 mm apart at each axial position (63 positions in total, for each power level).

-6 mm Axial Position						
				X Axis		
		−12 mm	−6 mm	Center	+6 mm	+12 mm
	+12 mm	-	1.067	1.067	1.100	-
	+6 mm	0.900	0.900	0.900	0.934	**1.167**
Y Axis	Center	0.800	0.834	0.834	0.934	1.134
	−6 mm	0.867	0.800	0.834	0.934	**1.167**
	−12 mm	-	0.867	1.034	1.067	-
Center Axial Position						
				X Axis		
		−12 mm	−6 mm	Center	+6 mm	+12 mm
	+12 mm	-	1.000	1.067	**1.167**	-
	+6 mm	0.934	0.967	0.900	1.000	1.134
Y Axis	Center	0.867	0.867	0.834	0.934	1.100
	−6 mm	0.934	0.834	0.900	1.000	1.200
	−12 mm	-	0.967	1.034	1.134	-
+6 mm Axial Position						
				X Axis		
		−12 mm	−6 mm	Center	+6 mm	+12 mm
	+12 mm	-	0.800	0.834	0.967	-
	+6 mm	0.767	0.734	0.800	0.800	0.900
Y Axis	Center	0.767	0.700	0.700	0.800	0.834
	−6 mm	0.734	0.667	0.734	0.867	0.867
	−12 mm	-	0.700	0.800	0.867	-

Table 3.5 Time–domain root mean square magnetic flux density, $tRMS_B$ values measured in mT from solenoid coil with round wire design for 25% power level at three different axial positions; −6, 0, +6 mm and 21 different transverse positions; 6 mm apart at each axial position (63 positions in total, for each power level).

-6 mm Axial Position						
				X Axis		
		−12 mm	−6 mm	Center	+6 mm	+12 mm
	+12 mm	-	0.383	0.400	0.433	-
	+6 mm	0.367	0.367	0.400	0.400	0.567
Y Axis	Center	0.383	0.417	0.383	0.433	0.484
	−6 mm	0.350	0.350	0.350	0.433	0.467
	−12 mm	-	0.467	0.484	0.500	-
Center Axial Position						
				X Axis		
		−12 mm	−6 mm	Center	+6 mm	+12 mm
	+12 mm	-	0.433	0.433	0.484	-
	+6 mm	0.450	0.400	0.400	0.467	**0.584**
Y Axis	Center	0.400	0.400	0.400	0.467	0.500
	−6 mm	0.450	0.400	0.367	0.467	0.567
	−12 mm	-	0.467	0.433	0.534	-
+6 mm Axial Position						
				X Axis		
		−12 mm	−6 mm	Center	+6 mm	+12 mm
	+12 mm	-	0.433	0.433	0.500	-
	+6 mm	0.383	0.333	0.383	0.467	0.500
Y Axis	Center	0.333	0.367	0.333	0.433	0.433
	−6 mm	0.467	0.383	0.400	0.467	0.467
	−12 mm	-	0.417	0.500	0.534	-

Table 3.6 Time–domain root mean square magnetic flux density, $tRMS_B$ values measured in mT from solenoid coil with round wire design for 10% power level at three different axial positions; −6, 0, +6 mm and 21 different transverse positions; 6 mm apart at each axial position (63 positions in total, for each power level).

-6 mm Axial Position						
				X Axis		
		−12 mm	−6 mm	Center	+6 mm	+12 mm
	+12 mm	-	0.250	0.267	0.300	-
	+6 mm	0.250	0.233	0.267	0.267	0.300
Y Axis	Center	0.250	**0.333**	0.300	0.250	0.267
	−6 mm	0.250	0.267	0.250	0.300	0.317
	−12 mm	-	0.250	0.283	0.300	-
Center Axial Position						
				X Axis		
		−12 mm	−6 mm	Center	+6 mm	+12 mm
	+12 mm	-	0.267	0.267	0.267	-
	+6 mm	0.233	0.250	0.233	0.300	0.300
Y Axis	Center	0.267	0.233	0.250	0.267	0.250
	−6 mm	0.250	0.267	0.250	0.250	0.300
	−12 mm	-	0.300	0.283	0.317	-
+6 mm Axial Position						
				X Axis		
		−12 mm	−6 mm	Center	+6 mm	+12 mm
	+12 mm	-	0.300	**0.333**	0.283	-
	+6 mm	0.267	0.233	0.250	0.250	0.233
Y Axis	Center	0.250	0.250	0.267	0.283	0.250
	−6 mm	0.233	0.283	0.300	0.300	0.300
	−12 mm	-	0.267	0.250	0.283	-

Table 3.7 Amount of temperature rise, Δ_T values measured in ^{o}C from 166.5 mg/mL concentration MNPs inside of solenoid coil with round wire design at three axial positions inside of the coil gap and five different transverse positions.

-6 mm Axial Position				
			X Axis	
		−6 mm	Center	+6 mm
	+6 mm	-	2.6	-
Y Axis	Center	2.4	2.5	**2.7**
	−6 mm	-	**2.7**	-
Center Axial Position				
			X Axis	
		−6 mm	Center	+6 mm
	+6 mm	-	2.5	-
Y Axis	Center	2.4	2.4	2.6
	−6 mm	-	2.6	-
+6 mm Axial Position				
			X Axis	
		−6 mm	Center	+6 mm
	+6 mm	-	2.6	-
Y Axis	Center	2.3	2.3	2.5
	−6 mm	-	2.5	-

Table 3.8 Amount of temperature rise, Δ_T values measured in ^{o}C from 120 mg/mL concentration MNPs inside of solenoid coil with round wire design at three axial positions inside of the coil gap and five different transverse positions.

-6 mm Axial Position				
			X Axis	
		−6 mm	Center	+6 mm
	+6 mm	-	2.0	-
Y Axis	Center	1.9	**2.1**	1.9
	−6 mm	-	**2.1**	-
Center Axial Position				
			X Axis	
		−6 mm	Center	+6 mm
	+6 mm	-	2.0	-
Y Axis	Center	1.8	1.8	1.9
	−6 mm	-	**2.1**	-
+6 mm Axial Position				
			X Axis	
		−6 mm	Center	+6 mm
	+6 mm	-	2.0	-
Y Axis	Center	1.9	2.0	1.9
	−6 mm	-	2.0	-

Table 3.9 Slope of linear regression fit for 40 minute temperature rise vs. time graph during MH experiments conducted with 166.5 mg/mL concentration SPION using solenoid coil with round wire at three axial positions inside of the coil gap and five different transverse positions.

-6 mm Axial Position				
			X Axis	
		−6 mm	Center	+6 mm
	+6 mm	-	0.075	-
Y Axis	Center	**0.078**	0.073	0.072
	−6 mm	-	0.072	-
Center Axial Position				
			X Axis	
		−6 mm	Center	+6 mm
	+6 mm	-	0.072	-
Y Axis	Center	0.072	0.071	0.071
	−6 mm	-	0.071	-
+6 mm Axial Position				
			X Axis	
		−6 mm	Center	+6 mm
	+6 mm	-	0.067	-
Y Axis	Center	0.069	0.067	0.068
	−6 mm	-	0.069	-

Table 3.10 Slope of linear regression fit for 40 minute temperature rise vs. time graph during MH experiments conducted with 120 mg/mL concentration SPION using solenoid coil with round wire at three axial positions inside of the coil gap and five different transverse positions.

-6 mm Axial Position				
		X Axis		
		−6 mm	Center	+6 mm
Y Axis	+6 mm	-	0.052	-
	Center	**0.054**	**0.054**	0.053
	−6 mm	-	0.053	-
Center Axial Position				
		X Axis		
		−6 mm	Center	+6 mm
Y Axis	+6 mm	-	0.052	-
	Center	0.052	0.051	0.051
	−6 mm	-	0.052	-
+6 mm Axial Position				
		X Axis		
		−6 mm	Center	+6 mm
Y Axis	+6 mm	-	0.052	-
	Center	0.053	0.053	**0.054**
	−6 mm	-	0.053	-

Table 3.11 Solenoid coil with round wire physical implementation measured thermal variables.

	$\mathbf{sm_T}$ (^{o} C)	$\mathbf{smin_T}$ (^{o} C)	$\mathbf{smax_T}$ (^{o} C)	$\mathbf{srange_T}$ (^{o} C)	$\mathbf{scenter_T}$ (^{o} C)	$\mathbf{s\sigma_T}$ (^{o} C)	$\mathbf{sHom_T}$	$\mathbf{sT_{coil}}$
166.5 mg/mL	2.51	2.30	2.70	0.40	2.40	0.13	19.31	52.14
120 mg/mL	1.90	1.80	2.10	0.30	1.80	0.27	7.04	14.78

3.2. Solenoid Coil with Round Litz Wire Measurements

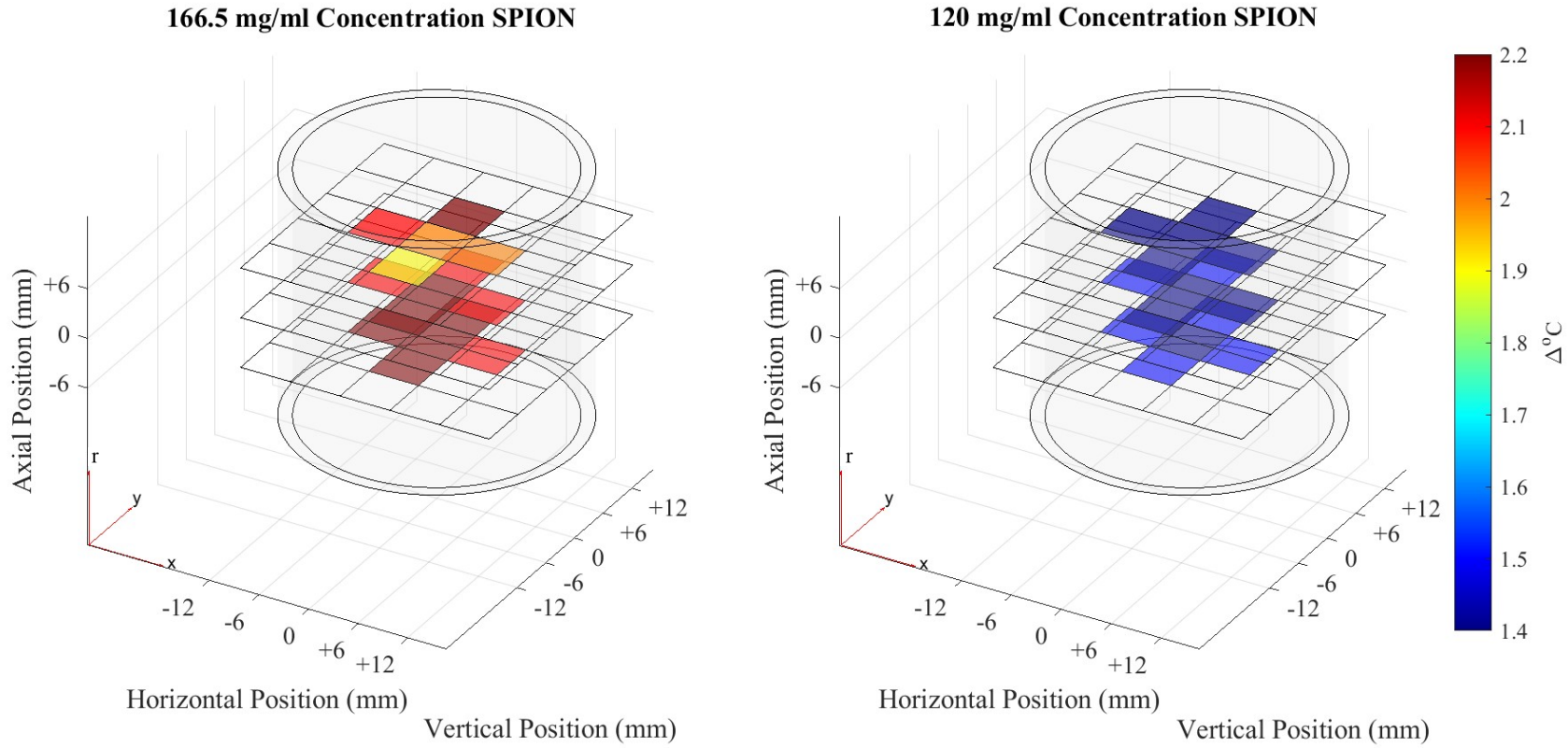


Figure 3.42 Amount of temperature rise, ΔT measured from two different SPION concentrations inside of solenoid coil with round Litz wire design at three different axial positions; -12, 0, $+12$ mm and five different transverse positions; 0, -6 and $+6$ mm horizontally, -6 and $+6$ mm vertically for each axial position (15 positions in total) inside of the coil gap.

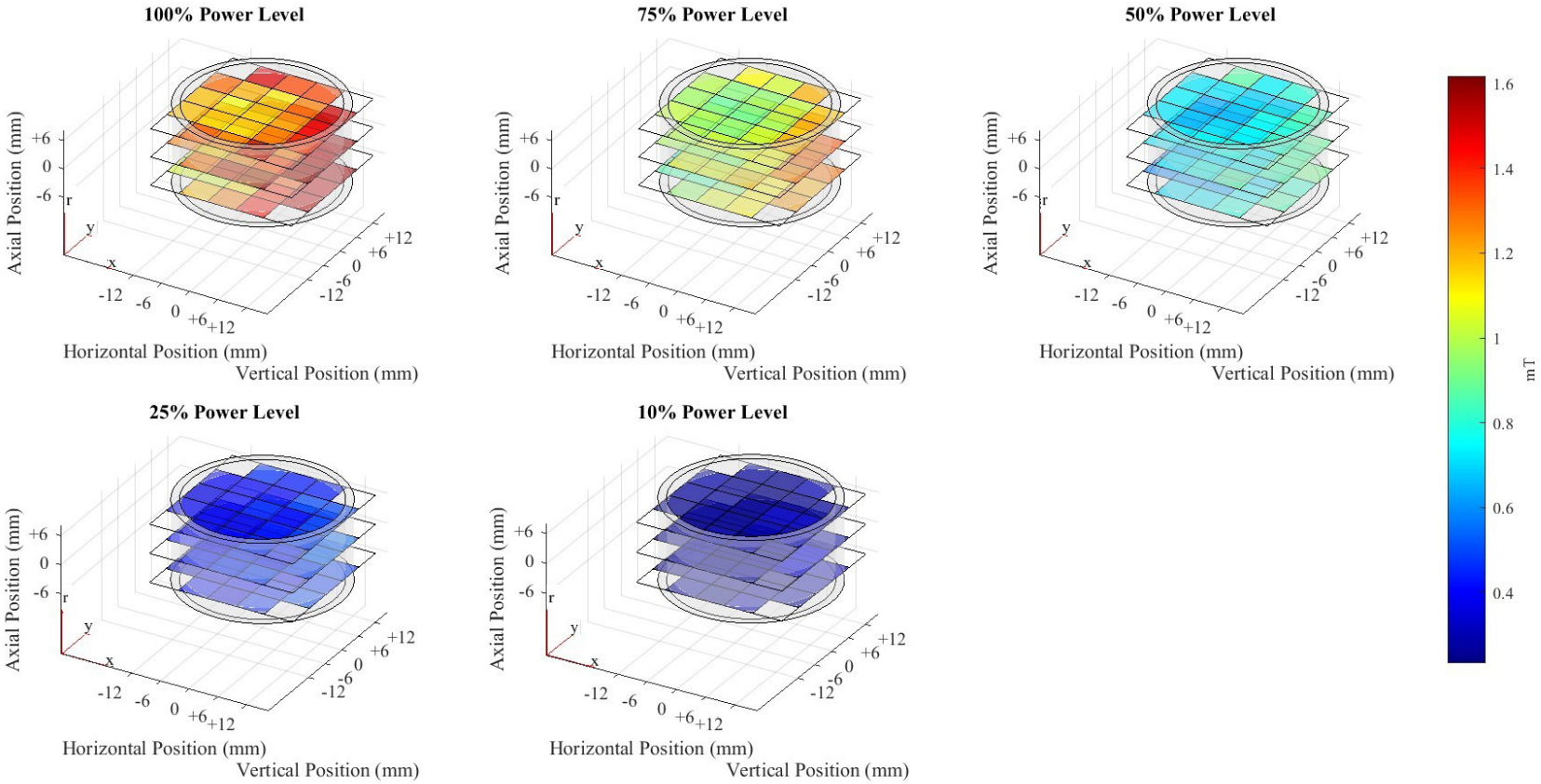


Figure 3.43 Time–domain root mean square magnetic flux density, $tRMS_B$ values measured in mT from solenoid coil with round Litz wire design for all power levels at three different axial positions; −6, 0, +6 mm and 21 different transverse positions; 6 mm apart at each axial position (63 positions in total, for each power level).

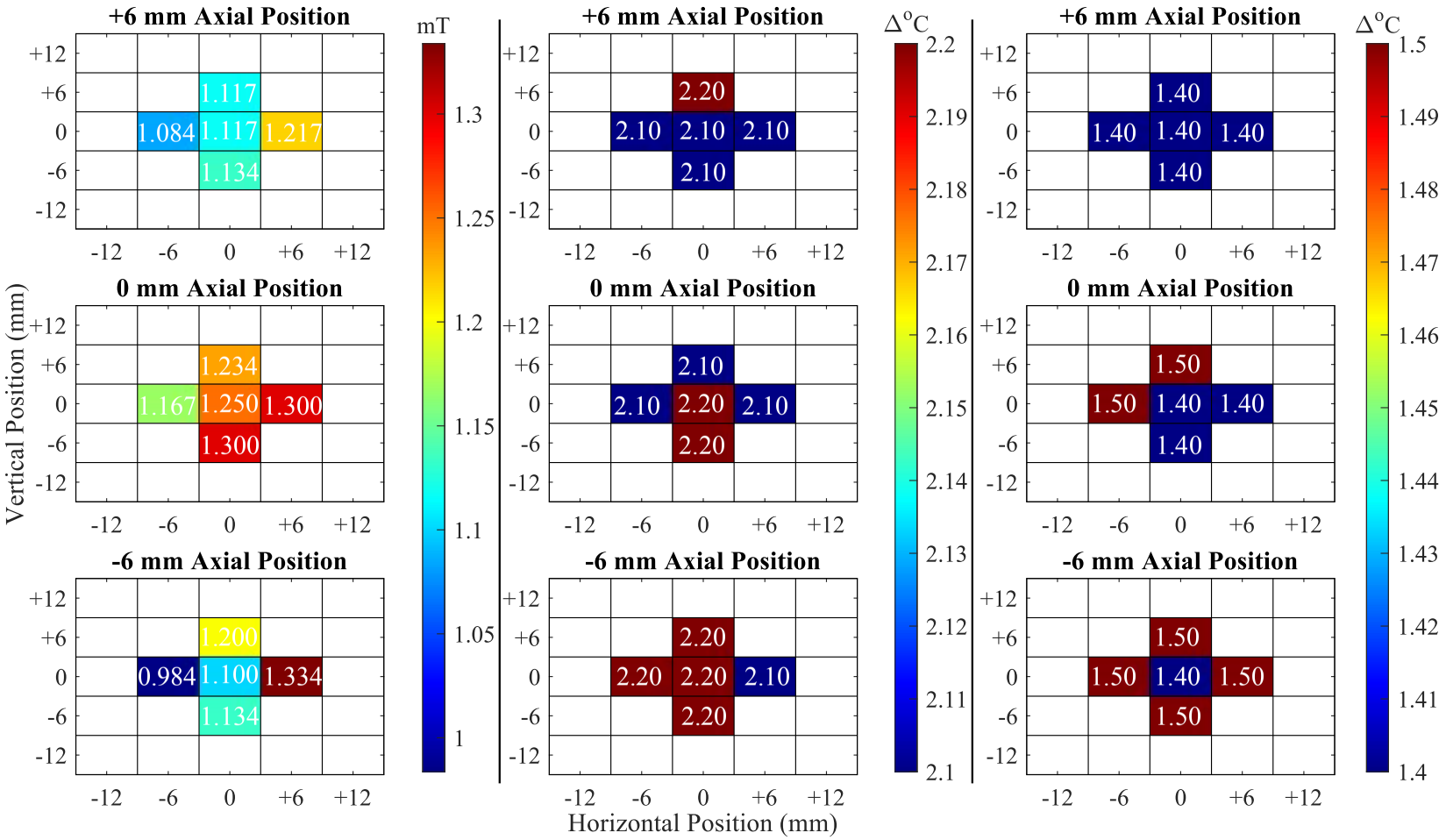


Figure 3.44 Time–domain root mean square magnetic flux density, $tRMS_B$ (left) and corresponding amount of temperature rise, ΔT with 166.5 (middle) and 120 mg/mL (right) SPION concentrations values measured from solenoid coil with round Litz wire design for 100% power level at three different axial positions; −6, 0, +6 mm.

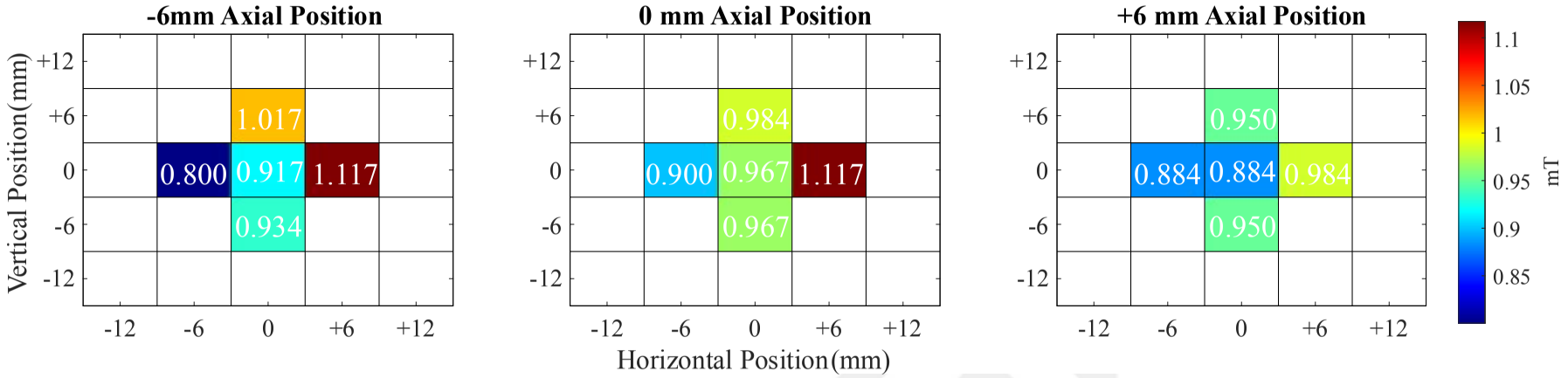


Figure 3.45 Time–domain root mean square magnetic flux density, $tRMS_B$ (top) values measured from solenoid coil with round Litz wire design for 75% power level at three different axial positions; −6, 0, +6 mm.

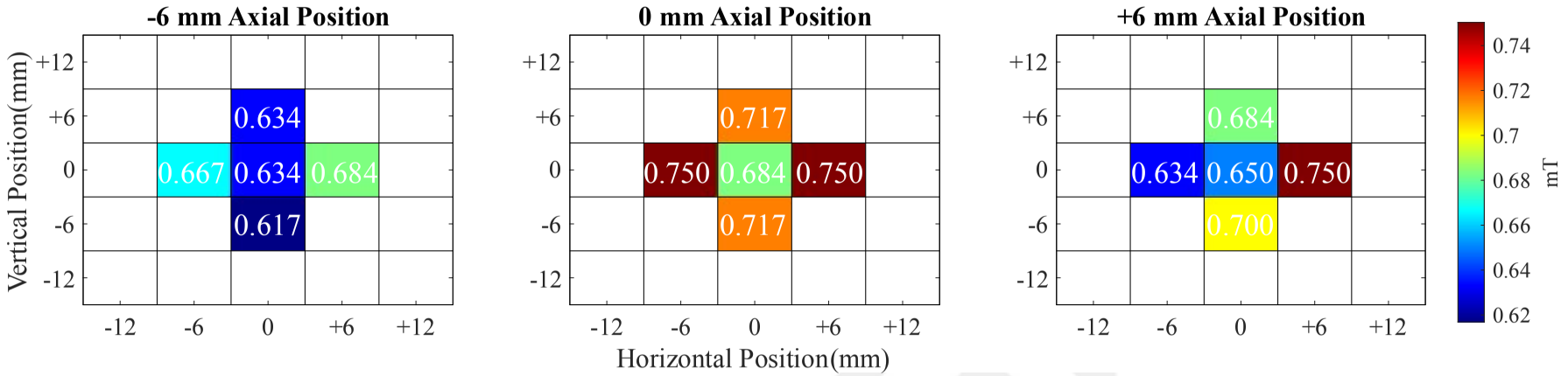


Figure 3.46 Time–domain root mean square magnetic flux density, $tRMS_B$ (top) values measured from solenoid coil with round Litz wire design for 50% power level at three different axial positions; −6, 0, +6 mm.

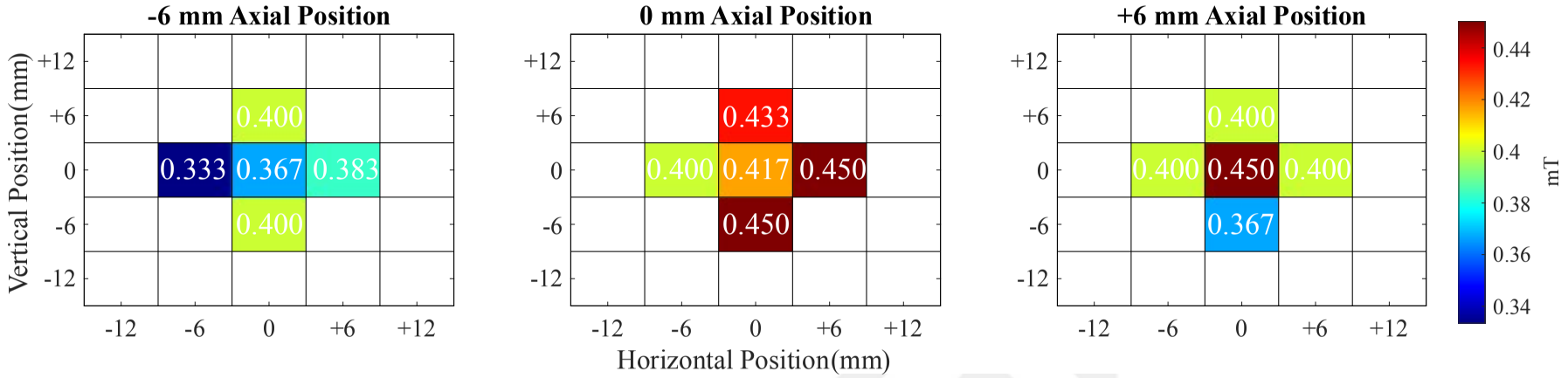


Figure 3.47 Time–domain root mean square magnetic flux density, $tRMS_B$ (top) values measured from solenoid coil with round Litz wire design for 25% power level at three different axial positions; −6, 0, +6 mm.

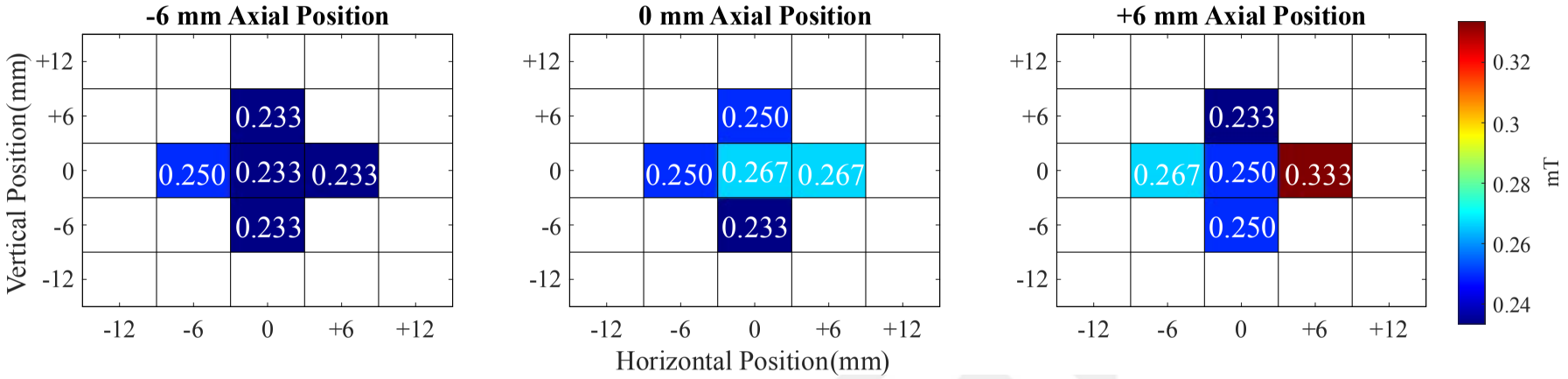


Figure 3.48 Time–domain root mean square magnetic flux density, $tRMS_B$ (top) values measured from solenoid coil with round Litz wire design for 10% power level at three different axial positions; −6, 0, +6 mm.

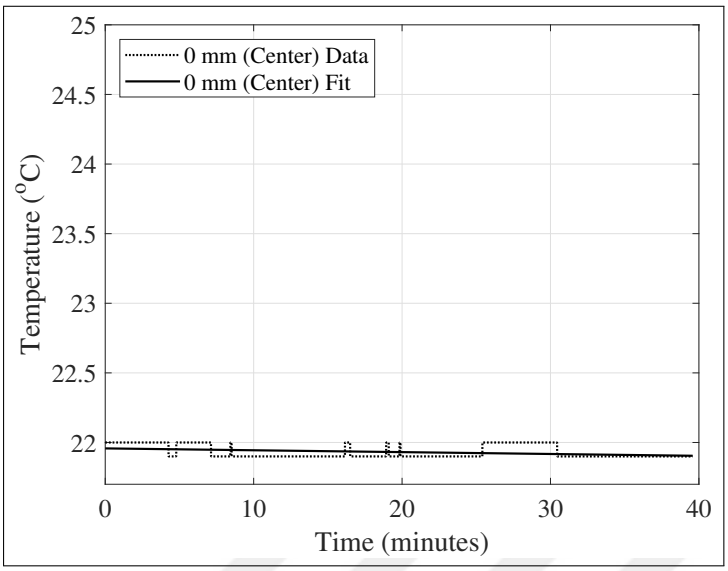


Figure 3.49 40 minute temperature vs. time graph during MH experiments conducted with distilled water as the control experiment using solenoid coil with round Litz wire at 0 mm axial position, 0 mm (center) position. Temperature–time data was fitted to a line using linear regression for analyzing positional related effects.

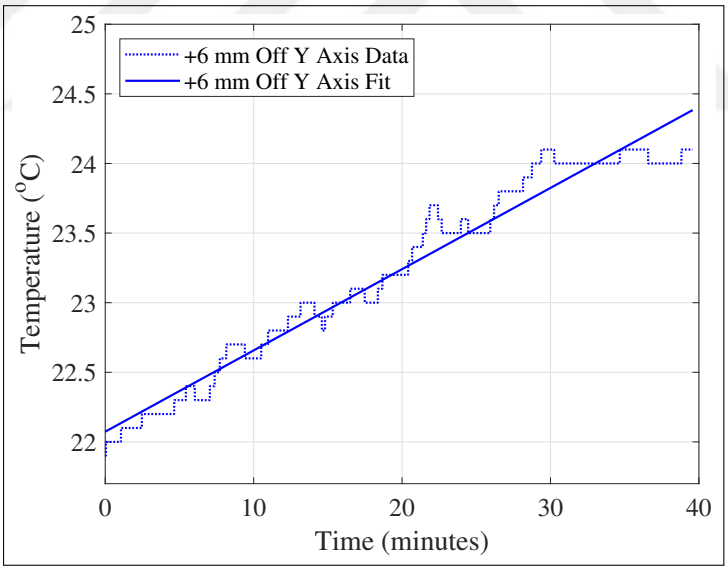


Figure 3.50 40 minute temperature rise vs. time graph during MH experiments conducted with 166.5 mg/mL concentration SPION using solenoid coil with round Litz wire at −6 mm axial position, +6 mm off Y-axis. Temperature–time data was fitted to a line using linear regression for analyzing positional related effects.

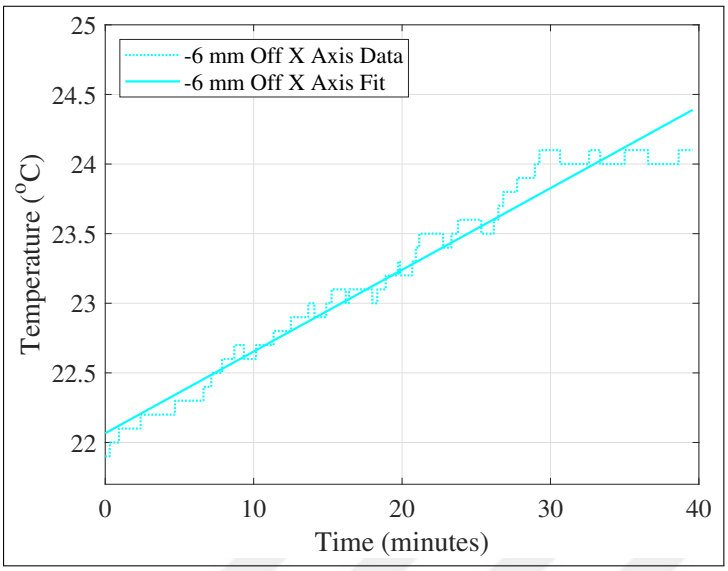


Figure 3.51 40 minute temperature rise vs. time graph during MH experiments conducted with 166.5 mg/mL concentration SPION using solenoid coil with round Litz wire at −6 mm axial position, −6 mm off X-axis. Temperature–time data was fitted to a line using linear regression for analyzing positional related effects.

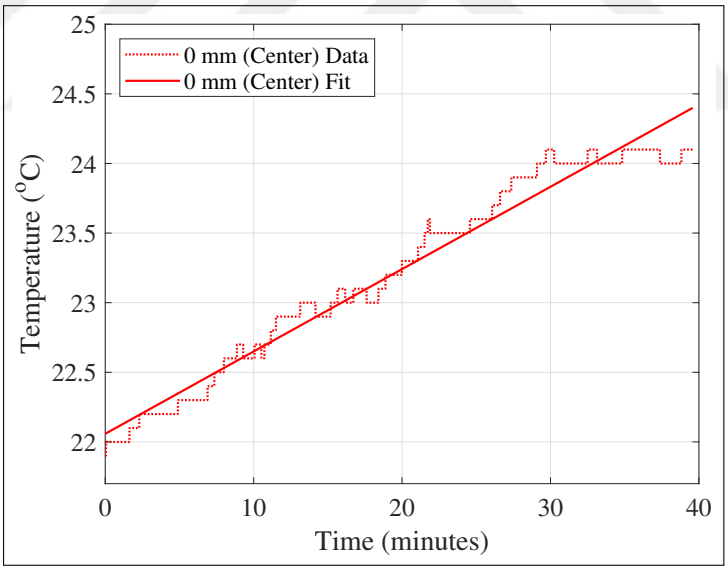


Figure 3.52 40 minute temperature rise vs. time graph during MH experiments conducted with 166.5 mg/mL concentration SPION using solenoid coil with round Litz wire at −6 mm axial position, 0 mm (center) position. Temperature–time data was fitted to a line using linear regression for analyzing positional related effects.

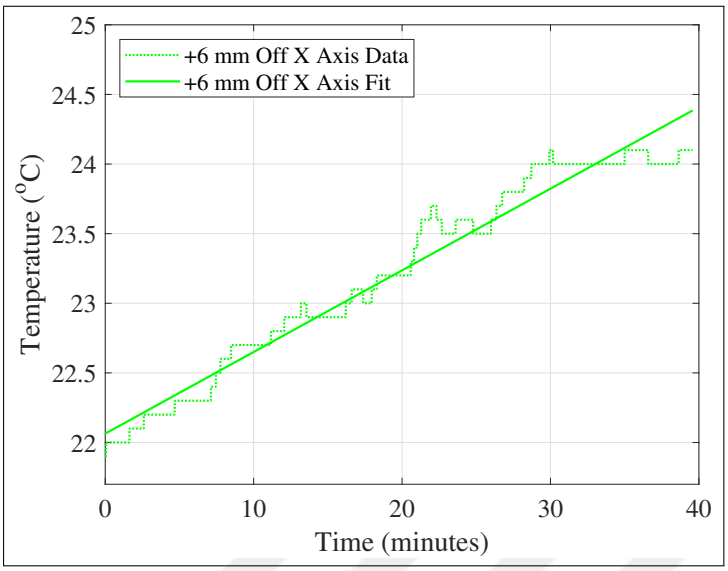


Figure 3.53 40 minute temperature rise vs. time graph during MH experiments conducted with 166.5 mg/mL concentration SPION using solenoid coil with round Litz wire at −6 mm axial position, +6 mm off X-axis. Temperature–time data was fitted to a line using linear regression for analyzing positional related effects.

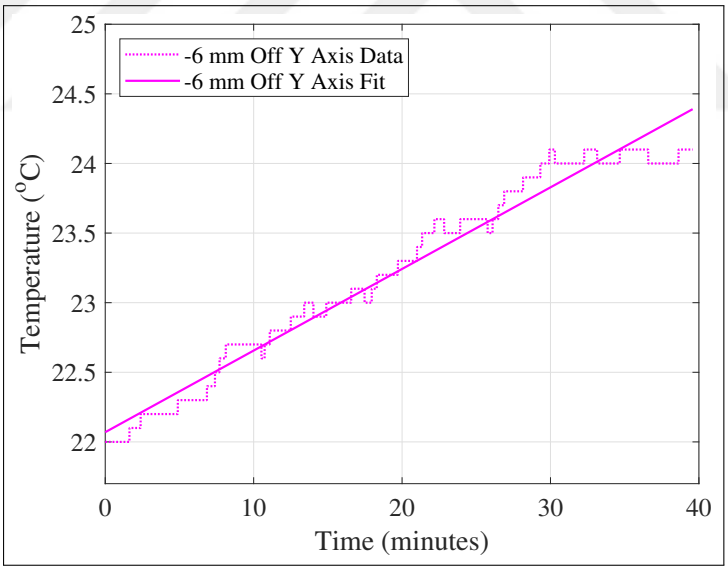


Figure 3.54 40 minute temperature rise vs. time graph during MH experiments conducted with 166.5 mg/mL concentration SPION using solenoid coil with round Litz wire at −6 mm axial position, −6 mm off Y-axis. Temperature–time data was fitted to a line using linear regression for analyzing positional related effects.

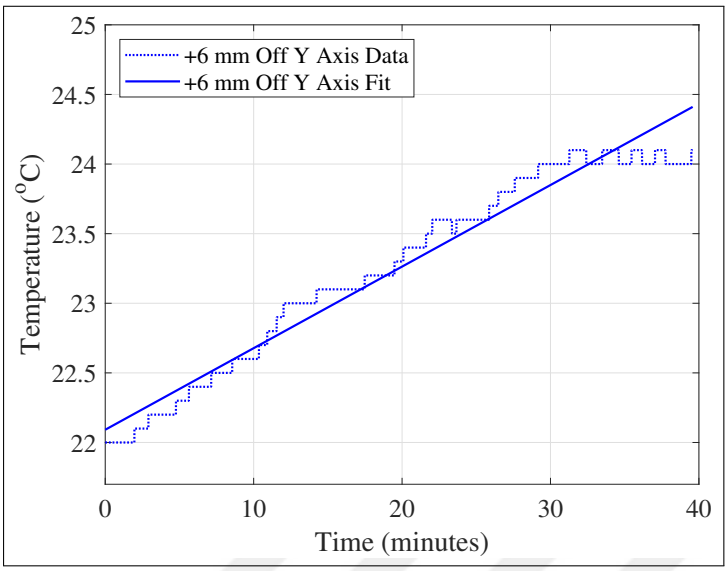


Figure 3.55 40 minute temperature rise vs. time graph during MH experiments conducted with 166.5 mg/mL concentration SPION using solenoid coil with round Litz wire at 0 mm axial position, +6 mm off Y-axis. Temperature–time data was fitted to a line using linear regression for analyzing positional related effects.

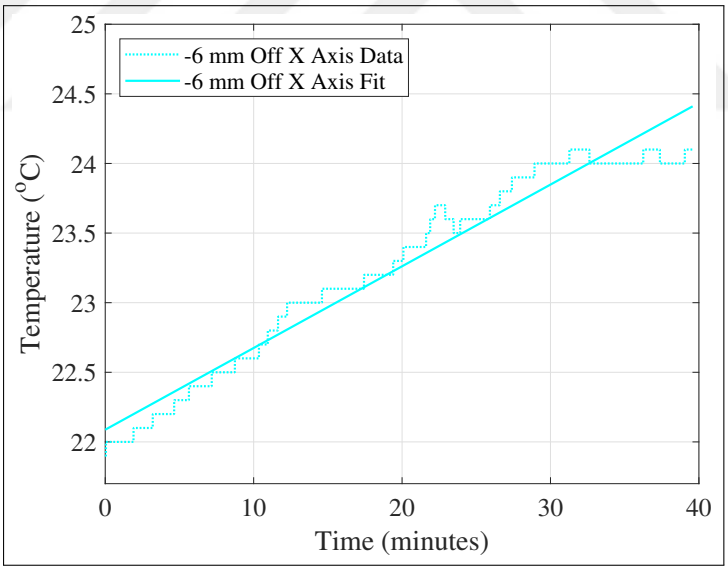


Figure 3.56 40 minute temperature rise vs. time graph during MH experiments conducted with 166.5 mg/mL concentration SPION using solenoid coil with round Litz wire at 0 mm axial position, −6 mm off X-axis. Temperature–time data was fitted to a line using linear regression for analyzing positional related effects.

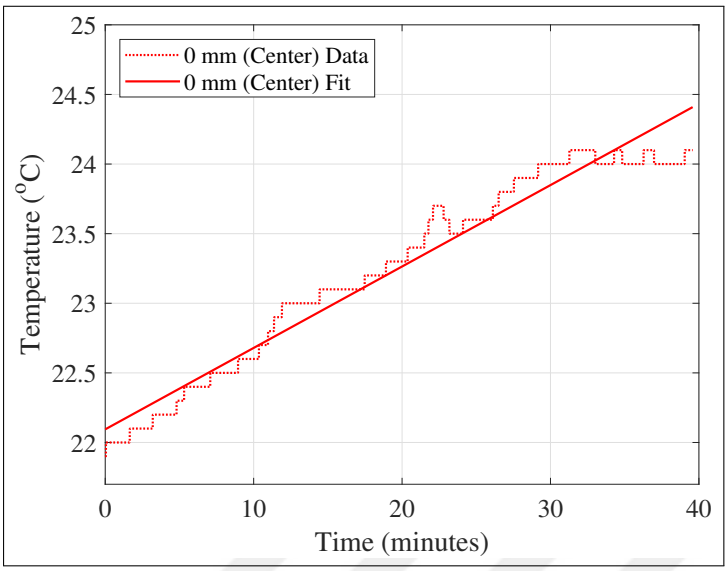


Figure 3.57 40 minute temperature rise vs. time graph during MH experiments conducted with 166.5 mg/mL concentration SPION using solenoid coil with round Litz wire at 0 mm axial position, 0 mm (center) position. Temperature–time data was fitted to a line using linear regression for analyzing positional related effects.

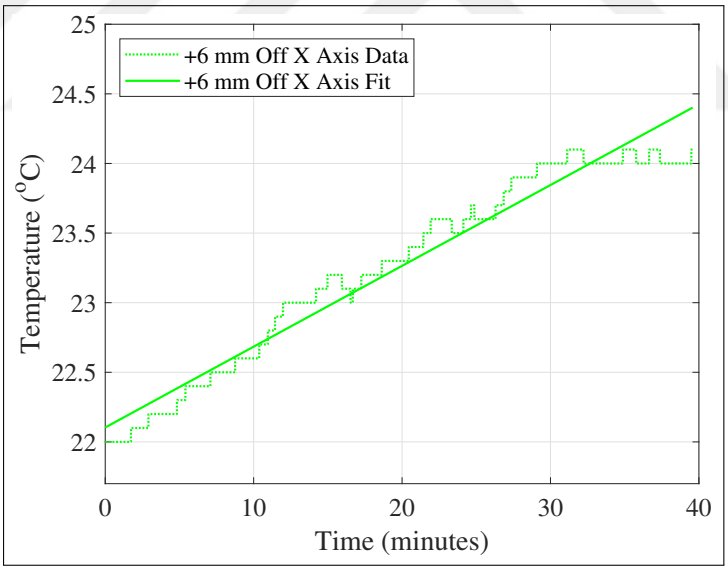


Figure 3.58 40 minute temperature rise vs. time graph during MH experiments conducted with 166.5 mg/mL concentration SPION using solenoid coil with round Litz wire at 0 mm axial position, +6 mm off X-axis. Temperature–time data was fitted to a line using linear regression for analyzing positional related effects.

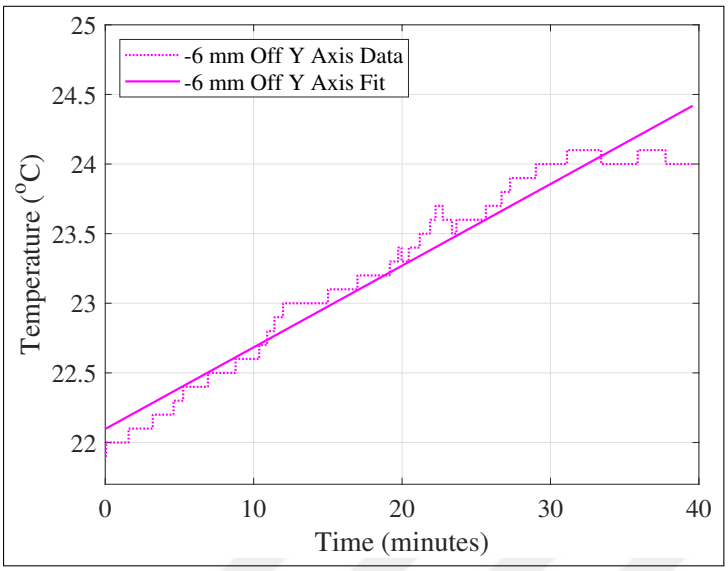


Figure 3.59 40 minute temperature rise vs. time graph during MH experiments conducted with 166.5 mg/mL concentration SPION using solenoid coil with round Litz wire at 0 mm axial position, −6 mm off Y-axis. Temperature–time data was fitted to a line using linear regression for analyzing positional related effects.

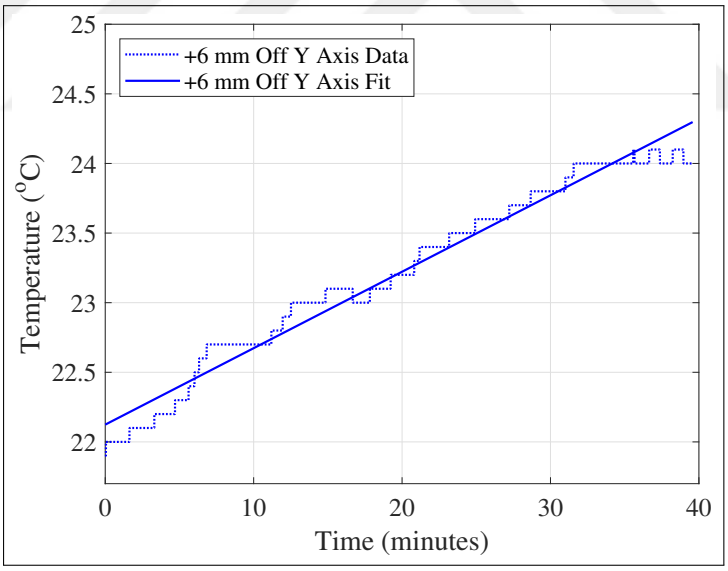


Figure 3.60 40 minute temperature rise vs. time graph during MH experiments conducted with 166.5 mg/mL concentration SPION using solenoid coil with round Litz wire at +6 mm axial position, +6 mm off Y-axis. Temperature–time data was fitted to a line using linear regression for analyzing positional related effects.

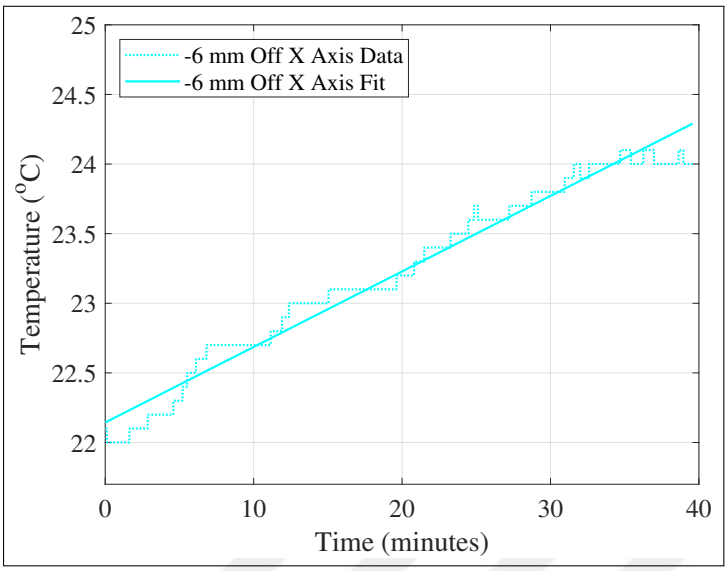


Figure 3.61 40 minute temperature rise vs. time graph during MH experiments conducted with 166.5 mg/mL concentration SPION using solenoid coil with round Litz wire at +6 mm axial position, −6 mm off X-axis. Temperature–time data was fitted to a line using linear regression for analyzing positional related effects.

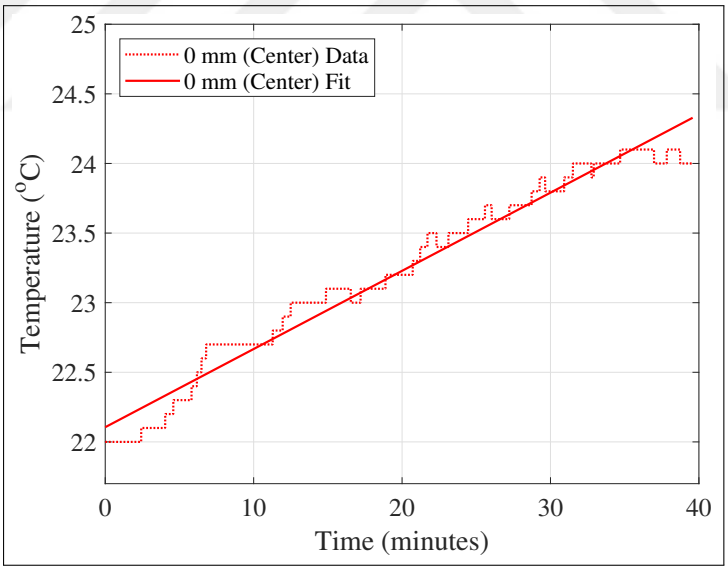


Figure 3.62 40 minute temperature rise vs. time graph during MH experiments conducted with 166.5 mg/mL concentration SPION using solenoid coil with round Litz wire at +6 mm axial position, 0 mm (center) position. Temperature–time data was fitted to a line using linear regression for analyzing positional related effects.

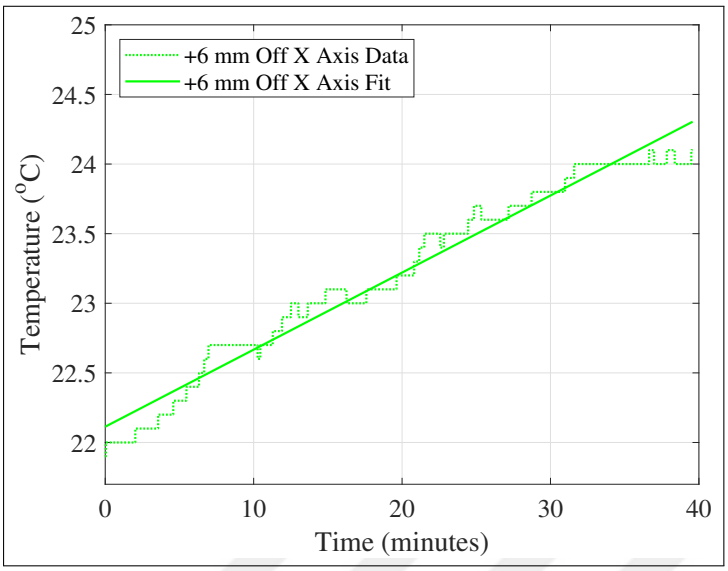


Figure 3.63 40 minute temperature rise vs. time graph during MH experiments conducted with 166.5 mg/mL concentration SPION using solenoid coil with round Litz wire at +6 mm axial position, +6 mm off X-axis. Temperature–time data was fitted to a line using linear regression for analyzing positional related effects.

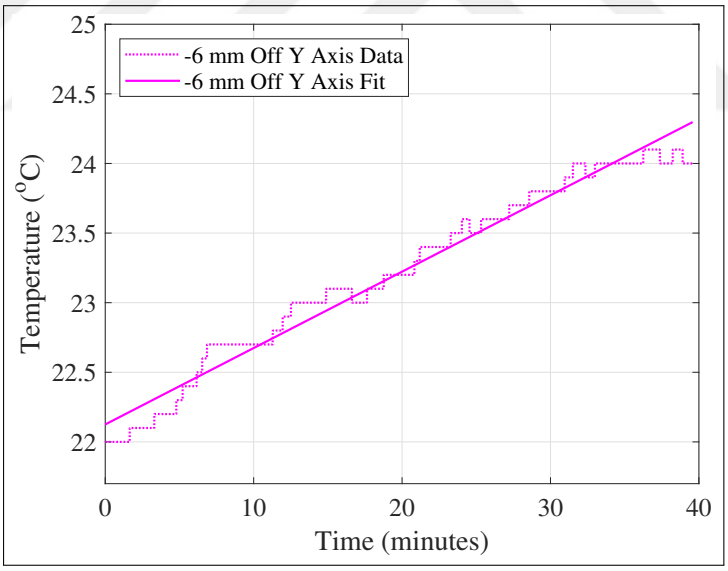


Figure 3.64 40 minute temperature rise vs. time graph during MH experiments conducted with 166.5 mg/mL concentration SPION using solenoid coil with round Litz wire at +6 mm axial position, −6 mm off Y-axis. Temperature–time data was fitted to a line using linear regression for analyzing positional related effects.

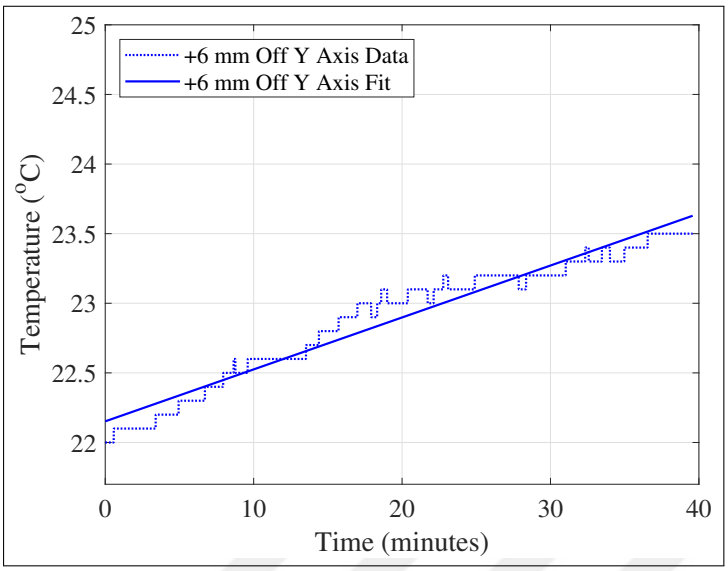


Figure 3.65 40 minute temperature rise vs. time graph during MH experiments conducted with 120 mg/mL concentration SPION using solenoid coil with round Litz wire at −6 mm axial position, +6 mm off Y-axis. Temperature–time data was fitted to a line using linear regression for analyzing positional related effects.

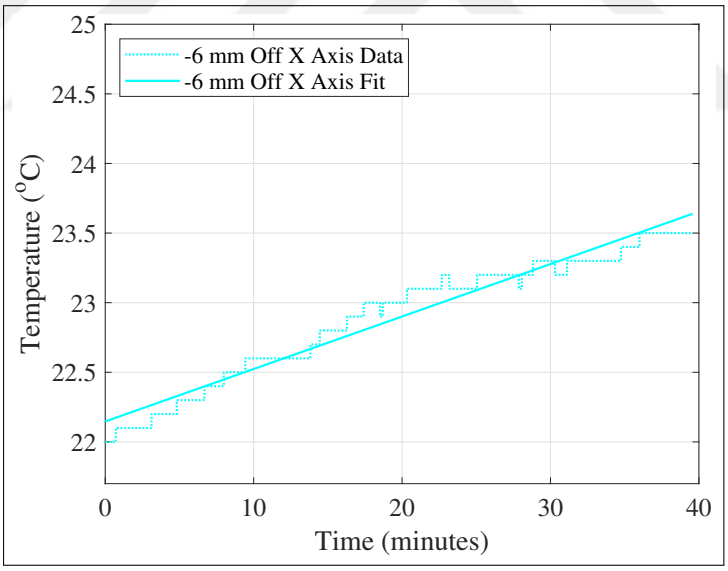


Figure 3.66 40 minute temperature rise vs. time graph during MH experiments conducted with 120 mg/mL concentration SPION using solenoid coil with round Litz wire at −6 mm axial position, −6 mm off X-axis. Temperature–time data was fitted to a line using linear regression for analyzing positional related effects.

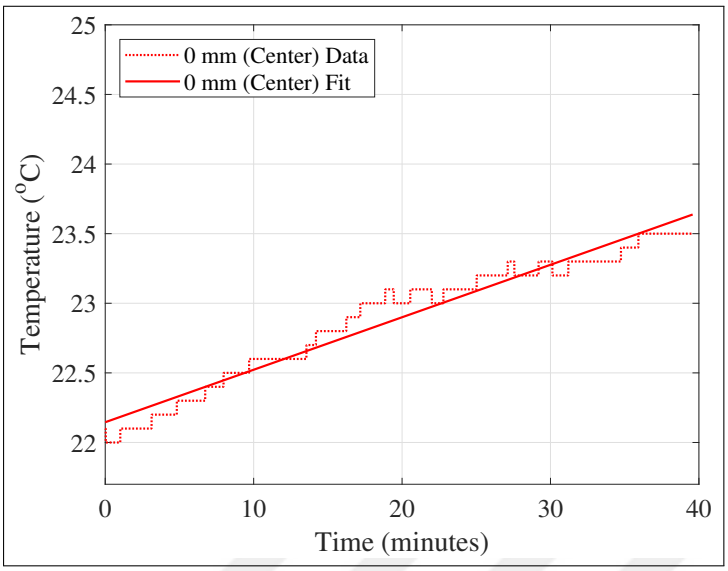


Figure 3.67 40 minute temperature rise vs. time graph during MH experiments conducted with 120 mg/mL concentration SPION using solenoid coil with round Litz wire at −6 mm axial position, 0 mm (center) position. Temperature–time data was fitted to a line using linear regression for analyzing positional related effects.

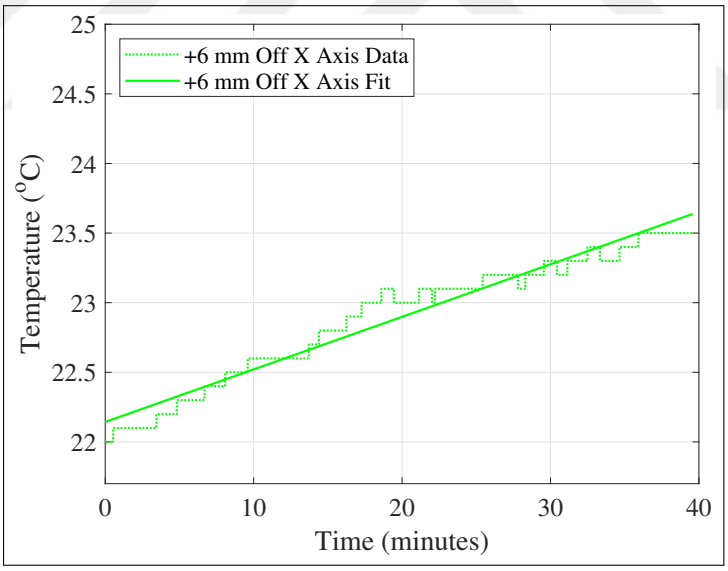


Figure 3.68 40 minute temperature rise vs. time graph during MH experiments conducted with 120 mg/mL concentration SPION using solenoid coil with round Litz wire at −6 mm axial position, +6 mm off X-axis. Temperature–time data was fitted to a line using linear regression for analyzing positional related effects.

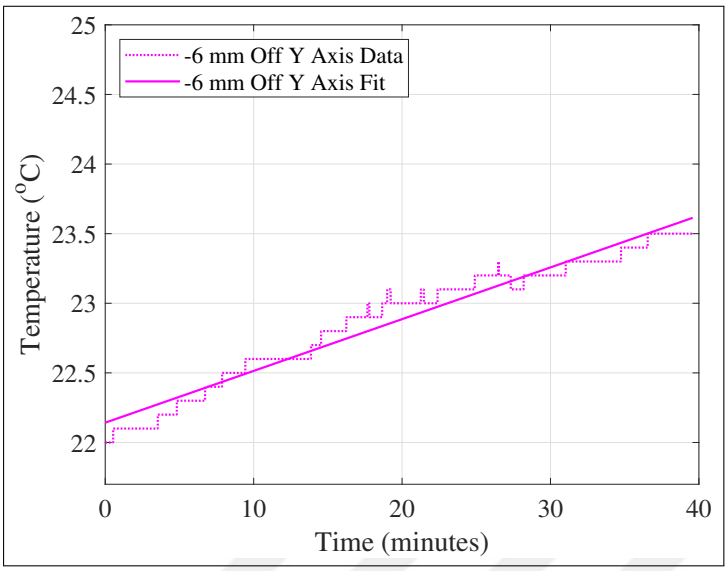


Figure 3.69 40 minute temperature rise vs. time graph during MH experiments conducted with 120 mg/mL concentration SPION using solenoid coil with round Litz wire at −6 mm axial position, −6 mm off Y-axis. Temperature–time data was fitted to a line using linear regression for analyzing positional related effects.

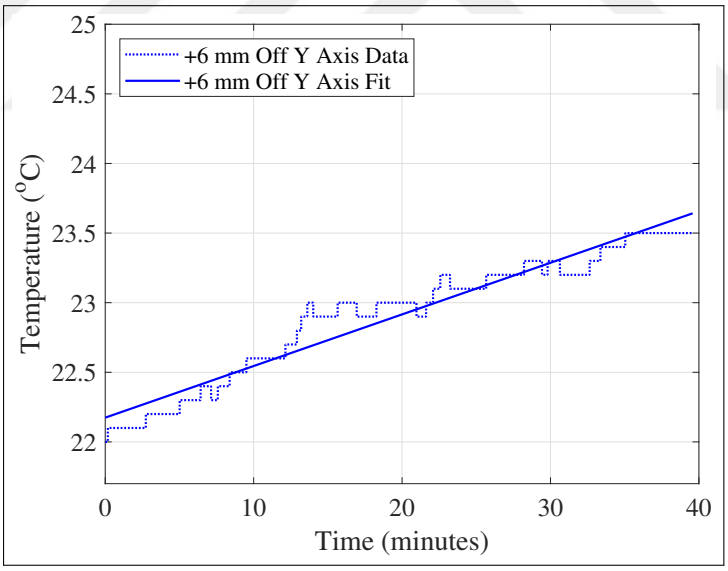


Figure 3.70 40 minute temperature rise vs. time graph during MH experiments conducted with 120 mg/mL concentration SPION using solenoid coil with round Litz wire at 0 mm axial position, +6 mm off Y-axis. Temperature–time data was fitted to a line using linear regression for analyzing positional related effects.

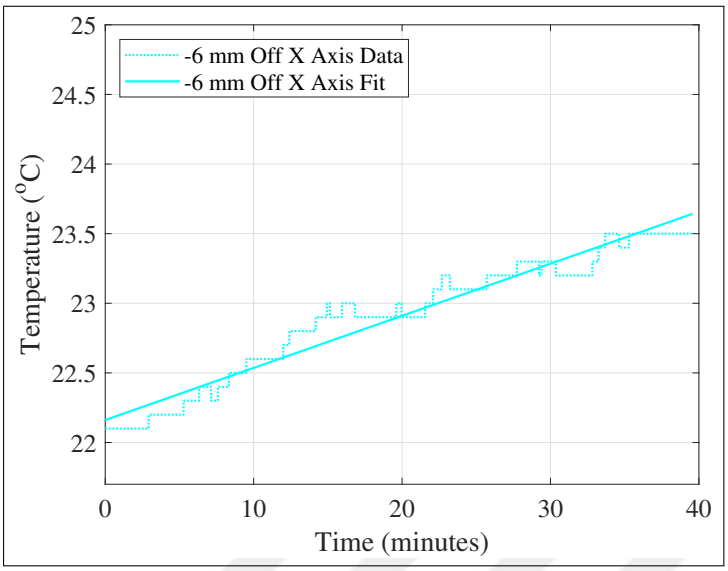


Figure 3.71 40 minute temperature rise vs. time graph during MH experiments conducted with 120 mg/mL concentration SPION using solenoid coil with round Litz wire at 0 mm axial position, −6 mm off X-axis. Temperature–time data was fitted to a line using linear regression for analyzing positional related effects.

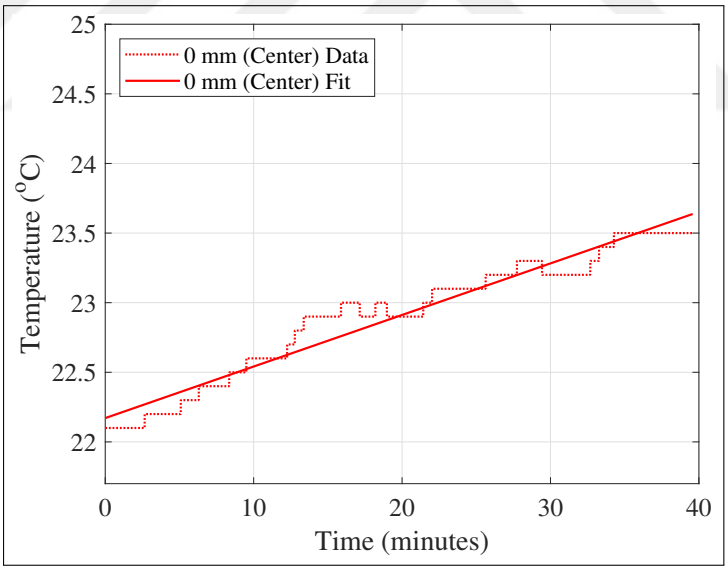


Figure 3.72 40 minute temperature rise vs. time graph during MH experiments conducted with 120 mg/mL concentration SPION using solenoid coil with round Litz wire at 0 mm axial position, 0 mm (center) position. Temperature–time data was fitted to a line using linear regression for analyzing positional related effects.

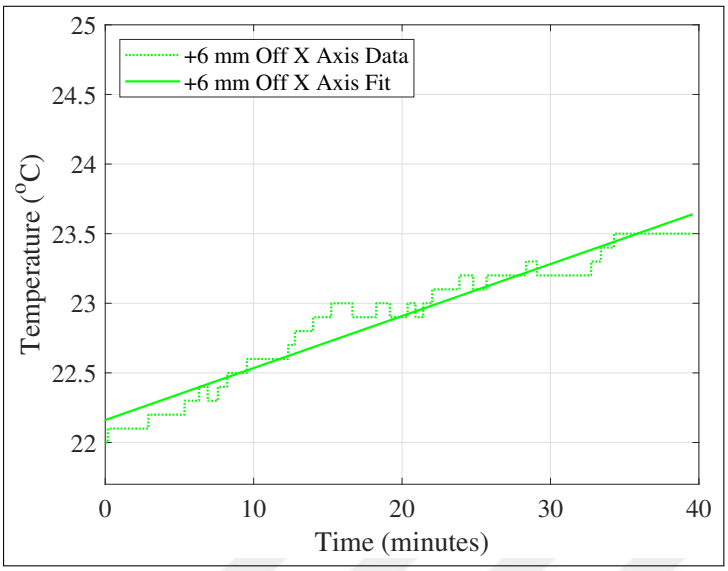


Figure 3.73 40 minute temperature rise vs. time graph during MH experiments conducted with 120 mg/mL concentration SPION using solenoid coil with round Litz wire at 0 mm axial position, +6 mm off X-axis. Temperature–time data was fitted to a line using linear regression for analyzing positional related effects.

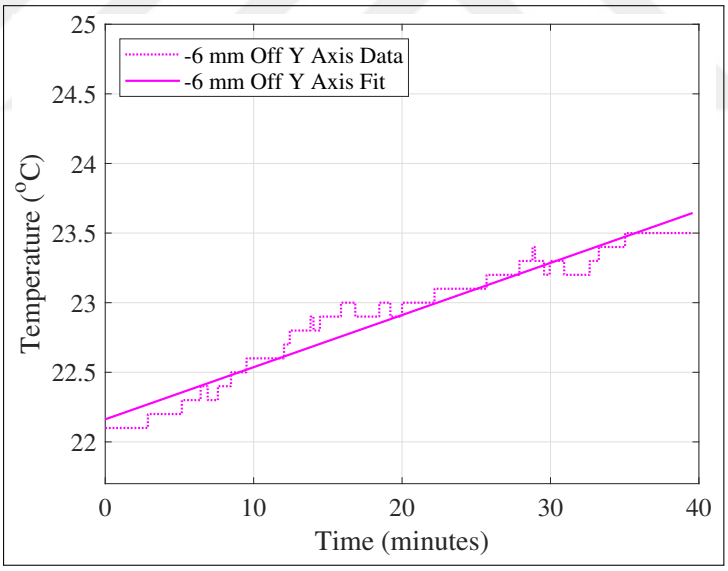


Figure 3.74 40 minute temperature rise vs. time graph during MH experiments conducted with 120 mg/mL concentration SPION using solenoid coil with round Litz wire at 0 mm axial position, −6 mm off Y-axis. Temperature–time data was fitted to a line using linear regression for analyzing positional related effects.

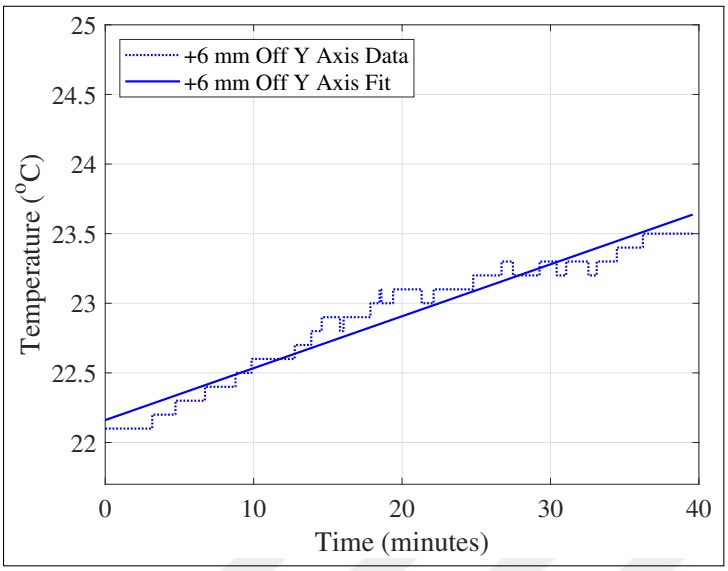


Figure 3.75 40 minute temperature rise vs. time graph during MH experiments conducted with 120 mg/mL concentration SPION using solenoid coil with round Litz wire at +6 mm axial position, +6 mm off Y-axis. Temperature–time data was fitted to a line using linear regression for analyzing positional related effects.

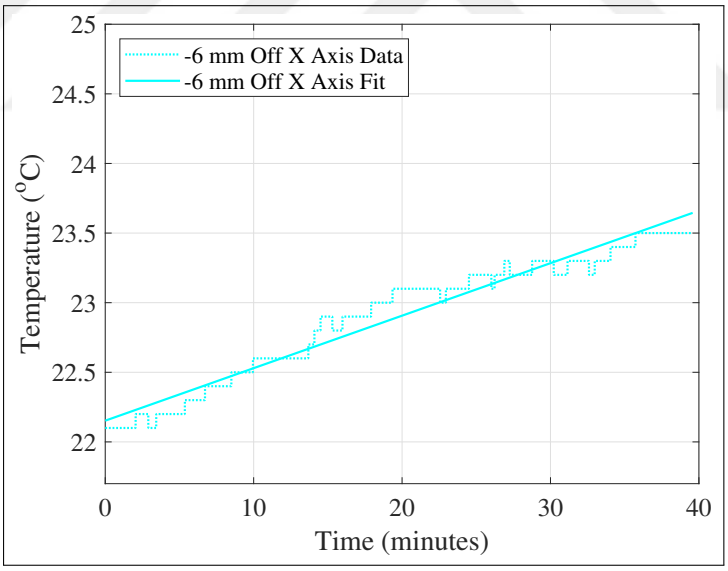


Figure 3.76 40 minute temperature rise vs. time graph during MH experiments conducted with 120 mg/mL concentration SPION using solenoid coil with round Litz wire at +6 mm axial position, −6 mm off X-axis. Temperature–time data was fitted to a line using linear regression for analyzing positional related effects.

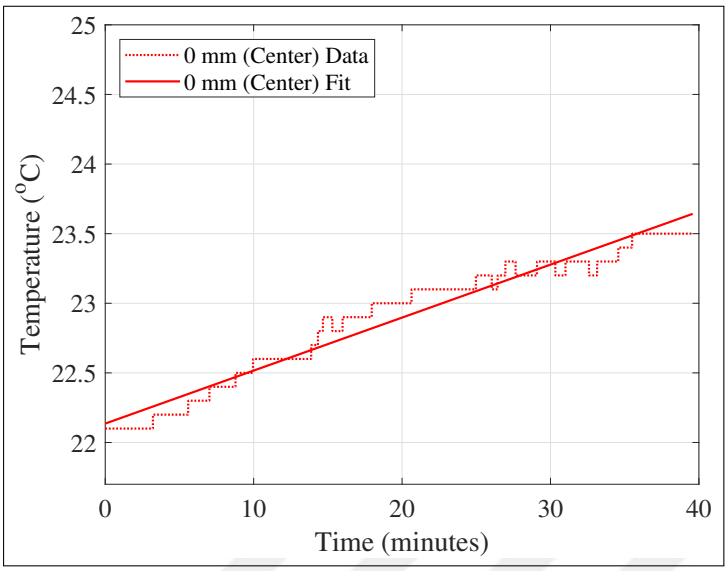


Figure 3.77 40 minute temperature rise vs. time graph during MH experiments conducted with 120 mg/mL concentration SPION using solenoid coil with round Litz wire at +6 mm axial position, 0 mm (center) position. Temperature–time data was fitted to a line using linear regression for analyzing positional related effects.

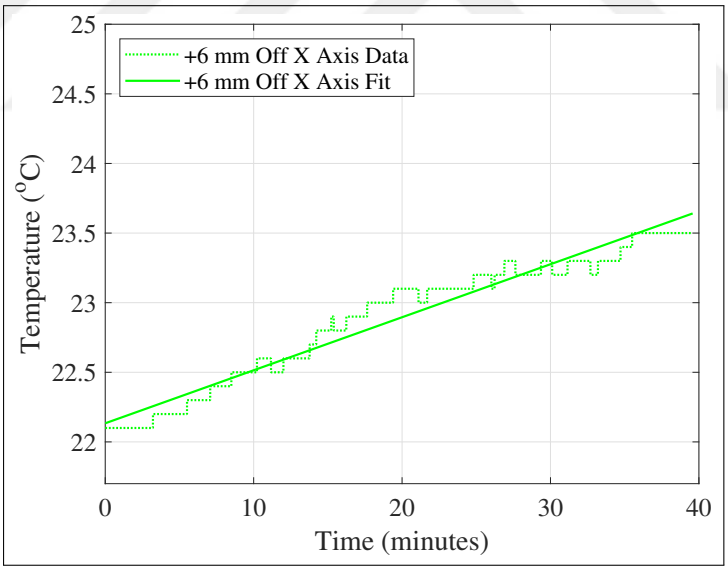


Figure 3.78 40 minute temperature rise vs. time graph during MH experiments conducted with 120 mg/mL concentration SPION using solenoid coil with round Litz wire at +6 mm axial position, +6 mm off X-axis. Temperature–time data was fitted to a line using linear regression for analyzing positional related effects.

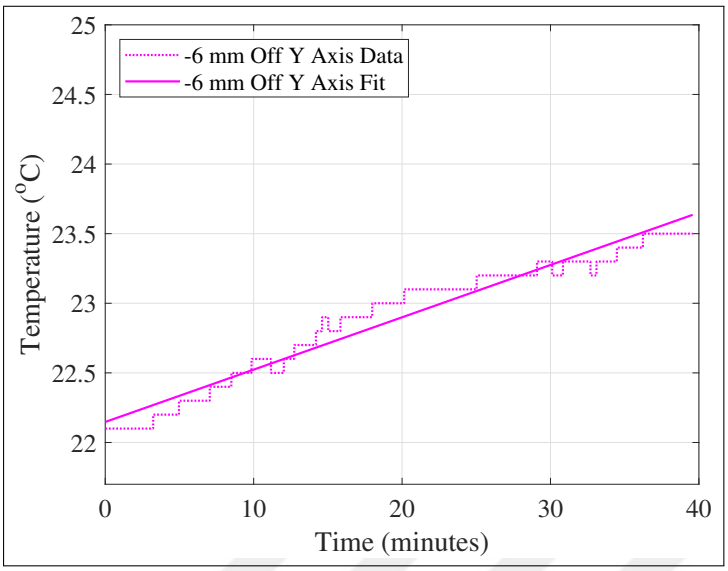


Figure 3.79 40 minute temperature rise vs. time graph during MH experiments conducted with 120 mg/mL concentration SPION using solenoid coil with round Litz wire at +6 mm axial position, −6 mm off Y-axis. Temperature–time data was fitted to a line using linear regression for analyzing positional related effects.

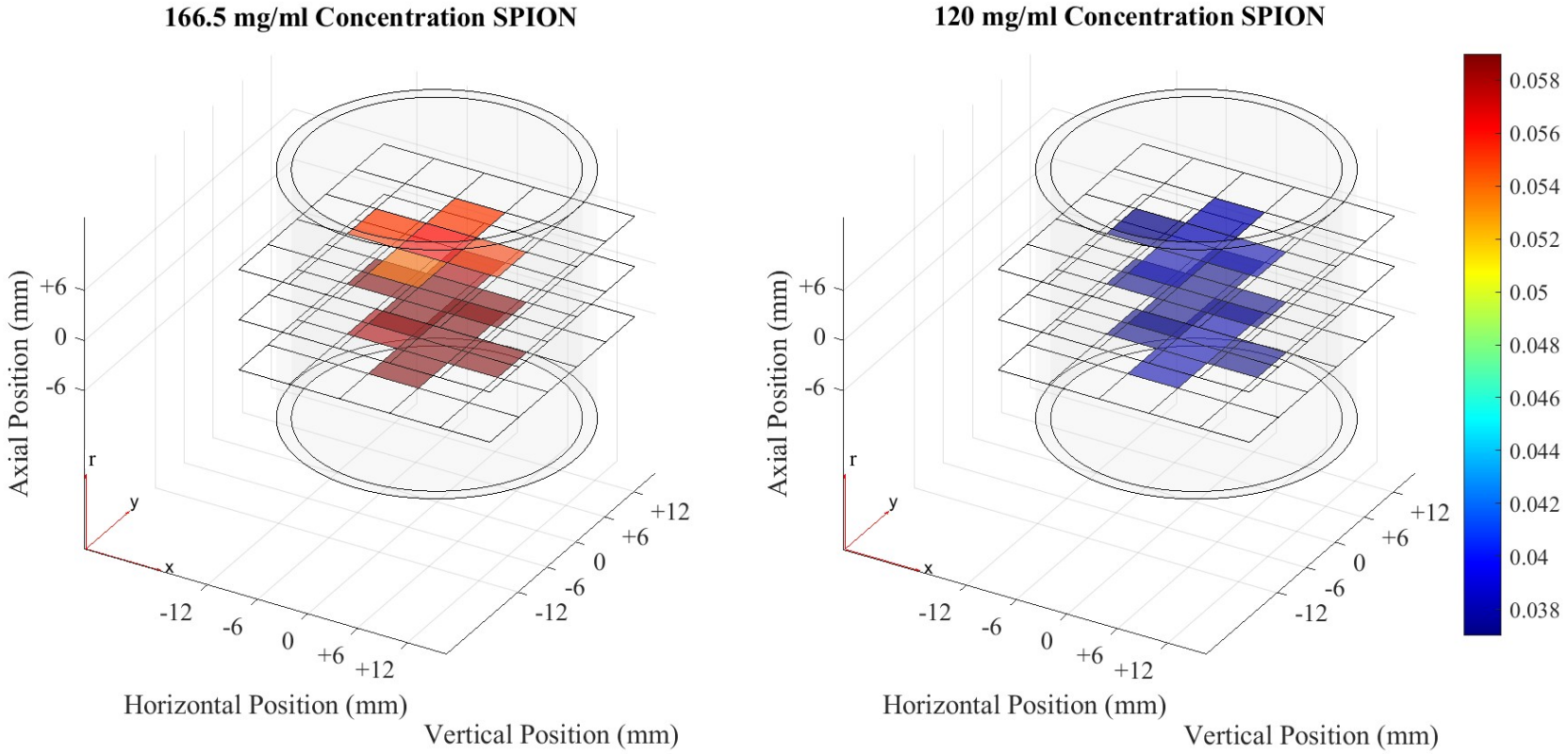


Figure 3.80 Slope of linear regression fit for 40 minute temperature rise vs. time graph during MH experiments conducted with 120 mg/mL concentration SPION using solenoid coil with round Litz wire at three axial positions inside of the coil gap and five different transverse positions.

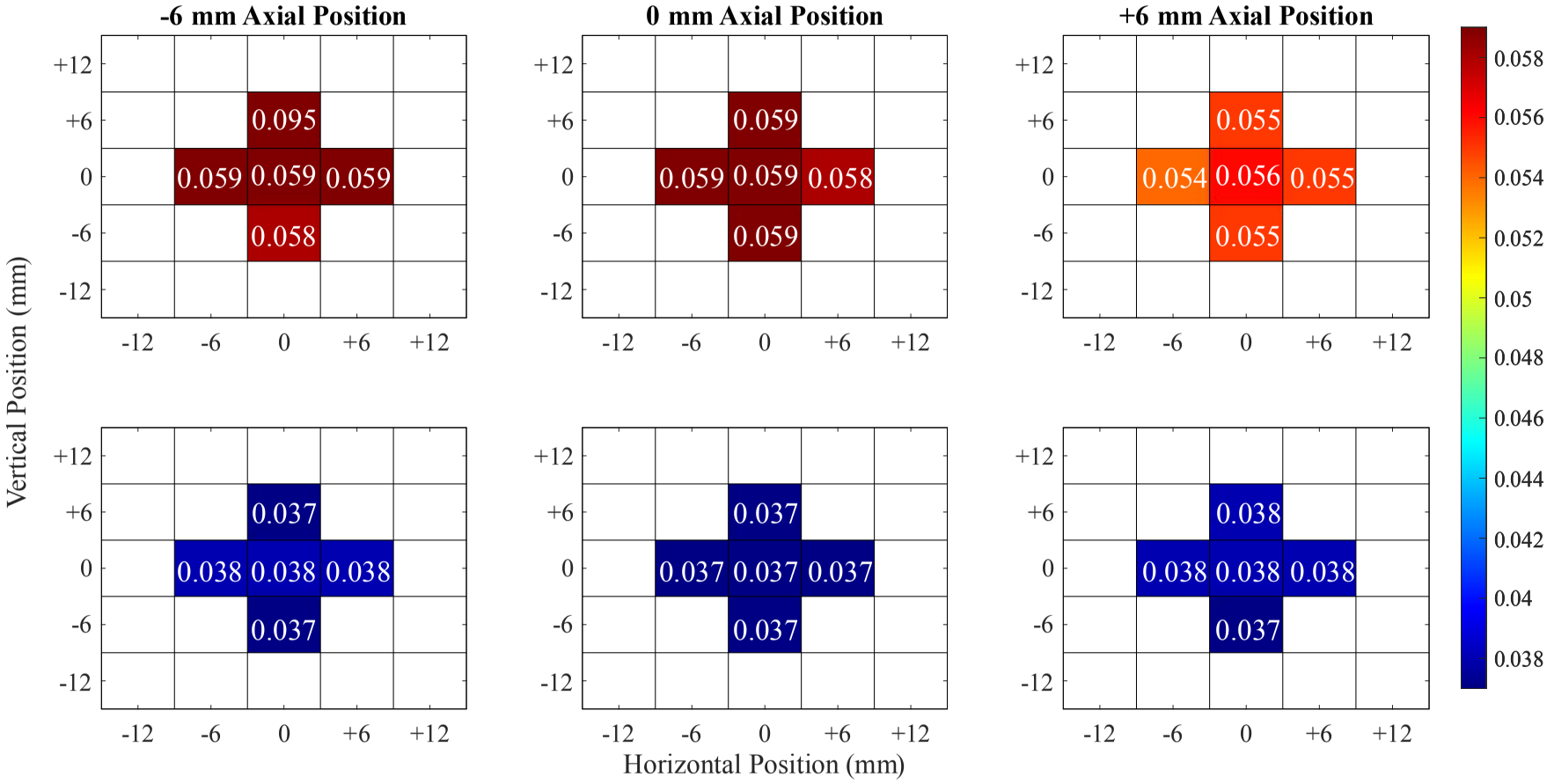


Figure 3.81 Slices showing slope of linear regression fit for 40 minute temperature rise vs. time graph during MH experiments conducted with 120 (top) and 166.5 mg/mL (bottom) SPION concentrations using solenoid coil with round Litz wire at three axial positions.

Table 3.12 Solenoid coil with round Litz wire physical implementation measured magnetic variables.

Power Levels	**sm_B (mT)**	**$smin_B$ (mT)**	**$smax_B$ (mT)**	**$srange_B$ (mT)**	**$scenter_B$ (mT)**	**$s\sigma_B$ (mT)**	**$sHom_B$**	**sP_{coil}**
100%	1.180	0.984	1.327	0.343	1.250	0.104	11.346	15.056
75%	0.958	0.784	1.121	0.337	0.967	0.085	11.270	12.634
50%	0.684	0.584	0.750	0.166	0.684	0.046	14.870	11.153
25%	0.403	0.334	0.447	0.113	0.417	0.034	11.853	5.298
10%	0.251	0.233	0.332	0.099	0.267	0.027	9.296	3.086

Table 3.13 Time–domain root mean square magnetic flux density, $tRMS_B$ values measured in mT from solenoid coil with round Litz wire design for 100% power level at three different axial positions; −6, 0, +6 mm and 21 different transverse positions; 6 mm apart at each axial position (63 positions in total, for each power level).

-6 mm Axial Position						
				X Axis		
		−12 mm	−6 mm	Center	+6 mm	+12 mm
Y Axis	+12 mm	-	1.334	1.334	1.451	-
	+6 mm	1.084	1.184	1.200	1.400	1.567
	Center	1.050	0.984	1.100	1.334	1.534
	−6 mm	1.050	1.034	1.134	1.400	1.534
	−12 mm	-	1.184	1.267	1.434	-
Center Axial Position						
				X Axis		
		−12 mm	−6 mm	Center	+6 mm	+12 mm
Y Axis	+12 mm	-	1.517	1.434	1.534	-
	+6 mm	1.384	1.300	1.234	1.417	1.584
	Center	1.250	1.167	1.250	1.300	1.584
	−6 mm	1.267	1.184	1.300	1.400	**1.617**
	−12 mm	-	1.334	1.534	1.601	-
+6 mm Axial Position						
				X Axis		
		−12 mm	−6 mm	Center	+6 mm	+12 mm
Y Axis	+12 mm	-	1.484	1.350	1.350	-
	+6 mm	1.300	1.200	1.117	1.267	1.501
	Center	1.184	1.084	1.117	1.217	1.451
	−6 mm	1.184	1.117	1.134	1.267	1.384
	−12 mm	-	1.317	1.284	1.534	-

Table 3.14 Time–domain root mean square magnetic flux density, $tRMS_B$ values measured in mT from solenoid coil with round Litz wire design for 75% power level at three different axial positions; −6, 0, +6 mm and 21 different transverse positions; 6 mm apart at each axial position (63 positions in total, for each power level).

-6 mm Axial Position						
				X Axis		
		−12 mm	−6 mm	Center	+6 mm	+12 mm
	+12 mm	-	0.917	1.017	1.034	-
	+6 mm	0.850	0.834	1.017	1.017	1.284
Y Axis	Center	0.784	0.800	0.917	1.117	1.200
	−6 mm	0.850	0.850	0.934	1.100	1.234
	−12 mm	-	0.950	1.050	1.100	-
Center Axial Position						
				X Axis		
		−12 mm	−6 mm	Center	+6 mm	+12 mm
	+12 mm	-	1.134	1.184	1.284	-
	+6 mm	1.100	0.984	0.984	1.117	1.334
Y Axis	Center	0.984	0.900	0.967	1.117	**1.350**
	−6 mm	0.984	1.017	0.967	1.100	1.300
	−12 mm	-	1.117	1.117	1.184	-
+6 mm Axial Position						
				X Axis		
		−12 mm	−6 mm	Center	+6 mm	+12 mm
	+12 mm	-	1.100	1.034	1.200	-
	+6 mm	1.000	0.934	0.950	1.017	1.167
Y Axis	Center	0.967	0.884	0.884	0.984	1.184
	−6 mm	1.017	0.950	0.950	1.050	1.217
	−12 mm	-	1.000	1.067	1.084	-

Table 3.15 Time–domain root mean square magnetic flux density, $tRMS_B$ values measured in mT from solenoid coil with round Litz wire design for 50% power level at three different axial positions; −6, 0, +6 mm and 21 different transverse positions; 6 mm apart at each axial position (63 positions in total, for each power level).

-6 mm Axial Position						
				X Axis		
		−12 mm	−6 mm	Center	+6 mm	+12 mm
	+12 mm	-	0.717	0.684	0.767	-
	+6 mm	0.584	0.684	0.634	0.784	**0.900**
Y Axis	Center	0.584	0.667	0.634	0.684	0.817
	−6 mm	0.584	0.617	0.617	0.734	0.850
	−12 mm	-	0.700	0.717	0.800	-
Center Axial Position						
				X Axis		
		−12 mm	−6 mm	Center	+6 mm	+12 mm
	+12 mm	-	0.750	0.850	0.884	-
	+6 mm	0.717	0.667	0.717	0.767	0.884
Y Axis	Center	0.667	0.750	0.684	0.750	0.884
	−6 mm	0.717	0.684	0.717	0.784	0.867
	−12 mm	-	0.750	0.800	0.884	-
+6 mm Axial Position						
				X Axis		
		−12 mm	−6 mm	Center	+6 mm	+12 mm
	+12 mm	-	0.867	0.734	0.800	-
	+6 mm	0.717	0.717	0.684	0.684	0.834
Y Axis	Center	0.734	0.634	0.650	0.750	0.800
	−6 mm	0.717	0.650	0.700	0.750	0.834
	−12 mm	-	0.734	0.767	0.800	-

Table 3.16 Time–domain root mean square magnetic flux density, $tRMS_B$ values measured in mT from solenoid coil with round Litz wire design for 25% power level at three different axial positions; −6, 0, +6 mm and 21 different transverse positions; 6 mm apart at each axial position (63 positions in total, for each power level).

-6 mm Axial Position						
				X Axis		
		−12 mm	−6 mm	Center	+6 mm	+12 mm
	+12 mm	-	0.417	0.383	0.433	-
	+6 mm	0.383	0.333	0.400	0.433	0.484
Y Axis	Center	0.367	0.333	0.367	0.383	0.467
	−6 mm	0.333	0.367	0.400	0.433	0.500
	−12 mm	-	0.417	0.367	0.450	-
Center Axial Position						
				X Axis		
		−12 mm	−6 mm	Center	+6 mm	+12 mm
	+12 mm	-	0.500	0.467	0.450	-
	+6 mm	0.383	0.433	0.433	0.450	0.550
Y Axis	Center	0.417	0.400	0.417	0.450	**0.567**
	−6 mm	0.417	0.383	0.450	0.433	0.500
	−12 mm	-	0.433	0.467	0.500	-
+6 mm Axial Position						
				X Axis		
		−12 mm	−6 mm	Center	+6 mm	+12 mm
	+12 mm	-	0.467	0.433	0.433	-
	+6 mm	0.400	0.400	0.400	0.500	0.500
Y Axis	Center	0.367	0.400	0.450	0.400	0.500
	−6 mm	0.383	0.383	0.367	0.433	0.500
	−12 mm	-	0.383	0.417	0.467	-

Table 3.17 Time–domain root mean square magnetic flux density, $tRMS_B$ values measured in mT from solenoid coil with round Litz wire design for 10% power level at three different axial positions; −6, 0, +6 mm and 21 different transverse positions; 6 mm apart at each axial position (63 positions in total, for each power level).

-6 mm Axial Position						
				X Axis		
		−12 mm	−6 mm	Center	+6 mm	+12 mm
	+12 mm	-	0.250	0.250	0.233	-
	+6 mm	0.267	0.250	0.233	0.367	0.300
Y Axis	Center	0.300	0.250	0.233	0.233	0.283
	−6 mm	0.233	0.267	0.233	0.267	0.283
	−12 mm	-	0.267	0.233	0.300	-
Center Axial Position						
				X Axis		
		−12 mm	−6 mm	Center	+6 mm	+12 mm
	+12 mm	-	0.283	0.267	0.283	-
	+6 mm	0.233	0.250	0.250	0.250	0.283
Y Axis	Center	0.233	0.250	0.267	0.267	**0.400**
	−6 mm	0.233	0.267	0.233	0.267	0.367
	−12 mm	-	0.267	0.233	0.267	-
+6 mm Axial Position						
				X Axis		
		−12 mm	−6 mm	Center	+6 mm	+12 mm
	+12 mm	-	0.267	0.250	0.300	-
	+6 mm	0.283	0.250	0.233	0.250	0.267
Y Axis	Center	0.267	0.267	0.250	0.333	0.333
	−6 mm	0.250	0.267	0.250	0.300	0.333
	−2 mm	-	0.267	0.300	0.300	-

Table 3.18 Amount of temperature rise, Δ_T values measured in ^{o}C from 166.5 mg/mL concentration MNPs inside of solenoid coil with round Litz wire design at three axial positions inside of the coil gap and five different transverse positions.

-6 mm Axial Position				
			X Axis	
		−6 mm	Center	+6 mm
	+6 mm	-	**2.2**	-
Y Axis	Center	**2.2**	**2.2**	2.1
	−6 mm	-	**2.2**	-
Center Axial Position				
			X Axis	
		−6 mm	Center	+6 mm
	+6 mm	-	2.1	-
Y Axis	Center	2.1	**2.2**	2.1
	−6 mm	-	**2.2**	-
+6 mm Axial Position				
			X Axis	
		−6 mm	Center	+6 mm
	+6 mm	-	**2.2**	-
Y Axis	Center	2.1	2.1	2.1
	−6 mm	-	2.1	-

Table 3.19 Amount of temperature rise, Δ_T values measured in ^{o}C from 120 mg/mL concentration MNPs inside of solenoid coil with round Litz wire design at three axial positions inside of the coil gap and five different transverse positions.

-6 mm Axial Position				
			X Axis	
		−6 mm	Center	+6 mm
	+6 mm	-	**1.5**	-
Y Axis	Center	**1.5**	1.4	**1.5**
	−6 mm	-	**1.5**	-
Center Axial Position				
			X Axis	
		−6 mm	Center	+6 mm
	+6 mm	-	**1.5**	-
Y Axis	Center	**1.5**	1.4	1.4
	−6 mm	-	1.4	-
+6 mm Axial Position				
			X Axis	
		−6 mm	Center	+6 mm
	+6 mm	-	1.4	-
Y Axis	Center	1.4	1.4	1.4
	−6 mm	-	1.4	-

Table 3.20 Slope of linear regression fit for 40 minute temperature rise vs. time graph during MH experiments conducted with 166.5 mg/mL concentration SPION using solenoid coil with round Litz wire at three axial positions inside of the coil gap and five different transverse positions.

-6 mm Axial Position				
			X Axis	
		−6 mm	Center	+6 mm
	+6 mm	-	**0.059**	-
Y Axis	Center	**0.059**	**0.059**	**0.059**
	−6 mm	-	0.058	-
Center Axial Position				
			X Axis	
		−6 mm	Center	+6 mm
	+6 mm	-	**0.059**	-
Y Axis	Center	**0.059**	**0.059**	0.058
	−6 mm	-	**0.059**	-
+6 mm Axial Position				
			X Axis	
		−6 mm	Center	+6 mm
	+6 mm	-	0.055	-
Y Axis	Center	0.054	0.056	0.055
	−6 mm	-	0.055	-

Table 3.21 Slope of linear regression fit for 40 minute temperature rise vs. time graph during MH experiments conducted with 120 mg/mL concentration SPION using solenoid coil with round Litz wire at three axial positions inside of the coil gap and five different transverse positions.

-6 mm Axial Position				
			X Axis	
		−6 mm	Center	+6 mm
	+6 mm	-	0.037	-
Y Axis	Center	**0.038**	**0.038**	**0.038**
	−6 mm	-	0.037	-
Center Axial Position				
			X Axis	
		−6 mm	Center	+6 mm
	+6 mm	-	0.037	-
Y Axis	Center	0.037	0.037	0.037
	−6 mm	-	0.037	-
+6 mm Axial Position				
			X Axis	
		−6 mm	Center	+6 mm
	+6 mm	-	**0.038**	-
Y Axis	Center	**0.038**	**0.038**	**0.038**
	−6 mm	-	0.037	-

Table 3.22 Solenoid coil with round Litz wire physical implementation measured thermal variables.

	$\mathbf{sm_T}$ (^{o} C)	$\mathbf{smin_T}$ (^{o} C)	$\mathbf{smax_T}$ (^{o} C)	$\mathbf{srange_T}$ (^{o} C)	$\mathbf{scenter_T}$ (^{o} C)	$\mathbf{s\sigma_T}$ (^{o} C)	$\mathbf{sHom_T}$	$\mathbf{sT_{coil}}$
166.5 mg/mL	2.15	2.10	2.20	0.10	2.20	0.06	35.83	78.83
120 mg/mL	1.44	1.40	1.50	0.10	1.40	0.05	28.80	43.20

3.3. Helmholtz Coil with Round Wire Measurements

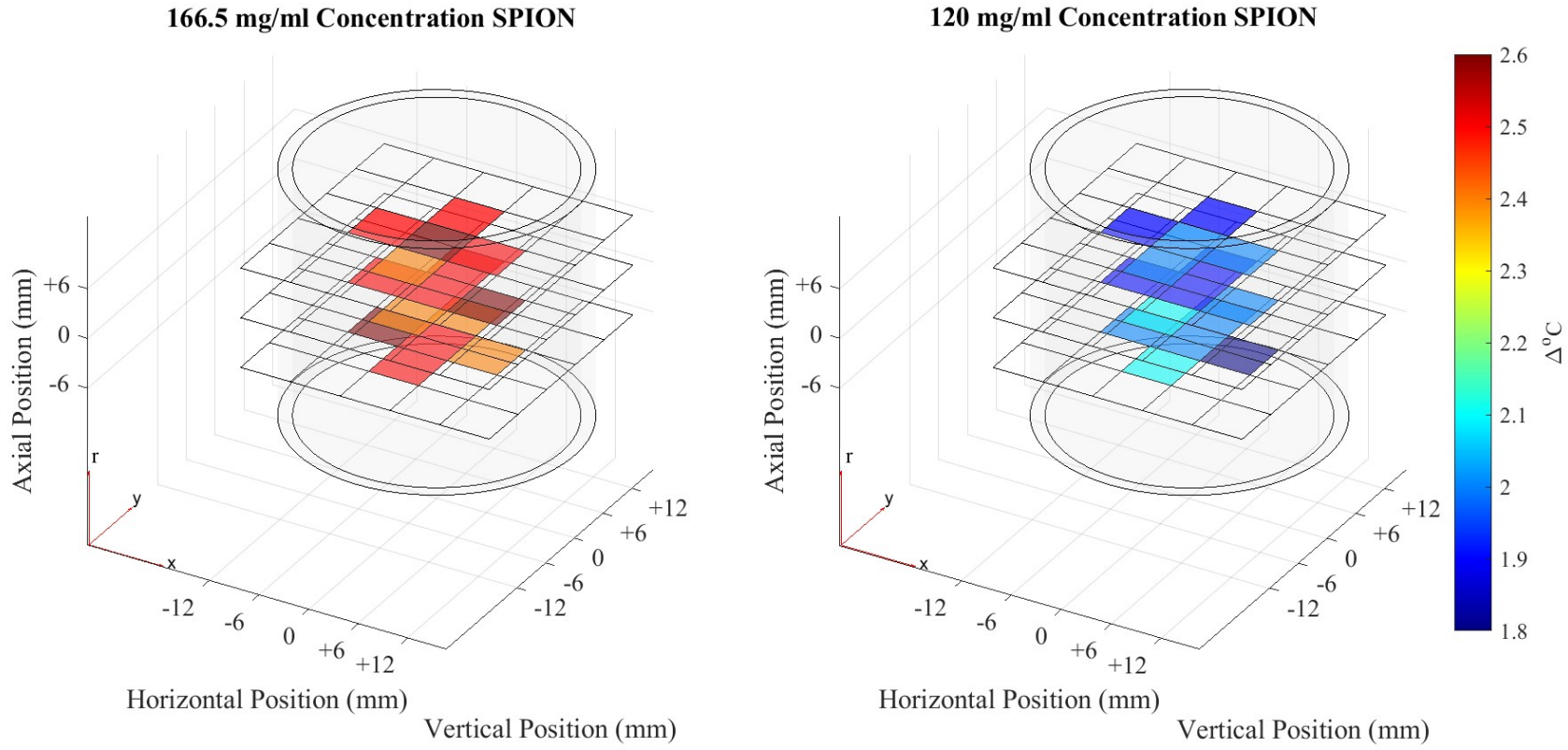


Figure 3.82 Amount of temperature rise, ΔT measured from two different SPION concentrations inside of Helmholtz coil with round wire design at three different axial positions; -12, 0, $+12$ mm and five different transverse positions; 0, -6 and $+6$ mm horizontally, -6 and $+6$ mm vertically for each axial position (15 positions in total) inside of the coil gap.

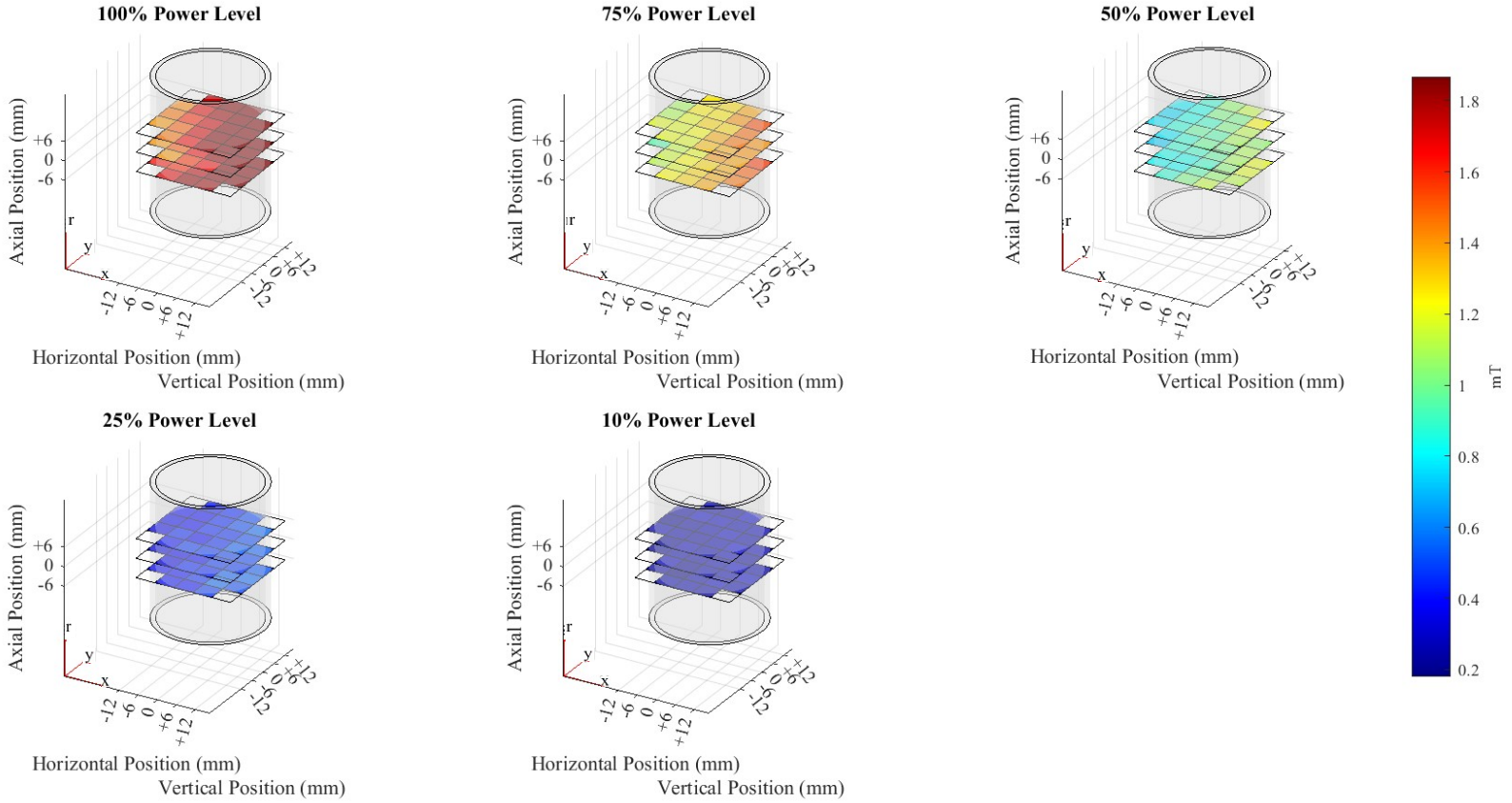


Figure 3.83 Time–domain root mean square magnetic flux density, $tRMS_B$ values measured from Helmholtz coil with round wire design for all power levels at three different axial positions; −6, 0, +6 mm and 21 different transverse positions; 6 mm apart at each axial position (63 positions in total, for each power level).

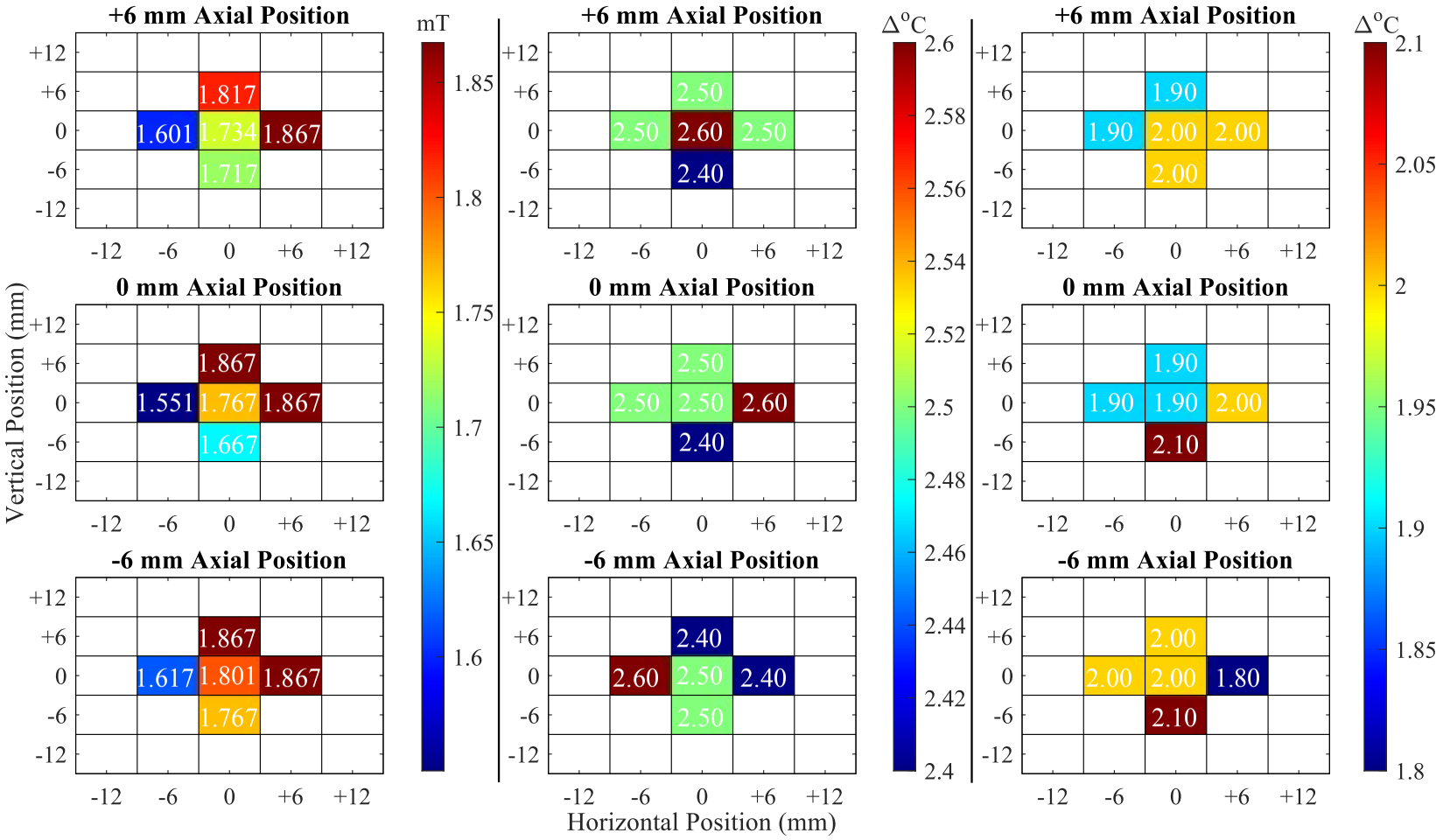


Figure 3.84 Time–domain root mean square magnetic flux density, $tRMS_B$ (left) and corresponding amount of temperature rise, ΔT with 166.5 (middle) and 120 mg/mL (right) SPION concentration values measured from Helmholtz coil with round wire design for 100% power level at three different axial positions; −6, 0, +6 mm.

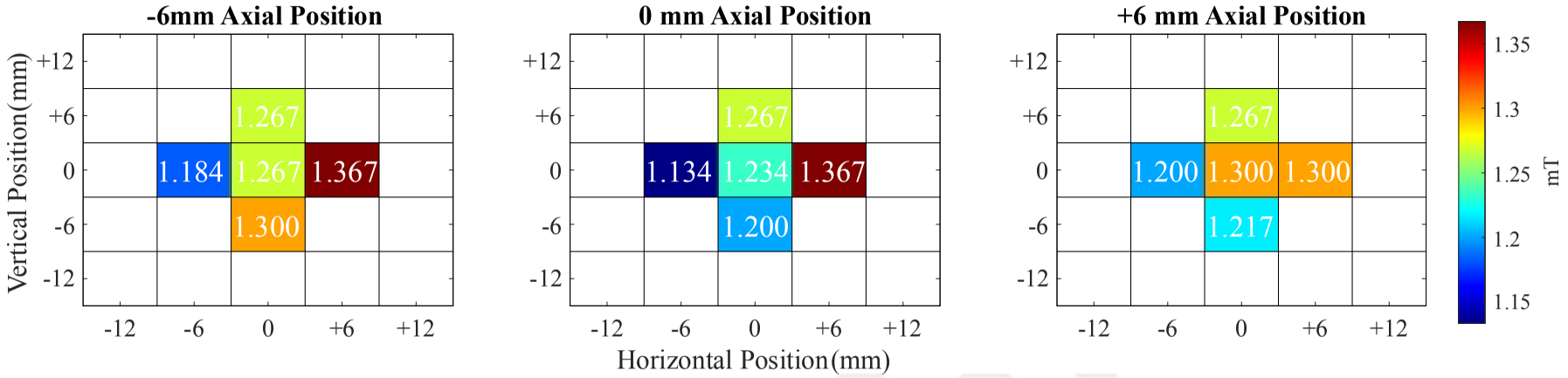


Figure 3.85 Time–domain root mean square magnetic flux density, $tRMS_B$ (top) values measured from Helmholtz coil with round wire design for 75% power level at three different axial positions; −6, 0, +6 mm.

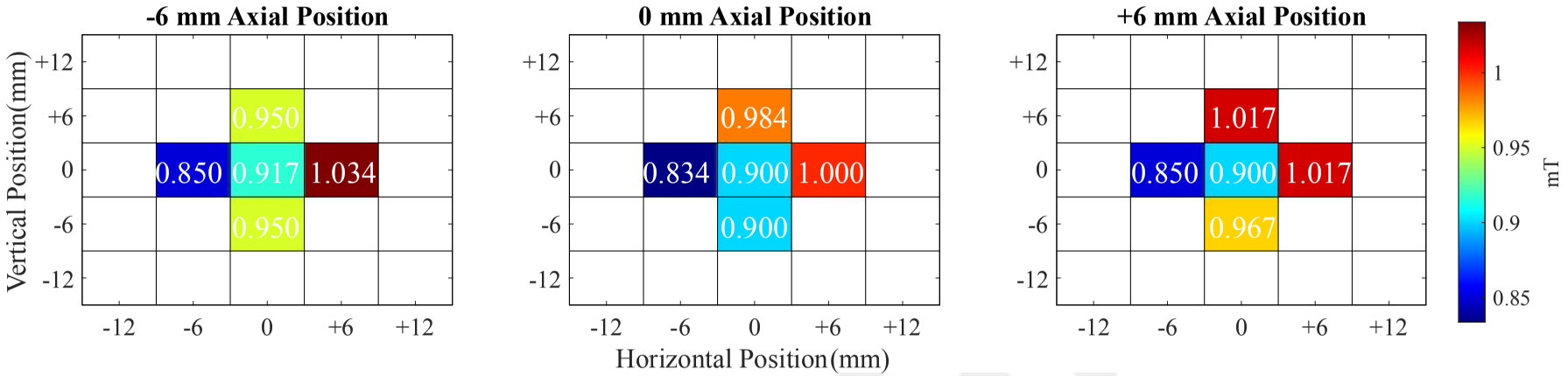


Figure 3.86 Time–domain root mean square magnetic flux density, $tRMS_B$ (top) values measured from Helmholtz coil with round wire design for 50% power level at three different axial positions; −6, 0, +6 mm.

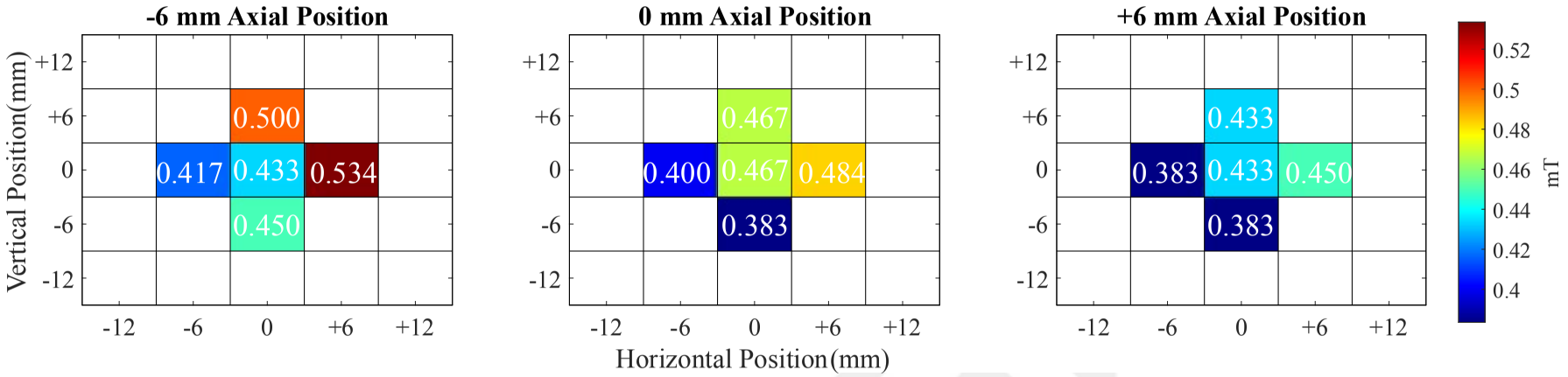


Figure 3.87 Time–domain root mean square magnetic flux density, $tRMS_B$ (top) values measured from Helmholtz coil with round wire design for 25% power level at three different axial positions; −6, 0, +6 mm.

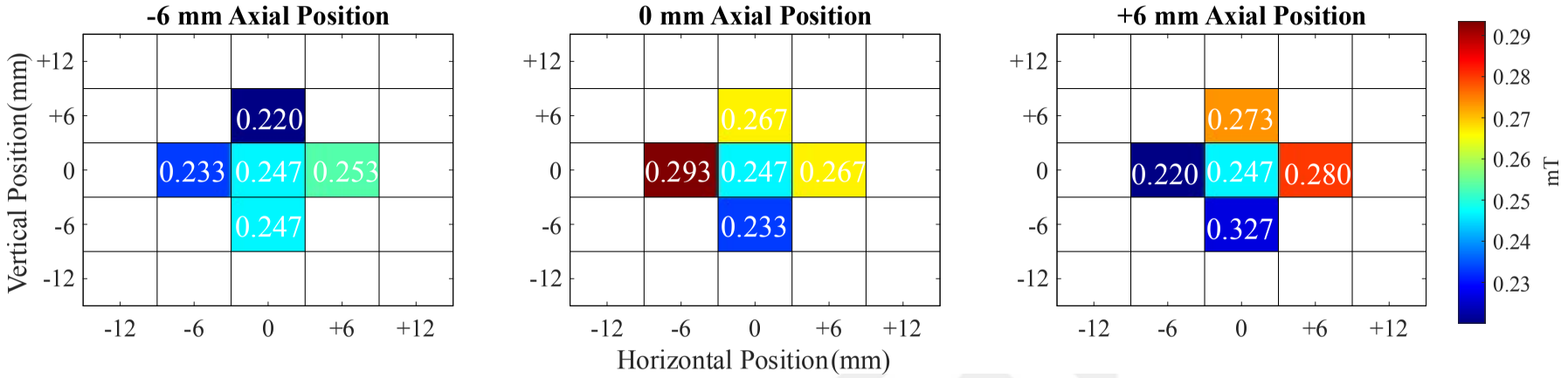


Figure 3.88 Time–domain root mean square magnetic flux density, $tRMS_B$ (top) values measured from Helmholtz coil with round wire design for 10% power level at three different axial positions; −6, 0, +6 mm.

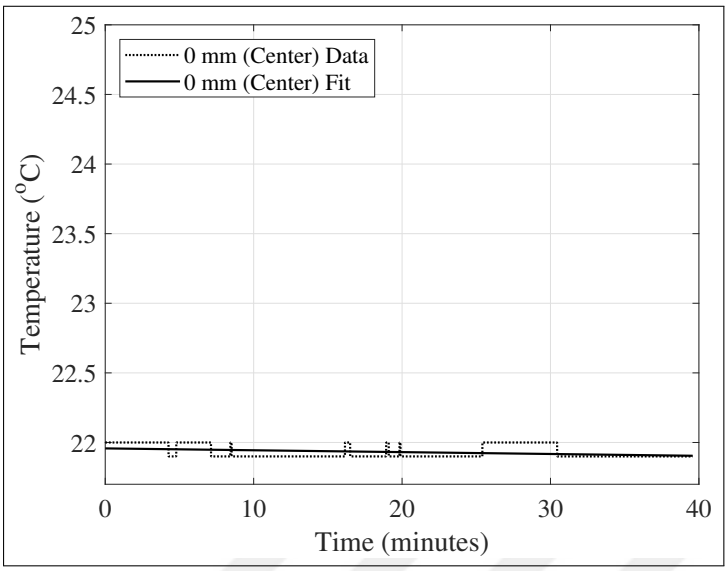


Figure 3.89 40 minute temperature vs. time graph during MH experiments conducted with distilled water as the control experiment using Helmholtz coil with round wire at 0 mm axial position, 0 mm (center) position. Temperature–time data was fitted to a line using linear regression for analyzing positional related effects.

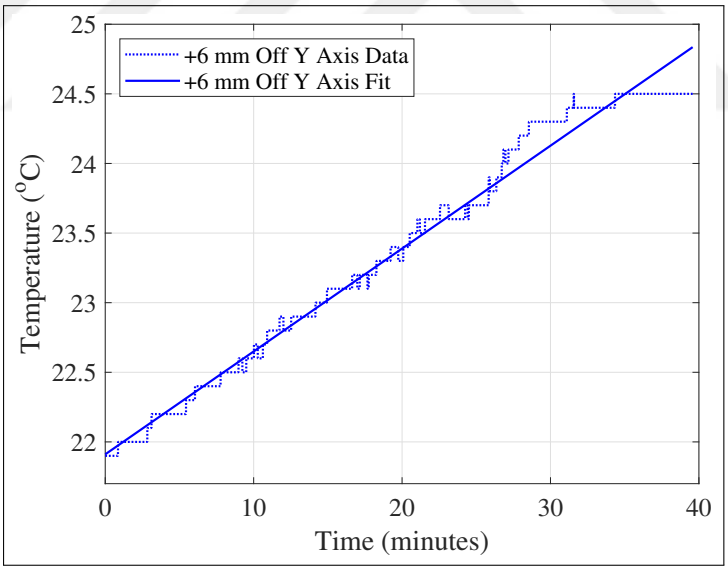


Figure 3.90 40 minute temperature rise vs. time graph during MH experiments conducted with 166.5 mg/mL concentration SPION using Helmholtz coil with round wire at −6 mm axial position, +6 mm off Y-axis. Temperature–time data was fitted to a line using linear regression for analyzing positional related effects.

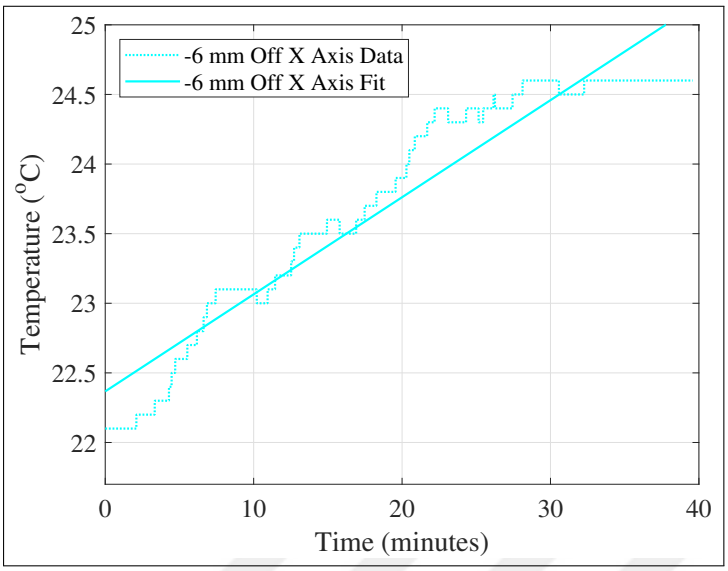


Figure 3.91 40 minute temperature rise vs. time graph during MH experiments conducted with 166.5 mg/mL concentration SPION using Helmholtz coil with round wire at −6 mm axial position, −6 mm off X-axis. Temperature–time data was fitted to a line using linear regression for analyzing positional related effects.

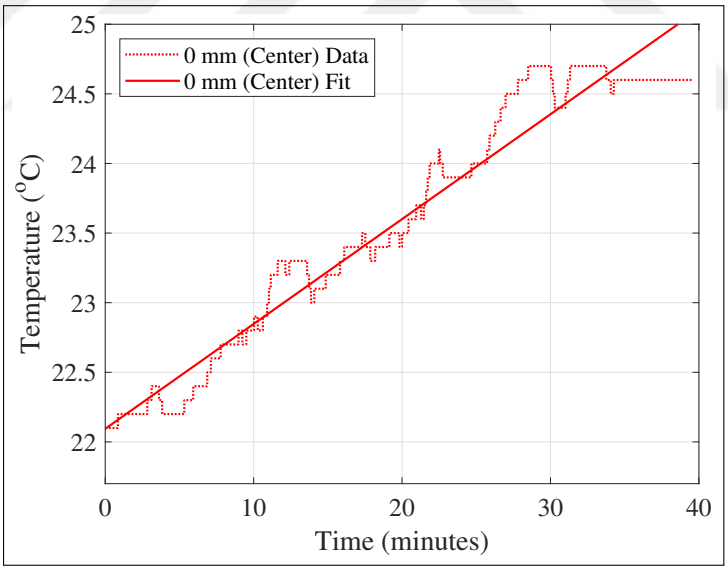


Figure 3.92 40 minute temperature rise vs. time graph during MH experiments conducted with 166.5 mg/mL concentration SPION using Helmholtz coil with round wire at −6 mm axial position, 0 mm (center) position. Temperature–time data was fitted to a line using linear regression for analyzing positional related effects.

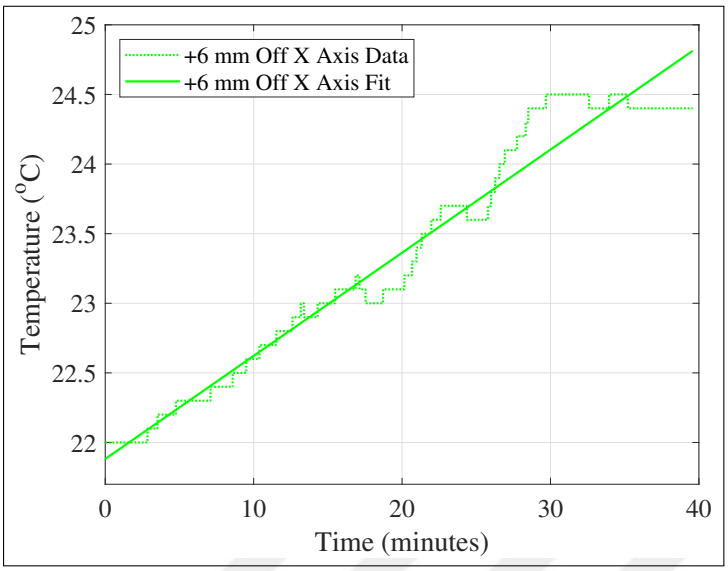


Figure 3.93 40 minute temperature rise vs. time graph during MH experiments conducted with 166.5 mg/mL concentration SPION using Helmholtz coil with round wire at −6 mm axial position, +6 mm off X-axis. Temperature–time data was fitted to a line using linear regression for analyzing positional related effects.

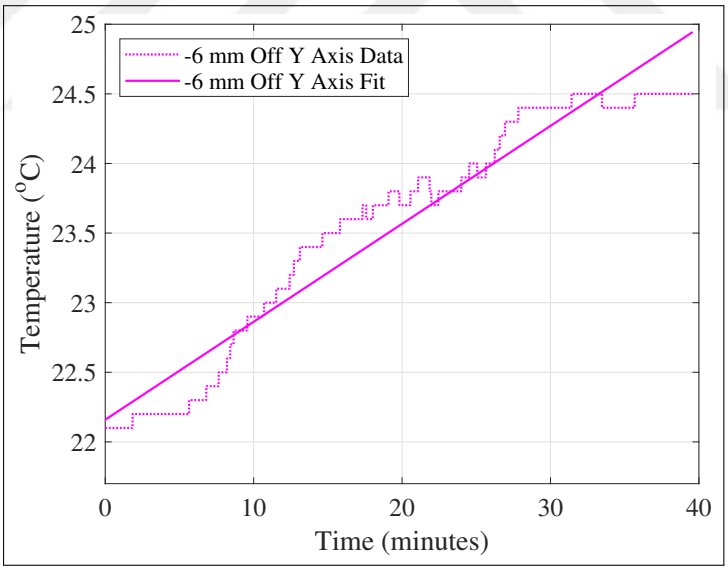


Figure 3.94 40 minute temperature rise vs. time graph during MH experiments conducted with 166.5 mg/mL concentration SPION using Helmholtz coil with round wire at −6 mm axial position, −6 mm off Y-axis. Temperature–time data was fitted to a line using linear regression for analyzing positional related effects.

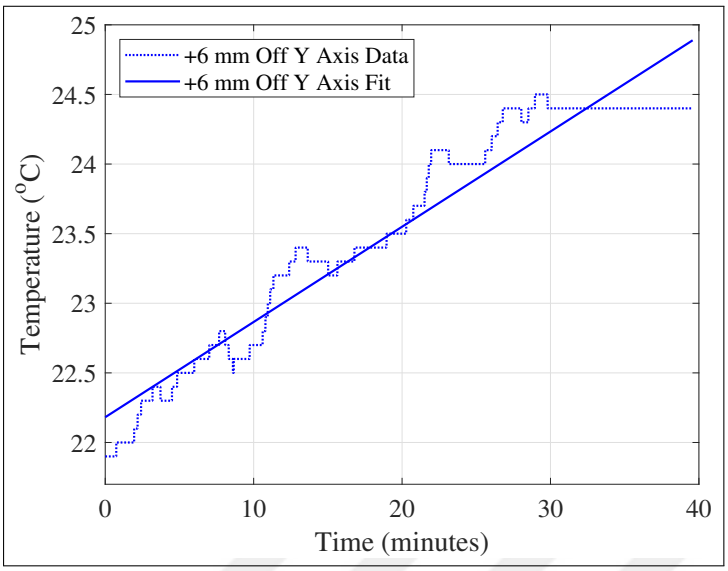


Figure 3.95 40 minute temperature rise vs. time graph during MH experiments conducted with 166.5 mg/mL concentration SPION using Helmholtz coil with round wire at 0 mm axial position, +6 mm off Y-axis. Temperature–time data was fitted to a line using linear regression for analyzing positional related effects.

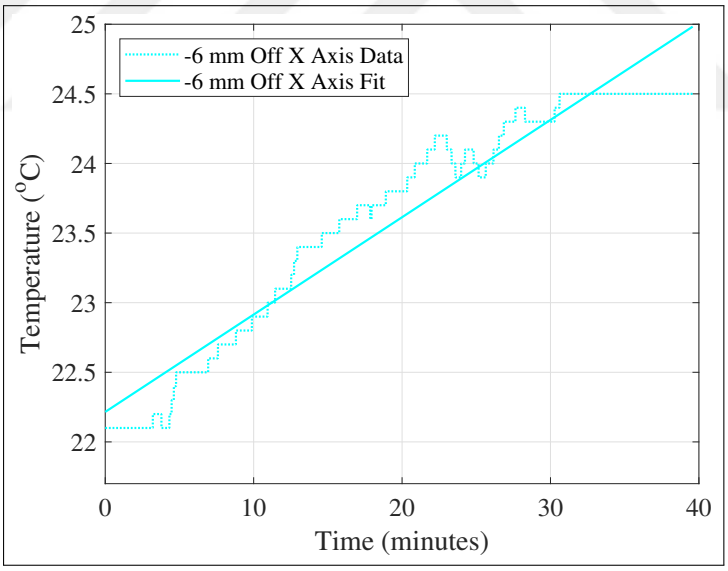


Figure 3.96 40 minute temperature rise vs. time graph during MH experiments conducted with 166.5 mg/mL concentration SPION using Helmholtz coil with round wire at 0 mm axial position, −6 mm off X-axis. Temperature–time data was fitted to a line using linear regression for analyzing positional related effects.

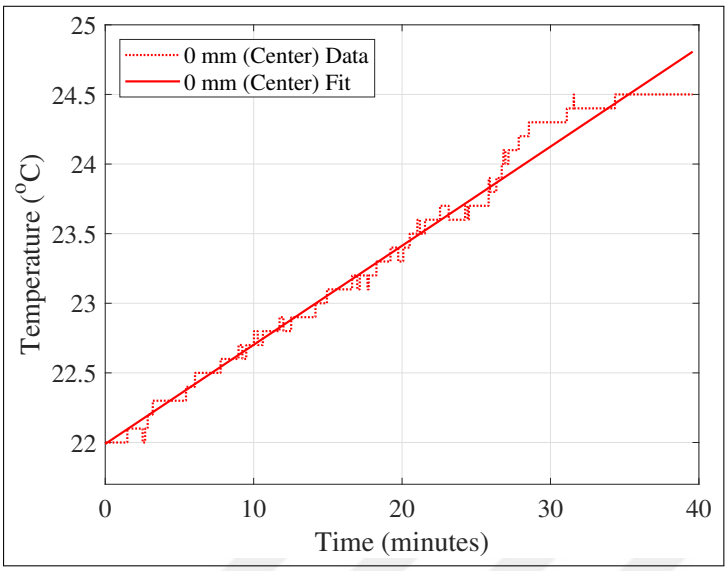


Figure 3.97 40 minute temperature rise vs. time graph during MH experiments conducted with 166.5 mg/mL concentration SPION using Helmholtz coil with round wire at 0 mm axial position, 0 mm (center) position. Temperature–time data was fitted to a line using linear regression for analyzing positional related effects.

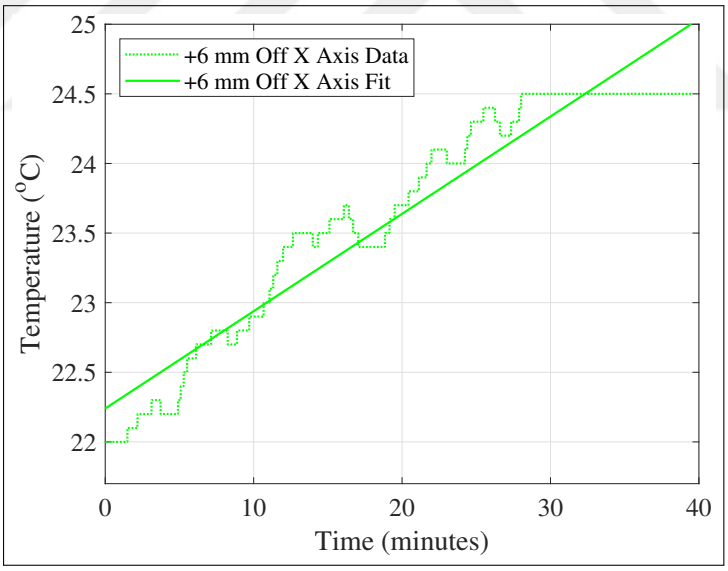


Figure 3.98 40 minute temperature rise vs. time graph during MH experiments conducted with 166.5 mg/mL concentration SPION using Helmholtz coil with round wire at 0 mm axial position, +6 mm off X-axis. Temperature–time data was fitted to a line using linear regression for analyzing positional related effects.

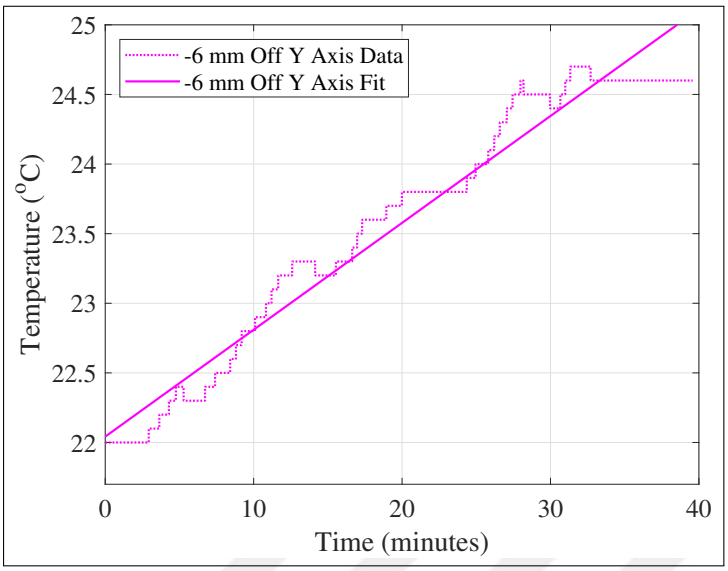


Figure 3.99 40 minute temperature rise vs. time graph during MH experiments conducted with 166.5 mg/mL concentration SPION using Helmholtz coil with round wire at 0 mm axial position, −6 mm off Y-axis. Temperature–time data was fitted to a line using linear regression for analyzing positional related effects.

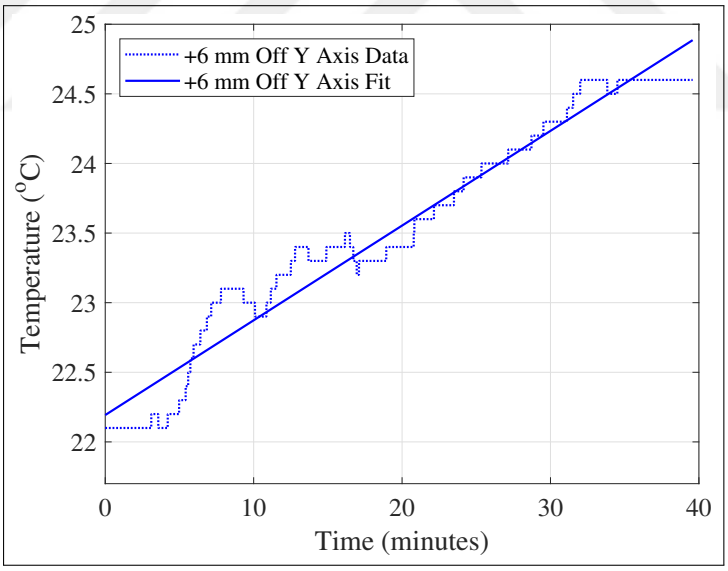


Figure 3.100 40 minute temperature rise vs. time graph during MH experiments conducted with 166.5 mg/mL concentration SPION using Helmholtz coil with round wire at +6 mm axial position, +6 mm off Y-axis. Temperature–time data was fitted to a line using linear regression for analyzing positional related effects.

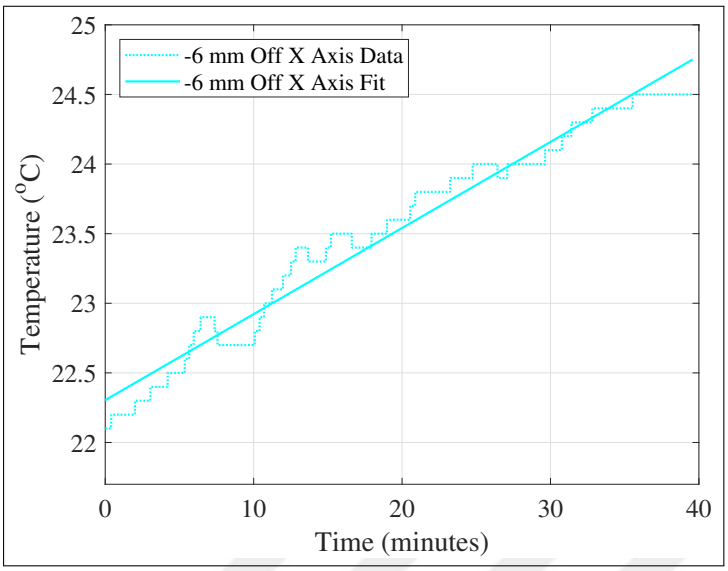


Figure 3.101 40 minute temperature rise vs. time graph during MH experiments conducted with 166.5 mg/mL concentration SPION using Helmholtz coil with round wire at +6 mm axial position, −6 mm off X-axis. Temperature–time data was fitted to a line using linear regression for analyzing positional related effects.

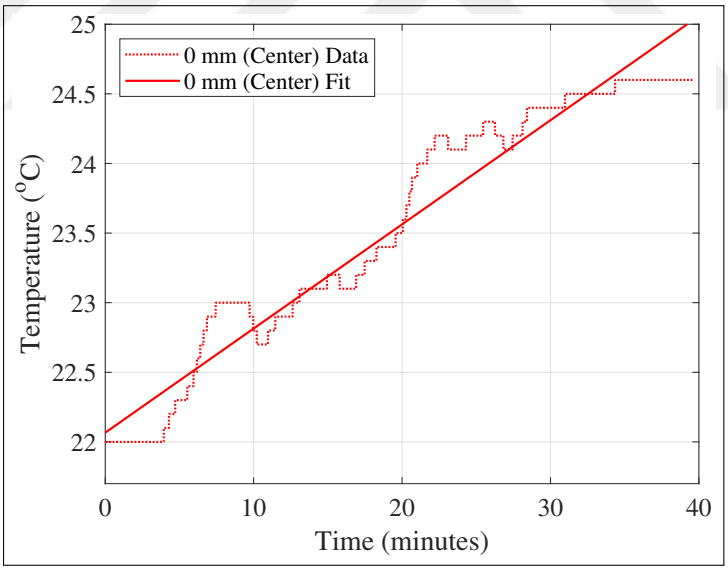


Figure 3.102 40 minute temperature rise vs. time graph during MH experiments conducted with 166.5 mg/mL concentration SPION using Helmholtz coil with round wire at +6 mm axial position, 0 mm (center) position. Temperature–time data was fitted to a line using linear regression for analyzing positional related effects.

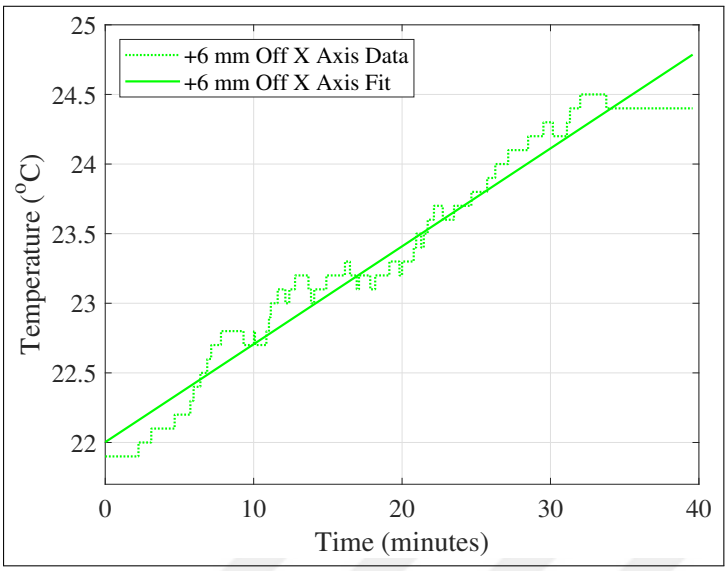


Figure 3.103 40 minute temperature rise vs. time graph during MH experiments conducted with 166.5 mg/mL concentration SPION using Helmholtz coil with round wire at +6 mm axial position, +6 mm off X-axis. Temperature–time data was fitted to a line using linear regression for analyzing positional related effects.

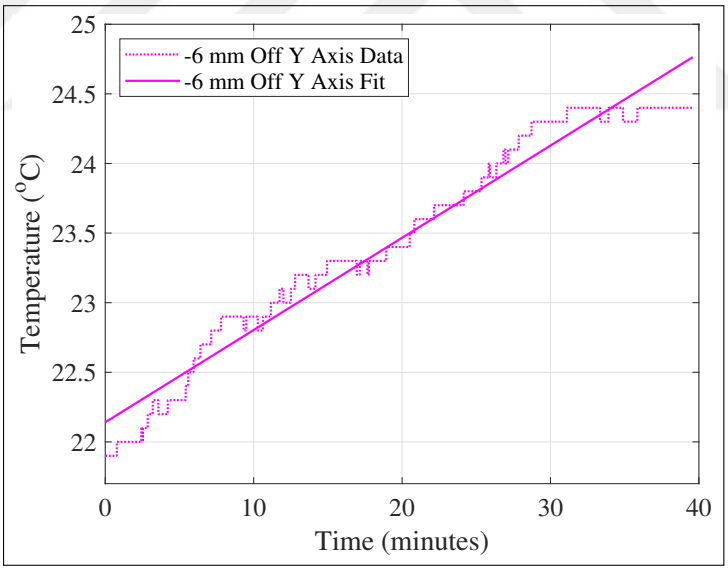


Figure 3.104 40 minute temperature rise vs. time graph during MH experiments conducted with 166.5 mg/mL concentration SPION using Helmholtz coil with round wire at +6 mm axial position, −6 mm off Y-axis. Temperature–time data was fitted to a line using linear regression for analyzing positional related effects.

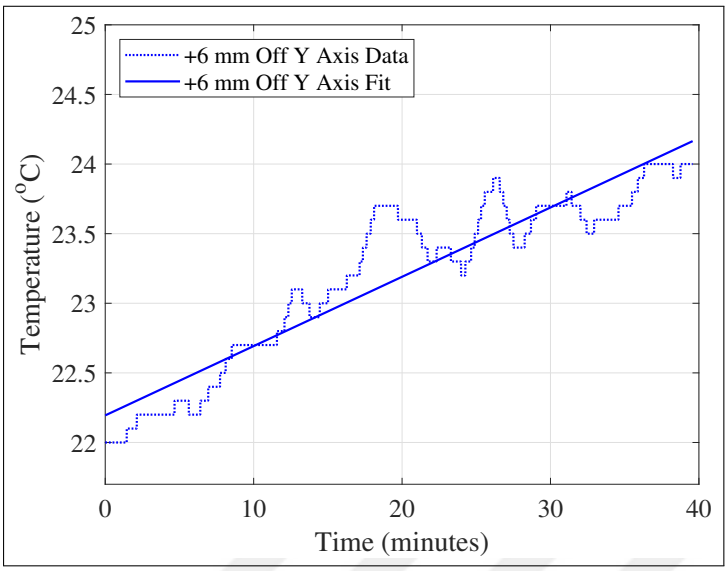


Figure 3.105 40 minute temperature rise vs. time graph during MH experiments conducted with 120 mg/mL concentration SPION using Helmholtz coil with round wire at −6 mm axial position, +6 mm off Y-axis. Temperature–time data was fitted to a line using linear regression for analyzing positional related effects.

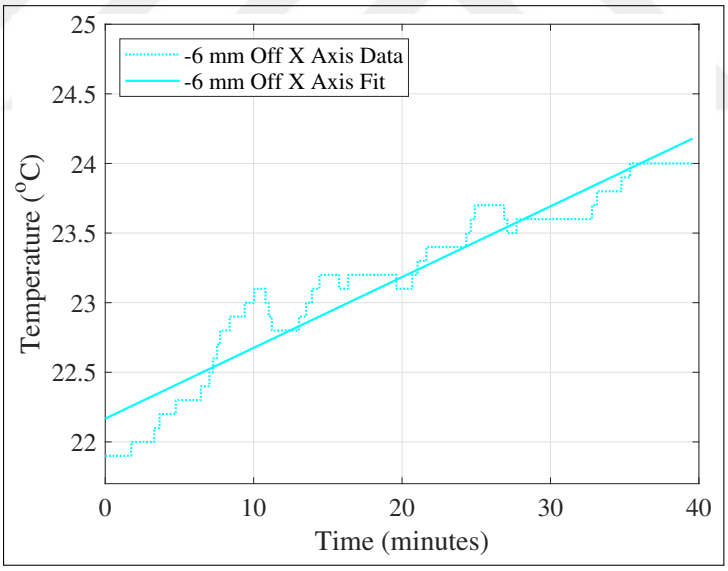


Figure 3.106 40 minute temperature rise vs. time graph during MH experiments conducted with 120 mg/mL concentration SPION using Helmholtz coil with round wire at −6 mm axial position, −6 mm off X-axis. Temperature–time data was fitted to a line using linear regression for analyzing positional related effects.

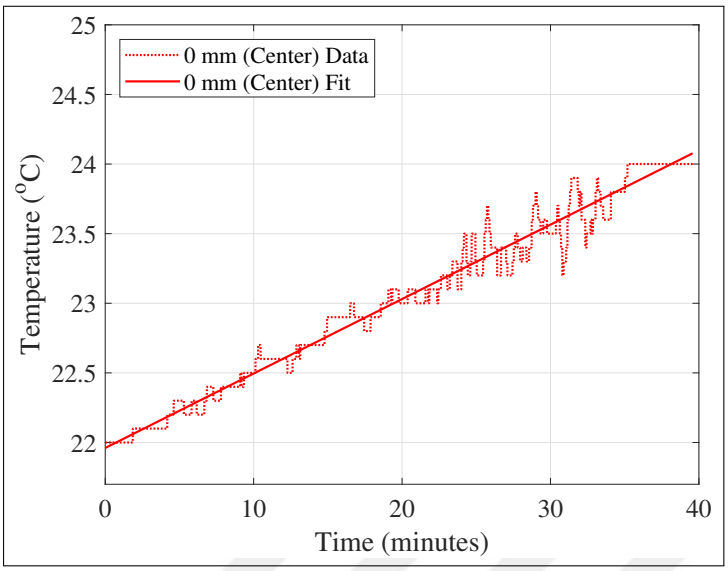


Figure 3.107 40 minute temperature rise vs. time graph during MH experiments conducted with 120 mg/mL concentration SPION using Helmholtz coil with round wire at −6 mm axial position, 0 mm (center) position. Temperature–time data was fitted to a line using linear regression for analyzing positional related effects.

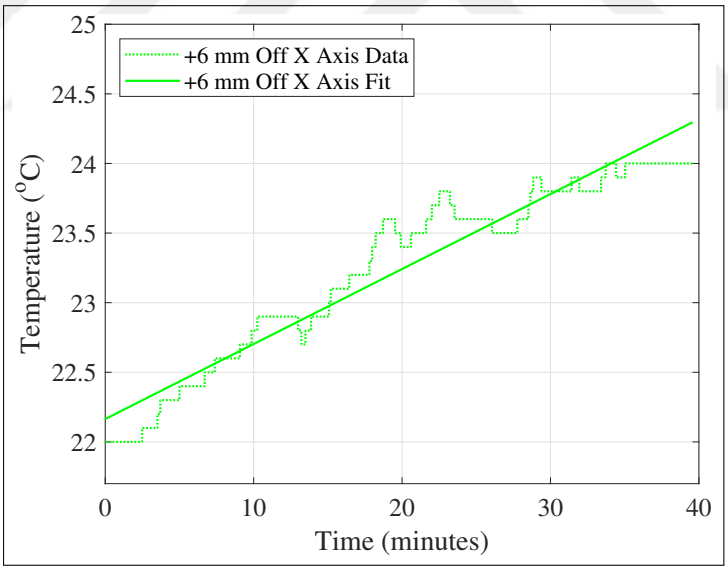


Figure 3.108 40 minute temperature rise vs. time graph during MH experiments conducted with 120 mg/mL concentration SPION using Helmholtz coil with round wire at −6 mm axial position, +6 mm off X-axis. Temperature–time data was fitted to a line using linear regression for analyzing positional related effects.

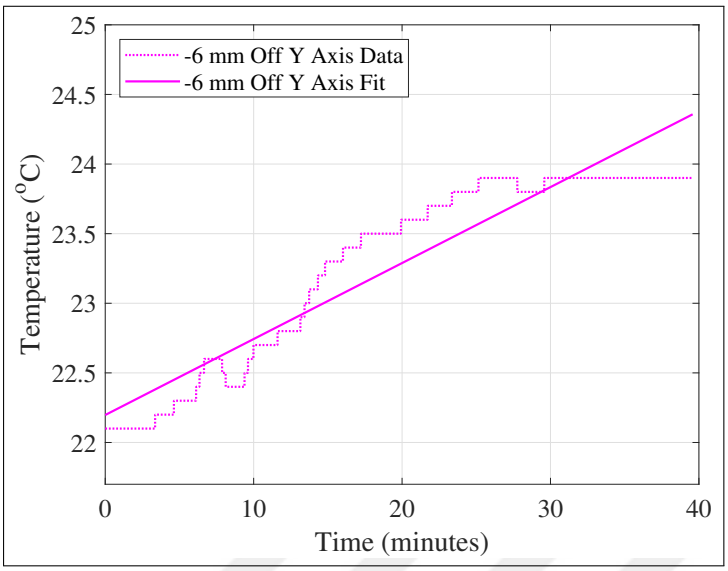


Figure 3.109 40 minute temperature rise vs. time graph during MH experiments conducted with 120 mg/mL concentration SPION using Helmholtz coil with round wire at −6 mm axial position, −6 mm off Y-axis. Temperature–time data was fitted to a line using linear regression for analyzing positional related effects.

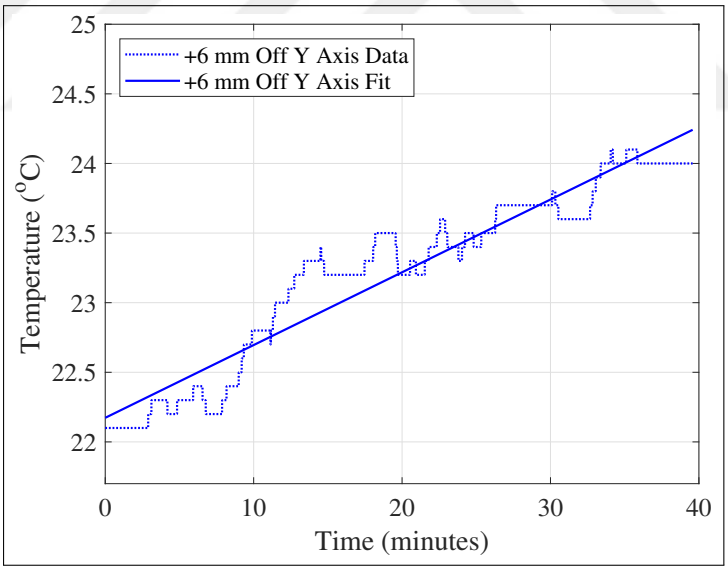


Figure 3.110 40 minute temperature rise vs. time graph during MH experiments conducted with 120 mg/mL concentration SPION using Helmholtz coil with round wire at 0 mm axial position, +6 mm off Y-axis. Temperature–time data was fitted to a line using linear regression for analyzing positional related effects.

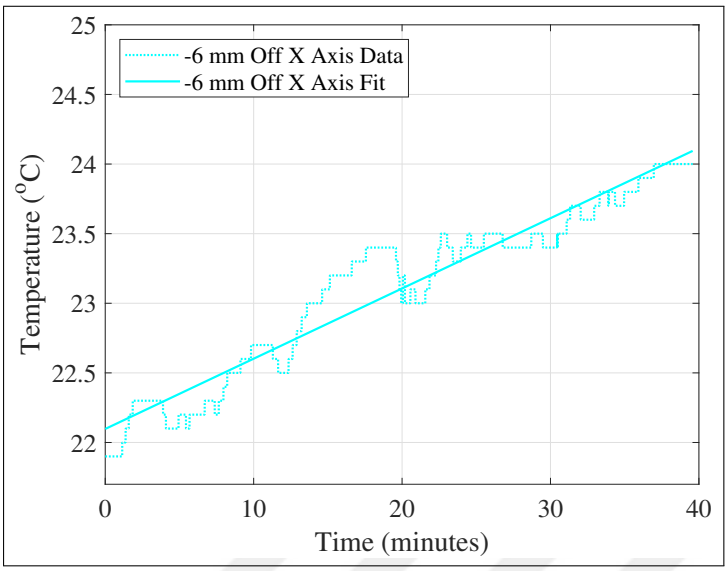


Figure 3.111 40 minute temperature rise vs. time graph during MH experiments conducted with 120 mg/mL concentration SPION using Helmholtz coil with round wire at 0 mm axial position, −6 mm off X-axis. Temperature–time data was fitted to a line using linear regression for analyzing positional related effects.

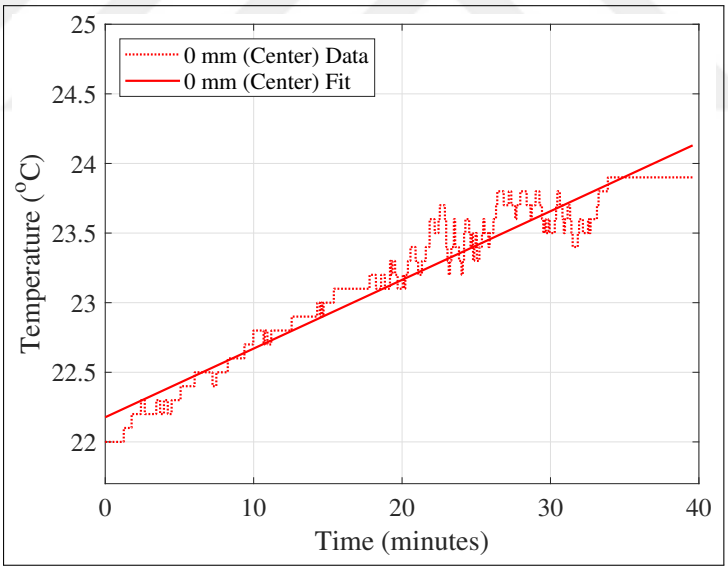


Figure 3.112 40 minute temperature rise vs. time graph during MH experiments conducted with 120 mg/mL concentration SPION using Helmholtz coil with round wire at 0 mm axial position, 0 mm (center) position. Temperature–time data was fitted to a line using linear regression for analyzing positional related effects.

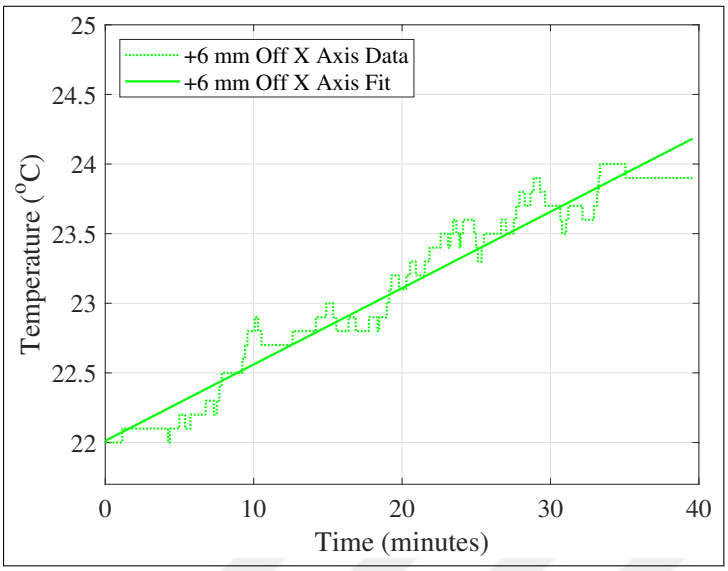


Figure 3.113 40 minute temperature rise vs. time graph during MH experiments conducted with 120 mg/mL concentration SPION using Helmholtz coil with round wire at 0 mm axial position, +6 mm off X-axis. Temperature–time data was fitted to a line using linear regression for analyzing positional related effects.

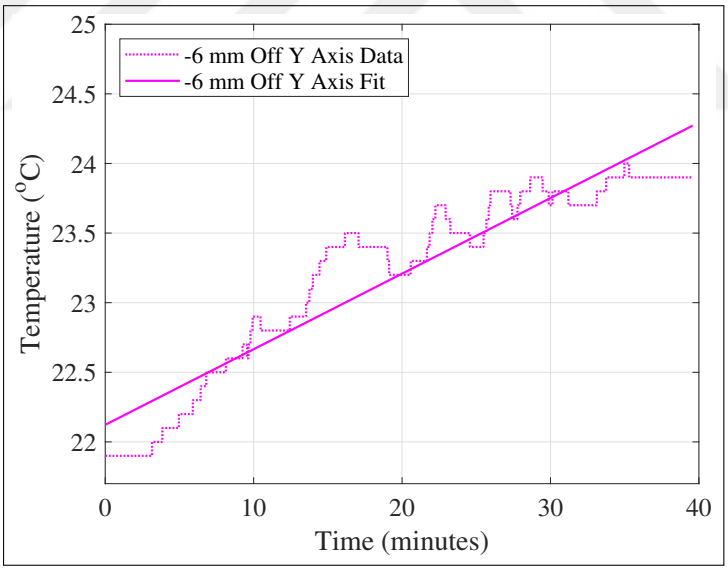


Figure 3.114 40 minute temperature rise vs. time graph during MH experiments conducted with 120 mg/mL concentration SPION using Helmholtz coil with round wire at 0 mm axial position, −6 mm off Y-axis. Temperature–time data was fitted to a line using linear regression for analyzing positional related effects.

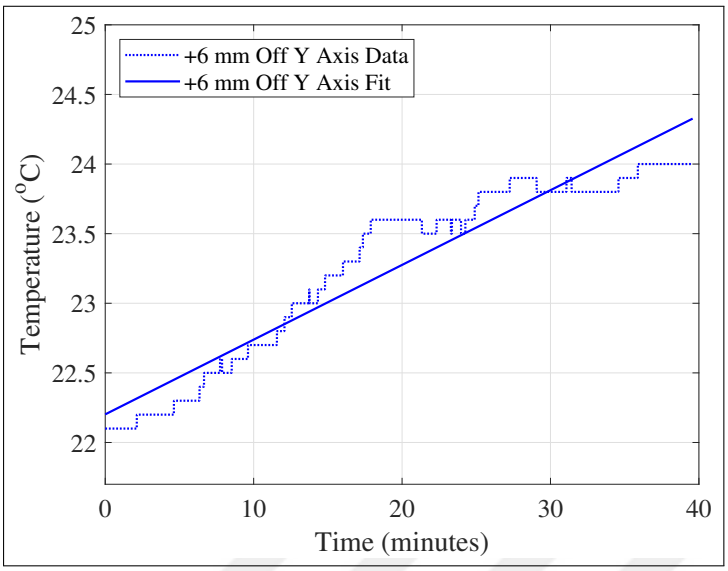


Figure 3.115 40 minute temperature rise vs. time graph during MH experiments conducted with 120 mg/mL concentration SPION using Helmholtz coil with round wire at +6 mm axial position, +6 mm off Y-axis. Temperature–time data was fitted to a line using linear regression for analyzing positional related effects.

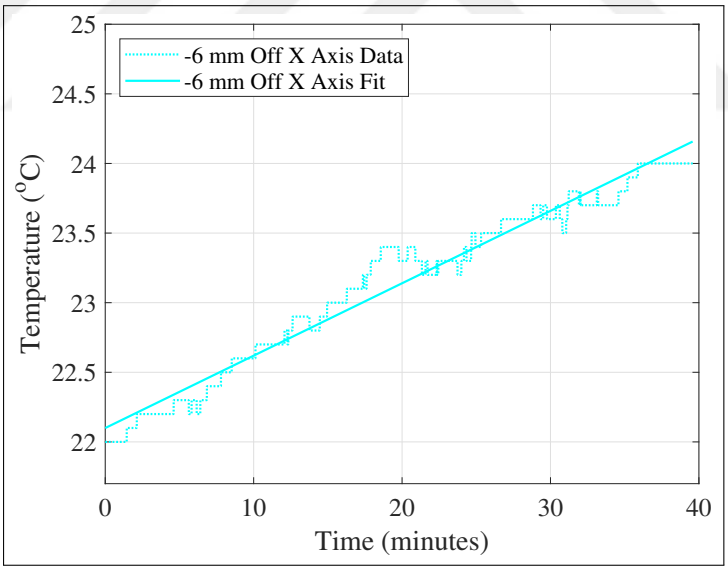


Figure 3.116 40 minute temperature rise vs. time graph during MH experiments conducted with 120 mg/mL concentration SPION using Helmholtz coil with round wire at +6 mm axial position, −6 mm off X-axis. Temperature–time data was fitted to a line using linear regression for analyzing positional related effects.

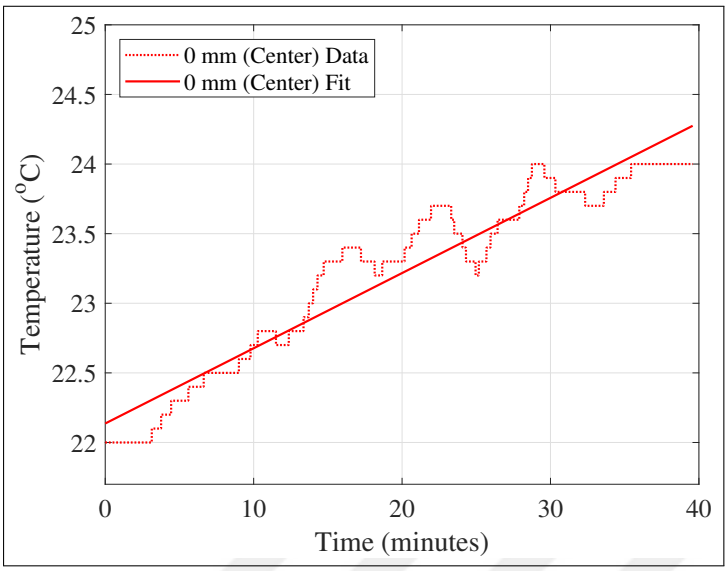


Figure 3.117 40 minute temperature rise vs. time graph during MH experiments conducted with 120 mg/mL concentration SPION using Helmholtz coil with round wire at +6 mm axial position, 0 mm (center) position. Temperature–time data was fitted to a line using linear regression for analyzing positional related effects.

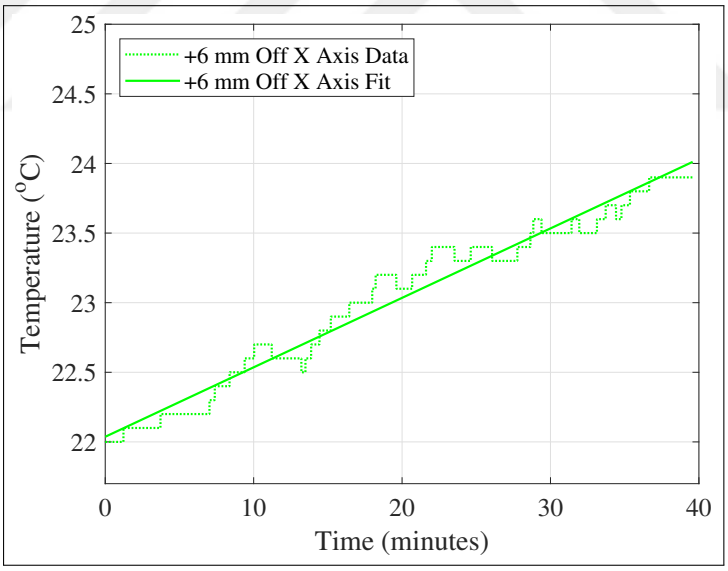


Figure 3.118 40 minute temperature rise vs. time graph during MH experiments conducted with 120 mg/mL concentration SPION using Helmholtz coil with round wire at +6 mm axial position, +6 mm off X-axis. Temperature–time data was fitted to a line using linear regression for analyzing positional related effects.

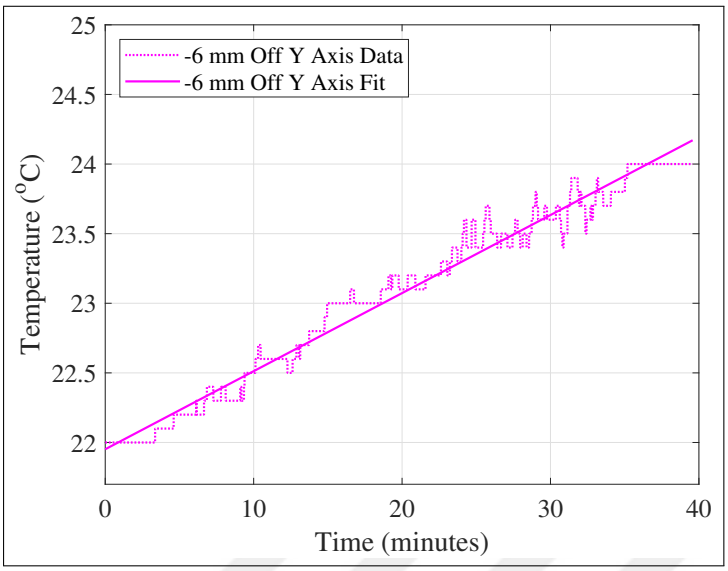


Figure 3.119 40 minute temperature rise vs. time graph during MH experiments conducted with 120 mg/mL concentration SPION using Helmholtz coil with round wire at +6 mm axial position, −6 mm off Y-axis. Temperature–time data was fitted to a line using linear regression for analyzing positional related effects.

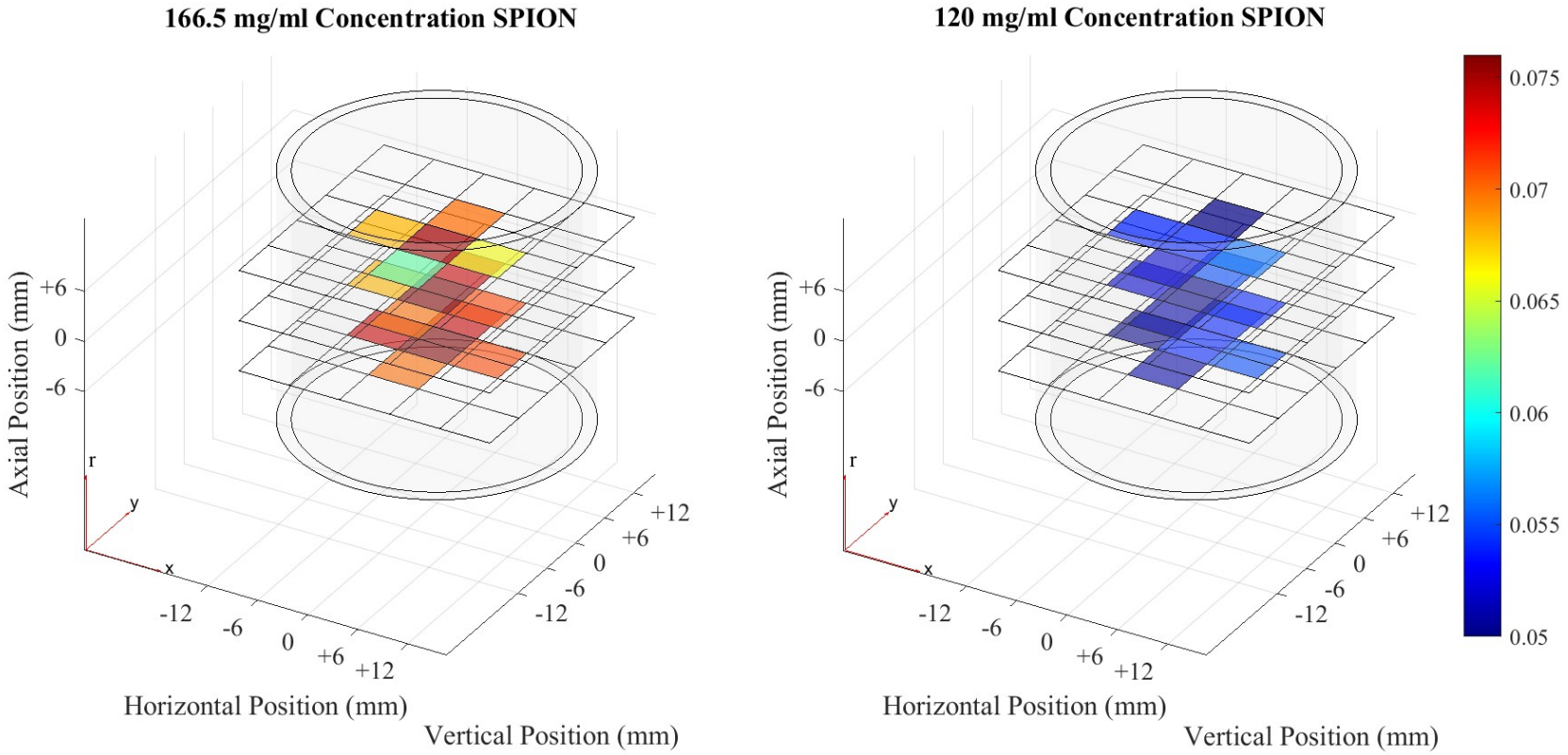


Figure 3.120 Slope of linear regression fit for 40 minute temperature rise vs. time graph during MH experiments conducted with 120 mg/mL concentration SPION using Helmholtz coil with round wire at three axial positions inside of the coil gap and five different transverse positions.

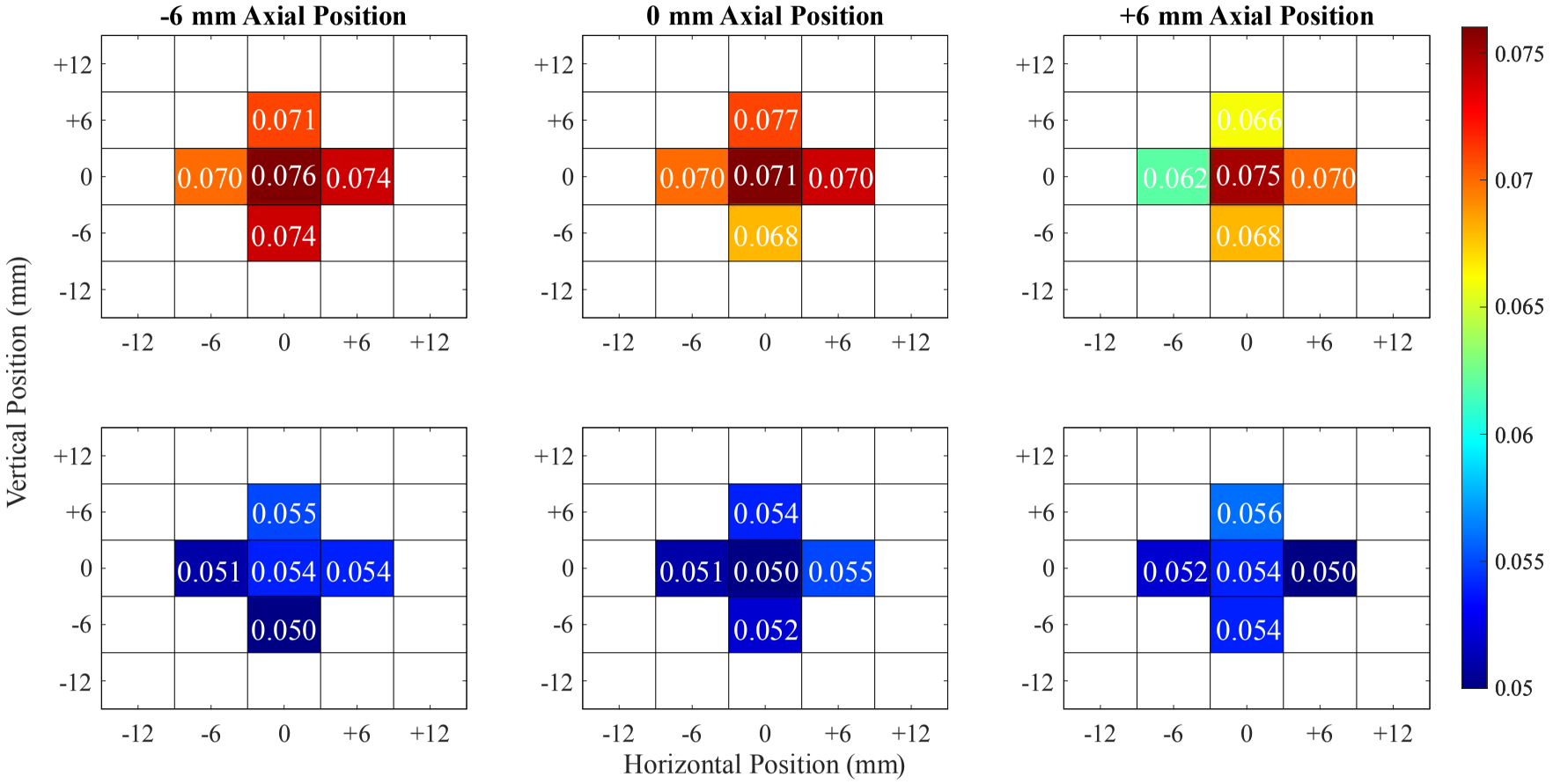


Figure 3.121 Slices showing slope of linear regression fit for 40 minute temperature rise vs. time graph during MH experiments conducted with 120 (top) and 166.5 mg/mL (bottom) SPION concentrations using Helmholtz coil with round wire at three axial positions.

Table 3.23 Helmholtz coil with round wire physical implementation measured magnetic variables.

Power Levels	**sm_B (mT)**	**$smin_B$ (mT)**	**$smax_B$ (mT)**	**$srange_B$ (mT)**	**$scenter_B$ (mT)**	**$s\sigma_B$ (mT)**	**$sHom_B$**	**sP_{coil}**
100%	1.759	1.401	1.867	0.466	1.767	0.112	15.705	29.321
75%	1.264	0.934	1.367	0.433	1.234	0.069	18.319	25.042
50%	0.939	0.717	1.034	0.317	0.900	0.074	12.689	13.120
25%	0.390	0.334	0.530	0.196	0.467	0.154	2.533	1.343
10%	0.245	0.180	0.287	0.107	0.247	0.023	10.652	3.057

Table 3.24 Time–domain root mean square magnetic flux density, $tRMS_B$ values measured in mT from Helmholtz coil with round wire design for 100% power level at three different axial positions; −6, 0, +6 mm and 21 different transverse positions; 6 mm apart at each axial position (63 positions in total, for each power level).

-6 mm Axial Position						
				X Axis		
		−12 mm	−6 mm	Center	+6 mm	+12 mm
Y Axis	+12 mm	-	1.784	**1.867**	**1.867**	-
	+6 mm	1.667	1.701	**1.867**	**1.867**	**1.867**
	Center	1.584	1.617	1.801	**1.867**	**1.867**
	−6 mm	1.634	1.601	1.767	**1.867**	**1.867**
	−12 mm	-	1.684	1.834	1.817	-
Center Axial Position						
				X Axis		
		−12 mm	−6 mm	Center	+6 mm	+12 mm
Y Axis	+12 mm	-	1.551	**1.867**	**1.867**	-
	+6 mm	1.501	1.584	**1.867**	**1.867**	**1.867**
	Center	1.434	1.551	1.767	**1.867**	**1.867**
	−6 mm	1.400	1.517	1.667	1.834	**1.867**
	−12 mm	-	1.400	1.584	1.667	-
+6 mm Axial Position						
				X Axis		
		−12 mm	−6 mm	Center	+6 mm	+12 mm
Y Axis	+12 mm	-	1.751	**1.867**	**1.867**	-
	+6 mm	1.434	1.701	1.817	**1.867**	**1.867**
	Center	1.467	1.601	1.734	**1.867**	**1.867**
	−6 mm	1.400	1.501	1.717	**1.867**	**1.867**
	−12 mm	-	1.467	1.667	1.834	-

Table 3.25 Time–domain root mean square magnetic flux density, $tRMS_B$ values measured in mT from Helmholtz coil with round wire design for 75% power level at three different axial positions; −6, 0, +6 mm and 21 different transverse positions; 6 mm apart at each axial position (63 positions in total, for each power level).

-6 mm Axial Position						
				X Axis		
		−12 mm	−6 mm	Center	+6 mm	+12 mm
	+12 mm	-	1.334	1.501	1.551	-
	+6 mm	1.167	1.184	1.267	1.451	**1.567**
Y Axis	Center	1.100	1.184	1.267	1.367	1.501
	−6 mm	1.117	1.184	1.300	1.367	1.467
	−12 mm	-	1.234	1.300	1.367	-
Center Axial Position						
				X Axis		
		−12 mm	−6 mm	Center	+6 mm	+12 mm
	+12 mm	-	1.017	1.184	1.334	-
	+6 mm	1.017	1.100	1.267	1.334	1.417
Y Axis	Center	0.934	1.134	1.234	1.367	1.417
	−6 mm	0.950	1.134	1.200	1.400	1.384
	−12 mm	-	1.150	1.234	1.300	-
+6 mm Axial Position						
				X Axis		
		−12 mm	−6 mm	Center	+6 mm	+12 mm
	+12 mm	-	1.267	1.284	1.384	-
	+6 mm	1.084	1.250	1.267	1.417	1.534
Y Axis	Center	1.100	1.200	1.300	1.300	1.484
	−6 mm	1.184	1.184	1.217	1.367	1.467
	−12 mm	-	1.200	1.184	1.334	-

Table 3.26 Time–domain root mean square magnetic flux density, $tRMS_B$ values measured in mT from Helmholtz coil with round wire design for 50% power level at three different axial positions; −6, 0, +6 mm and 21 different transverse positions; 6 mm apart at each axial position (63 positions in total, for each power level).

-6 mm Axial Position						
				X Axis		
		−12 mm	−6 mm	Center	+6 mm	+12 mm
	+12 mm	-	0.900	1.050	1.200	-
	+6 mm	0.850	0.850	0.950	1.100	1.200
Y Axis	Center	0.817	0.850	0.917	1.034	1.184
	−6 mm	0.817	0.817	0.950	1.050	1.117
	−12 mm	-	0.884	1.017	1.134	-
Center Axial Position						
				X Axis		
		−12 mm	−6 mm	Center	+6 mm	+12 mm
	+12 mm	-	0.900	0.934	1.017	-
	+6 mm	0.717	0.850	0.984	1.084	1.050
Y Axis	Center	0.717	0.834	0.900	1.000	1.100
	−6 mm	0.734	0.884	0.900	0.967	1.084
	−12 mm	-	0.834	0.834	0.900	-
+6 mm Axial Position						
				X Axis		
		−12 mm	−6 mm	Center	+6 mm	+12 mm
	+12 mm	-	0.884	1.050	1.134	-
	+6 mm	0.784	0.850	1.017	1.000	**1.234**
Y Axis	Center	0.750	0.850	0.900	1.017	1.117
	−6 mm	0.767	0.867	0.967	0.950	1.084
	−12 mm	-	0.784	0.884	0.984	-

Table 3.27 Time–domain root mean square magnetic flux density, $tRMS_B$ values measured in mT from Helmholtz coil with round wire design for 25% power level at three different axial positions; −6, 0, +6 mm and 21 different transverse positions; 6 mm apart at each axial position (63 positions in total, for each power level).

-6 mm Axial Position						
				X Axis		
		−12 mm	−6 mm	Center	+6 mm	+12 mm
	+12 mm	-	0.450	0.484	0.484	-
	+6 mm	0.400	0.433	0.500	0.517	0.517
Y Axis	Center	0.383	0.417	0.433	0.534	**0.550**
	−6 mm	0.383	0.400	0.450	**0.550**	0.500
	−12 mm	-	0.400	0.400	0.467	-
Center Axial Position						
				X Axis		
		−12 mm	−6 mm	Center	+6 mm	+12 mm
	+12 mm	-	0.417	0.433	0.484	-
	+6 mm	0.350	0.433	0.467	0.484	0.534
Y Axis	Center	0.400	0.400	0.467	0.484	0.484
	−6 mm	0.434	0.484	0.400	0.467	0.484
	−12 mm	-	0.350	0.433	0.433	-
+6 mm Axial Position						
				X Axis		
		−12 mm	−6 mm	Center	+6 mm	+12 mm
	+12 mm	-	0.417	0.433	0.500	-
	+6 mm	0.383	0.383	0.433	0.500	**0.550**
Y Axis	Center	0.367	0.383	0.433	0.450	0.500
	−6 mm	0.350	0.433	0.383	0.450	0.534
	−12 mm	-	0.400	0.467	0.467	-

Table 3.28 Time–domain root mean square magnetic flux density, $tRMS_B$ values measured in mT from Helmholtz coil with round wire design for 10% power level at three different axial positions; −6, 0, +6 mm and 21 different transverse positions; 6 mm apart at each axial position (63 positions in total, for each power level).

-6 mm Axial Position						
				X Axis		
		−12 mm	−6 mm	Center	+6 mm	+12 mm
	+12 mm	-	0.200	0.247	0.273	-
	+6 mm	0.227	0.207	0.220	**0.307**	0.247
Y Axis	Center	0.213	0.233	0.247	0.253	0.287
	−6 mm	0.233	0.180	0.247	0.287	0.247
	−12 mm	-	0.247	0.247	0.233	-
Center Axial Position						
				X Axis		
		−12 mm	−6 mm	Center	+6 mm	+12 mm
	+12 mm	-	0.267	0.227	0.253	-
	+6 mm	0.193	0.220	0.267	0.273	0.260
Y Axis	Center	0.207	0.293	0.247	0.267	0.220
	−6 mm	0.207	0.240	0.233	0.253	0.287
	−12 mm	-	0.273	0.207	0.247	-
+6 mm Axial Position						
				X Axis		
		−12 mm	−6 mm	Center	+6 mm	+12 mm
	+12 mm	-	0.253	0.233	0.287	-
	+6 mm	0.233	0.287	0.273	0.247	0.260
Y Axis	Center	0.200	0.220	0.247	0.280	0.240
	−6 mm	0.253	0.240	0.227	0.247	**0.307**
	−12 mm	-	0.213	0.267	0.247	-

Table 3.29 Amount of temperature rise, Δ_T values measured in ^{o}C from 166.5 mg/mL concentration MNPs inside of Helmholtz coil with round wire design at three axial positions inside of the coil gap and five different transverse positions.

-6 mm Axial Position				
			X Axis	
		−6 mm	Center	+6 mm
	+6 mm	-	2.4	-
Y Axis	Center	**2.6**	2.5	2.4
	−6 mm	-	2.5	-
Center Axial Position				
			X Axis	
		−6 mm	Center	+6 mm
	+6 mm	-	2.5	-
Y Axis	Center	2.5	2.5	**2.6**
	−6 mm	-	2.4	-
+6 mm Axial Position				
			X Axis	
		−6 mm	Center	+6 mm
	+6 mm	-	2.5	-
Y Axis	Center	2.5	**2.6**	2.5
	−6 mm	-	2.4	-

Table 3.30 Amount of temperature rise, Δ_T values measured in ^{o}C from 120 mg/mL concentration MNPs inside of Helmholtz coil with round wire design at three axial positions inside of the coil gap and five different transverse positions.

-6 mm Axial Position				
			X Axis	
		−6 mm	Center	+6 mm
	+6 mm	-	2.0	-
Y Axis	Center	2.0	2.0	1.8
	−6 mm	-	**2.1**	-
Center Axial Position				
			X Axis	
		−6 mm	Center	+6 mm
	+6 mm	-	1.9	-
Y Axis	Center	1.9	1.9	2.0
	−6 mm	-	**2.1**	-
+6 mm Axial Position				
			X Axis	
		−6 mm	Center	+6 mm
	+6 mm	-	1.9	-
Y Axis	Center	1.9	2.0	2.0
	−6 mm	-	2.0	-

Table 3.31 Slope of linear regression fit for 40 minute temperature rise vs. time graph during MH experiments conducted with 166.5 mg/mL concentration SPION using Helmholtz coil with round wire at three axial positions inside of the coil gap and five different transverse positions.

-6 mm Axial Position				
		X Axis		
		−6 mm	Center	+6 mm
Y Axis	+6 mm	-	0.071	-
	Center	0.070	0.076	0.074
	−6 mm	-	0.074	-
Center Axial Position				
		X Axis		
		−6 mm	Center	+6 mm
Y Axis	+6 mm	-	**0.077**	-
	Center	0.070	0.071	0.070
	−6 mm	-	0.068	-
+6 mm Axial Position				
		X Axis		
		−6 mm	Center	+6 mm
Y Axis	+6 mm	-	0.066	-
	Center	0.062	0.075	0.070
	−6 mm	-	0.068	-

Table 3.32 Slope of linear regression fit for 40 minute temperature rise vs. time graph during MH experiments conducted with 120 mg/mL concentration SPION using Helmholtz coil with round wire at three axial positions inside of the coil gap and five different transverse positions.

-6 mm Axial Position				
		X Axis		
		−6 mm	Center	+6 mm
	+6 mm	-	0.055	-
Y Axis	Center	0.051	0.054	0.054
	−6 mm	-	0.050	-
Center Axial Position				
		X Axis		
		−6 mm	Center	+6 mm
	+6 mm	-	0.054	-
Y Axis	Center	0.051	0.050	0.055
	−6 mm	-	0.052	-
+6 mm Axial Position				
		X Axis		
		−6 mm	Center	+6 mm
	+6 mm	-	**0.056**	-
Y Axis	Center	0.052	0.054	0.050
	−6 mm	-	0.054	-

Table 3.33 Helmholtz coil with round wire physical implementation measured thermal variables.

	$\mathbf{sm_T}$ (^{o} C)	$\mathbf{smin_T}$ (^{o} C)	$\mathbf{smax_T}$ (^{o} C)	$\mathbf{srange_T}$ (^{o} C)	$\mathbf{scenter_T}$ (^{o} C)	$\mathbf{s\sigma_T}$ (^{o} C)	$\mathbf{sHom_T}$	$\mathbf{sT_{coil}}$
166.5 mg/mL	2.49	2.40	2.60	0.20	2.50	0.07	35.57	92.48
120 mg/mL	1.97	1.80	2.10	0.30	1.90	0.08	24.63	51.72

B Novel Liquid Cooling System

3.4 Electromagnetic Benchmarking

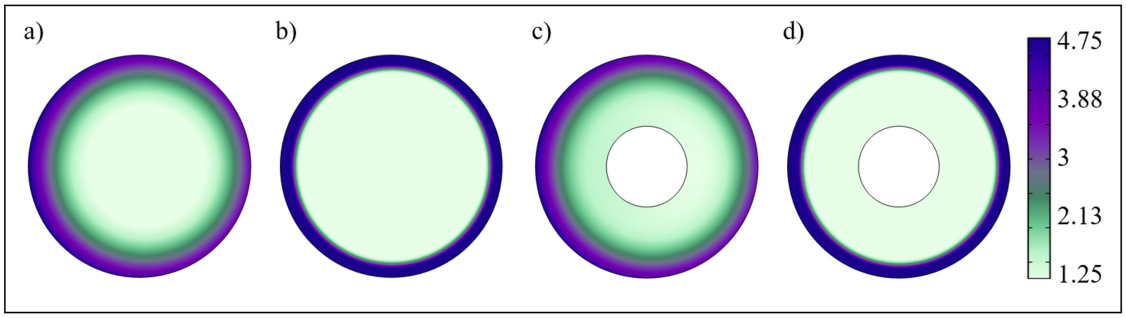


Figure 3.122 Basic simulation results comparing 2D slice plots of the spatial maximum current density normal, smJ in solid coil wires and coil wires with microchannel radius of 0.25 mm at 0.1 and 2.9 MHz applied frequencies. Solid coil wire results are shown at (a) 0.1, and (b) 2.9 MHz, while results for coil wires with microchannel radius of 0.25 mm are shown at (c) 0.1, and (d) 2.9 MHz. (The color bar on the right indicates the magnitude of current density normal $\times 10^7$ A/m^2).

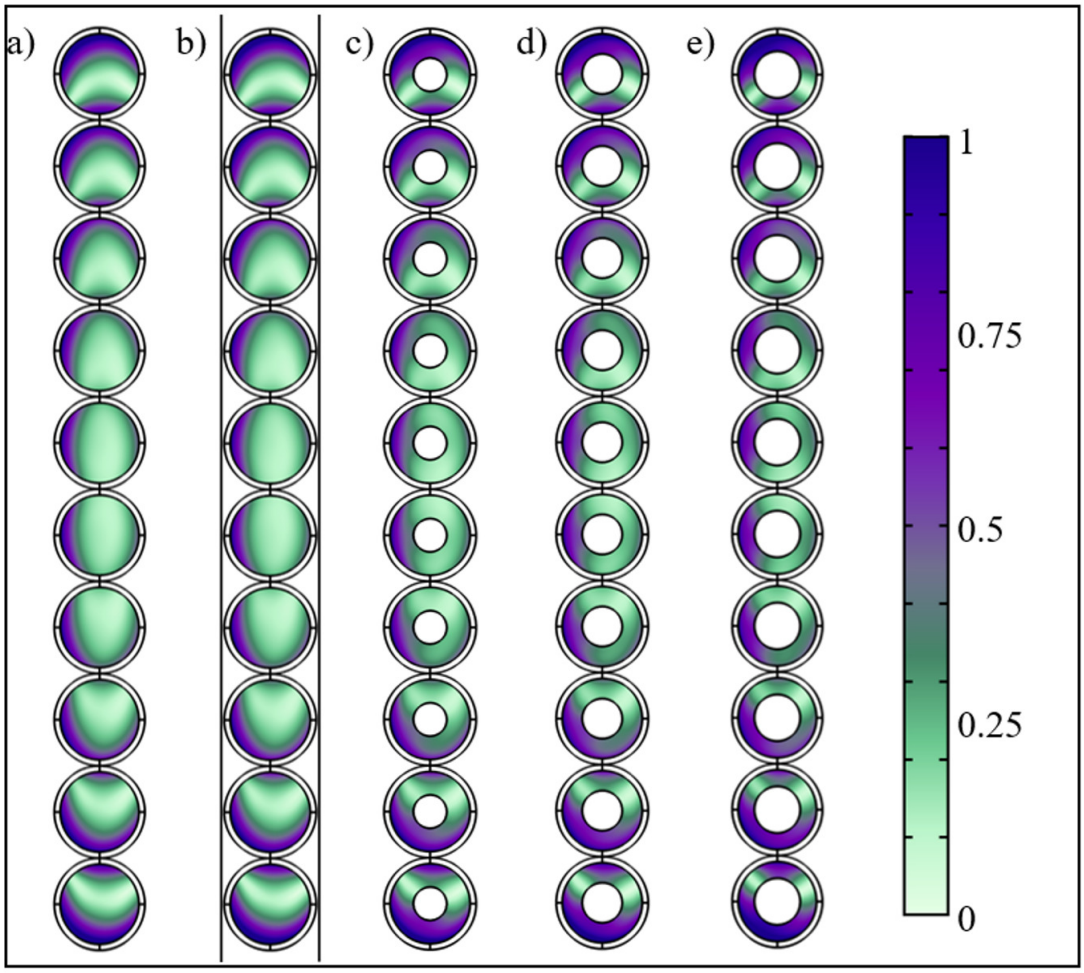


Figure 3.123 Simulation results showing 2D slice plots of the spatial maximum current density normal, *smJ* in coil wires at 0.1 MHz applied frequency for all cooling systems; (a) conventional passive, (b) conventional liquid, and (c–e) novel liquid with microchannel radii of 0.25, 0.30, and 0.35 mm, respectively. (The color bar on the right indicates the magnitude of current density normal $\times 10^8$ A/m^2).

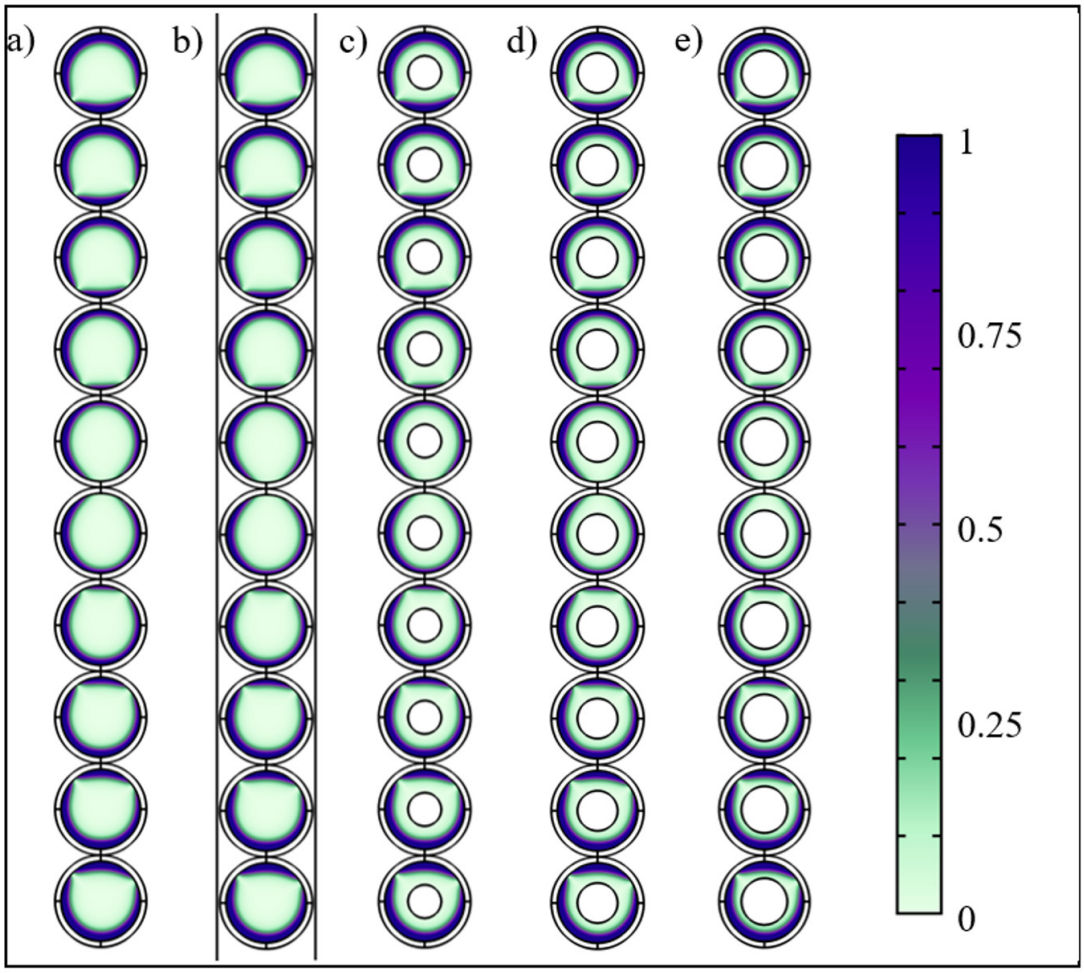


Figure 3.124 Simulation results showing 2D slice plots of the spatial maximum current density normal, *smJ* in coil wires at 1.5 MHz applied frequency for all cooling systems; (a) conventional passive, (b) conventional liquid, and (c–e) novel liquid with microchannel radii of 0.25, 0.30, and 0.35 mm, respectively. (The color bar on the right indicates the magnitude of current density normal $\times 10^8$ A/m^2).

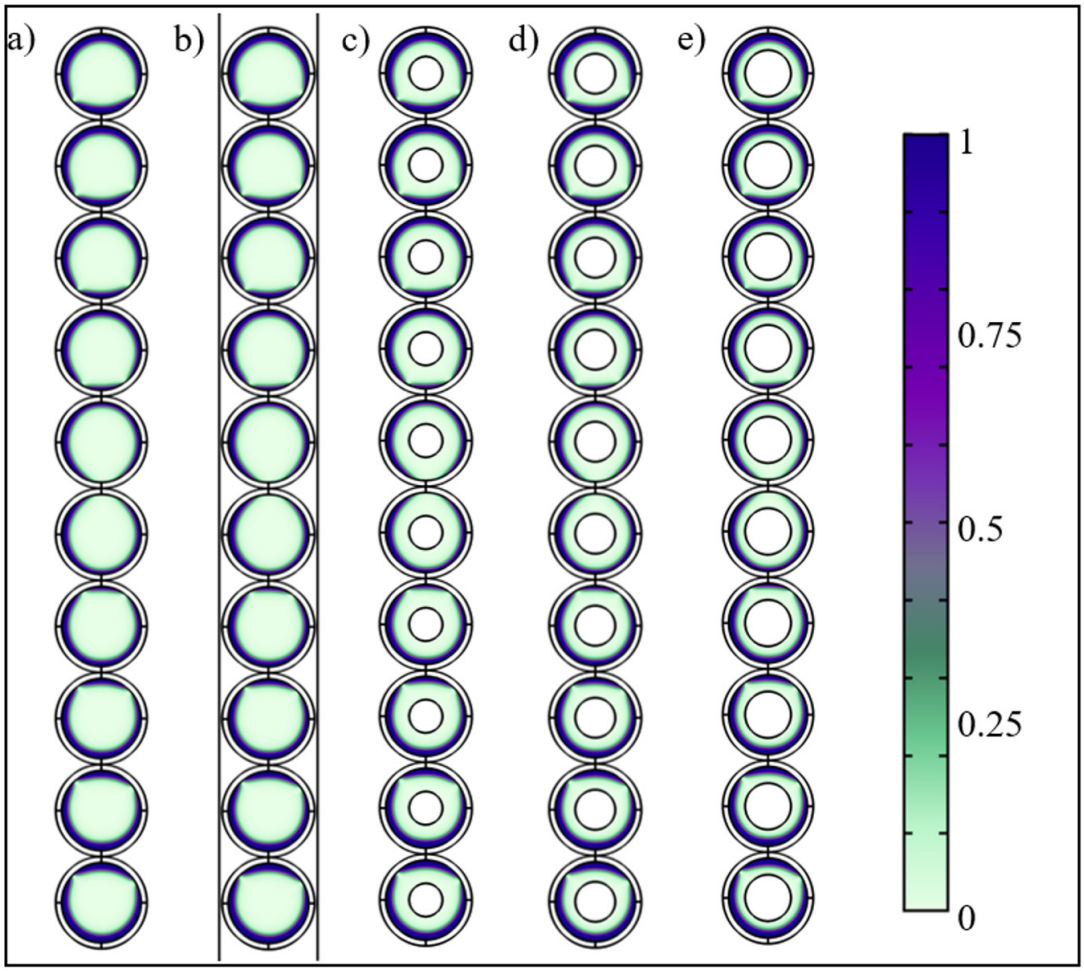


Figure 3.125 Simulation results showing 2D slice plots of the spatial maximum current density normal, *smJ* in coil wires at 2.9 MHz applied frequency for all cooling systems; (a) conventional passive, (b) conventional liquid, and (c–e) novel liquid with microchannel radii of 0.25, 0.30, and 0.35 mm, respectively. (The color bar on the right indicates the magnitude of current density normal $\times 10^8$ A/m^2).

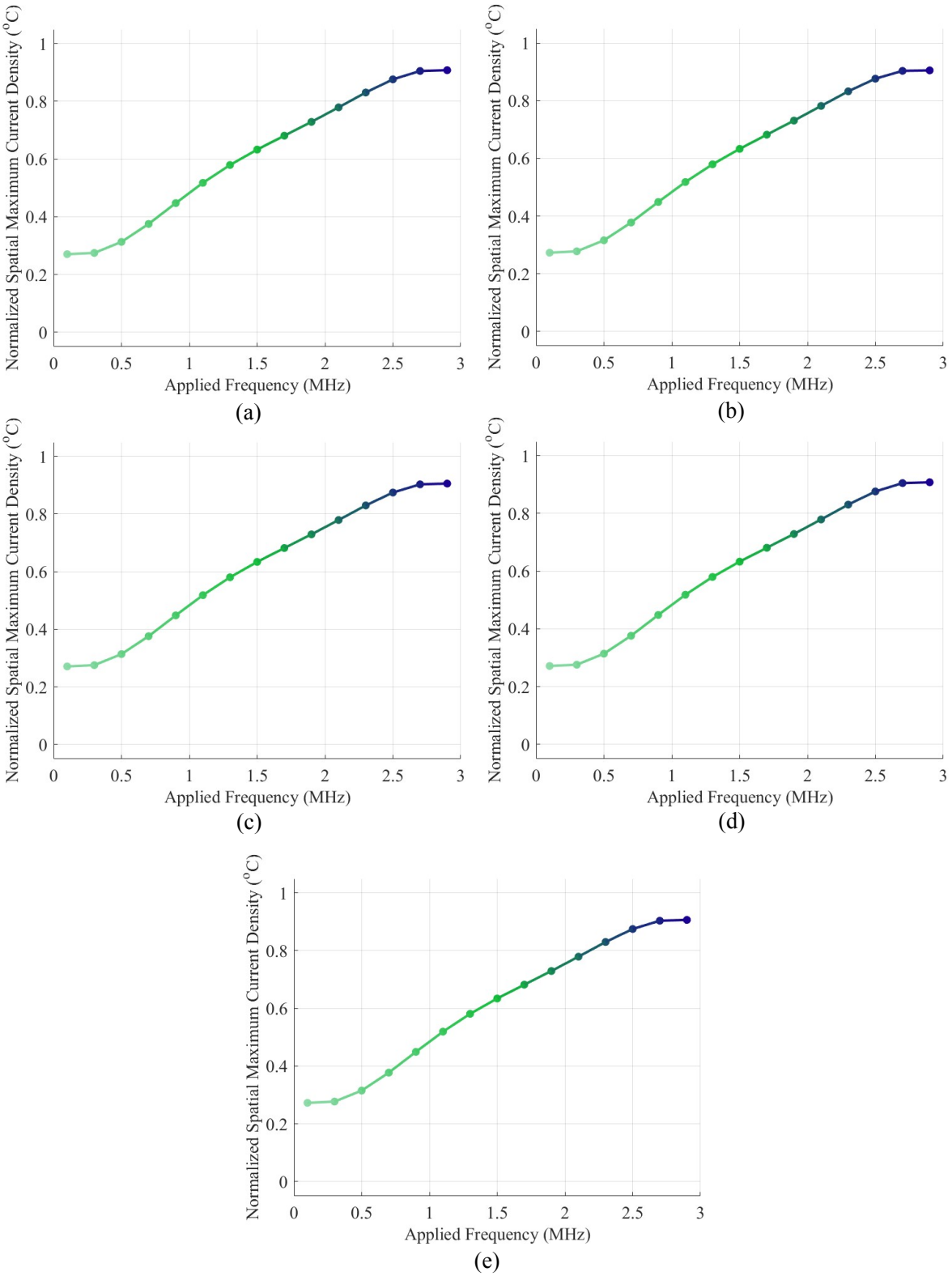


Figure 3.126 Data and SVR model predictions of applied frequency, f_a vs. normalized spatial maximum current density normal, $nsmJ$ for various cooling systems:
(a) conventional passive, (b) conventional liquid, and (c–e) novel liquid with microchannel radii of 0.25, 0.30, and 0.35 mm, respectively (Scatter: data, line: predicted).

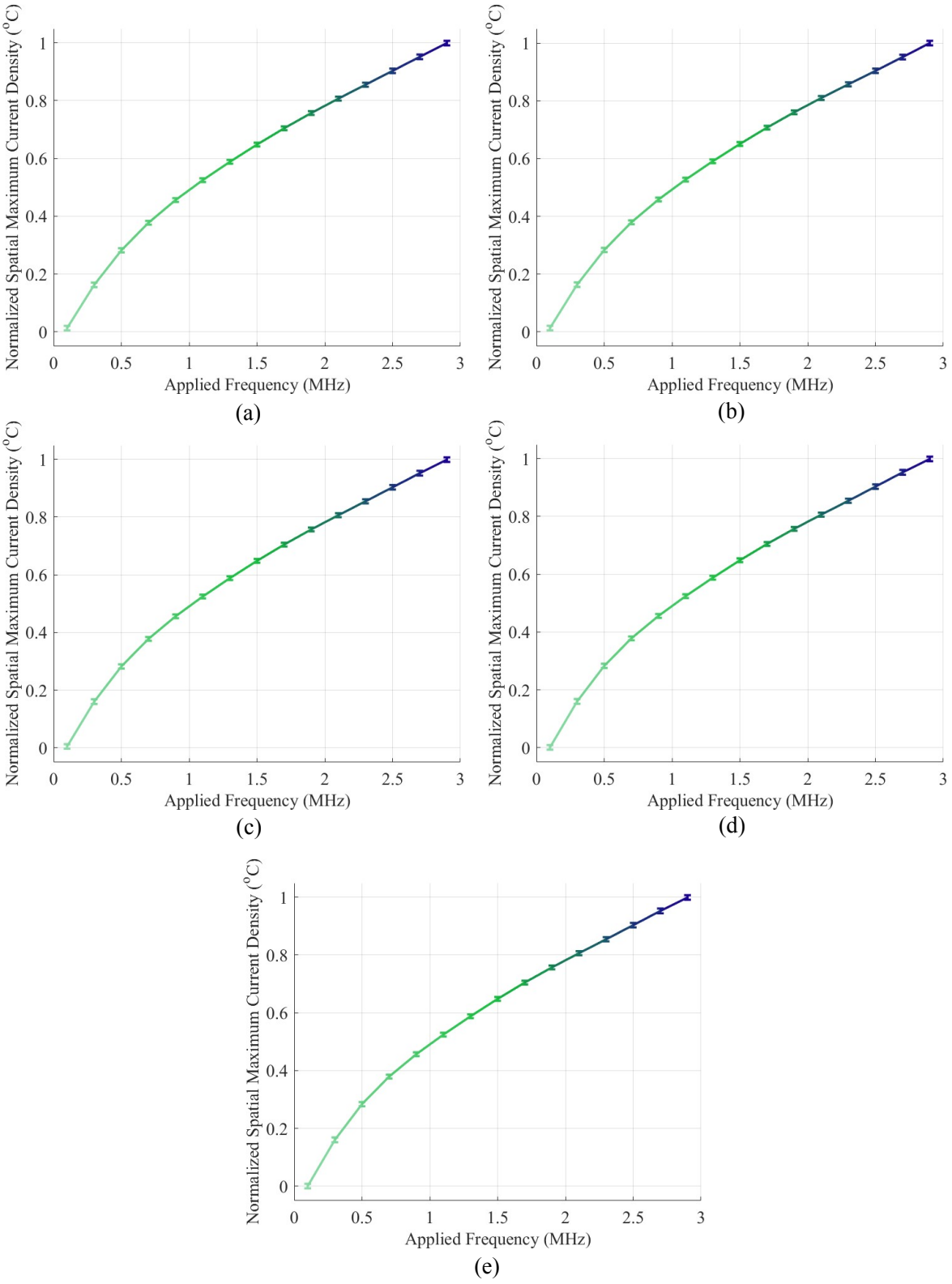


Figure 3.127 Data and GPR model predictions of applied frequency, f_a vs. normalized spatial maximum current density normal, $nsmJ$ for various cooling systems:
(a) conventional passive, (b) conventional liquid, and (c–e) novel liquid with microchannel radii of 0.25, 0.30, and 0.35 mm, respectively. (Error bars: uncertainty estimates of the predicted data at a 95% confidence level, line: predicted).

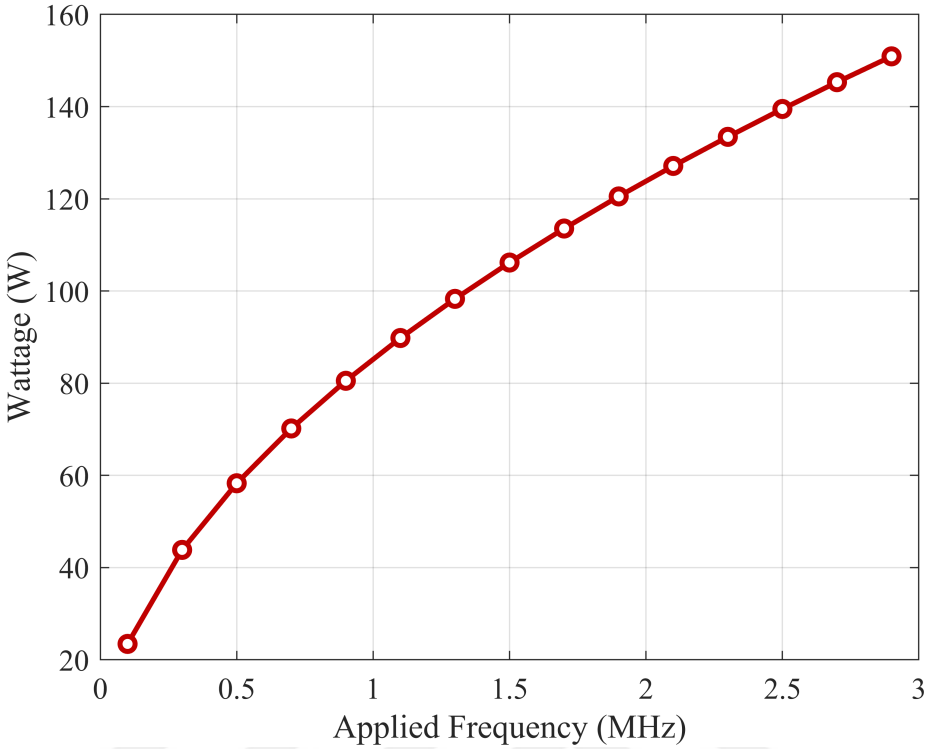


Figure 3.128 Computed coil power consumption across the range of applied frequencies for all design configurations. (Single line is used to represent all designs, as their wattage values were nearly identical across the frequency range).

Table 3.34 Simulation spatial maximum current density normal, smJ ($\times 10^8$ A/m^2) in coil wires for all cooling systems.

	Cooling Systems				
Applied Frequency (MHz)	**Conventional Passive**	**Conventional Liquid**	**Novel Liquid with 0.25 mm Channel Radius**	**Novel Liquid with 0.30 mm Channel Radius**	**Novel Liquid with 0.35 mm Channel Radius**
0.1	1.430	1.433	1.375	1.351	1.347
0.3	2.524	2.531	2.532	2.525	2.482
0.5	3.283	3.293	3.284	3.291	3.295
0.7	3.901	3.913	3.900	3.902	3.912
0.9	4.435	4.449	4.435	4.435	4.439
1.1	4.914	4.929	4.914	4.913	4.914
1.3	5.350	5.366	5.350	5.350	5.349
1.5	5.754	5.772	5.754	5.754	5.753
1.7	6.132	6.151	6.132	6.132	6.131
1.9	6.488	6.508	6.488	6.488	6.488
2.1	6.826	6.847	6.826	6.826	6.826
2.3	7.149	7.171	7.149	7.149	7.149
2.5	7.485	7.489	7.485	7.485	7.485
2.7	7.816	7.820	7.816	7.816	7.816
2.9	8.135	8.140	8.135	8.135	8.135

Table 3.35 Adjusted R^2 error metric calculations for model predictions of applied frequency, f_a vs. normalized spatial maximum current density normal, $nsmJ$ across all cooling systems.

Cooling Systems	**SVR**	**GPR** 95% **Confidence Level**
Conventional Passive	0.9272	0.9994
Conventional Liquid	0.9235	0.9994
Novel Liquid with 0.25 mm Microchannel Radius	0.9263	0.9989
Novel Liquid with 0.30 mm Microchannel Radius	0.9261	0.9990
Novel Liquid with 0.35 mm Microchannel Radius	0.9177	0.9998

3.5 Thermal Benchmarking

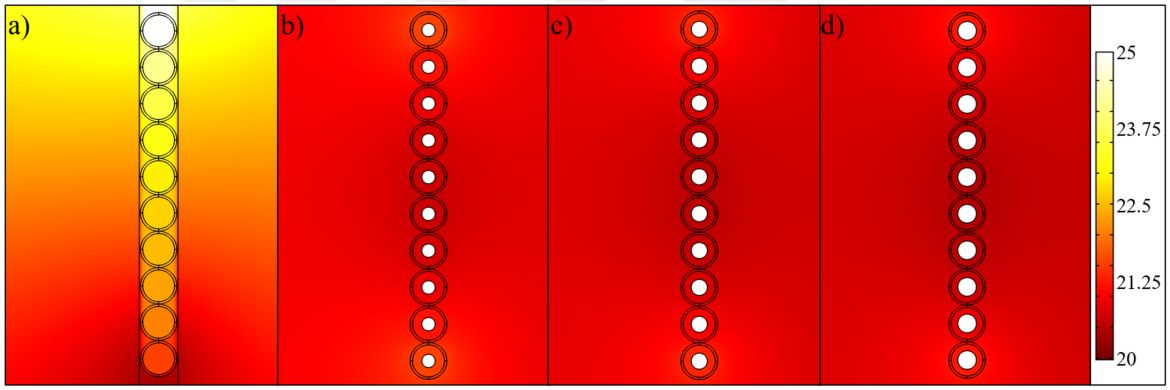


Figure 3.129 Simulation results showing 2D slice plots of the spatial maximum temperature, smT in and around coil wires at 0.1 MHz applied frequency and 0.1 m/s water flow rate for liquid cooling systems; (a) conventional liquid, and (b–d) novel liquid with microchannel radii of 0.25, 0.30, and 0.35 mm, respectively. (The color bar on the right indicates the magnitude of temperature ^oC).

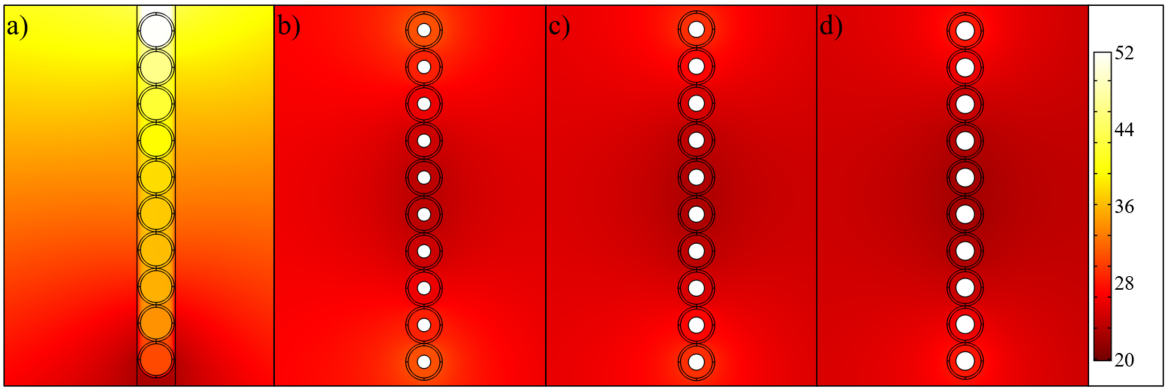


Figure 3.130 Simulation results showing 2D slice plots of the spatial maximum temperature, smT in and around coil wires at 2.9 MHz applied frequency and 0.1 m/s water flow rate for liquid cooling systems; (a) conventional liquid, and (b–d) novel liquid with microchannel radii of 0.25, 0.30, and 0.35 mm, respectively. (The color bar on the right indicates the magnitude of temperature ^oC).

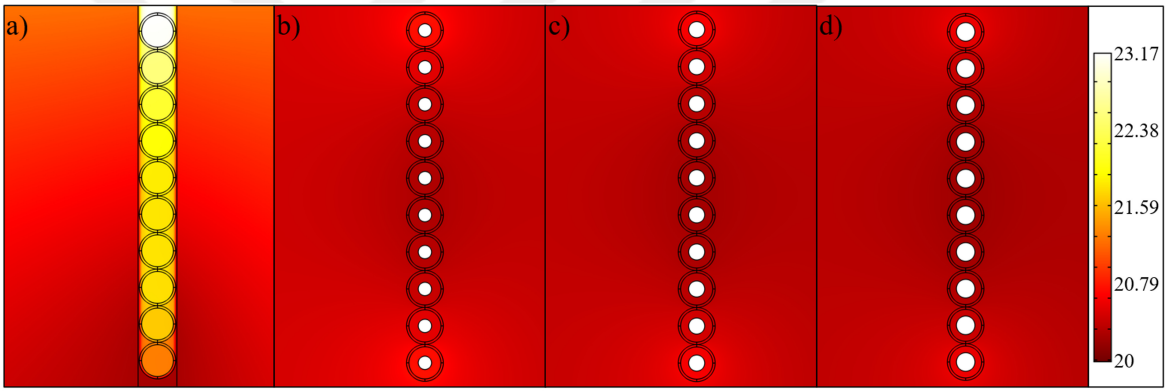


Figure 3.131 Simulation results showing 2D slice plots of the spatial maximum temperature, smT in and around coil wires at 0.1 MHz applied frequency and 0.5 m/s water flow rate for liquid cooling systems; (a) conventional liquid, and (b–d) novel liquid with microchannel radii of 0.25, 0.30, and 0.35 mm, respectively. (The color bar on the right indicates the magnitude of temperature ^oC).

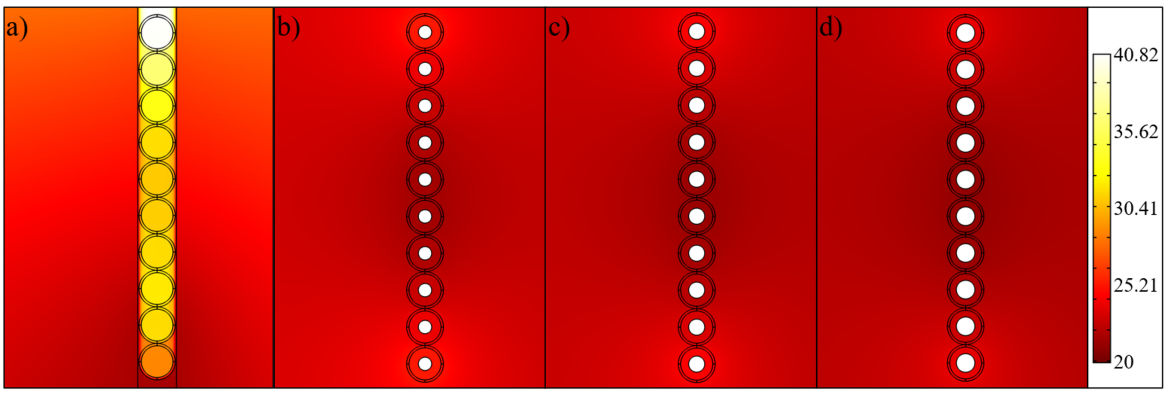


Figure 3.132 Simulation results showing 2D slice plots of the spatial maximum temperature, smT in and around coil wires at 2.9 MHz applied frequency and 0.5 m/s water flow rate for liquid cooling systems; (a) conventional liquid, and (b–d) novel liquid with microchannel radii of 0.25, 0.30, and 0.35 mm, respectively. (The color bar on the right indicates the magnitude of temperature ^oC).

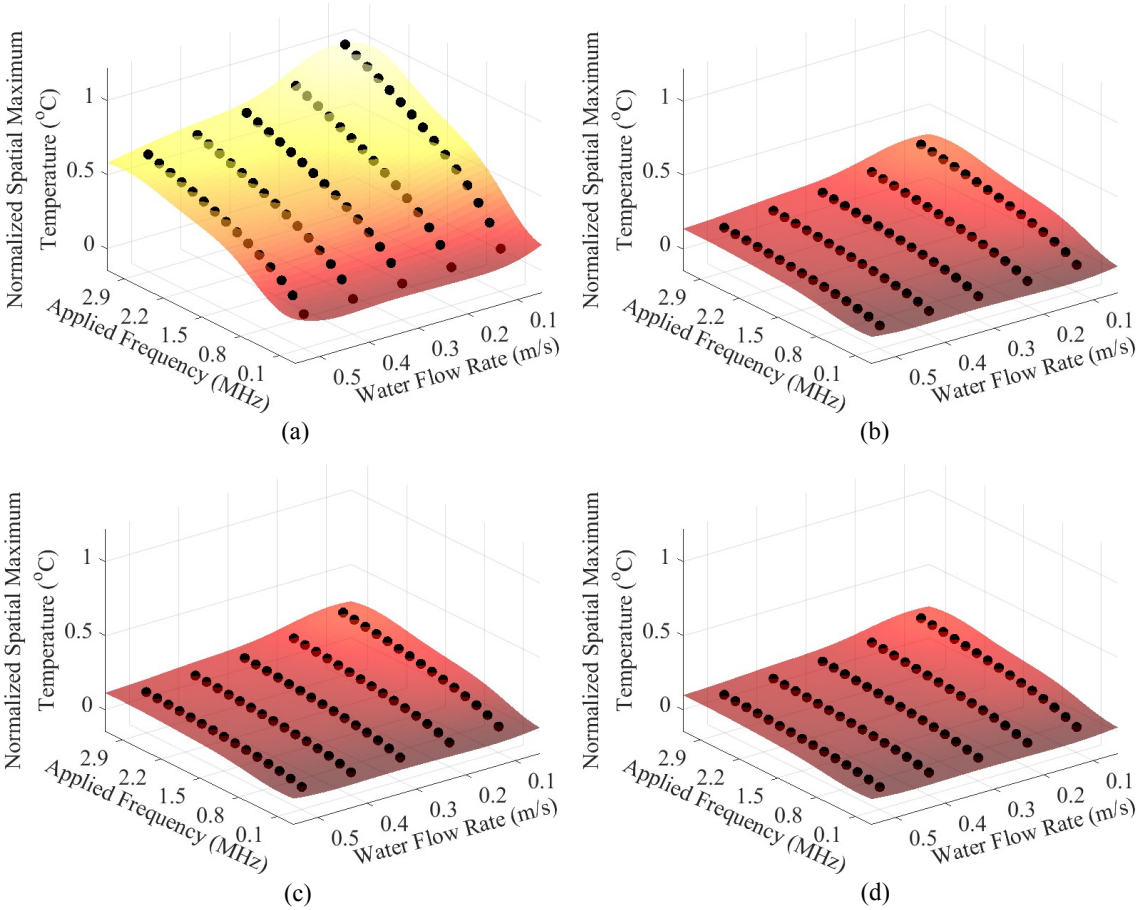


Figure 3.133 Data and SVR model predictions of applied frequency, f_a – water flow rate, v_{wf} vs. normalized spatial maximum temperature, $nsmT$ for all liquid cooling systems: (a) conventional liquid, and (c–d) novel liquid with microchannel radii of 0.25, 0.30, and 0.35 mm, respectively. (Scatter: data, surface: predicted).

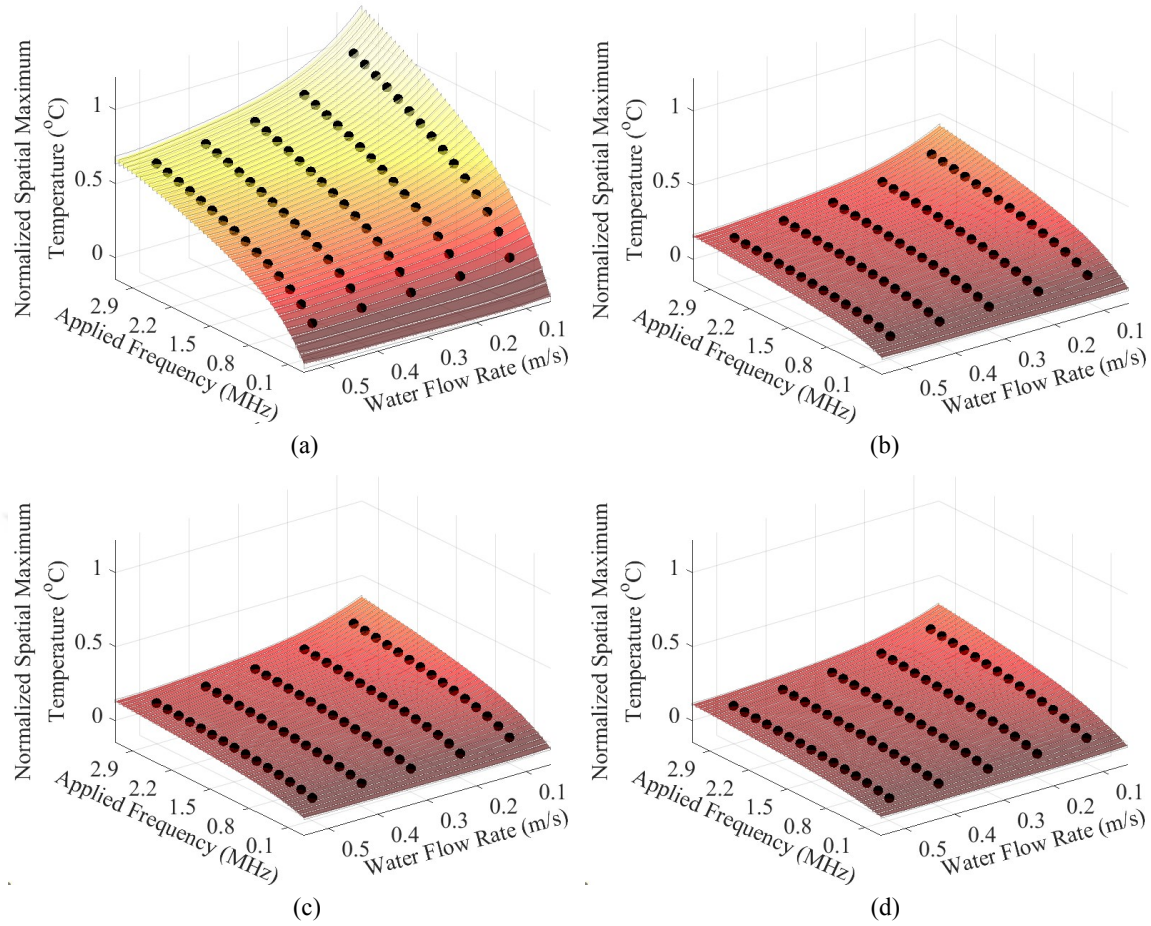


Figure 3.134 Data and GPR model predictions of applied frequency, f_a – water flow rate, v_{wf} vs. normalized spatial maximum temperature, $nsmT$ for all liquid cooling systems: (a) conventional liquid, and (c–d) novel liquid with microchannel radii of 0.25, 0.30, and 0.35 mm, respectively. (Scatter: data, surface: predicted, the lines encircling the color surface indicate uncertainty estimates at a 95% confidence level).

Table 3.36 Key simulation results for the spatial maximum temperature, $smT\,(^oC)$ in coil wires presented for all four liquid cooling system.

Applied Frequency (MHz)	**Cooling Systems**	**Water Flow Rate** (m/s)	
		0.1	**0.5**
0.1	Conventional Liquid	**24.964**	**23.172**
	Novel Liquid with 0.25 mm Microchannel Radius	21.590	20.773
	Novel Liquid with 0.30 mm Microchannel Radius	21.376	20.667
	Novel Liquid with 0.35 mm Microchannel Radius	21.275	20.618
2.9	Conventional Liquid	**52.050**	**40.816**
	Novel Liquid with 0.25 mm Microchannel Radius	30.948	25.374
	Novel Liquid with 0.30 mm Microchannel Radius	29.319	24.550
	Novel Liquid with 0.35 mm Microchannel Radius	28.134	23.960

Table 3.37 Simulation spatial maximum temperature, $smT\,(^oC)$ in coil wires for the conventional liquid cooling system.

Applied Frequency	**Water Flow Rate** (m/s)				
(MHz)	**0.1**	**0.2**	**0.3**	**0.4**	**0.5**
0.1	24.964	24.050	23.621	23.359	23.172
0.3	29.317	27.621	26.827	26.340	26.007
0.5	32.398	30.153	29.092	28.454	28.016
0.7	34.928	32.231	30.967	30.191	29.663
0.9	37.131	34.037	32.592	31.700	31.096
1.1	39.102	35.657	34.046	33.058	32.384
1.3	40.906	37.140	35.382	34.293	33.556
1.5	42.577	38.514	36.609	35.442	34.644
1.7	44.141	39.797	37.765	36.516	35.664
1.9	45.616	41.009	38.854	37.531	36.628
2.1	47.018	42.158	39.888	38.493	37.541
2.3	48.355	43.257	40.873	39.410	38.414
2.5	49.634	44.307	41.818	40.287	39.243
2.7	50.865	45.312	42.727	41.128	40.047
2.9	52.050	46.286	43.600	41.946	40.816

Table 3.38 Simulation spatial maximum temperature data, $smT\,(^oC)$ in coil wires for the novel liquid cooling system with 0.25 mm cooling microchannel radius.

Applied Frequency	**Water Flow Rate** (m/s)				
(MHz)	**0.1**	**0.2**	**0.3**	**0.4**	**0.5**
0.1	21.590	21.171	20.976	20.856	20.773
0.3	23.134	22.311	21.927	21.692	21.528
0.5	24.210	23.106	22.591	22.274	22.054
0.7	25.081	23.751	23.129	22.747	22.482
0.9	25.840	24.313	23.598	23.160	22.854
1.1	26.521	24.817	24.019	23.529	23.189
1.3	27.141	25.277	24.404	23.867	23.494
1.5	27.715	25.702	24.759	24.180	23.777
1.7	28.251	26.100	25.092	24.472	24.041
1.9	28.756	26.475	25.405	24.748	24.290
2.1	29.235	26.831	25.703	25.009	24.527
2.3	29.691	27.169	25.986	25.259	24.752
2.5	30.127	27.493	26.257	25.497	24.968
2.7	30.545	27.804	26.517	25.726	25.175
2.9	30.948	28.104	26.768	25.946	25.374

Table 3.39 Simulation spatial maximum temperature data, $smT\,(^oC)$ in coil wires for the novel liquid cooling system with 0.30 mm cooling microchannel radius.

Applied Frequency	**Water Flow Rate** (m/s)				
(MHz)	**0.1**	**0.2**	**0.3**	**0.4**	**0.5**
0.1	21.376	21.012	20.842	20.739	20.667
0.3	22.636	21.940	21.616	21.417	21.280
0.5	23.582	22.637	22.197	21.927	21.740
0.7	24.324	23.184	22.653	22.328	22.102
0.9	24.967	23.659	23.049	22.675	22.416
1.1	25.544	24.085	23.405	22.988	22.698
1.3	26.073	24.476	23.730	23.274	22.957
1.5	26.562	24.837	24.032	23.539	23.196
1.7	27.019	25.175	24.314	23.787	23.420
1.9	27.450	25.494	24.580	24.020	23.631
2.1	27.858	25.796	24.832	24.242	23.832
2.3	28.247	26.083	25.073	24.453	24.023
2.5	28.619	26.359	25.303	24.655	24.205
2.7	28.976	26.623	25.524	24.850	24.381
2.9	29.319	26.878	25.737	25.037	24.550

Table 3.40 Simulation spatial maximum temperature data, $smT\,(^oC)$ in coil wires for the novel liquid cooling system with 0.35 mm cooling microchannel radius.

Applied Frequency	**Water Flow Rate** (m/s)				
(MHz)	**0.1**	**0.2**	**0.3**	**0.4**	**0.5**
0.1	21.275	20.936	20.780	20.684	20.618
0.3	22.245	21.650	21.374	21.206	21.089
0.5	23.104	22.282	21.901	21.668	21.506
0.7	23.776	22.777	22.313	22.029	21.833
0.9	24.339	23.192	22.658	22.333	22.106
1.1	24.840	23.560	22.966	22.602	22.350
1.3	25.298	23.898	23.248	22.850	22.574
1.5	25.724	24.213	23.510	23.080	22.782
1.7	26.123	24.507	23.755	23.295	22.976
1.9	26.499	24.785	23.987	23.499	23.160
2.1	26.856	25.048	24.207	23.692	23.335
2.3	27.196	25.299	24.416	23.876	23.501
2.5	27.521	25.539	24.617	24.052	23.660
2.7	27.833	25.770	24.809	24.221	23.813
2.9	28.134	25.992	24.994	24.384	23.960

Table 3.41 Adjusted R^2 error metric calculations for model predictions of applied frequency, f_a – water flow rate, v_{wf} vs. normalized spatial maximum temperature, $nsmT$ across all liquid cooling systems.

Cooling Systems	**SVR**	**GPR** 95% **Confidence Level**
Conventional Liquid	0.9581	0.9999
Novel Liquid with 0.25 mm Microchannel Radius	0.9597	0.9998
Novel Liquid with 0.30 mm Microchannel Radius	0.9593	0.9998
Novel Liquid with 0.35 mm Microchannel Radius	0.9587	0.9999

3.6 Performance Index

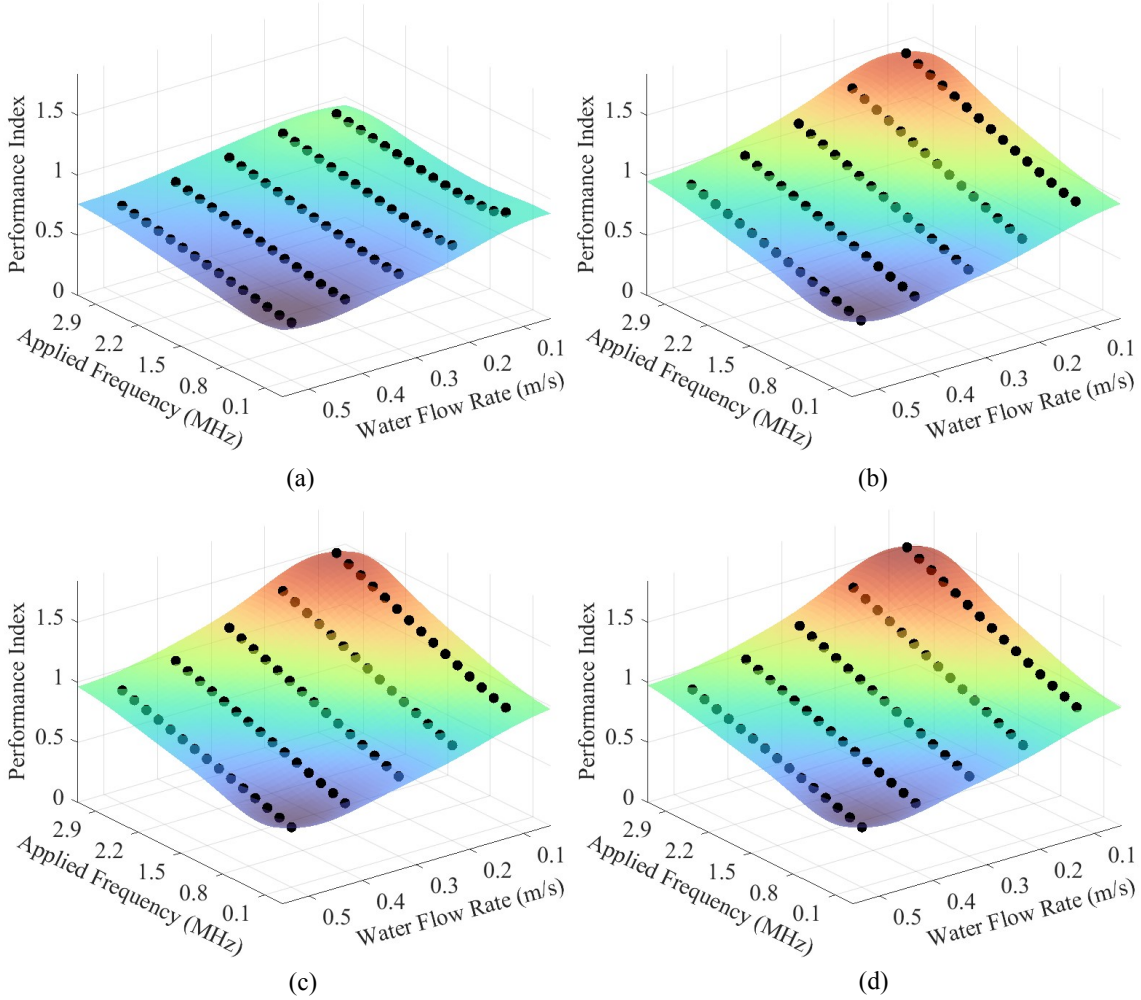


Figure 3.135 Data and SVR model predictions of applied frequency, f_a – water flow rate, v_{wf} vs. performance index, PI for all liquid cooling systems: (a) conventional liquid, and (c–d) novel liquid with microchannel radii of 0.25, 0.30, and 0.35 mm, respectively. (Scatter: data, surface: predicted).

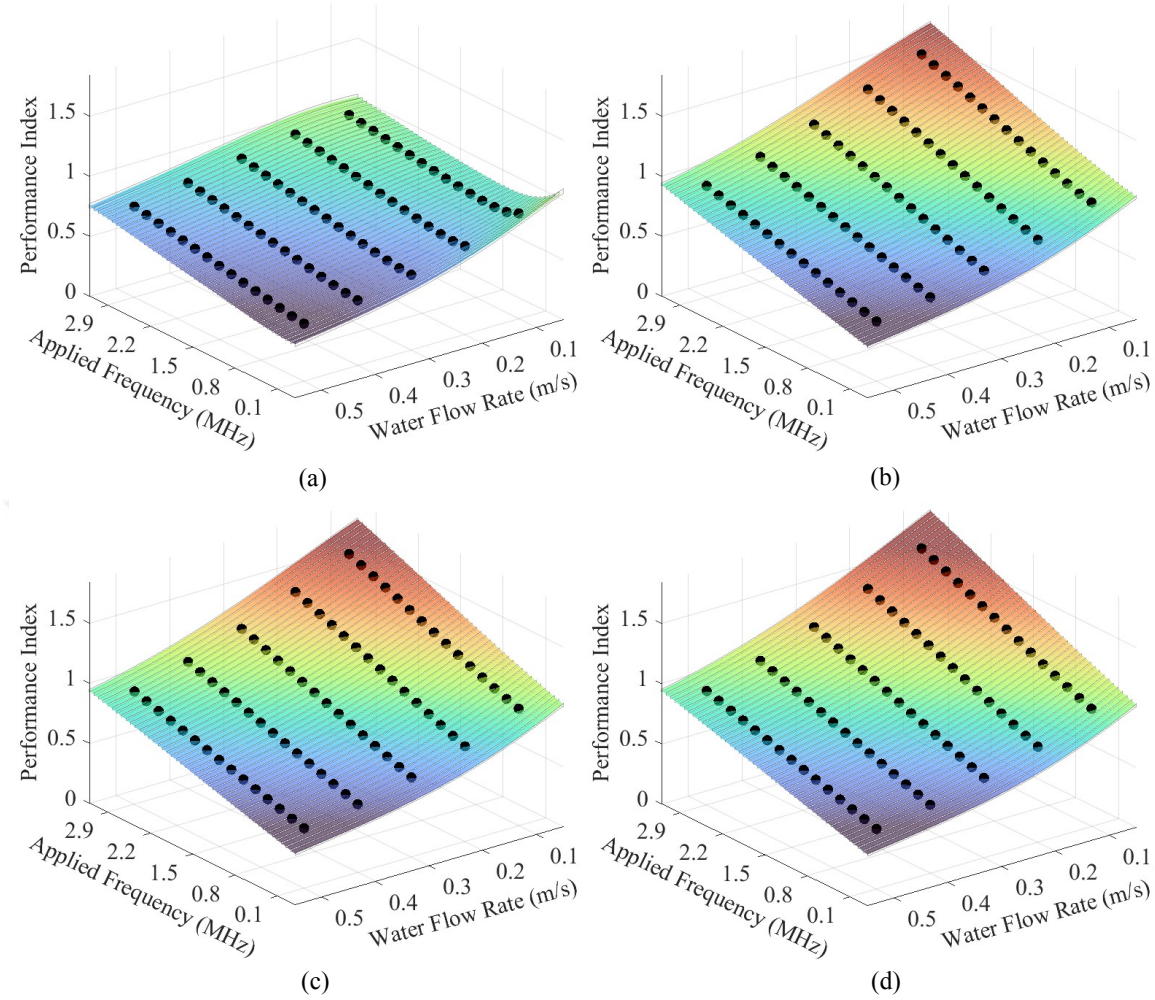


Figure 3.136 Data and GPR model predictions of applied frequency, f_a – water flow rate, v_{wf} vs. performance index, PI for all liquid cooling systems: (a) conventional liquid, and (c–d) novel liquid with microchannel radii of 0.25, 0.30, and 0.35 mm, respectively. (Scatter: data, surface: predicted, the lines encircling the color surface indicate uncertainty estimates at a 95% confidence level).

Table 3.42 Performance index, PI (unitless) for the conventional liquid cooling system.

Applied Frequency	**Water Flow Rate** (m/s)				
(MHz)	**0.1**	**0.2**	**0.3**	**0.4**	**0.5**
0.1	**0.879**	**0.736**	0.627	0.544	**0.480**
0.3	**0.839**	**0.727**	0.631	0.555	0.493
0.5	**0.831**	0.736	0.646	0.572	0.511
0.7	0.834	0.750	0.664	0.591	0.531
0.9	0.843	0.767	0.684	0.611	0.551
1.1	0.855	0.785	0.704	0.632	0.572
1.3	0.868	0.805	0.725	0.654	0.592
1.5	0.883	0.824	0.747	0.675	0.613
1.7	0.899	0.845	0.768	0.697	0.634
1.9	0.915	0.865	0.790	0.718	0.655
2.1	0.932	0.886	0.811	0.739	0.675
2.3	0.949	0.906	0.833	0.761	0.696
2.5	0.966	0.927	0.854	0.782	0.716
2.7	0.983	0.947	0.875	0.803	0.737
2.9	**1.000**	0.968	0.896	0.824	0.757

Table 3.43 Performance index, PI (unitless) for the novel liquid cooling system with 0.25 mm microchannel radius.

Applied Frequency	**Water Flow Rate** (m/s)				
(MHz)	**0.1**	**0.2**	**0.3**	**0.4**	**0.5**
0.1	0.970	0.789	0.662	0.569	**0.499**
0.3	0.992	0.822	0.695	0.601	0.528
0.5	1.026	0.860	0.731	0.634	0.559
0.7	1.063	0.900	0.769	0.668	0.590
0.9	1.103	0.940	0.806	0.702	0.621
1.1	1.143	0.981	0.844	0.737	0.652
1.3	1.183	1.022	0.882	0.771	0.683
1.5	1.224	1.063	0.919	0.805	0.714
1.7	1.264	1.103	0.957	0.839	0.745
1.9	1.305	1.144	0.994	0.873	0.776
2.1	1.345	1.184	1.032	0.907	0.807
2.3	1.386	1.224	1.069	0.941	0.838
2.5	1.426	1.264	1.106	0.975	0.868
2.7	1.466	1.304	1.143	1.008	0.899
2.9	**1.505**	1.344	1.179	1.042	0.930

Table 3.44 Performance index, PI (unitless) for the novel liquid cooling system with 0.30 mm microchannel radius.

Applied Frequency	**Water Flow Rate** (m/s)				
(MHz)	**0.1**	**0.2**	**0.3**	**0.4**	**0.5**
0.1	0.976	0.792	0.664	0.570	**0.500**
0.3	1.007	0.829	0.699	0.603	0.530
0.5	1.044	0.870	0.737	0.638	0.561
0.7	1.086	0.912	0.776	0.673	0.593
0.9	1.129	0.955	0.815	0.708	0.625
1.1	1.173	0.998	0.854	0.743	0.657
1.3	1.217	1.041	0.893	0.779	0.689
1.5	1.261	1.084	0.932	0.814	0.720
1.7	1.306	1.126	0.971	0.849	0.752
1.9	1.350	1.169	1.010	0.884	0.784
2.1	1.393	1.212	1.049	0.919	0.815
2.3	1.437	1.254	1.088	0.954	0.847
2.5	1.480	1.296	1.126	0.989	0.878
2.7	1.523	1.338	1.165	1.023	0.910
2.9	**1.566**	1.380	1.203	1.058	0.941

Table 3.45 Performance index, PI (unitless) for the novel liquid cooling system with 0.35 mm microchannel radius.

Applied Frequency	**Water Flow Rate** (m/s)				
(MHz)	**0.1**	**0.2**	**0.3**	**0.4**	**0.5**
0.1	0.980	0.794	0.664	0.571	**0.500**
0.3	1.019	0.835	0.703	0.606	0.532
0.5	1.059	0.877	0.742	0.641	0.563
0.7	1.103	0.921	0.781	0.677	0.596
0.9	1.150	0.965	0.822	0.712	0.628
1.1	1.196	1.010	0.862	0.749	0.660
1.3	1.243	1.055	0.902	0.784	0.693
1.5	1.290	1.099	0.942	0.820	0.725
1.7	1.337	1.144	0.982	0.856	0.757
1.9	1.384	1.188	1.022	0.892	0.790
2.1	1.430	1.232	1.062	0.928	0.822
2.3	1.477	1.276	1.102	0.963	0.854
2.5	1.523	1.320	1.141	0.999	0.886
2.7	1.569	1.364	1.181	1.034	0.918
2.9	**1.614**	1.407	1.220	1.070	0.950

Table 3.46 Adjusted R^2 error metric calculations for SVR and GPR–based model predictions of applied frequency, f_a – water flow rate, v_{wf} vs. performance index, PI across all liquid cooling systems.

Cooling Systems	**SVR**	**GPR** 95% **Confidence Level**
Conventional Liquid	0.9777	0.9999
Novel Liquid with 0.25 mm Microchannel Radius	0.9705	0.9999
Novel Liquid with 0.30 mm Microchannel Radius	0.9695	0.9999
Novel Liquid with 0.35 mm Microchannel Radius	0.9687	0.9999

Table 3.47 Sensitivity analysis of input parameter influence on SVR model predictions, and ReliefF feature weights indicating input parameter importance for predictions.

Cooling Systems	**Parameters**	**SVR**	
		Sensitivity Analysis	**ReliefF Feature Weights**
Conventional Liquid	Applied Frequency	0.0161	2
	Water Flow Rate	0.0173	1
Novel Liquid with 0.25 mm	Applied Frequency	0.0335	1
Microchannel Radius	Water Flow Rate	0.0262	2
Novel Liquid with 0.30 mm	Applied Frequency	0.0355	1
Microchannel Radius	Water Flow Rate	0.0271	2
Novel Liquid with 0.35 mm	Applied Frequency	0.0370	1
Microchannel Radius	Water Flow Rate	0.0277	2

Table 3.48 Sensitivity analysis of input parameter influence on GPR model predictions, and ReliefF feature weights indicating input parameter importance for predictions.

Cooling Systems	**Parameters**	**GPR**	
		Sensitivity Analysis	**ReliefF Feature Weights**
Conventional Liquid	Applied Frequency	0.0161	2
	Water Flow Rate	0.0197	1
Novel Liquid with 0.25 mm	Applied Frequency	0.0291	1
Microchannel Radius	Water Flow Rate	0.0319	2
Novel Liquid with 0.30 mm	Applied Frequency	0.0308	1
Microchannel Radius	Water Flow Rate	0.0335	2
Novel Liquid with 0.35 mm	Applied Frequency	0.0322	1
Microchannel Radius	Water Flow Rate	0.0348	2

4. DISCUSSION

A Coil Optimization

Magnetic flux density and heat maps of the MNP concentrations are summarized as spatial distributions of magnetic flux density and MNP heating in Figure 3.1. Tables 3.1, 3.12, 3.23 provide calculations from physical measurements analogous to the simulation results of Table 2.1, with magnetic flux densities in agreement with existing literature [44, 75, 54], while Tables 3.11, 3.22, 3.33 present physical measurements of MNP heating. Therein, first and foremost, higher temperatures with higher MNP concentrations [76] and additionally the lack of heating with water only (See Results Section Figures 3.9, 3.49, 3.89) validated proper operation of the MH device.

When the intended purpose of an MH system is to provide a spatially homogenous AMF on the largest possible volume for potentially heating up all of the 'MNP–attached cells', the temperature indices herein constitute the most appropriate performance measures. However, inherently, MH mechanisms [77] make the simulation even of a small number of MNPs computationally difficult [78]. Moreover, considering potential variations in MNP design and production resulting in different heating characteristics, using magnetic field indices was essential for providing an MNP–independent design criteria. Accordingly, magnetic flux density simulations were used for pre–selecting the coil geometries. Therein, the numerical simulations resulted in similar performance for both of the solenoid coils along with a superior performance from the Helmotz coil as displayed in Table 2.1. In contrast, for the experimental data the magnetic field indices throughout the Tables 3.1, 3.12, 3.23 show differences between the two solenoid coils. Also in contrast to Table 2.1, in Tables 3.1, 3.12, 3.23 the performance of the Helmholtz coil was close to the solenoid coil with round wire.

Simulations' failure to capture real–world losses due to lack of boundary conditions may poorly approximate, especially for Litz wire characteristics, parasitic resistances, manufacturing imperfections, skin effects and proximity effects which are harder to replicate in a simulation environment, contributing to the observed discrepancies [79, 80]. These raise the need for caution when interpreting and relying on simulation results in MNP–MH device design which is also noticed in [44].

In Tables 3.1, 3.12, 3.23 the lower magnetic performance of the solenoid coil with round Litz wire compared to the solenoid coil with round wire in contrast to the simulations suggests that Litz wire manual stranding introduced inconsistencies in strand alignment and tension, reducing effective conductivity, compromising magnetic field uniformity, and potentially increasing coil capacitance.

However, in Figure 3.1, inline with the $s\sigma_B$ and $srange_B$ columns of Tables 3.1, 3.12, 3.23 and 3.11, 3.22, 3.33 the histograms for magnetic flux densities and temperature rises of solenoid coil with round Litz wire show a more narrow base, indicating a more homogeneous spatial magnetic field, creating also a more homogeneous heating distribution. On the other hand, when additionally inspecting $smax_B$ and $srange_B$ in Tables 3.1, 3.12, 3.23 the coils without Litz wire both demonstrated distributions with stronger but more dispersed magnetic flux density. They might be seen as better suited for applications requiring narrowly focused heating. However, in Tables 3.1, 3.12, 3.23 and in Figures 3.4, 3.44, 3.84 left panels, none of the coils attain the maximum field at the coil center. This might indicate that, in addition to the physical impediments aforementioned for the simulations, impurities in non–magnetic materials in construction might affect the magnetic flux density patterns.

Likewise, Tables 3.11, 3.22, 3.33 and Figures 3.4, 3.44, 3.84 show that only the solenoid coil with Litz wire achieves maximum heating at the center with the high MNP concentration. Intuitively, higher heating would be expected in positions with strong magnetic flux density but the measurements in Figures 3.4, 3.44, 3.84 contradict that for all of the coils. This might be caused by the high density of iron particles that can enhance interaction between their own electric fields, potentially causing greater

energy dissipation variations through non–thermal pathways [81, 82]. By contrast, the thermal homogeneity properties seen in Figure 3.1 are visible, i.e., the solenoid coil with Litz wire provides the most homogeneous heating in Figure 3.44 compared to Figures 3.4, 3.84.

As in Tables 3.1, 3.12, 3.23 $s\sigma_B$ values were fairly similar, $sHom_B$ and sP_{coil} of the solenoid coil with Litz wire had smaller values because of its distribution shift in Figure 3.1 (left panel). Furthermore, the 'disconnect' between magnetic and thermal properties also reflected onto the heating properties in Tables 3.11, 3.22, 3.33: higher $s\sigma_T$ value of the solenoid coil with round wire lowered $sHom_T$ and sT_{coil} values but this decrease was compensated with the higher sm_T and $smax_T$. While the Helmholtz coil was the overall best performer, solenoid coil with Litz wire performed closer to it in heating whereas the magnetic performance of the solenoid coil with round wire was closer to the Helmholtz coil.

The differences observed between the simulated and measured results highlight the difficulties in precisely modeling the physical processes in an MH system. Accordingly, it's important to note that this study focuses on the electromagnetic and thermal performances of the coils and does not include experiments with tumor tissue or the delivery of MNPs to a tumor. For MH therapy to work, MNPs need to be effectively delivered to the tumor and then heated by the electromagnetic fields. Therefore, future research should look at how to inject MNPs and how the heating works in environments that are similar to real tumors. This would give a better idea of how well this MH system could work for treating cancer.

Overall, these observations suggest evaluating all of the statistics presented in the tables along with the distributions of Figure 3.1 and of Figures 3.4, 3.44, 3.84 is essential for performance assessment rather than a single performance index.

B Novel Liquid Cooling System

Many high–performance coil designs incorporate liquid cooling systems with coolant flowing axially along the coil axis [62, 63]. However, the enclosure surrounding such liquid cooling systems occupies valuable space, particularly on the inner side of the coil, reducing the total volume of the gap found in coil designs. These gaps are critical functional volumes in MH coils, where the anatomical region containing the tumor site is positioned during MH therapy. The coil radius can be increased to compensate for the reduction in functional volume caused by a decrease in the radial dimension, resulting in increased coil impedance. This, in turn, leads to higher power requirement to maintain the initial magnetic field strength [47, 83]. Also, literature reports indicate that MNPs like Fe_3O_4 and $MnFe_2O_4$, at 2 mg/mL concentrations under clinical field conditions, generate only $\approx 0.75 - 2\,\mathrm{W}$ of thermal energy [84, 85]. In contrast, the coil wattage in our system exceeds 150 W at higher frequencies (See Figure 3.128). This disparity underscores the risk of non–selective heating from coil resistive losses, which can inadvertently warm healthy tissues and compromise therapeutic precision. Thus, implementing effective coil cooling is essential to ensure selective and safe MH treatment.

In this study, a novel liquid cooling system utilizing microchannel structures [86] was designed within FEA simulation environment to operate in a frequency range of $0.1 - 2.9\,\mathrm{MHz}$ and a water flow rate range of $0.1 - 0.5\,\mathrm{m/s}$. The frequency range was selected based on its prevalence in MH systems [31], ensuring relevance to current biomedical applications. In contrast, the water flow rate range was determined heuristically, taking into account the microchannel [87] dimensions of the cooling system (0.25, 0.30, and 0.35 mm radii) and the need to maintain stable, laminar flow for effective heat dissipation. Although not derived from empirical tuning or experimental optimization, this range was considered a practical starting point for assessing the cooling system's thermal performance [88, 89]. It provides a realistic baseline for future refinement. Distilled water was chosen as a widely used cooling fluid due to its purity, which reduces the risk of scale deposition and maintains consistent thermal performance. This min-

imizes the impact on heat transfer efficiency, ensuring that the coil's electromagnetic properties are not compromised by impurities or scaling [90, 91]. Results indicate that the proposed novel liquid cooling system (See Figure 2.13 (c)), in which the coolant flows through a microchannel inside the wires axially along the wire axis and contacts the inner wire surface, can effectively address the design challenge mention in the preceding paragraph. This novel design leverages skin effect phenomenon (The tendency of AC to flow on the surface of the wire, with the current density decreasing with depth as the applied frequency increases [92]) by incorporating a cooling microchannel inside the wires, occupying the electron–free region corresponding to AC resistance (See Figure 3.122 (c–d)). This approach enhances thermal management compared to the conventional liquid cooling system (See Table 3.36), while either preserving or reducing the original coil radius. It is important to note that the novel liquid cooling systems with microchannel radii of 0.25, 0.30, and 0.35 mm dissipate heat not only through the microchannel and into the coolant but also via the outer surface of the wires into the surrounding stagnant air. This dual heat dissipation mechanism helps clarify how the novel cooling system outperforms the conventional liquid cooling system. The correct selection of applied frequency–water flow rate combination is crucial, as increase in the applied frequency enhances therapeutic effectiveness by increasing the energy transfer [41, 65], and increase in the water flow rate imposes higher power demands on the pumping system. Disruptive effects of the coil wire temperature on the selectivity of MH thermal therapy [66, 67] may be used as the deciding factor when selecting the optimum operation point. Traditional systems address the reduced selectivity of MH therapy caused by increased coil wire temperature by increasing the coolant flow rate or enlarging the coil wire. However, these approaches often overlook the increased power demands on the pumping system [93] and the reduction in functional volume [94], respectively. Therefore, optimizing the applied frequency and water flow rate input parameters is critical for reducing power demands in any form.

The trend of the performance index across all cooling systems (See Tables 3.42–3.45) highlights the critical interplay between applied frequency and water flow rate. Systems that maintain higher performance indices under increased applied frequencies and reduced water flow rates demonstrate enhanced efficiency, under such less favorable

thermal loads. Notably, the novel liquid cooling system with a 0.35 mm microchannel radius consistently outperformed others, especially conventional liquid cooling system with a prominent performance index difference of 0.614 under 2.9 MHz applied frequency and 0.1 m/s water flow rate condition, indicating that the novel cooling microchannel contributes significantly to thermal regulation effectiveness, with additional passive heat dissipation naturally occurring through the outer surface of the wires to the surrounding stagnant air, further improving the overall cooling efficiency of the system. Additionally, performance gap between the conventional liquid cooling system and the novel liquid cooling system widens with the increasing applied frequency, in favor of the latter. A further increase in the applied frequency is likely to amplify this gap even more, which is promising in terms of the adoptability of the novel liquid cooling system in other RF applications operating at higher frequencies, broadening the significance of the study for future advancements in thermal management across a range of RF technologies. The markedly inferior performance of the conventional liquid cooling system, along with its irregular behavior under certain parameter combinations (Performance indices corresponding to the applied frequency–water flow rate combinations of 0.1 to 0.5 MHz at 0.1 m/s and 0.1 to 0.3 MHz at 0.2 m/s, as bolded entries at Table 3.42), underscores the limitations of traditional cooling approaches under dynamic operating conditions. These findings reinforce the value of the developed performance index as a comparative metric and suggest that fine-tuning structural parameters like microchannel radius can be a key enabler of thermal performance gains.

Two ML models, SVR and GPR, were employed for predictions. SVR was chosen for its flexibility, particularly in handling complex relationships and its robustness to outliers [95]. On the other hand, GPR was selected for its ability to not only predict values but also quantify the uncertainty associated with those predictions, offering deeper insights into the reliability of the performance index [96]. The use of both models enabled a thorough analysis and comparison of different approaches, allowing for an informed decision on the most appropriate algorithm based on the available data. The results demonstrated that the GPR model provided the most accurate performance index predictions (See Figures 3.135, 3.136 and Table 3.46), and consequently, it was adopted for all subsequent model predictions. In practical applications, deviations in

manufacturing precision, operational conditions, and environmental factors can introduce variations in coil liquid cooling system performance compared to simulations. Factors such as material inconsistencies, coolant property fluctuations, flow rate variations, and real–world electrical effects may lead to discrepancies in current density distribution and thermal management efficiency. GPR's uncertainty estimates provide a means to interpret and anticipate these variations, highlighting regions where deviations are more likely and guiding experimental validation or design refinements [96]. Sensitivity analysis and the ReliefF algorithm were applied to the SVR and GPR predictions of the performance index for a deeper evaluation of system behavior (See Table 3.48). The sensitivity analysis results indicate that the water flow rate has a slightly greater impact on performance than the applied frequency across all cooling systems. Meanwhile, the ReliefF algorithm reveals that the overall performance of the conventional liquid cooling system is more influenced by changes in the applied frequency, whereas the novel liquid cooling system's performance is more sensitive to variations in the water flow rate. These results suggest that sensitivity analysis is more relevant (Dominance of water flow rate) when targeting optimal performance at a specific operating point [97] while ReliefF analysis is more applicable (Dominance of applied frequency on the conventional liquid cooling system; water flow rate on the novel liquid cooling systems) when designing an optimized system intended to operate efficiently across a wide range of conditions [73, 74]. This ML–driven approach significantly reduces the computational burden, eliminating the need for a dedicated FEA simulation for every design point and enabling faster design cycles.

It is important to acknowledge prominent limitations of the study. The simulations assumed a steady and uniform flow of the cooling liquid, which may not fully represent the complexities of real–world flow dynamics, such as turbulence or variations in flow rate [98]. Also, keeping the total channel surface area fixed when varying the tube radius is theoretically crucial for better thermal comparisons, but this approach was not preferred in our study. The coil wire length, and thus the available channel length, was fixed to preserve the electromagnetic characteristics of the coil, such as magnetic field distribution and intensity. Adjusting channel length to equalize surface area would disrupt these properties and compromise the system's therapeutic effec-

tiveness. Therefore, thermal optimization was carried out within the constraints of a fixed electromagnetic design. Furthermore, while the ML models demonstrated high predictive accuracy within the studied parameter range, their predictive capability is inherently limited by the scope of the training data [70, 72]. The study's focus on a specific coil geometry and operating conditions also limits the generalizability of the findings to other coil designs or operational scenarios. To address these limitations, future work should primarily focus on experimental validation, representing an important next step in the ongoing development and refinement of this approach.

5. CONCLUSION

This thesis presents a comprehensive framework for the design, optimization, and evaluation of MH systems, addressing critical technical challenges and proposing novel methodologies to enhance therapeutic efficacy and safety.

In the first part of this study, a novel methodology was introduced for quantitatively assessing the performance of MH coils, offering a foundation for more standardized and comprehensive evaluation. Economically viable prototype coils were built in–house for testing this methodology. A systems theoretical approach was undertaken for system identification, utilizing a pickup coil and MNPs with a guiding frame designed and implemented for magnetic flux density and MNP heating measurements at the same spatial locations within the coil volumes. These positional measurements were subsequently used to define performance indices that assess intensity and homogeneity of heating throughout the coil volume for comprehensive cancer cell targeting. The experimental results demonstrated that considering all statistical and distribution data is essential for proper performance assessment rather than relying solely on one or two performance indices. This approach, to the best of our knowledge, is unique. This multidimensional and spatially resolved methodology contrasts with traditional MH assessment techniques, which often rely on average values or peak heating points, potentially overlooking local heating deficiencies that may compromise therapeutic outcomes [99, 100].

The study highlighted several critical aspects and challenges in MH coil design. The results revealed that while economically viable in–house Litz wires provided satisfactory performance, industrial–grade versions could potentially offer significant enhancements in field homogeneity and thermal efficiency. This trade–off between cost and performance aligns with prior findings that highlight the importance of wire geometry, insulation, and strand count in reducing eddy currents and improving heating efficiency [101]. Additionally, it became apparent that the impulse function system

identification using small–size MNP samples was possibly insufficient for capturing inherent non–linearities of the MNP–MH interaction. This led to a disconnect between magnetic and thermal values, necessitating further research into nonlinear dynamic behaviors within MH systems. This observation reflects challenges identified in prior studies where the complex hysteresis and non–equilibrium behavior of MNPs under AMFs could not be adequately captured by linear models [102]. As a result, the thermal output often deviates from predictions based solely on magnetic field parameters.

The absence of eddy current–induced heating in this study was a notable limitation. However, it was recognized that tissue types and sizes, as well as variations in MNP characteristics, would have distinct eddy current responses. Accordingly, the conception and design of large–volume phantoms mimicking tissue properties, e.g., susceptibility and containing an adequate density of MNPs similar to those found in biological tissue are recommended for future studies. Such phantoms would allow for the evaluation of both Joule and magnetic heating, enabling more realistic preclinical assessments and better aligning with emerging standards in MH phantom design [103]. The development of pickup coils capable of measuring all three components of the magnetic flux density would also significantly enhance the accuracy and relevance of performance assessments. To date, few studies have implemented such comprehensive field sensing, which could improve characterization of spatial gradients and anisotropic effects crucial for safe and effective MH treatments.

Furthermore, the findings emphasize the need for more detailed and computationally intensive simulations for pre–assessing coil designs. Incorporating advanced models that account for non–linearities, boundary conditions, and coupling effects with surrounding tissues would allow for a more accurate prediction of coil behavior in clinical settings. This need has been previously acknowledged in studies attempting to bridge the gap between in–vitro tests and in–vivo applications, where oversimplified models have often failed to predict patient specific outcomes [104]. These advancements would be particularly beneficial in bridging the observed gap between magnetic performance and thermal effects.

Another promising avenue for future research involves the integration of real–time monitoring and control systems into MH devices. The addition of magnetic and thermal sensors within coil structures could provide dynamic feedback, enabling adaptive control of heating profiles to maximize therapeutic efficiency while minimizing potential harm to healthy tissue. This strategy supports the emerging field of closed–loop hyperthermia systems, which are gaining attention for their potential to personalize cancer treatment and improve clinical safety [105]. This capability would further enhance the clinical viability of MH technology.

Finally, the scalability and manufacturability of the proposed designs must be explored in greater depth. This includes investigating automated manufacturing techniques and scalable production methods to ensure consistent quality and performance. As discussed in translational device literature, achieving consistent coil geometry and reproducible performance is critical to meet regulatory and clinical standards [106]. Expanding the scope of experiments to include in–vivo studies and clinical trials would provide critical insights into the practical challenges and opportunities associated with the MH therapy.

In the second part of this thesis, three innovative liquid cooling systems for RF coils in MH were developed and evaluated using FEA simulations and ML techniques. Electromagnetic benchmarking confirmed that microchannels with radii of 0.25, 0.30, and 0.35 mm maintained the electromagnetic behavior of solid wires, thereby validating the strategic application of the skin effect in this novel cooling system design [107].

Thermal benchmarking demonstrated a significant performance improvement over conventional liquid cooling systems, with the novel designs achieving lower spatial maximum temperatures, thereby enhancing thermal management in MH RF coils. Notably, the 0.35 mm microchannel design achieved an optimal balance between heat removal and energy efficiency. These findings are consistent with earlier research indicating that microchannel cooling can effectively mitigate thermal issues in high–frequency applications [108].

The application of GPR algorithms further corroborated the superiority of the novel liquid cooling systems. Leveraging uncertainty quantification, the GPR algorithm accurately predicted system behavior, enabling pre–manufacturing design optimization and precise forecasting of performance deviations under experimental conditions. This integration of ML into the design process reflects a growing trend in electromagnetic device optimization, where data–driven models are employed to expedite and enhance design accuracy [109].

To the best of our knowledge, both the implementation of microchannel structured liquid cooling systems and the application of ML for cooling system optimization represent novel contributions to the field of MH RF coil cooling system design, offering the potential for substantial advancements in performance and efficiency. The proposed novel liquid cooling system offers a promising pathway to mitigate RF coil heating, potentially enhancing the efficacy and safety of MH treatment. Furthermore, the promising performance of the novel liquid cooling system suggests its adoptability in other RF applications operating at higher frequencies, broadening the significance of the study for future advancements in thermal management across a range of RF technologies.

In summary, this thesis provides a comprehensive framework for the design and evaluation of MH devices, addressing critical technical challenges while proposing novel systematic assessments. Compared to existing coil evaluation methods, the approach taken here offers superior spatial fidelity and a more nuanced interpretation of performance trade–offs. The insights gained here contribute significantly to the advancement of MH technology, paving the way for future innovations that will enhance the precision, efficiency, and accessibility of this promising therapeutic modality. Despite its limitations, such as the exclusion of tissue-mimicking environments and real–time control systems, this work lays a strong foundation for clinically relevant MH system development. This work represents a foundational step toward the widespread adoption of MH in clinical cancer treatments and sets the stage for further developments in this rapidly evolving field.

REFERENCES

1. Beji, Z., M. Sun, L. S. Smiri, F. Herbst, and et al., "Polyol synthesis of non-stoichiometric mn-zn ferrite nanocrystals: structural/microstructural characterization and catalytic application," *RSC Adv.*, Vol. 5, no. 80, pp. 65010–65022, 2015.

2. Maity, D., and D. C. Agrawal, "Synthesis of iron oxide nanoparticles under oxidizing environment and their stabilization in aqueous and non-aqueous media," *J. Magn. Magn. Mater.*, Vol. 308, no. 1, pp. 46–55, 2007.

3. Wu, Y., Y. Wang, G. Luo, and Y. Dai, "In situ preparation of magnetic fe3o4-chitosan nanoparticles for lipase immobilization by cross-linking and oxidation in aqueous solution," *Bioresour. Technol.*, Vol. 100, no. 14, pp. 3459–3464, 2009.

4. Chin, A. B., and I. I. Yaacob, "Synthesis and characterization of magnetic iron oxide nanoparticles via w/o microemulsion and massart's procedure," *J. Mater. Process. Technol.*, Vol. 191, no. 1-3, pp. 235–237, 2007.

5. Herring, N. P., A. B. Panda, K. AbouZeid, S. H. Almahoudi, and et al., "Microwave synthesis of metal oxide nanoparticles in: A.m. carpenter, s. mathur, a. kolmakov," *Metal Oxide Nanomaterials for Chemical Sensors*, pp. 245–284, 2013.

6. "Defining cancer." https://www.cancer.gov/about-cancer/understanding/what-is-cancer, 2021. Accessed: 5-6-2021.

7. Davis, M. E., "Glioblastoma: Overview of disease and treatment," *Clin. J. Oncol. Nurse*, Vol. 20, Oct 2016.

8. Ishiguro, A., Y. Uno, and Y. Ishiguro, "Correlation of lifting versus non-lifting and microscopic depth if invasion in early colorectal cancer," *Gastrointest Endosc.*, Vol. 50, pp. 329–333, 1999.

9. Skeel, R. T., *Handbook of Cancer Chemotherapy*, Lippincott Williams and Wilkins, 2003.

10. J.Nastoupil, L., A. C. Rose, and C. R. Flowers, "Diffuse large b-cell lymphoma: current treatment approaches," *Oncology*, Vol. 26, pp. 488–495, May 2012.

11. Freedman, A., "Follicular lymphoma: 2012 update on diagnosis and management," *American Journal of Hematology*, Vol. 87, pp. 988–995, Oct 2012.

12. Lindley, C., J. S. McCune, T. E. Thomason, D. Lauder, and et al., "Perception of chemotherapy side effects cancer versus noncancer patients," *Cancer Practice*, Vol. 7, pp. 59–65, Dec 2001.

13. Pinkel, D., "The use of body surface area as a criterion of drug dosage in cancer chemotherapy," *Cancer Research*, Vol. 18, pp. 853–856, Aug 1958.

14. Felici, A., J. Verweij, and A. Sparreboom, "Dosing strategies for anticancer drugs: the good, the bad and body-surface area," *European Journal of Cancer*, Vol. 38, pp. 1677–1684, Sep 2002.

15. Baker, S. D., J.Verweij, E. K. Rowinsky, R. Donehower, and et al., "Role of body surface area in dosing of investigational anticancer agents in adults, 1991-2001," *Journal of the National Cancer Institute*, Vol. 94, pp. 1883–1888, Dec 2002.

16. Hickman, J. A., "Apoptosis and chemotherapy resistance," *European Journal of Cancer*, Vol. 32, pp. 921–926, Jun 1996.

17. Maverakis, E., L. A. Cornelius, G. M. Bowen, T. Phan, and et al., "Metastatic melanoma - a review of current and future treatment options," *Acta Dermato-Venereologica*, Vol. 95, pp. 516–524, May 2015.

18. Brown, A., and H. Suit, "The centenary of the discovery of the bragg peak," *Radiotherapy and Oncology*, Vol. 73, pp. 265–268, Dec 2004.

19. Cesmeli, S., and C. B. Avci, "Application of titanium dioxide (tio2) nanoparticles in cancer therapies," *Journal of Drug Targeting*, Vol. 27, pp. 762–766, Oct 2019.

20. Zhou, J., G. Wang, Y. Chen, H. Wang, and et al., "Immunogenic cell death in cancer therapy: Present and emerging inducers," *Journal of Cellular and Molecular Medicine*, Vol. 23, pp. 4854–4865, Jun 2019.

21. Khiabani, S. S., M. Farshbaf, A. Akbarzadeh, and S. Davaran, "Magnetic nanoparticles: preparation methods, applications in cancer diagnosisand cancer therapy," *Artificial Cells, Nanomedicine, and Biotechnology*, Vol. 45, pp. 6–17, Apr 2016.

22. "Hyperthermia to treat cancer." https://www.cancer.gov/about-cancer/treatment/types/hyperthermia, 2021. Accessed: 10-7-2021.

23. Gilchrist, R. K., "Selective inductive heating of lymph nodes," *Ann. Surg.*, Vol. 146, pp. 596–606, Oct 1957.

24. Perigo, E. A., "Fundamentals and advances in magnetic hyperthermia," *Phys. Rev.*, Vol. 2, no. 4, 2015.

25. Mallory, M., E. Gogineni, G. C. Jones, L. Greer, and et al., "Therapeutic hyperthermia: The old, the new and the upcoming," *Crit. Rev. Oncol. Hematol.*, Vol. 97, pp. 30018–30024, Aug 2015.

26. Javidi, M., M. Heydari, A. Karimi, M. Haghpanahi, and et al., "Evaluation of the effects of injection velocity and different gel concentrations on nanoparticles in hyperthermia therapy," *Journal of Biomedical Physics and Engineering*, Vol. 4, no. 4, pp. 151–162, 2014.

27. Javidi, M., M. Heydari, M. M. Attar, M. Haghpanahi, and et al., "Cylindrical agar gel with fluid flow subjected to an alternating magnetic field during hyperthermia," *International Journal of Hyperthermia*, Vol. 31, no. 1, pp. 33–39, 2014.

28. Heydari, M., M. Javidi, M. M. Attar, A. Karimi, and et al., "Magnetic fluid hyperthermia in a cylindrical gel contains water flow," *Journal of Mechanics in Medicine and Biology*, Vol. 15, no. 5, 2015.

29. Seip, R., and E. S. Ebbini, "Noninvasive estimation of tissue temperature response to heating fields using diagnostic ultrasound," *IEEE Trans. Biomed. Eng.*, Vol. 42, no. 8, pp. 828–839, 1995.

30. Oura, S., "Radiofrequency ablation therapy in patients with breast cancers two centimeters or less in size," *Breast Cancer*, Vol. 14, no. 1, pp. 48–54, 2007.

31. Tishin, A. M., A. A. Shtil, A. P. Pyatakov, and V. I. Zvrev, "Developng antitumor magnetic hyperthermia: Principles, materials and devices," *Recent Patents on Anti-Cancer Srug Discovery*, Vol. 11, pp. 360–375, 2016.

32. Biase, J. N., E. D. Whitehead, F. Miller, and S. Hoffman, "Unilateral unitary inflatable penile prosthesis to correct impaired tumescence and severr penile deformity resulting from traumatic rupture of 1 corpus cavernosum," *J. Urol.*, Vol. 152, pp. 2098–2100, Dec 1994.

33. Chen, G., I. Roy, C. Yang, and P. N. Prasad, "Nanochemistry and nanomedicine for nanoparticle-based diagnostics and therapy," *Chem. Rev.*, Vol. 116, no. 5, pp. 2826–2885, 2016.

34. Khalili, S. R., R. E. Farsani, N. Soleimani, and Z. Hedayatnasab, "Charpy impact behavior of clay/basalt fiber-reinforced polypropylene nanocomposites at various temperatures," *J. Thermoplast Compos. Mater.*, 2014.

35. Reddy, L. H., J. L. Arias, J. Nicolas, and P. Couvreur, "Magnetic nanoparticles: design and characterization, toxicity and biocompatibility, pharmaceutical and biomedical applications," *Chem. Rev.*, Vol. 112, no. 11, pp. 5818–5878, 2012.

36. Ali, R., A. Mahmood, M. A. Khan, A. H. Chughtai, and et al., "Impacts of ni-co substitution on the structural, magnetic and dielectric properties of magnesium nanoferrites fabricated by micro-emulsion method," *J. Alloys Compd.*, Vol. 584, pp. 363–368, 2014.

37. Tailhades, P., B. Gillot, and A. Rousset, "Mixed-valence defect ferrites: a new family of fine powders and thin films of spinel ferrites," *Journal de Physique IV Colloque 07*, pp. 241–252, 1997.

38. Ito, A., M. Shinkai, H. Honda, and T. Kobayashi, "Medical applications of functionalized magnetic nanoparticles," *J. Biosci. Bioeng.*, Vol. 100, pp. 1–11, 2005.

39. Murase, K., H. Takata, Y. Takeuchi, and S. Saito, "Control of the temperature rise in magnetic hyperthermia with use of an external static magnetic field," *Physica Medica*, Vol. 29, pp. 624–630, 2013.

40. Stigliano, R. V., F. Shubitidze, J. D. Petryk, L. Shoshiashvili, and et al., "Mitigation of eddy current heating during magnetic nanoparticle hyperthermia therapy," *International Journal of Hyperthermia*, Vol. 32, pp. 735–748, Jul 2016.

41. Atkinson, W. J., I. A. Brezovich, and P. Chakraborty, "Usable frequencies in hyperthermia with thermal seeds," *IEEE Transactions on Biomedical Engineering*, Vol. BME-31, Jan 1984.

42. Khan, A. S., M. F. Nasir, M. T. Khan, A. Murtaza, and et al., "Study of structural, magnetic and radio frequency heating aptitudes of pure and (fe-iii) doped manganite (la1-xsrxmno3) and their incorporation with sodium poly-styrene sulfonate (pss) for magnetic hyperthermia appliacations," *Phys. B. Condens. Matter.*, 2021.

43. Ernst, R. R., "Measurement and control of magnetic field homogeneity," *The Review of Scientific Instruments*, Vol. 39, Jan 1968.

44. Attaluri, A., "Design and construction of a maxwell-type induction coil for magnetic nanoparticle hyperthermia," *Int. J. Hyperth.*, Vol. 37, no. 1, pp. 1–14, 2020.

45. Skumiel, A., B. Leszczynski, M. Molcan, and M. Timko, "The comparison of magnetic circuits used in magnetic hyperthermia," *J. Magn. Mater.*, Vol. 420, pp. 177–184, 2016.

46. Abetti, P. A., and F. J. Maginniss, "Natural frequencies of coils and windings determined by equivalent circuit," *Transactions of the American Institute of Electrical Engineers. Part III Power Apparatusand Systems*, Vol. 72, pp. 495–504, Jun 1953.

47. Kazimierczuk, M. K., *High-Frequency Magnetic Components: 2nd Edition*, Wiley, 2013.

48. Oppenheim, A. V., A. S. Willsky, and I. T. Young, *Signals and Systems*, Prentice Hall, 1996.

49. Bowick, C., *RF Circuit Design*, Newnes; 2nd edition, 1982.

50. Garaio, E., J. M. Collantes, F. Plazaola, J. A. Garcia, and et al., "A multifrequency electromagnetic applicator with an integrated ac magnetometer for magnetic hyperthermia experiments," *Meas. Sci. Technol.*, Vol. 25, no. 11, 2014.

51. "Electronics and innovation 1140la rf amplifier, 9 khz to 2 mhz, class ab, 1000 w." https://www.bellnw.com/manufacturer/Electronics-and-Innovation/1140LA.htm, 2021. Accessed: 20-7-2021.

52. "Draper iht-30 liquid cooled 3.5kw induction heater." https://www.machinemart.co.uk/p/draper-76171-liquid-cooled-35kw-induction-heat/, 2021. Accessed: 19-7-2021.

53. Cao, X., D. Zu, X. Zhao, Y. Fan, and et al., "The design of a low-noise preamplifier for mri," *Sci. China Technol. Sci.*, Vol. 54, no. 7, pp. 1766–1770, 2011.

54. Zhao, Q., "Magnetic nanoparticle-based hyperthermia for head and neck cancer in mouse models," *Theranostics*, Vol. 2, no. 1, pp. 113–121, 2012.

55. Biron, M., *Thermoplastics and Thermoplastic Composites*, William Andrew, 2013.

56. Nelson, J. C. C., *Operation Amplifier Circuits: Analysis and Design*, Butterworth-Heinemann, 1995.

57. Prabhakaran, S., and C. R. Sullivan, "Impedance-analyzer measurements of high-frequency power passives: techniques for high power and low impedance," in *IEEE Industry Applications Conference Book. 37th IAS Annual Meeting*, IEEE Industry Applications Conference. 37th IAS Annual Meeting, 2002.

58. Alexander, C., and M. Sadik, *Fundamentals of Electric Circuits*, McGraw-Hill Education; 6th edition, 2016.

59. Abidin, M., and N. M. Y., "Numerical simulation of heat transfer using finite element method," *J. Adv. Res. Fluid Mech. Therm. Sci.*, Vol. 92, pp. 104–115, 2022.

60. Kuczmann, M., and N. Ivanyi, *The Finite Element Method in Magnetics*, Akademiai Kiado, 2008.

61. Reddy, J., *An Introduction to The Finite Element Method*, McGraw Hill, 2006.

62. Lei, J., L. Shen, Y. Bi, and J. Chen, "A design of cooling water jacket structure and an analysis of its coolant flow characteristics for a horizontal diesel engine," *SAE Technol. Pap.*, Vol. 21, 2011.

63. Thulukkanam, K., *Heat Exchanger Design Handbook*, CRC Press, 2013.

64. Engineering, T. M. D. A., "Total materia database," 2023.

65. Parte, B., I. Rodrigo, J. Gutierrez-Basoa, S. I. Correcher, and et al., "Proposal of new safety limits for in vivo experiments of magnetic hyperthermia antitumor therapy," *Cancers*, Vol. 14, no. 3084, 2022.

66. Sharma, A., A. Jangam, J. L. Y. Shen, A. Ahmad, and et al., "Validation of a temperature-feedback controlled automated magnetic hyperthermia therapy device," *Cancers*, Vol. 15, no. 327, 2023.

67. Vilas-Boas, V., F. Carvalho, and B. Espina, "Magnetic hyperthermia for cancer treatment: Main parameters affecting the outcome of in vitro and in vivo studies," *Molecules*, Vol. 25, no. 2874, 2020.

68. Baldick, R., *Applied Optimization: Formulation and Algorithms for Engineering Systems*, IEEE Control. Syst. Mag., 2008.

69. Rao, S., *Engineering Optimization Theory and Practice*, John Wiley and Sons, 2019.

70. Muller, A., and S. Guido, *Introduction to Machine Learning with Python: A Guide for Data Scientists*, O'Reilly Media, 2016.

71. Draper, N., and H. Smith, *Applied Regression Analysis*, John Wiley and Sons, 1998.

72. Kuhn, M., and K. Johnson, *Applied Predictive Modeling*, Springer, 2013.

73. Kira, K., and L. Rendell, "The feature selection problem: Traditional methods and a new algorithm," in *Proceedings of AAAI*, 10th Conference on Artificial Intelligence, 1992.

74. Robnik-Sikonja, M., and I. Kononenko, "Theoretical and empirical analysis of relieff and rrelieff," *Mach. Learn. J.*, Vol. 53, pp. 23–69, 2003.

75. Hadadian, Y., M. Azimbagirad, E. A. Navas, and T. Z. Pavan, "A versatile induction heating system for magnetic hyperthermia studies under different experimental conditions," *Review of Scientific Instruments*, Vol. 90, p. 074701, 2019.

76. Arunima, R., and S. Kumar, "Review on magnetic nanoparticle-mediated hyperthermia for cancer therapy," *Journal of Nanoparticle Research*, Vol. 22, no. 11, 2020.

77. Suriyanto, M. G. R. I., E. Ng, and S. D. Kumar, "Physical mechanism and modeling of heat generation and transfer in magnetic fluid hyperthermia through néelian and brownian relaxation: a review," *BioMedical Engineering OnLine*, Vol. 16, no. 1, p. 36, 2017.

78. Yoner, S. I., and A. Ozcan, "Finite element method modelling of iron – oxide nanoparticle heat generation under low radio frequency field conditions," in *IFMBE Conference Proceedings*, 19th Nordic–Baltic Conference on Biomedical Engineering and Medical Physics, 2023.

79. Guillod, T., J. Huber, F. Krismer, and J. W. Kolar, "Litz wire losses: Effects of twisting imperfections," in *IEEE Conference Proceedings*, IEEE 18th Workshop on Control and Modeling for Power Electronics (COMPEL), 2017.

80. Salk, N., and C. Cooke, "A versatile simulation–assisted layered mesh analysis for generalized litz wire performance," *IEEE Transactions on Magnetics*, Vol. 58, no. 6, pp. 17501–17510, 2022.

81. Jackson, J., *Classical Electrodynamics*, John Wiley and Sons, 1998.

82. Ashcroft, N., and D. Mermin, *Solid–State Physics*, Brooks/Cole Cengage Learning, 2021.

83. Welsby, V., *The Theory and Design of Inductance Coils*, Macdonald and Co. Ltd., 1950.

84. Nemala, H., J. S. Thakur, G. Lawes, V. Naik, and et al., "Investigation of magnetic properties of fe3o4 nanoparticles using temperature dependent magnetic hyperthermia in ferrofluids," *J. Appl. Phys.*, Vol. 116, 2014.

85. Patade, S., D. D. Andhare, S. B. Samvanshi, S. A. Jadhav, and et al., "Self-heating evaluation of superparamagnetic mnfe2o4 nanoparticles for magnetic fluid hyperthermia application towards cancer treatment," *Ceram. Int.*, Vol. 46, pp. 25576–25583, 2020.

86. Bognar, G., G. Takacs, and P. G. Szabo, "A novel approach for cooling chiplets in heterogeneously integrated 2.5-d packages applying microchannel heatsink embedded in the interposer," *IEEE Trans. Compon. Packag. Manuf. Technol.*, Vol. 13, pp. 1155–1163, 2023.

87. Haridas, D., A. D. Tharkar, and U. Nimbalkar, *Precision Cooling: Microchannel Heat Exchangers in Modern Engineering*, Uttar Pradesh, India: Parab Publications, 2024.

88. Ray, D., and D. Das, "Simulations of flows via cfd in microchannels for characterizing entrance region and developing new correlations for hydrodynamic entrance length," *Micromachines*, Vol. 14, p. 1418, 2023.

89. Christov, I., V. Cognet, T. C. Shidhore, and H. A. Stone, "Flow rate-pressure drop relation for deformable shallow microfluidic channels," *J. Fluid Mech.*, Vol. 841, pp. 267–286, 2018.

90. Bhatkar, O., P. Kudav, S. Pendhari, A. Bhojane, and et al., "Study and design of engine cooling system with distilled water as a coolant for fsae car," *Int. Res. J. Eng. Technol.*, Vol. 4, pp. 585–587, 2017.

91. Abdulmunem, A., "Experimental comparison between conventional coolants and (tio2/water) nanofluid to select the best coolant for automobiles in iraq's summer season," *Eng. Technol. J.*, Vol. 34, p. 15, 2016.

92. Lorrain, P., D. R. Corson, and F. Lorrain, *Electromagnetic Fields and Waves*, New York, NY, USA: W.H. Freeman & Co., 1987.

93. Kleinstreuer, C., *Microfluidics and Nanofluidics: Theory and Selected Applications*, Hoboken, NJ, USA: John Wiley & Sons Inc., 2013.

94. Tang, Y., Y. Ding, T. Jin, and R. C. C. Flesch, "Improvement for magnetic field uniformity of helmholtz coils and its influence on magnetic hyperthermia," *IEEE Trans. Instrum. Meas.*, Vol. 72, p. 3325860, 2023.

95. SchÃ¶lkopf, B., *Learning with Kernels: Support Vector Machines, Regularization, Optimization, and Beyond*, Cambridge, MA, USA: MIT Press, 2002.

96. Rasmussen, C., and C. Williams, *Gaussian Processes for Machine Learning*, Cambridge, MA, USA: MIT Press, 2006.

97. Kleijnen, J., "Sensitivity analysis and related analyses: A review of some statistical techniques," *J. Stat. Comput. Simul.*, Vol. 57, pp. 111–142, 1997.

98. White, F., *Viscous Fluid Flow*, New York, NY, USA: McGraw Hill, 2005.

99. Pankhurst, Q., J. Connolly, S. K. Jones, and J. Dobson, "Applications of magnetic nanoparticles in biomedicine," *Journal of Physics D: Applied Physics*, Vol. 36, no. 13, pp. R167–R181, 2003.

100. Hergt, R., S. Dutz, R. Muller, and M. Zeisberger, "Magnetic particle hyperthermia: nanoparticle magnetism and materials development for cancer therapy," *Journal of Physics: Condensed Matter*, Vol. 18, no. 38, pp. S2919–S2934, 2006.

101. Dutz, S., and R. Hergt, "Magnetic particle hyperthermia-a promising tumor therapy?," *Nanotechnology*, Vol. 25, no. 45, p. 452001, 2014.

102. Carrey, J., B. Mehdaoui, and M. Respaud, "Simple models for dynamic hysteresis loop calculations of magnetic single-domain nanoparticles: Application to magnetic hyperthermia optimization," *Journal of Applied Physics*, Vol. 109, no. 8, p. 083921, 2011.

103. Dennis, C., A. J. Jackson, J. A. Borchers, and R. Ivkov, "The influence of collective behavior on the magnetic and heating properties of iron oxide nanoparticles: Initial insights into ideal particle designs for magnetic hyperthermia," *Journal of Applied Physics*, Vol. 103, no. 7, p. 07A319, 2008.

104. Zorbas, G., and T. Samaras, "Numerical modeling of radiofrequency ablation of tumors embedded in realistic anatomy," in *Proceedings of the BIOEM 2024*, (Cape Town, South Africa), 2014.

105. Thiesen, B., and A. Jordan, "Clinical applications of magnetic nanoparticles for hyperthermia," *International Journal of Hyperthermia*, Vol. 24, no. 6, pp. 467–474, 2008.

106. Khandhar, A., R. M. Ferguson, J. A. Simon, and K. M. Krishnan, "Tailored magnetic nanoparticles for optimizing magnetic fluid hyperthermia," *Journal of Biomedical Materials Research Part A*, Vol. 101, no. 9, pp. 2246–2253, 2013.

107. Yoner, S., and A. Ozcan, "Design of a novel liquid cooling system in simulation environment for radio frequency coils used in magnetic hyperthermia systems," in *Proceedings of the 12th International Conference on Biomedical Engineering Systems*, (Barcelona, Spain), August 19-21 2024.

108. Koo, C., R. F. Godley, J. Park, M. P. McDougall, and et al., "A magnetic resonance (mr) microscopy system using a microfluidically cryo-cooled planar coil," *Lab Chip*, Vol. 11, no. 13, pp. 2197–2203, 2011.

109. Giovannetti, G., N. Fontana, A. Flori, M. F. Santarelli, and et al., "Machine learning for the design and the simulation of radiofrequency magnetic resonance coils: Literature review, challenges, and perspectives," *Sensors*, Vol. 24, no. 6, p. 1954, 2024.

110. Mussa, A., *New Technologies in SUrgical Oncology*, Springer, 2010.

111. Cera, S., and S. D. Wexner, "Minimally invasive treatment of colon cancer," *Cancer J.*, Vol. 11, pp. 26–35, 2005.

112. Kalloo, A. N., V. K. Singh, and S. B. Jagannath, "Flexible transgastric peritoneoscopy: a novel approach to diagnostic and therapeutic interventions in the peritoneal cavity," *Gastrointest Endosc.*, Vol. 60, pp. 114–117, 2004.

113. Buess, G., K. Kipfmuller, and R. Ibald, "Transanal endoscopic microsurgery in rectal cancer," *Chirurg*, Vol. 60, pp. 901–904, 1989.

114. Povoski, S., R. L. Neff, and C. M. Mojzisik, "A comprehensive overview of radioguided surgery using gamma detection probe technology," *World J. Surg. Oncol.*, Vol. 7, no. 11, 2009.

115. Rampaul, R. S., M. Bagnall, and H. Burrell, "Randomized clinical trial comparing radioisotope occult lesion localization and wire-guided excision for biopsy of occult breast lesions," *Br. J. Surg.*, Vol. 91, pp. 1575–1577, 2004.

116. Ronka, R., L. Krogerus, and E. Leppanen, "Radio-guided occult lesion localization in patients undergoing breast conserving surgery and sentinel node biopsy," *Am. J. Surg.*, Vol. 187, pp. 491–496, 2004.

117. Ju, M. V., and T. G. Moizhess, "Tumorigenicity of sarcoma cells is enhanced by the local environment of implanted foreign body," *Int. J. Cancer*, Vol. 30, pp. 525–529, 1982.

118. Jennings, T. A., L. Peterson, and C. A. Axiotis, "Angiosarcoma associated with foreign body material. a report of three cases," *Cancer*, Vol. 62, pp. 2436–2444, 1988.

119. Ghadimi, B. M., C. Langer, and H. Becker, "The carcinogenic potential of biomaterials in hernia surgery," *Chirung*, Vol. 73, pp. 833–837, 2002.

120. Bann, S., M. Khan, and J. Hernandez, "Robotics in surgery," *Am. Coll. Surg.*, Vol. 5, pp. 784–795, 2003.

121. Ballantyne, G. H., "Robotic surgery, telerobotic surgery, telepresence and telementoring. review of early clinical results," *Surg. Endosc.*, Vol. 16, pp. 1389–1402, 2002.

122. Estey, E. P., "Robotic prostatectomy: The new standard of care or a marketing success?," *Canadian Urological Association Journal*, Vol. 3, no. 6, pp. 488–490, 2009.

123. Barbash, G. I., and S. A. Glied, "New technology and health care costs - the case of robot-assisted surgery," *The New England Journal of Medicine*, Vol. 363, pp. 701–704, Aug 2010.

124. Finkelstein, J., E. Eckersberger, H. Sadri, S. S. Taneja, and et al., "Open versus laparoscopic versus robot-asissted laparoscopic prostatectomy: The european and us experience," *Reviews in Urology*, Vol. 12, no. 1, pp. 35–43, 2010.

125. Spinelli, A., G. David, S. Gidaro, M. Carvello, and et al., "First experience in colorectal surgery with a new robotic platform with haptic feedback," *Colorectal Disease*, Vol. 20, no. 3, pp. 228–235, 2018.

126. Lee, D. I., "Robotic prostatectomy: what we have learned and where we are going," *Yonsei Medical Journal*, Vol. 50, pp. 177–181, Apr 2009.

127. Tajiri, H., K. Matsuda, and J. Fujisaki, "What can we see with the endoscope? present status and future perspectives," *Dig Endosc.*, Vol. 14, pp. 131–137, 2002.

128. Alfarouk, K., C. Stock, S. Taylor, M. Walsh, and et al., "Resistance to cancer chemotherapy: failure in drug response from adme to p-gp," *Cancer Cell International*, Vol. 15, p. 71, Jul 2015.

129. Johnstone, R. W., A. A. Ruefli, and S. W. Lowe, "Apoptosis: a link between cancer genetics and chemotherapy," *Cell*, Vol. 108, pp. 153–164, Jan 2002.

130. Chabner, B., and D. L. Longo, *Cancer Chemotherapy and Biotherapy: Principles and Practice*, Lippincott Williams and Wilkins, 2005.

131. Corrie, P. G., and G. Pippa, "Cytotoxic chemotherapy: clinical aspects," *Medicine*, Vol. 36, no. 1, pp. 24–28, 2008.

132. Rampling, R., A. James, and V. Papanastassiou, "The present and future management of malignant brain tumours: surgery, radiotherapy, chemotherapy," *Journal of Neurology, Neurosurgery, and Psychiatry*, Vol. 75, pp. 24–30, Jun 2004.

133. DuBois, D., and E. F. DuBois, "A formula to estimate the approximate surface area if height and weight be known. 1916," *Nutrition*, Vol. 5, no. 5, pp. 303–311, 1989.

134. Kaestner, S. A., and G. J. Sewell, "Chemotherapy dosing part i: scientific basis for current practice and use of body surface area," *Clinical Oncology*, Vol. 19, pp. 23–27, Feb 2007.

135. "Radiation therapy." https://www.cancer.org.au/cancer-information/treatment/radiation-therapy, 2021. Accessed: 4-7-2021.

136. Gerbaulet, A., R. Potter, J. J. Mazeron, H. Meertens, and et al., *The GEC ESTRO Handbook of Brachytherapy*, Leuven, Belgium: European Society for Therapeutic Radiology and Oncology, 2002.

137. Pollack, A., and A. Mansoor, *Hypofractionation: Scientific Concepts and Clinical Experiences*, Ellicot City: LimiText Publishing, 2011.

138. Bomford, C. K., I. H. Kunkler, and J. Walter, *Walter and Miller's Textbook of Radiation Therapy*, Churchill Livingstone; 7th edition, 2012.

139. Lee, V. H., S. C. Ng, T. W. Leung, G. K. Au, and et al., "Dosimetric predictors of radiation-induced acute nausea and vomiting in imrt for nasopharyngeal cancer," *International Journal of Radiation Oncology, Biology, Physics*, Vol. 84, pp. 176–182, Sep 2012.

140. "Radiation therapy side effects and ways to manage them." https://www.cancer.gov/publications/patient-education/radiation-therapy-and-you, 2007. Accessed: 2-5-2012.

141. Hall, E. J., *Radiobiology for the Radiologist*, Philadelphia: Lippincott Williams Wilkins., 2000.

142. Carretero, C., M. Munoz-Navas, M. Betes, R. Angos, and et al., "Gastroduodenal injury after radioembolization of hepatic tumors," *The American Journal of Gastroenterology*, Vol. 102, pp. 1216–1220, Jun 2007.

143. Henson, C. C., S. Burden, S. E. Davidson, and S. Lal, "Nutritional interventions for reducing gastrointestinal toxicity in adults undergoing radical pelvic radiotherapy," *Cochrane Database of Systematic Reviews*, Vol. 11, Nov 2013.

144. Meek, A. G., "Breast radiotherapy and lymphedema," *Cancer*, Vol. 83, pp. 2788–2797, Dec 1998.

145. Kamran, S. C., A. B. de Gonzalez, A. Ng, D. Haas-Kogan, and et al., "Therapeutic radiation and the potential risk of second malignancies," *Cancer*, Vol. 122, pp. 1809–1821, Jun 2016.

146. Mohamad, O., T. Tabuchi, Y. Nitta, A. Nomoto, and et al., "Risk of subsequent primary cancers after carbon ion radiotherapy, photon radiotherapy, or surgery for localised prostate cancer: a propensity score-weighted, retrospective, cohort study," *The Lancet. Oncology*, Vol. 20, pp. 674–685, May 2019.

147. Weintraub, N. L., W. K. Jones, and D. Manka, "Understanding radiation-induced vascular disease," *Journal of the American College of Cardiology*, Vol. 55, pp. 1237–1239, Mar 2010.

148. Klee, N. S., C. G. McCarthy, P. Martinez-Quinones, and R. C. Webb, "Out of the frying pan and into the fire: damage-associated molecular patterns and cardiovascular toxicity following cancer therapy," *Therapeutic Advances in Cardiovascular Disease*, Vol. 11, pp. 297–317, Nov 2017.

149. "Late effects of treatment for childhood cancer." https://www.cancer.gov/types/childhood-cancers, 2012. Accessed: 7-6-2012.

150. Hauer-Jensen, M., J. W. Denham, and H. J. Andreyev, "Radiation enteropathy-pathogenesis, treatment and prevention," *Nature Reviews. Gastroenterology and Hepatology*, Vol. 11, pp. 470–479, Aug 2014.

151. Custodio, C., and C. C. Andrews, "Radiation plexopathy," *American Academy of Physical Medicine and Rehabilitation*, Aug 2017.

152. Delanian, S., J. L. Lefaix, and P. F. Pradat, "Radiation-induced neuropathy in cancer survivors," *Radiotherapy and Oncology*, Vol. 105, pp. 273–282, Dec 2012.

153. "Radiation necrosis: Background, pathophysiology, epidemiology." https://emedicine.medscape.com/article/1157533-overview, 2019. Accessed: 9-11-2019.

154. Arnon, J., D. Meirow, H. Lewis-Roness, and A. Ornoy, "Genetic and teratogenic effects of cancer treatments on gametes and embryos," *Human Reproduction Update*, Vol. 7, no. 4, pp. 394–403, 2001.

155. Fernandez, A., M. Brada, L. Zabuliene, N. Karavitaki, and et al., "Radiation-induced hypopitutarism," *Endocrine-Related Cancer*, Vol. 16, pp. 733–772, Sep 2009.

156. Adachi, J., and et al., "Enhancing heating efficiency of magnetic hyperthermia using pulsed magnetic fields," in *AIP Conference Proceedings*, 68th Annual Conference on Magnetism and Magnetic Materials, 2024.

157. Bullivant, Y., and et al., "Materials characterization of feraheme/ferumoxytol and preliminary evaluation of its potential for magnetic fluid hyperthermia," *Int. J. Mol. Sci.*, pp. 17501–17510, 2013.

158. Incropera, F., and et al., *Fundamentals of Heat and Mass Transfer*, John Wiley and Sons, 2007.

159. Lee, M., and J. Seo, *Heat Transfer in Engineering*, MDPI AG, 2022.

160. “Health, n.i.o. turkey-us collaborative program for affordable medical technologies (r01).” https://grants.nih.gov/grants/guide/pa-files/PAR-15-276.html, 2015. Accessed: 17-10-2022.